

DISS. ETH NO. 25854

**GNSS receiver synchronisation and antenna
calibration**

A thesis submitted to attain the degree of
DOCTOR OF SCIENCES of ETH ZURICH
(Dr. sc. ETH Zurich)

presented by

Daniel Henry Willi
MSc ETH Geom Eng, ETH Zurich

born on 27.08.1990
citizen of Domat/Ems GR

accepted on the recommendation of
Prof. Dr. Markus Rothacher
Prof. Dr.-Ing. Steffen Schön

2019

*'Suave, mari magno turbantibus aequora ventis
E terra magnum alterius spectare laborem;
Non quia vexari quemquamst iucunda voluptas,
Sed quibus ipse malis careas quia cernere suavest.
Suave etiam belli certamina magna tueri
Per campos instructa tua sine parte pericli;
Sed nihil dulcius est, bene quam munita tenere
Edita doctrina sapientum templa serena,
Despicere unde queas alios passimque videre
Errare atque viam palantis quaerere vitae,
Certare ingenio, contendere nobilitate,
Noctes atque dies niti praestante labore
Ad summas emergere opes rerumque potiri.'*

'Il est doux, quand la vaste mer est soulevée par les vents, d'assister du rivage à la détresse d'autrui; non qu'on trouve si grand plaisir à regarder souffrir; mais on se plaît à voir quels maux vous épargnent. Il est doux aussi d'assister aux grandes luttes de la guerre, de suivre les batailles rangées dans les plaines, sans prendre sa part du danger. Mais la plus grande douceur est d'occuper les hauts lieux fortifiés par la pensée des sages, ces régions sereines d'où s'aperçoit au loin le reste des hommes, qui errent çà et là en cherchant au hasard le chemin de la vie, qui luttent de génie où se disputent la gloire de la naissance, qui s'épuisent en efforts de jour et de nuit pour s'élever au faite des richesses ou s'emparer du pouvoir.'

Lucrèce, *De rerum natura*, Liber II, I^{er} siècle avant notre ère.

Traduction par Henri Clouard.

Abstract

CubETH is a project of a scientific nano-satellite of $10 \times 10 \times 10 \text{ cm}^3$ size. Its destination is a Low Earth Orbit (LEO) at 450 km height above the Earth surface. The spacecraft is equipped with ten Global Navigation Satellite Systems (GNSS) receivers and five GNSS antennas. The employed GNSS receivers are manufactured by the Swiss company u-blox. They are called ‘commercial off-the-shelf’ chipsets, but are extremely well suited to be used in space: their power consumption, their weight and their size are very small.

As the satellite is equipped with four antennas on its upper size, GNSS attitude determination can be performed. The attitude is the orientation of the spacecraft relatively to a reference frame, for instance the terrestrial reference frame. In GNSS attitude determination, the relative position of the antennas with respect to each other is used.

As a first part of the present doctoral thesis, an algorithm for GNSS attitude determination was developed. Compared to the algorithms in the scientific literature, the GNSS measurements are extrapolated. The extrapolation term ranges approximately from -6 to +6 m. The need for extrapolation is a consequence of the non-synchronicity of the receivers. The measurement epoch lies within a window of 1 ms around the nominal measurement epoch. Because of the high velocity of the spacecraft in LEO (about 8 km/s), extrapolation of the measurements is crucial.

The new algorithm was tested throughout. A hardware in the loop signal simulator test campaign was conducted successfully. The algorithm was also proven to work in a static real data experiment on the ground.

From the first experiences with a model of the CubETH spacecraft, it became obvious that the limiting factor for the accuracy are the antennas. Mutual coupling of the antennas can theoretically not be excluded for baselines shorter than one wavelength. A relative field calibration was set up to obtain Phase Centre Corrections (PCC) for the antennas on the satellite model. PCC are correction values that depend on the frequency and on the direction of the incoming signals. PCC have been studied since the beginning of the US Global Positioning System (GPS) in the 80s, theoretically and experimentally. However, low-cost antennas in the vicinity of each other, as onboard CubETH, have never been in the scientific focus.

The results from the relative field calibration show that mutual coupling occurs. The magnitude of the PCC range up to several centimetres. It is shown that the application of PCC is crucial in order to estimate an unbiased attitude with GNSS. The experiments also showed the limitation of the relative field calibration. It is extremely prone to multipath errors.

The focus of the second part of the present doctoral thesis lies on absolute field calibration for GNSS antennas. This reorientation is a consequence of unexpected delay in the CubETH project. In less than 18 months, an operational GNSS antenna calibration facility was developed. It uses a six-axis industrial robot to bring the antenna to be calibrated into various orientations. Reference data is collected on a station just a few metres away from the robot. The data is processed on the triple-difference level, i.e., on time-differences of classical double-differences.

The system is currently able to generate calibrations for any Code Division Multiple Access (CDMA) signal, if enough GNSS spacecraft are visible. Calibration of the Russian GLONASS Frequency Division Multiple Access (FDMA) signals is a matter of implementation.

Various analyses show that the repeatability of the calibrations is below the millimetre-level. A comparison with the de facto standard, PCC from the German company Geo++[®] GmbH, allowed to verify that the results are meaningful and that they are in the same accuracy range as the reference PCC. Calibrations of GNSS receiver antennas for signals of the European satellite navigation system Galileo were presented at the International GNSS Service (IGS) Workshop 2018 in Wuhan. Our new system is the first absolute field calibration that reportedly generated calibrations for Galileo signals. This is an important step towards a better combination of all available GNSS.

In contrast to the US GPS, Galileo satellites have calibrated emitter antennas. Eventually, PCC of receiver antennas for Galileo signals could be the key to obtain a scale of the terrestrial reference frame from GNSS measurements. This scale would be independent of other space geodetic techniques. This requires both, the transmitter and the receiver antennas to be accurately calibrated.

Zusammenfassung

CubETH ist ein Projekt für einen wissenschaftlichen Satelliten von $10 \times 10 \times 10 \text{ cm}^3$. Sein Ziel ist eine tiefe Erdumlaufbahn in ungefähr 450 km Höhe über der Erdoberfläche. Der Satellit ist mit zehn Global Navigation Satellite System (GNSS)-Empfängern und fünf GNSS-Antennen ausgerüstet. Die verwendeten Empfänger werden von der Schweizer Firma u-blox hergestellt. Es sind Chips aus der Serienproduktion, doch weisen sie Eigenschaften auf, die sie für einen Einsatz im Weltraum attraktiv machen: sie brauchen wenig Strom, sind leicht und kompakt.

Weil der Satellit vier Antennen auf seiner nach oben gerichteten Fläche aufweist, kann mittels GNSS die Attitude bestimmt werden. Die Attitude ist die Orientierung des Satelliten relativ zu einem Referenzrahmen, zum Beispiel dem terrestrischen Referenzrahmen. Für die GNSS-Attitude-Bestimmung wird das Prinzip der relativen Positionierung der Antennen gegenüber den anderen Antennen ausgenutzt.

Als erster Teil der vorliegenden Doktorarbeit wurde ein Algorithmus für die Attitude-Bestimmung entwickelt. Entgegen den in der wissenschaftlichen Literatur erwähnten Algorithmen enthält der Algorithmus einen Extrapolationsterm. Der Extrapolationsterm beträgt zwischen -6 und $+6$ m. Die Ursache für den Extrapolationsterm liegt in den nicht synchronisierten Empfängern. Der Messzeitpunkt liegt innerhalb eines Zeitfensters von 1 ms um den nominalen Messzeitpunkt. Wegen der hohen Geschwindigkeit des Satelliten (ungefähr 8 km/s) ist eine Extrapolation der Messungen unabdingbar.

Der neue Algorithmus wurde intensiv getestet. Eine Studie mit einem Signalgenerator und den Empfängern wurde erfolgreich durchgeführt. Der Algorithmus wurde ebenfalls mit echten Daten aus einem statischen Experiment am Boden validiert.

Aus den ersten Experimenten liess sich schliessen, dass die Antennen den entscheidenden Faktor für die Genauigkeit darstellen. Gegenseitige Beeinflussung der Antennen kann theoretisch nicht ausgeschlossen werden, wenn die Basislinienlänge kürzer ist als eine Wellenlänge. Eine relative Feldkalibration wurde aufgesetzt um Phasenzentrumskalibrationen (PZK) für ein Modell des CubETH zu erhalten. PZK sind frequenz- und richtungsabhängige Korrekturwerte für die eintreffenden GNSS-Signale. PZK werden seit Beginn des amerikanischen Global Positioning System (GPS) untersucht, sowohl theoretisch wie auch experimentell. Dennoch war die Kalibration von preiswerten Antennen in direkter Nähe zueinander, wie sie auf CubETH vorkommen, nie im wissenschaftlichen Fokus.

Die Resultate der relativen Feldkalibration zeigen auf, dass gegenseitige Beeinflussung der Antennen untereinander stattfindet. Die ermittelten PZK betragen mehrere Zentimeter. Es wurde aufgezeigt, dass die Verwendung von PZK für die fehlerfreie Schätzung von Attitude unabdingbar ist. Gleichzeitig wurden die Grenzen der relativen Antennenkalibration aufgezeigt. Sie ist extrem empfänglich für Fehler aus Mehrwegausbreitung.

Der Fokus des zweiten Teils der vorliegenden Doktorarbeit liegt bei absoluten Feldkalibrationen für GNSS-Antennen. Unerwartete Verzögerungen im CubETH-Projekt sind der Grund für

diese Neuausrichtung. In weniger als 18 Monaten wurde ein operationelles Kalibrierungssystem für GNSS-Antennen entwickelt. Es benutzt einen Sechs-Achsen-Industrieroboter, um die Antenne in alle möglichen Orientierungen zu bringen. Referenzdaten werden von einer nur wenige Meter vom Roboter entfernten Station aufgenommen. Die Daten werden auf Dreifachdifferenz-Stufe ausgewertet. Dreifachdifferenzen sind Zeitdifferenzen von klassischen Doppeldifferenzen.

Das System kann im jetzigen Zustand Kalibrationen für alle Code Division Multiple Access (CDMA) Signale generieren, vorausgesetzt es sind genug Satelliten sichtbar. Kalibrationen für die russischen GLONASS Frequency Division Multiple Access (FDMA) Signale sind auch denkbar, sofern diese auch implementiert werden.

Diverse Analysen zeigen, dass die Wiederholbarkeit der Kalibrationen bei unter einem Millimeter liegt. Ein Vergleich mit dem de facto Standard, den PZK der deutschen Firma Geo++[®] GmbH, zeigen auf, dass die erhaltenen Resultate plausibel sind und im selben Genauigkeitsbereich liegen wie die Referenz. Kalibrationen von GNSS-Empfangsantenne für die Signale vom europäischen Satelliten-Navigationssystem Galileo wurden am International GNSS Service (IGS) Workshop 2018 in Wuhan vorgestellt. Unser System ist das erste absolute Feldkalibrationssystem, das nachweislich Galileo-Kalibrationen generiert hat. Dies ist ein wichtiger Schritt zur besseren Kombination aller verfügbaren GNSS.

Im Gegensatz zum amerikanischen GPS weisen Galileo-Satelliten kalibrierte Sendeantennen auf. Letzten Endes wird die Kalibration von Empfängerantennen für die Galileo-Signale der Schlüssel zur Bestimmung des Massstabs des terrestrischen Referenzrahmens aus GNSS sein. Dieser Massstab wäre unabhängig von demjenigen anderer weltraumgeodätischen Techniken. Dies erfordert jedoch, dass sowohl die Sendeantennen wie auch die Bodenantennen hochgenau kalibriert werden.

Résumé

CubETH est le projet d'un nano-satellite de $10 \times 10 \times 10 \text{ cm}^3$. Il est destiné à une orbite basse à environ 450 km d'altitude au-dessus de la surface de la terre. Cet astronef est équipé de dix récepteurs de système de positionnement par satellites (Global Navigation Satellite System, GNSS) et cinq antennes GNSS. Les récepteurs GNSS utilisés sont fabriqués par l'entreprise suisse u-blox. Il s'agit d'équipement électronique standard, mais leurs performances les rendent parfaits pour une utilisation dans l'espace : ils sont peu énergivores, de petite taille et légers.

Le satellite étant équipé de quatre antennes sur sa face supérieure, la détermination de l'attitude devient possible. L'attitude est l'orientation du satellite par rapport à un cadre de référence, par exemple le cadre de référence terrestre. La détermination de l'attitude par GNSS est basée sur le positionnement relatif des antennes par rapport aux autres antennes.

Dans la première partie de cette thèse de doctorat, un algorithme pour la détermination de l'attitude par GNSS a été développé. Contrairement aux autres algorithmes présents dans la littérature scientifique, les données GNSS sont extrapolées. Le terme d'extrapolation mesure entre -6 et +6 mètres. La nécessité du terme d'extrapolation découle du non-synchronisme des récepteurs. L'instant de mesure se situe dans une plage de 1 ms autour de l'époque nominale. A cause de la grande vitesse du satellite en orbite basse (environ 8 km/s), l'extrapolation des mesures est indispensable.

Le nouvel algorithme a été soigneusement testé. Une simulation avec un générateur de signaux GNSS et les récepteurs a été menée avec succès. Le bon fonctionnement de l'algorithme a aussi été prouvé dans une expérience statique au sol et avec de vrais signaux GNSS.

Dès les premières expériences avec un modèle du satellite, il était évident que les antennes seraient le facteur limitant la précision. Une influence mutuelle des antennes ne peut pas être exclue pour des lignes de bases plus courtes qu'une longueur d'onde. Une calibration de terrain relative est mise en place afin d'obtenir les Corrections des Centres de Phases (CCP) pour les antennes du satellite. Les CCP sont des valeurs de correction qui dépendent de la fréquence et de la direction du signal reçu. Les CCP sont étudiées depuis les débuts du Global Positioning System (GPS) des États-Unis d'Amérique dans les années 80, tant à un niveau théorique qu'expérimental. Cependant, la calibration d'antennes à bas coût à proximité l'une de l'autre, comme sur CubETH, n'a jamais été au centre de l'attention scientifique.

Les résultats obtenus lors des calibrations relatives montrent qu'une influence mutuelle des antennes se produit. La magnitude des CCP est de plusieurs centimètres. Il est démontré que la prise en compte des CCP est cruciale afin d'estimer une attitude GNSS qui soit libre de biais. Les expériences ont aussi montré les limites de la calibration de terrain relative. Elle est susceptible aux erreurs dues aux propagation par trajets multiples.

Le focus de la deuxième partie de la présente thèse de doctorat sont les calibrations de terrain absolues pour les antennes GNSS. Cette réorientation est une conséquence de retards imprévus

dans le projet CubETH. En moins de 18 mois, un système opérationnel de calibrations d'antennes GNSS a été développé. Il utilise un robot industriel à six axes afin de tourner l'antenne GNSS dans tous les sens. Des données de références sont collectées par une station à quelques mètres du robot. Les mesures sont traitées sous forme de triple-différences. Les triples-différences sont des différences temporelles des doubles-différences classiques.

Le système est actuellement capable de générer des calibrations pour n'importe quel signal modulé par accès multiple par répartition en code (AMRC), tant que suffisamment de satellites sont visibles. Les calibrations pour les signaux modulés par accès multiple par répartition en fréquence (AMRF) du système russe GLONASS sont en principe également possible; il s'agit de les implémenter dans le logiciel.

Diverses analyses ont montré que la répétabilité des calibrations était meilleure que le millimètre. Une comparaison avec le standard de facto, les PCC de l'entreprise allemande Geo++[®] GmbH, ont permis de vérifier la vraisemblance des résultats. La précision des résultats est similaire à la précision des résultats de référence. La calibration d'antennes pour les signaux du système européen de navigation Galileo ont été présentés au Workshop 2018 du « International GNSS Service » (IGS) à Wuhan. Notre nouveau système est la première calibration de terrain absolue avérée à générer des calibrations pour les signaux Galileo. Ceci est une étape importante vers une meilleure combinaison de tous les GNSS disponibles.

Contrairement au GPS américain, les antennes d'émission des satellites Galileo sont calibrées. Un jour ou l'autre, les CCP des antennes de récepteurs pour les signaux Galileo pourraient être la clé pour déterminer l'échelle du système de référence terrestre à partir de mesures GNSS. Cette échelle serait indépendante des autres techniques de géodésie spatiale. Ceci requiert que les antennes de transmission ainsi que les antennes de réception soient précisément calibrées.

Foreword

The present thesis is the results of four years spent at the Chair of Mathematical and Physical Geodesy (MPG) at ETH Zurich. Every single person that went through a doctoral thesis will attest that this fabulous adventure has ups and downs. After a very enthusiastic start first complications appeared in the CubETH project. Nothing but one thing was certain: the launch of the mini-satellite with the Global Navigation Satellite System (GNSS) experiment on-board would be delayed. The following period was difficult. What is the sense of working on a very specific algorithm, tailored to an application, if the application is not going to exist before the end of the doctoral thesis?

A slight reorientation of the topic, away from pure attitude determination towards antenna calibration resolved the situation. The new branch of research was exciting and fascinating. The usage of a robot gave me insights into a new field. But more importantly, with GNSS antenna calibration I found a topic which is extremely meaningful in my eyes. The evident lack of antenna field calibrations for Galileo was the biggest motivation. The European satellite navigation system Galileo was designed as a civilian system from its very beginning. Unlike the other GNSS, it has not principally a military, but economical, social and scientific goals. It was a real pleasure to develop an antenna field calibration for Galileo, especially because of the interest from the scientific community. I will leave ETH Zurich with a pleasant anticipation, looking forward to new professional challenges, but also with a bit of sadness. *Il faut s'arrêter quand c'est le plus beau...*

Acknowledgement

I would like to thank the following people:

- Prof. Dr. Markus Rothacher, for leading my doctoral thesis and giving me guidance during the four years. I am grateful for the opportunity of doing a doctoral thesis under his supervision.
- Prof. Dr.-Ing. Steffen Schön, Institut für Erdmessung, Leibniz University Hanover, for accepting to review my doctoral thesis and the very valuable input regarding the absolute antenna calibration and the development of the system at ETH Zurich.
- Dr. Oliver Montenbruck and Markus Markgraf, DLR, for all the support during the simulator experiments at the DLR in Oberpfaffenhofen.
- Dr. Elmar Brockmann and Dr. Simon Lutz, swisstopo, for the scientific and instrumental support for the validation of the Galileo antenna calibrations.
- Prof. Dr. Alain Geiger, for all his support and his help. His knowledge in so many field was extremely helpful.
- Jrene Müller-Gantenbein, for being the ‘heart’ of the lab. She always had an ear for the doctoral students.
- Dr. Sébastien Guillaume, for always helping me to find the intellectual courage to tackle new challenges. I would also like to thank him for all the knowledge he transmitted, for his enthusiasm and his advices all along my work.
- Donovan Koch, for all the hours spent helping to debug the KUKA. I doubt there would be a running antenna calibration at ETH Zurich if Donovan had not been here.
- Dr. Karina Wilgan, for being a very supportive office mate. She created a good atmosphere in the office.
- Dr. Benjamin Männel, for all his advices regarding the GNSS processing in Bernese and his tips regarding the general course of the doctoral thesis.
- Roland Hohensinn, for the fruitful sharing of Matlab routines related to GNSS processing.
- Dr. Michael Meindl, for his very useful Bernese support and all his special Bernese hacks.
- Dr. Christine Hollenstein and Michael Fisler, for their help during the GNSS simulator data acquisition at the DLR in Oberpfaffenhofen.
- Hui Xu, for her help in acquiring data for the relative field calibration of the CubETH model and her idea on how to proceed in order to calibrate the antennas.
- All my very supportive colleagues, namely Kangkang Chen, Dr. Simon Häberling, Iván Darío Herrera Pinzón, Solomon Kamugasa, Dr. Krisztina Kelevitz, Flavio Kreiliger, Dr. Philippe Limpach, Fabio Luchsinger, Dr. Fabian Neyer, Roxane Pott, Yara Rossi, Endrit Shehaj,

Ladina Steiner, Dr. Guillaume Stern, Dr. Zengzhong Su, Hang Su, Vasileios Vlachakis and Dr. Kan Wang.

- Robert Presl, for all the customised equipment he engineered and manufactured.
- Paul Sorber and Alexander Wolf, for their help in any issue regarding electronic equipment.
- Jules Fenner and Thomas Posur, for their support in any matter related to geodetic instrumentation.
- Michael Lyrenmann, for his advice regarding the commissioning of the KUKA.
- Valérie-Anne Hellmüller and Patrik Eugster, for the data acquisition they accomplished during their Bachelor thesis.
- Timon Januth for the establishment of a high-accuracy network on our Institute's roof.
- The anonymous reviewers of the four published papers. Reviewers do a barely visible, but extremely important job. With their remarks, they always helped to improve the manuscripts we published.

I would like to thank my father Henry Willi and my brother Benjamin Willi for their support. Many thanks to Dr. Roswitha Jeanmonod and Dr. Rolf Jeanmonod for always being interested in my work and my well-being. My deepest thankfulness goes to Muriel Jeanmonod and Catherine Willi Renaud-dit-Louis. I would never have finished my thesis without their support.

Contents

Frontmatter	xix
List of Figures	xix
List of Tables	xxi
Abbreviations	xxiii
Constants	xxv
Symbols	xxvii
1 Introduction	1
2 GNSS Attitude Determination	3
2.1 State of the Art	3
2.2 Research gap	5
2.3 Parametrisation of attitude	5
2.3.1 Euler angle sequences	6
2.3.2 Quaternions	8
2.4 Principle of GNSS attitude determination	9
2.5 Extrapolation of the GNSS measurements	13
2.6 Practical aspects of GNSS measurement extrapolation with Bernese	14
2.7 Phase ambiguity resolution	17
2.8 Filter formulation	18
2.8.1 State propagation	19
2.8.2 Stochastic model	20
2.9 Paper I –GNSS Attitude Determination with Non-Synchronized Receivers and Short Baselines Onboard a Spacecraft	21
2.9.1 Abstract	22
2.9.2 Author’s contribution	22
2.9.3 Relevance to the field	22
2.10 Outlook	24

3	GNSS Antenna Calibration	25
3.1	Definitions	26
3.2	State of the art	28
3.2.1	Relative field calibration	28
3.2.2	Anechoic chamber calibration	29
3.2.3	Absolute field calibration	29
3.3	Phase Centre Correction Model	30
3.4	Phase Centre Parametrisations	31
3.4.1	Grid parametrisation	31
3.4.2	Grid partial derivatives	32
3.4.3	Spherical harmonics parametrisation	34
3.4.4	Spherical harmonics partial derivatives	37
3.5	Multi-GNSS requirements	37
3.6	Validation strategies	38
4	Relative GNSS antennas field calibrations	41
4.1	Observation equation	42
4.2	Relative calibration of an attitude estimation platform	43
4.3	Paper II – GNSS Antenna Phase Center Variation Calibration for Attitude Determination on Short Baselines	46
4.3.1	Abstract	46
4.3.2	Author’s contribution	48
4.3.3	Relevance to the field	48
4.4	Outlook	48
5	Robot geometry	51
5.1	Definitions	51
5.2	KUKA Agilus KR 6 R900 sixx	53
5.3	QKuka control software	56
5.4	Robot Kinematics	56
5.4.1	Forward kinematics	58
5.4.2	Inverse kinematics	63
5.5	Enhanced kinematic model	68
5.5.1	State of the art	68
5.5.2	Denavit-Hartenberg parametrisation	68
5.5.3	Calibration model	72
5.5.4	Model limitations	72

5.6	Paper III – Calibration of a Six-Axis Robot for GNSS Antenna Phase Center Estimation	73
5.6.1	Abstract	73
5.6.2	Author’s contribution	74
5.6.3	Relevance to the field	74
5.7	Outlook	74
6	Absolute GNSS antenna field calibration	77
6.1	Time-differencing mode	77
6.2	Triple-difference observation equation	78
6.3	Absolute character of triple-difference antenna calibration	80
6.4	Rotation sequence	82
6.5	Receiver dynamical stress	84
6.6	Differencing strategy	85
6.7	Processing pipeline	86
6.8	Paper IV – Absolute GNSS Antenna Phase Center Calibration with a Robot . . .	89
6.8.1	Abstract	89
6.8.2	Author’s contribution	90
6.8.3	Relevance to the field	90
6.9	Pending publication	90
6.10	Outlook	94
7	Conclusions and outlook	95
	Bibliography	97
	Appendix A Paper I	107
	Appendix B Paper II	135
	Appendix C Paper III	151
	Appendix D Paper IV	177
	Appendix E Curriculum vitae	197

List of Figures

1.0.1 Digital rendering of a CAD model of CubETH	2
2.4.1 Principle of GNSS attitude determination	12
3.1.1 Illustration of PCC, PCO and PCV	27
3.4.1 Principle of grid interpolation	33
3.4.2 Spherical harmonics coefficients up to degree and order five	35
3.4.3 Contribution of odd and even spherical harmonics coefficients	36
3.5.1 Graphical overview of the frequencies of the main four GNSS	40
4.0.1 Principle of PCO estimation	42
4.2.1 Summary of the processing of relative field calibrations	44
4.2.2 Preprocessing of the observations	45
4.2.3 Baseline processing of the observations	47
4.2.4 Principle of PCO estimation on CubETH	47
5.0.1 KUKA Agilus KR 6 R900 sixx during antenna calibration	52
5.1.1 KUKA robot in two different postures	54
5.1.2 Robot coordinate system and flange coordinate system	54
5.1.3 Robot relevant coordinate systems	55
5.2.1 KUKA control equipment	57
5.2.2 KUKA interfaces	57
5.3.1 Message sent by the robot controller	57
5.3.2 Message received by the robot controller	58
5.3.3 Principle of XML based message echange	58
5.4.1 Geometrical parameters of the KUKA Agilus KR 6 R900 sixx	59
5.4.2 Front view of the KUKA Agilus KR 6 R900 sixx	60
5.4.3 KUKA angle convention	63
5.4.4 Robot postures one to four	66
5.4.5 Robot postures five to eight	67
5.5.1 DH convention applied to a robot	70
5.5.2 DH length parameters of the KUKA	71

LIST OF FIGURES

6.4.1	Flowchart of the algorithm for the generation of the randomized rotation sequence	83
6.4.2	Algorithm for the generation of the randomized rotation sequence	83
6.4.3	Skyplot illustrating azimuthal and zenithal resolution	84
6.6.1	Differencing strategy	85
6.7.1	Overview of the processing of the GNSS observations for PCC estimation	87
6.9.1	Set-up for the short baseline calibration	92
6.9.2	Galileo E1 residuals of the short baseline validation	93
6.9.3	Galileo E5 residuals of the short baseline validation	94

List of Tables

2.6.1 Summary of modifications to the Bernese GNSS Software	16
2.9.1 Summary of the author's contribution to paper I	23
3.5.1 Centre frequencies of the current GNSS	39
4.2.1 Relative field calibration NEQ parameters	45
4.3.1 Summary of the author's contribution to paper II	49
5.2.1 Principal properties of the KUKA Agilus KR 6 R900 sixx	56
5.4.1 The seven geometrical parameters of the KUKA Agilus KR 6 R900 sixx	59
5.5.1 DH parameters for the KUKA Agilus KR 6 R900 sixx	69
5.5.3 KUKA DH calibration model parameters	73
5.6.1 Summary of the author's contribution to paper III	75
6.3.1 Results from the synthetic data PCC bias study	81
6.7.1 Configuration options for PCC estimation	88
6.8.1 Summary of the author's contribution to paper IV	91
6.9.1 Antennas used in the short baseline validation	93

Abbreviations

ANTEX	Antenna Exchange Format
APC	Actual Phase Centre
ARP	Antenna Reference Point
AWG	Antenna Working Group
CDDIS	Crustal Dynamics Data Information System
CDMA	Code Division Multiple Access
CODE	Centre for Orbit Determination in Europe
COTS	Commercial off-the-Shelf
DH	Denavit-Hartenberg
DLR	Deutsches Zentrum für Luft- und Raumfahrt
EPN	European Permanent Network
ETH	Eidgenössische Technische Hochschule
FDMA	Frequency Division Multiple Access
GNSS	Global Navigation Satellite System
GPS	Global Positioning System
ICD	Interface Control Document
IERS	International Earth Rotation and Reference Systems Service
IGP	Institute of Geodesy and Photogrammetry
IGS	International GNSS Service
IGS AWG	International GNSS Service Antenna Working Group
INS	Inertial Navigation System
ION	Institute of Navigation
ITRF	International Terrestrial Reference Frame

LAMBDA	L east S quares A mbiguity D ecorrelation A djustment
LEO	L ow E arth O rbital
LLF	L ocal L evel F rame
LOS	L ine of S ight
MJD	M odified J ulian D ate
MPC	M ean P hase C entre
NASA	(U S) N ational A eronautics and S pace A dministration
NEQ	N ormal E quation
PCC	P hase C entre C orrection
PCO	P hase C entre O ffset
PCV	P hase C entre V ariations
PPP	P recise P oint P ositioning
PVT	P osition, V elocity and T ime
RINEX	R eceiver I ndependent E xchange F ormat
RMS	R oot M ean S quare
RMSE	R oot M ean S quare E rror
RSI	R obot S ensor I nterface
SDR	S oftware D efined R adio
SPP	S ingle P oint P ositioning
UAV	U nmanned A erial V ehicle
UBX	U - b lox B inary F ormat
UDP	U ser D ata P rotocol
WGS84	W orld G lobal S ystem 1984
XML	E xtensible M arkup L anguage

Constants

Physical constants according to IS-GPS-200 (2015)

Speed of light	c	$=$	$2.997\,924\,58 \times 10^8 \text{ m s}^{-1}$
Earth's gravitational constant	μ_e	$=$	$3.986\,005 \times 10^{14} \text{ m}^3 \text{ s}^{-2}$

Physical constants according to IERS (Petit and Luzum, 2010)

Speed of light	c	$=$	$2.997\,924\,58 \times 10^8 \text{ m s}^{-1}$
Earth's gravitational constant	μ_e	$=$	$3.986\,004\,418 \times 10^{14} \text{ m}^3 \text{ s}^{-2}$

GNSS centre frequencies

GPS

L1 signal	f_c	$=$	1 575.42 MHz
L2 signal	f_c	$=$	1 227.6 MHz
L5 signal	f_c	$=$	1 176.45 MHz

GLONASS

G1 signal, with $k \in [-7, -6, \dots, 6]$	f_c	$=$	$1\,602 + \frac{9}{16}k$ MHz
G2 signal, with $k \in [-7, -6, \dots, 6]$	f_c	$=$	$1\,246 + \frac{7}{16}k$ MHz
G3 signal	f_c	$=$	1 202.025 MHz

Galileo

E1 signal	f_c	$=$	1 575.42 MHz
E5a signal	f_c	$=$	1 176.45 MHz
E5b signal	f_c	$=$	1 207.14 MHz
E5 (E5a+E5b) signal	f_c	$=$	1 191.795 MHz
E6 signal	f_c	$=$	1 278.75 MHz

SBAS

L1 signal	f_c	$=$	1 575.42 MHz
L2 signal	f_c	$=$	1 176.45 MHz

BeiDou

B1 signal $f_c = 1\,561.098$ MHz

B2 signal $f_c = 1\,207.14$ MHz

B3 signal $f_c = 1\,268.52$ MHz

QZSS

L1 signal $f_c = 1\,575.42$ MHz

L2 signal $f_c = 1\,227.6$ MHz

L5 signal $f_c = 1\,176.45$ MHz

LEX signal $f_c = 1\,278.75$ MHz

IRNSS

L5 signal $f_c = 1\,176.45$ MHz

S signal $f_c = 2\,492.028$ MHz

Symbols

General symbols

\mathbf{X}	a matrix
\mathbf{x}	a vector
$\mathbf{X}_{3 \times 3}$	size of \mathbf{X}
X_{ij}	element on line i and column j of \mathbf{X}
x_i	i^{th} element of \mathbf{x}
X	a scalar
\mathbf{X}^T	a transposed matrix
$\mathbf{x}^T \mathbf{y}$	a scalar product, equals $\langle \mathbf{x}, \mathbf{y} \rangle$
\tilde{X}	approximation of quantity X
\hat{X}	estimation of quantity X
X^-	propagation of quantity X
\dot{X}	time derivative of quantity X

Spaces

\mathbb{Z}	Integer number
--------------	----------------

Attitude representation

$\mathbf{0}_{i \times j}$	a i times j matrix with zeros
\mathbf{I}_i	the i times i identity matrix
\mathbf{R}	orthogonal rotation or attitude matrix
\mathbf{R}_i	rotation around the i^{th} coordinate axis
\mathbf{T}	quaternion rates matrix
\mathbf{b}	baseline vector (in the body fixed frame)
\mathbf{n}	rotation axis unit vector
\mathbf{q}	quaternion
α, β, γ	yaw, pitch and roll angles
$\boldsymbol{\omega}$	rotation vector

GNSS symbolism

D	Zero-difference to double-difference operator
Q_{ll}	Variance-covariance of the observations
e	line-of-sight unit vector
v	velocity vector
x	position vector
E	GNSS attitude extrapolation term
I	ionospheric delay
N	integer phase ambiguity (in cycles)
P	GNSS phase observation
T	tropospheric delay
W	GNSS phase wind-up
v	residual
z	zenith angle
α	azimuth
δt	receiver or satellite clock error
σ_p	standard deviation of a phase observation
λ	GNSS carrier phase wavelength

Kalman filter symbolism

A	system model function Jacobian matrix
F	state transition function Jacobian matrix
G	noise shaping matrix
H	observation function Jacobian matrix
K	Kalman gain matrix
P	state variance-covariance
U	process variance-covariance
V	observation variance-covariance
a(x)	system model function
f(x)	state transition function
h(x)	observation function
u	process noise
v	observation residuals
x	state vector
z	observation vector

Robot kinematics symbolism

$\mathbf{R}_{r \leftarrow f}$	Rotation from flange coordinates to robot coordinates
$\mathbf{R}_{r \leftarrow t}$	Rotation from tool coordinates to robot coordinates
$\mathbf{R}_{f \leftarrow t}$	Rotation from tool coordinates to flange coordinates
\mathbf{c}	Coordinates of the intersection of the last three robot axis
\mathbf{t}	Robot tool coordinates
\mathbf{u}	Robot flange coordinates
θ_i	Angle of the i^{th} axis of the robot
t'_x, t'_y, t'_z	Robot x- y- and z-coordinates in the world frame
t''_x, t''_y, t''_z	Tool x- y and z-offsets in the tool frame
α', β', γ'	Robot yaw, pitch and roll angles in the world frame
$\alpha'', \beta'', \gamma''$	Tool yaw, pitch and roll angles in the flange frame

Geometrical robot model

a_i	Offset parameters
b	Alignment parameter
d_i	Length parameters

Denavit-Hartenberg model

\mathbf{T}	Homogeneous transformation matrix (of the flange)
\mathbf{T}_i	Homogeneous transformation matrix associated to joint and link pair i
Θ_i	Joint angular reading parameter
α_i	Joint torsion parameter
a_i	Link offset parameter
d_i	Link length parameter

Various

$N(\mu, \sigma^2)$	Normal distribution with mean μ and standard deviation σ
atan2	multi-valued inverse tangent

Dédié à Claude Renaud

Chapter 1

Introduction

CubETH is a nano-satellite project under the lead of the Institute of Geodesy and Photogrammetry (IGP) at ETH Zurich. It is a collaboration between several universities, universities of applied sciences and companies in Switzerland. This work is part of the CubETH project and was supported by ETH Research Grant ETH-43 14-2.

The idea for CubETH was triggered by recent developments in Global Navigation Satellite System (GNSS) receiver technology. u-blox, a receiver manufacturer located in Thalwil (Switzerland), is a world leader in miniaturized multi-GNSS receivers. Because of their remarkable performance, the idea came up to use these commercial off-the-shelf (COTS) chipsets for a space mission. This would highly reduce the cost of GNSS positioning in space and make precise positioning affordable for small missions.

The design study foresees a spacecraft of $10 \times 10 \times 10 \text{ cm}^3$, equipped with five GNSS antennas and ten GNSS receivers (see Figure 1.0.1). The main mission goal is technology demonstration. It will be attempted to prove that the u-blox receivers can be used in space. The secondary mission goal is attitude determination. Attitude is a body's orientation in space. Attitude determination is possible because the tiny satellite is equipped with several antennas. Through the relative positioning of the antennas with respect to each other, the attitude can be estimated.

The first part of this thesis deals with the challenge of **attitude determination** with the u-blox receivers. The u-blox chips are not equipped with clock steering. Therefore, the different receivers are not synchronised with each other. The goal of the work presented in **Chapter 2** is to develop an algorithm for attitude determination with non-synchronised receivers.

The classical way to enhance the accuracy of GNSS attitude determination is to increase the length of the baselines between the antennas. On the small CubETH, the baseline lengths are limited by the size of the satellite. Because the accuracy cannot be increased by increasing the baseline length, special attention has to be put on the accuracy of the antennas. The shorter the baseline, the larger the influence of antenna errors onto the estimation of the attitude. A **general introduction to antenna calibration** is provided in **Chapter 3**.

An additional difficulty on very short baselines is the potential coupling of the antennas

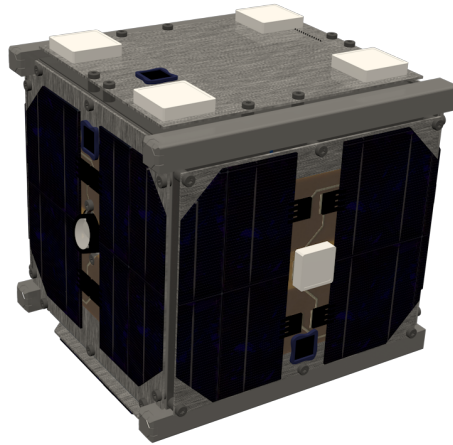


Figure 1.0.1 : Digital rendering of a CAD model of the $10 \times 10 \times 10 \text{ cm}^3$ CubETH spacecraft. The white patches are the GNSS antennas. Four antennas are placed on the zenith looking face, one antenna on the side serves experimental purposes.

because of their proximity. This challenge was addressed in **Chapter 4**; a **relative field calibration** method was set up and a campaign was conducted with the goal to investigate the behaviour of the antennas on the CubETH model.

The subsequent chapters present the development of an absolute field calibration method for GNSS antennas. This method, using a robotic arm, is able to reduce the impact of multipath on the estimated antenna calibration. Thus, it is expected to deliver more reliable results than the relative field calibration.

In order to use the robotic arm for high-accuracy antenna calibration, its kinematics and its accuracy needed to be studied: all aspects related to the **kinematics of the robotic arm** are covered in **Chapter 5**. The **absolute field calibration** method using this robot is detailed in **Chapter 6**.

Chapter 2

GNSS Attitude Determination

GNSS attitude determination has been performed since the very beginning of the Global Positioning System (GPS). An excellent introduction on general attitude determination is provided in Giorgi (2017). On spacecraft in Low Earth Orbit (LEO), GNSS attitude determination is performed since the nineties (Cohen, 1992). GNSS attitude determination has some appreciable advantages over other techniques, as star trackers or inertial navigation systems (INS). It is autonomous in acquiring an initial solution, it needs only two visible GNSS satellites for a deterministic solution, it is resistant to high spin rates and it provides position, velocity and time (PVT; Arbinger and Enderle, 2000). Compared to INS, it is free of drift.

On the other hand, the amount of raw data to process is considerable and the system is very sensitive to multipath. And maybe more importantly, its accuracy is very modest compared to star trackers.

Nevertheless, GNSS attitude determination remains an attractive technique, especially if its availability is granted for free, as in the case of the satellite CubETH. The four antennas on the upper side of the spacecraft allow for GNSS attitude determination.

In the following chapter, the state of art of attitude determination onboard spacecraft in LEO is discussed, followed by a presentation of the governing equations and principles. The chapter is concluded by a summary of the first publication.

2.1 State of the Art

RADCAL was one of the first missions to perform attitude determination in space (Cohen et al., 1994). Dedicated Trimble TANS Quadrex receivers, specially adapted by Stanford University, were used. A receiver was connected to the four antennas, and a second receiver was carried as spare. The four antennas are evenly distributed on the upper face of the cylindrical spacecraft with a diameter of about 0.75 meters. The authors of the study compared the GPS attitude to the attitude obtained from the gravitational dynamics of the spacecraft. The estimated accuracy lies around 1 deg and is limited by uncertainties in the antenna Phase Centre Variations (PCV)

and in the electrical delays. The authors state that the accuracy inherent to the system lies around 0.3 deg.

In 2000, a modified Trimble Force-19 receiver was flown onboard the space shuttle Atlantis in order to perform an attitude determination experiment (Um and Lightsey, 2001). Again, dedicated space receivers were used. Attitude from a star tracker served as ground truth. Interestingly, the authors tried to model the multipath originating from the spacecraft with a spherical harmonics model. This approach was qualified unsuccessful. The lack of flight data and the complex geometry of the environment were given as explanations. The authors also compared two approaches for the combination with the INS, firstly using differentiated phase observables, secondly using quaternion observations previously generated from GPS. The first approach was clearly preferred, as the accuracy of the results increased. Additionally, phase measurements can enter the filter algorithm even if not enough satellites are visible for a quaternion solution. In the conclusions, the authors estimate that 90% of the error budget is due to multipath.

Other authors studied attitude determination (designed for space) in ground tests. All authors use carrier phase observables, but many differences are found in the way of processing the observations and in the parametrisation of the attitude.

Arbinger and Enderle (2000) tested a combination of GPS and a star tracker on a turn table on the ground. The GPS-based solution is obtained using an iterative solution to Wahba's problem and after solving the phase ambiguities. The comparison led to the conclusion that the GPS solution is affected by much more jitter than the star tracker solution. Furthermore, an offset between the GPS solution and the star tracker solution remains unexplained.

Kim and Langley (2007) studied a system based on the COTS receivers Novatel OEM4-G2L, aimed to operate on the small satellite CASSIOPE. The system consists of three receivers (and an additional spare). Ambiguities are solved epoch-wise using a wide-lane linear combination and adding the baseline lengths as pseudo-observations in the adjustment. The normalization of the attitude matrix is achieved by transforming the matrix into Euler angles and then computing an orthogonal matrix with these Euler angles. An experiment with a turning table demonstrated the ability to reach 5 deg accuracy with baseline lengths between 1 and 1.6 m.

A last group of authors studied the behaviour of algorithms in GNSS simulator studies. Ziebart and Cross (2003) used synthetic data and a very complete attitude determination algorithm. Euler angles were chosen as parametrisation. The initial ambiguity resolution is performed using a search in the attitude space. Under realistic observation noise, sub-degree accuracy was found to be achievable with 2 to 3 m baselines. Assuming a realistic stochastic model, the algorithm performs well in outlier detection.

Nadarajah et al. (2012) performed hardware-in-the-loop simulator tests with a Spirent GSS6560 signal generator. NamuruV2Rx receivers were used. The processing is achieved in two steps. First, an epoch-wise solution is generated with a modified version of the LAMBDA algorithm (see for instance Park and Teunissen, 2003; Teunissen, 1995; Teunissen, 2010), then this solution is filtered in an unscented Kalman filter. In conclusion, the angular error was found

to depend strongly on the geometry of the GPS constellation. Root Mean Square Errors (RMSE) in the order of one degree were obtained for a configuration with two baselines of one metre length.

GNSS attitude determination is also intensely studied for other applications than on spacecraft. This includes studies on Earth, for instance on ships (Giorgi et al., 2012), onboard planes (Van Graas and Braasch, 1991; Cannon and Sun, 1996), for UAV (Sabatini et al., 2012) or for terrestrial applications (Chen and Qin, 2012; Aghili and Salerno, 2013).

2.2 Research gap

The CubETH project aims at using COTS receivers of the type u-blox M8. The u-blox receiver clock is only partially steered, resulting in an actual measurement epoch within a time window of 1 ms around the nominal 1 Hz measurement epoch (u-blox, 2014). The velocity of an Earth's satellite in an circular orbit can be computed as:

$$v = \sqrt{\frac{\mu_e}{r}} \quad (2.1)$$

with μ_e being the Earth's gravitational constant and r the radius of the orbit. For a satellite in a 400 km orbit, this results in approximately 8 km/s. At this speed, the spacecraft travels 8 m in one millisecond, which is the synchronisation error of the receivers. It is obvious, that under these circumstances, an extrapolation of the measurements is of tremendous importance.

In previous studies, either dedicated receivers running on a common oscillator or receivers with well steered clocks were used.

Furthermore, no paper gave a fully satisfactory solution for the handling of the parametrisation of the attitude. The present chapter addresses both issues: a consistent mathematical formulation for the attitude parametrisation within a Kalman filter is derived on the observation level and a procedure for the extrapolation of the measurements is developed. The chosen extrapolation method works in real-time and is not dependent on any precise products, like precise orbits or precise clocks.

2.3 Parametrisation of attitude

The attitude describes the orientation of a body in space:

$$\mathbf{b}_{\text{world}} = \mathbf{R}_{\text{world} \leftarrow \text{body}} \mathbf{b}_{\text{body}} \quad (2.2)$$

where $\mathbf{b}_{\text{system}}$ is the baseline vector in the respective coordinate system and \mathbf{R} is the rotation matrix between the two coordinate systems. The body coordinate system is usually attached to the rigid body. For example, a rigid body coordinate system attached to a plane could have its x-axis pointing in flight direction, its y-axis in wing direction, and the z-axis complementing

the right-hand system. The space of all rotations is the 3D special orthogonal group $SO(3)$. Because attitude is described by a rotation, $\mathbf{R} \in SO(3)$.

In consequence:

$$\mathbf{R} \mathbf{R}^T = \mathbf{R} \mathbf{R}^{-1} = \mathbf{I}_3 \quad (2.3)$$

with \mathbf{I}_3 being the identity matrix. This condition expresses the orthogonality of the matrix. Within an adjustment process, rotation matrices are difficult to handle, as additional constraints are necessary in order to maintain the orthogonality.

The main alternatives to rotation matrices are Euler angle sequences and quaternions. Euler angle sequences suffer from singularities, the so-called ‘gimbal lock’. Quaternions do not have this disadvantage, but an additional parameter is needed. Various conventions exist for both representation forms. The following section briefly presents the chosen convention. A complete overview of attitude parametrisations is provided in Diebel (2006). Attitude parametrisation is also discussed in the inertial navigation or GNSS literature, for instance in Jekeli (2001) respectively in Giorgi (2017).

2.3.1 Euler angle sequences

An Euler angle sequence is the combination of three different coordinate axis rotations. Coordinate axis rotations rotate a vector around one axis of the coordinate system and are defined as follows:

$$\mathbf{R}_1(\alpha) = \begin{pmatrix} 1 & 0 & 0 \\ 0 & \cos \alpha & \sin \alpha \\ 0 & -\sin \alpha & \cos \alpha \end{pmatrix} \quad (2.4)$$

$$\mathbf{R}_2(\alpha) = \begin{pmatrix} \cos \alpha & 0 & -\sin \alpha \\ 0 & 1 & 0 \\ \sin \alpha & 0 & \cos \alpha \end{pmatrix} \quad (2.5)$$

$$\mathbf{R}_3(\alpha) = \begin{pmatrix} \cos \alpha & \sin \alpha & 0 \\ -\sin \alpha & \cos \alpha & 0 \\ 0 & 0 & 1 \end{pmatrix} \quad (2.6)$$

where \mathbf{R}_i is a rotation around the i^{th} axis of the coordinate system and α is the angle of rotation. The 321 Euler sequence is defined as follows:

$$\mathbf{R}_{\text{local} \leftarrow \text{global}} = \mathbf{R}_1(\gamma) \mathbf{R}_2(\beta) \mathbf{R}_3(\alpha) \quad (2.7)$$

Note that this rotation matrix would be the transpose of the attitude matrix as defined in Eq. 2.2. α , β and γ are the yaw, pitch and roll angles. If $\beta = \frac{\pi}{2} + n\pi, n \in \mathbb{Z}$, the system is in a singularity. In that case, the rotations \mathbf{R}_1 and \mathbf{R}_3 have the same derivatives and the system loses one degree of freedom. Mechanically spoken, if thinking of cardans, the first and the last

cardan would be parallel, thus being in gimbal lock.

The inverse function reads:

$$\left. \begin{aligned} \alpha &= \operatorname{atan2}(R_{12}, R_{11}) \\ \beta &= -\arcsin(R_{13}) \\ \gamma &= \operatorname{atan2}(R_{23}, R_{33}) \end{aligned} \right\} \text{if } |R_{13}| \neq 1 \quad (2.8)$$

$$\left. \begin{aligned} \alpha &= \operatorname{atan2}(-R_{21}, R_{22}) \\ \beta &= -\arcsin(R_{13}) \\ \gamma &= 0 \end{aligned} \right\} \text{if } |R_{13}| = 1 \quad (2.9)$$

where $R_{i,j}$ is the element in line i and column j of the matrix $\mathbf{R}_{\text{local} \leftarrow \text{global}}$. In case of a singularity, an infinite number of solutions exists. One way to resolve this singularity is to set γ to zero.

The 323 Euler sequence consistently reads:

$$\mathbf{R}_{\text{local} \leftarrow \text{global}} = \mathbf{R}_3(\gamma) \mathbf{R}_2(\beta) \mathbf{R}_3(\alpha) \quad (2.10)$$

This parametrisation has a singularity at $\beta = 0 + n\pi, n \in \mathbb{Z}$ and would therefore be useless for the estimation of the attitude, but is convenient in other cases, for instance for the description of the position of a robot. To give another example, for the Earth orientation, the sequence 313 is frequently used.

The inverse function of the 323 Euler sequence reads:

$$\left. \begin{aligned} \alpha &= \operatorname{atan2}(R_{32}, R_{31}) \\ \beta &= \arccos(R_{33}) \\ \gamma &= \operatorname{atan2}(R_{23}, -R_{13}) \end{aligned} \right\} \text{if } |R_{33}| \neq 1 \quad (2.11)$$

$$\left. \begin{aligned} \alpha &= \operatorname{atan2}(-R_{21}, R_{22}) \\ \beta &= \arccos(R_{33}) \\ \gamma &= 0 \end{aligned} \right\} \text{if } |R_{33}| = 1 \quad (2.12)$$

2.3.2 Quaternions

Quaternions are four element vectors with a scalar part and a vector part:

$$\mathbf{q}_{\text{local} \leftarrow \text{global}} = \begin{pmatrix} q_0 \\ q_1 \\ q_2 \\ q_3 \end{pmatrix} = \begin{pmatrix} q_0 \\ \mathbf{q}_{1:3} \end{pmatrix} = \begin{pmatrix} \cos\left(\frac{\alpha}{2}\right) \\ \sin\left(\frac{\alpha}{2}\right) \mathbf{n} \end{pmatrix} \quad (2.13)$$

where \mathbf{q} is a quaternion that represents a rotation by the angle α around the axis \mathbf{n} . The advantage of this parametrisation is its constant norm:

$$q = \sqrt{q_0^2 + q_1^2 + q_2^2 + q_3^2} = 1 \quad (2.14)$$

Quaternions not having a norm equal to one do not represent pure rotations. Within the adjustment, several techniques can be applied to guarantee a norm of one:

- i. Only three quaternion elements are estimated and the fourth one is computed,
- ii. All four elements are estimated and a constraint on the norm is applied or
- iii. All four elements are estimated and the quaternion is normalised after each iteration in the estimation.

In the case of a Kalman filter, (iii) is largely sufficient, if the update rate of the filter is high compared to the dynamics of the system. In this case, the change of the norm of the quaternion is very small at every iteration step and can well be handled with normalisation.

Quaternions can be transformed to rotation matrices using following formula:

$$\mathbf{R} = \begin{pmatrix} q_0^2 + q_1^2 - q_2^2 - q_3^2 & 2 q_1 q_2 + 2 q_0 q_3 & 2 q_1 q_3 - 2 q_0 q_2 \\ 2 q_1 q_2 - 2 q_0 q_3 & q_0^2 - q_1^2 + q_2^2 - q_3^2 & 2 q_2 q_3 + 2 q_0 q_1 \\ 2 q_1 q_3 + 2 q_0 q_2 & 2 q_2 q_3 - 2 q_0 q_1 & q_0^2 - q_1^2 - q_2^2 + q_3^2 \end{pmatrix} \quad (2.15)$$

A quaternion can be obtained from a rotation matrix using following relationship:

$$\left. \begin{aligned} \mathbf{q} &= \frac{1}{2\sqrt{k}} (k, R_{23} - R_{32}, R_{31} - R_{13}, R_{12} - R_{21})^T \\ k &= 1 + R_{11} + R_{22} + R_{33} \end{aligned} \right\} \begin{aligned} &\text{if } R_{22} \geq -R_{33}, R_{11} \geq -R_{22}, \\ &R_{11} \geq -R_{33} \end{aligned} \quad (2.16)$$

$$\left. \begin{aligned} \mathbf{q} &= \frac{1}{2\sqrt{k}} (R_{23} - R_{32}, k, R_{12} + R_{21}, R_{31} + R_{13})^T \\ k &= 1 + R_{11} - R_{22} - R_{33} \end{aligned} \right\} \begin{aligned} &\text{if } R_{22} < -R_{33}, R_{11} \geq R_{22}, \\ &R_{11} \geq R_{33} \end{aligned} \quad (2.17)$$

$$\left. \begin{aligned} \mathbf{q} &= \frac{1}{2\sqrt{k}}(R_{31} - R_{13}, R_{12} + R_{21}, k, R_{23} + R_{32})^T \\ k &= 1 - R_{11} + R_{22} - R_{33} \end{aligned} \right\} \begin{aligned} &\text{if } R_{22} \geq R_{33}, R_{11} < R_{22}, \\ &R_{11} < -R_{33} \end{aligned} \quad (2.18)$$

$$\left. \begin{aligned} \mathbf{q} &= \frac{1}{2\sqrt{k}}(R_{12} - R_{21}, R_{31} + R_{13}, R_{23} + R_{32}, k)^T \\ k &= 1 - R_{11} - R_{22} + R_{33} \end{aligned} \right\} \begin{aligned} &\text{if } R_{22} < R_{33}, R_{11} < -R_{22}, \\ &R_{11} < R_{33} \end{aligned} \quad (2.19)$$

The derivatives of the quaternions can be linked to angular velocities via the following function:

$$\dot{\mathbf{q}}(\mathbf{q}, \boldsymbol{\omega}) = (\dot{q}_0, \dot{q}_1, \dot{q}_2, \dot{q}_3)^T = \frac{1}{2} \mathbf{T}^T(\mathbf{q}) \boldsymbol{\omega} \quad (2.20)$$

$$\mathbf{T}(\mathbf{q}) = \begin{pmatrix} -q_1 & +q_0 & -q_3 & +q_2 \\ -q_2 & +q_3 & +q_0 & -q_1 \\ -q_3 & -q_2 & +q_1 & +q_0 \end{pmatrix} \quad (2.21)$$

where $\boldsymbol{\omega}$ is the rotation vector in the global frame and \mathbf{T} is the quaternion rate matrix. Alternative formulations allow to express the angular velocities in the local (or body) frame (see Diebel, 2006).

2.4 Principle of GNSS attitude determination

GNSS attitude determination is based on the following principle (see Figure 2.4.1): the baseline vectors are perfectly known in the body-fixed frame of the spacecraft, but observed in a world coordinate system, for instance WGS84:

$$r = \mathbf{e}_{\text{world}}^T \mathbf{R}_{\text{world} \leftarrow \text{body}} \mathbf{b}_{\text{body}} + v \quad (2.22)$$

where r is a range difference, $\mathbf{e}_{\text{world}}^T$ is the line-of-sight (LOS) in the world frame and v is the observation noise, which is assumed to be normally distributed. This last term makes obvious that Eq. 2.22 is an observation equation. The observable is typically a carrier phase observation. Eq. 2.22 is valid assuming that the baselines are shorter than a few meters and that the body is rigid.

If measurements are taken over several baselines and several satellites are seen by the antennas, the attitude is over-determined and can be estimated with least-squares:

$$L(\mathbf{R}) = \sum_k \sum_i \frac{1}{\sigma_{ik}^2} \left(r_{ik} - \mathbf{e}_i^T \mathbf{R} \mathbf{b}_k \right)^2 \quad (2.23)$$

where L is the cost function and σ_{ik} is the observation noise of the range difference on baseline

k to satellite i . The minimization of this function is well known as Wahba's problem (Farrell et al., 1966). Some analytical solutions exist to solve this problem, but are limited to the case of vector observations (Cohen, 1992). As processing speed is not critical nowadays, these methods are not of much interest anymore. Preferentially, raw GNSS phase observations are processed directly. The main advantage of a proper least-squares formulation is, that correlations between the observations are properly taken into account, which is not the case in Eq. 2.23.

A GNSS phase observation reads (Hauschild, 2017a):

$$P_A^i = \mathbf{e}_A^{i\text{T}} \left(\mathbf{x}^i(t_A - \tau_A) - \mathbf{x}_A(t_A) \right) + c \delta t_A - c \delta t^i + \lambda N_A^i + T_A^i + I_A^i + \text{PCV}_A^i + v_A^i \quad (2.24)$$

where

P_A^i	is the carrier phase observation between antenna A and satellite i ,
\mathbf{e}_A^i	is the line-of-sight vector,
\mathbf{x}^i	is the GNSS satellite position at signal emission time,
t_A	is the measurement epoch,
τ_A	is the signal travel time,
\mathbf{x}_A	is the position of the receiver antenna at signal reception,
c	is the speed of light,
δt_A	is the receiver clock error,
δt^i	is the satellite clock error,
λ	is the carrier wavelength,
N_A^i	is the integer phase ambiguity,
T_A^i	is the tropospheric delay,
I_A^i	is ionospheric delay,
PCV_A^i	is the Phase Centre Variation (PCV) and
v_A^i	is the zero-difference observation noise.

The observations of two antennas can be subtracted from each other in order to obtain a single-difference observation:

$$P_{AB}^i = P_B^i - P_A^i = \mathbf{e}_B^{i\text{T}} \left(\mathbf{x}^i(t_B - \tau_B) - \mathbf{x}_B(t_B) \right) - \mathbf{e}_A^{i\text{T}} \left(\mathbf{x}^i(t_A - \tau_A) - \mathbf{x}_A(t_A) \right) + c \delta t_B - c \delta t_A + \lambda N_{AB}^i + v_{AB}^i \quad (2.25)$$

where

P_{AB}^i	is a phase single-difference between antenna A and B,
N_{AB}^i	is the single-difference ambiguity term and
v_{AB}^i	is the single-difference observation noise.

The satellite clock error as well as the tropospheric and ionospheric delays vanish as the baseline is assumed to be short. The PCV vanish hypothetically, if identical antennas are used (the following chapter will show that this assumption does not hold).

The baseline between antenna A and B, \mathbf{b}_{AB} , is defined as follows:

$$\mathbf{b}_{AB} = \mathbf{R}^T (\mathbf{x}_A - \mathbf{x}_B) \quad (2.26)$$

where \mathbf{b}_{AB} is the baseline vector between antennas A and B in the body frame and \mathbf{R} is the attitude matrix from Eqs. 2.2 and 2.23. Assuming that:

- i. The baseline is short and therefore $\mathbf{e}_A^i = \mathbf{e}_B^i$,
- ii. The baseline is short and therefore $\tau_A = \tau_B$ and
- iii. The receivers are synchronised and therefore $t_A = t_B$.

Introducing Eq. 2.26 into Eq. 2.25 leads to the final expression for the single-difference observation equation:

$$P_{AB}^i = P_B^i - P_A^i = \mathbf{e}^{i^T} \mathbf{R} \mathbf{b}_{AB} + c \delta t_B - c \delta t_A + \lambda N_{AB}^i + v_{AB}^i \quad (2.27)$$

The error which is induced due to approximation (i) is about:

$$\epsilon = b \sin \left(\arctan \frac{b}{2d} \right) \quad (2.28)$$

where

- ϵ is the range error due to the approximation,
- b is the length of the baseline and
- d is the distance to the GNSS satellite.

Assuming a baseline length of 1 m and a distance to the GNSS spacecraft of 20 000 km, the range error amounts to $2.5 \cdot 10^{-8}$ m and is therefore negligible. The error due to approximation (ii) is always smaller than the length of the baseline divided by the speed of light. For a baseline length of 1 m, the resulting timing error never exceeds $3.3 \cdot 10^{-9}$ seconds and thus, can be neglected as well.

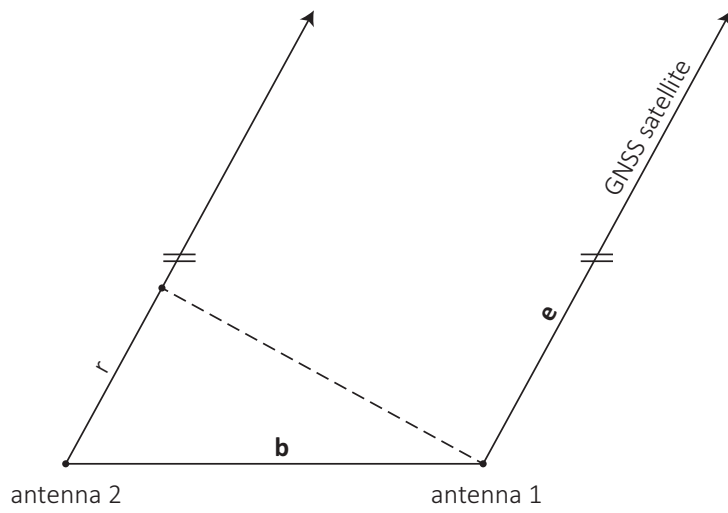


Figure 2.4.1 : Principle of GNSS attitude determination. \mathbf{b} is the baseline, r is the range difference and \mathbf{e} is the line-of-sight unit vector.

2.5 Extrapolation of the GNSS measurements

Eq. 2.27 is based on assumptions that are not valid onboard a fast vehicle equipped with non-synchronised receivers, for instance a spacecraft in LEO. As shown in Eq. 2.1, the velocity of such a spacecraft is approximately 8 km/s. Within a millisecond, which is the maximal synchronisation error, the spacecraft travels 8 m. That means that the receiver connected to antenna A performs the GNSS measurements up to 8 m further from the coordinates, where the receiver connected to antenna B performed its GNSS measurement. From this example, it is obvious that an extrapolation is necessary.

Assuming that $\mathbf{e}_A^i = \mathbf{e}_B^i = \mathbf{e}^i$, Eq. 2.25 can be simplified to lead to following expression.

$$P_{AB}^i = P_B^i - P_A^i = \mathbf{e}^{i\top} \left(\mathbf{x}^i(t_B - \tau_B) - \mathbf{x}_B(t_B) - \mathbf{x}^i(t_A - \tau_A) + \mathbf{x}_A(t_A) \right) + c\delta t_B - c\delta t_A + \lambda N_{AB}^i + v_{AB}^i \quad (2.29)$$

The attitude of the spacecraft does not appear explicitly in this last equation. Therefore, we introduce:

$$\mathbf{x}_A(t_A) = \mathbf{x}_A(t_A) + \mathbf{x}_A(t_{\text{nom}}) - \mathbf{x}_A(t_{\text{nom}}) \quad (2.30)$$

$$\mathbf{x}_B(t_B) = \mathbf{x}_B(t_B) + \mathbf{x}_B(t_{\text{nom}}) - \mathbf{x}_B(t_{\text{nom}}) \quad (2.31)$$

where t_{nom} is the nominal measurement epoch. Substitution of Eqs. 2.30 and 2.31 into Eq. 2.29 leads to:

$$P_{AB}^i = \mathbf{e}^{i\top} \left(\mathbf{x}^i(t_B - \tau_B) - \mathbf{x}_B(t_{\text{nom}}) - \mathbf{x}^i(t_A - \tau_A) + \mathbf{x}_A(t_{\text{nom}}) - \mathbf{x}_B(t_B) + \mathbf{x}_B(t_{\text{nom}}) + \mathbf{x}_A(t_A) - \mathbf{x}_A(t_{\text{nom}}) \right) + c\delta t_B - c\delta t_A + \lambda N_{AB}^i + v_{AB}^i \quad (2.32)$$

At this state, the equation can be combined with Eq. 2.26 again, as \mathbf{x}_A and \mathbf{x}_B appear with the same time argument.

$$P_{AB}^i = \mathbf{e}^{i\top} \mathbf{R}(t_{\text{nom}}) \mathbf{b}_{AB} + E_{AB}^i + c\delta t_B - c\delta t_A + \lambda N_{AB}^i + v_{AB}^i \quad (2.33)$$

$$E_{AB}^i = \mathbf{e}^{i\top} \left(\mathbf{x}^i(t_B - \tau_B) - \mathbf{x}^i(t_A - \tau_A) - \mathbf{x}_B(t_B) + \mathbf{x}_B(t_{\text{nom}}) + \mathbf{x}_A(t_A) - \mathbf{x}_A(t_{\text{nom}}) \right) \quad (2.34)$$

where E_{AB}^i is the extrapolation term.

The coordinates of an antenna can be expressed relatively to the coordinates of the centre of mass of the spacecraft and the attitude of the spacecraft:

$$\mathbf{x}_A(t) = \mathbf{x}_{\text{cm}}(t) + \mathbf{R}(t) \mathbf{b}_{\text{cm},A} \quad (2.35)$$

where

- $\mathbf{x}_A(t)$ are the coordinates of the antenna A,
- $\mathbf{x}_{\text{cm}}(t)$ are the coordinates of the centre of mass of the spacecraft,
- $\mathbf{R}(t)$ is the attitude matrix of the spacecraft and
- $\mathbf{b}_{\text{cm},A}$ is the vector from the centre of mass of the spacecraft to antenna A.

Therefore:

$$\mathbf{x}_A(t_A) = \mathbf{x}_{\text{cm}}(t_A) + \mathbf{R}(t_A) \mathbf{b}_{\text{cm},A} \quad (2.36)$$

$$\mathbf{x}_A(t_{\text{nom}}) = \mathbf{x}_{\text{cm}}(t_{\text{nom}}) + \mathbf{R}(t_{\text{nom}}) \mathbf{b}_{\text{cm},A} \quad (2.37)$$

$$\mathbf{x}_B(t_B) = \mathbf{x}_{\text{cm}}(t_B) + \mathbf{R}(t_B) \mathbf{b}_{\text{cm},B} \quad (2.38)$$

$$\mathbf{x}_B(t_{\text{nom}}) = \mathbf{x}_{\text{cm}}(t_{\text{nom}}) + \mathbf{R}(t_{\text{nom}}) \mathbf{b}_{\text{cm},B} \quad (2.39)$$

Because the rotation rate of the satellite is small and the baselines are short, $\mathbf{R}(t_A) = \mathbf{R}(t_B) = \mathbf{R}(t_{\text{nom}})$ can be assumed. The first order error introduced by this simplification is $\Delta \mathbf{x} = (t_B - t_A) \dot{\mathbf{R}} \mathbf{b}_{AB}$. For a baseline of 10 cm, the error is smaller than 2 μm for rates up to 1 degree per second.

Introducing this simplification and Eqs. 2.36 to 2.39 into Eq. 2.34 leads to the final expression for the extrapolation term:

$$E_{AB}^i = \mathbf{e}^{i^T} \left(\mathbf{x}^i(t_B - \tau_B) - \mathbf{x}^i(t_A - \tau_A) - \mathbf{x}_{\text{cm}}(t_B) + \mathbf{x}_{\text{cm}}(t_A) \right) \quad (2.40)$$

The first part of this expression can be calculated with the broadcast ephemeris (see for instance IS-GPS-200, 2015 for GPS broadcast ephemeris). The second half of this expression can be computed using the receiver navigation solution or any other PVT solution. The quality of the extrapolation will depend on the quality of the PVT estimation. The uncertainty in the line-of-sight propagates linearly with time. Assuming an accuracy of the velocity of 1 m/s and an extrapolation span of 1 ms, the accuracy of the extrapolation is 1 mm. In orbit, the accuracy of the u-blox velocity estimation is better than 10 cm/s, as reported in Hollenstein et al. (2014).

The velocity of a GNSS spacecraft can be computed using the broadcast ephemeris. The accuracy of GNSS spacecraft velocities derived in that way is around 1 mm/s for GPS (Zhang et al., 2006) and therefore negligible compared to the accuracy of the PVT solution.

2.6 Practical aspects of GNSS measurement extrapolation with Bernese

The Bernese GNSS Software V5.2 (Dach et al., 2015) was used to generate synthetic data. Bernese is a widely used and well established GNSS processing and analysis software. It has a more than 30 years long history. However, the processing of very fast stations with non-synchronised receivers was originally not foreseen. In order to obtain reliable results, some minor software

modifications had to be performed. These changes are documented here. The modifications were validated by performing a comparison in Matlab. After the software modifications, the synthetic observations are consistent to 10^{-6} m for LEO spacecraft.

In Bernese, `GTLEOCO.f` is the subroutine which allows to retrieve the coordinates of the centre of mass of a LEO spacecraft in different coordinate systems, `LEOSKY.f90` computes distance, azimuth and elevation to GNSS satellites as seen from a LEO spacecraft and `SMPRNG.f` is the actual range simulation routine. Table 2.6.1 holds a summary of the performed changes.

The main obstacle is the limited precision of the internal time representation. A Fortran double is used for the representation of epochs, thus providing 15 digits. Because the time is saved as a fractional Modified Julian Date (MJD), five digits are used for the integer part. Ten digits are left for the fractional part of a day (which counts 86 400 seconds), leading to a time resolution of only $86\,400 \text{ s} \cdot 10^{-10} = 8.64 \mu\text{s}$. This is insufficient to precisely position a spacecraft with a speed of 8 km/s. A workaround consists of using the receiver clock error in `SMPRNG.f`, which is in seconds, to hold the difference to the actual time and thus compensating the truncation error due to the time representation in MJD.

Another change is the addition of the second order term in the position computation of the LEO satellite in `LEOSKY.f90`. Finally, a new function is added in order to check whether a signal is obstructed by the Earth or not. This feature was not present, as it is not necessary when generating synthetic observations for stations with an antenna always pointing in zenith direction. This is the case for stations on Earth, but also for GNSS antennas onboard satellites with sophisticated attitude control.

Table 2.6.1 : Summary of modifications to the Bernese GNSS Software.

Subroutine	Performed changes
GTLEOCO.f	Modified call of COOTRA
LEOSKY.f90	Added second order term in the position computation of the LEO satellite
SMPRNG.f	Modified call of XYZTIM Modified call of TRUEEARTH Modified call of LEOSKY Correction of the rounding error due to the time representation in MJD Computation of Earth shadowing of signals and removal of those

2.7 Phase ambiguity resolution

Eq. 2.33 is still affected by an unknown integer phase ambiguity N_{AB}^i . In order to solve for phase ambiguities, a double-difference solution is computed. At this stage, phase ambiguities can most easily be resolved to integer numbers. Instantaneous methods are simple in the implementation, but provide lower ambiguity resolution success rates. Methods using several epochs show better success rates, but are sensitive to phase cycle slips. These must be detected and corrected or dealt with properly in order not to bias the ambiguity resolution process.

Ambiguity resolution has been extensively studied in the past. A general introduction to ambiguity resolution is provided in Teunissen (2017). The most prominent algorithm is the so-called LAMBDA algorithm (Teunissen, 1995). In the case of ambiguity resolution for attitude determination, prior information about the geometry of the antenna system can be provided to the adjustment as pseudo-observations or as constraints and help to reduce the ambiguity search space and do increase the ambiguity resolution success rate. Such algorithms were presented in Park and Teunissen (2003) or Teunissen (2010) and successfully employed in different use-cases (Teunissen et al., 2011). Ambiguity resolution for attitude determination is also presented in Giorgi (2017, pp. 793–798).

In the case of the CubETH spacecraft, the simplest implementation proved to be very efficient. An approximation for the carrier phase ambiguities was generated by setting the baseline length to zero at double-difference level. The double-difference can for instance be derived from Eq. 2.33:

$$P_{AB}^{ij} = (\mathbf{e}^j - \mathbf{e}^i)^T \mathbf{R} \mathbf{b}_{AB} + E_{AB}^{ij} + \lambda N_{AB}^{ij} + v_{AB}^{ij} \quad (2.41)$$

where

$$\begin{aligned} P_{AB}^{ij} & \text{ is the double-difference phase observation,} \\ E_{AB}^{ij} & \text{ is the double-difference extrapolation term,} \\ N_{AB}^{ij} & \text{ is the double-difference phase ambiguity and} \\ v_{AB}^{ij} & \text{ is the double-difference observation residual.} \end{aligned}$$

The receiver clock vanishes, as every antenna observes two GNSS satellites at exactly the same time. The approximation for the phase ambiguity is:

$$\tilde{N}_{AB}^{ij} = P_{AB}^{ij} - E_{AB}^{ij} \quad (2.42)$$

Strictly spoken, this approximation is only valid for baselines shorter than half a wavelength or approximatively 10 cm. The true ambiguity must then lie in the interval $[-1, 1]$ around \tilde{N}_{AB}^{ij} (Van Graas and Braasch, 1991). As this search space is very narrow, it can easily be fully searched through. The size of the search space for single-frequency receivers is:

$$n_{\text{candidates}} = 3^{n_{\text{satellites}} - 1} \quad (2.43)$$

where $n_{\text{candidates}}$ is the number of candidates in total and $n_{\text{satellites}}$ is the number of satellites. If the baseline length is significantly increased, other search strategies, as mentioned before, have to be used.

2.8 Filter formulation

In the absence of a strong attitude control, a spacecraft will have a very regular attitude and typically constant turn rates. This dynamics predestines the Kalman filter for the estimation of the attitude. Details on the Kalman filter can be found in Welch and Bishop (2006). Two successive states are linked by a process:

$$\mathbf{x}_s = \mathbf{f}(\mathbf{x}_{s-1}) + \mathbf{u}_{s-1} \quad (2.44)$$

$$\mathbf{u}_{s-1} \sim N(0, \mathbf{U}_{s-1}) \quad (2.45)$$

where

- \mathbf{x}_s is the state at the epoch s ,
- \mathbf{f} is the state transition function,
- \mathbf{x}_{s-1} is the state at the epoch $s - 1$,
- \mathbf{u}_{s-1} is the process noise and
- \mathbf{U}_{s-1} is the process noise variance-covariance.

The observation equation reads as follows.

$$\mathbf{z}_s = \mathbf{h}(\mathbf{x}_s) + \mathbf{v}_s \quad (2.46)$$

$$\mathbf{v}_s \sim N(0, \mathbf{V}_s) \quad (2.47)$$

where

- \mathbf{z} is the observation vector,
- \mathbf{h} is the observation function,
- \mathbf{v} is the observation noise and
- \mathbf{V} is the observation variance-covariance.

The filter update step is given by:

$$\hat{\mathbf{x}}_s^- = \mathbf{f}(\hat{\mathbf{x}}_{s-1}) \quad (2.48)$$

$$\mathbf{P}_{s-1}^- = \mathbf{F}_{s-1} \mathbf{P}_{s-1} \mathbf{F}_{s-1}^T + \mathbf{U}_{s-1} \quad (2.49)$$

$$F_{ij} = \frac{\partial f_i(\mathbf{x})}{\partial x_j} \quad (2.50)$$

$\hat{\mathbf{x}}_s^-$ is the propagated state, $\hat{\mathbf{x}}_{s-1}$ is the state estimate of the previous epoch, \mathbf{P}_{s-1}^- is the propagated state variance-covariance, \mathbf{F}_{s-1} is the matrix of partial derivatives and \mathbf{P}_{s-1} is the variance-covariance of the state estimate of epoch $s - 1$. The filter measurement update reads as:

$$\mathbf{K}_s = \mathbf{P}_s^- \mathbf{H}_s^T \left(\mathbf{H}_s \mathbf{P}_s^- \mathbf{H}_s^T + \mathbf{V}_s \right) \quad (2.51)$$

$$\hat{\mathbf{x}}_s = \hat{\mathbf{x}}_s^- + \mathbf{K}_s \left(\mathbf{z}_s - \mathbf{h}(\hat{\mathbf{x}}_s^-) \right) \quad (2.52)$$

$$\mathbf{P}_s = (\mathbf{I} - \mathbf{K}_s \mathbf{H}_s) \mathbf{P}_s^- \quad (2.53)$$

$$H_{ij} = \frac{\partial h_i(\mathbf{x})}{\partial x_j} \quad (2.54)$$

where

\mathbf{K}_s is the Kalman gain matrix,

\mathbf{H}_s is the matrix of partial derivatives,

$\hat{\mathbf{x}}_s$ is the estimated state and therefore the result of the Kalman filter and

\mathbf{P}_s is the variance-covariance matrix of this state.

2.8.1 State propagation

The Kalman filter state vector is composed of the quaternion \mathbf{q} and the turn rates $\boldsymbol{\omega}$ and reads as follows:

$$\underset{7 \times 1}{\mathbf{x}} = \begin{pmatrix} \mathbf{q} \\ \boldsymbol{\omega} \end{pmatrix} = \left(q_0 \quad q_1 \quad q_2 \quad q_3 \quad \omega_1 \quad \omega_2 \quad \omega_3 \right)^T \quad (2.55)$$

As the spacecraft is symmetrical, it is expected to have very regular turn rates. Furthermore, no information about the attitude control (e.g. torques) is available. Therefore, a very simple dynamical model has been chosen:

$$\mathbf{x}_s = \mathbf{x}_{s-1} + (t_s - t_{s-1}) \dot{\mathbf{x}}_{s-1} \quad (2.56)$$

$$= \begin{pmatrix} \mathbf{q} \\ \boldsymbol{\omega} \end{pmatrix}_{s-1} + (t_s - t_{s-1}) \begin{pmatrix} \dot{\mathbf{q}} \\ \mathbf{0} \end{pmatrix}_{s-1} \quad (2.57)$$

where $(t_s - t_{s-1})$ is the time between two successive epochs. This model assumes constant turn rates.

2.8.2 Stochastic model

The associated stochastic model can be derived starting from the state-space equation. It is assumed, that the process noise affects the system only depends on the rotation rates, leading to:

$$\dot{\mathbf{x}}(t) = \begin{pmatrix} \dot{\mathbf{q}}(t) \\ \dot{\boldsymbol{\omega}}(t) \end{pmatrix} = \mathbf{a}(\mathbf{x}(t)) + \mathbf{G} \mathbf{w}(t) \quad (2.58)$$

$$= \begin{pmatrix} \dot{\mathbf{q}}(\mathbf{q}(t), \boldsymbol{\omega}(t)) \\ \mathbf{0}_{3 \times 1} \end{pmatrix} + \begin{pmatrix} \mathbf{0}_{4 \times 3} \\ \mathbf{I}_3 \end{pmatrix} \begin{pmatrix} w_1(t) \\ w_2(t) \\ w_3(t) \end{pmatrix} \quad (2.59)$$

where

- $\dot{\mathbf{x}}$ is the time derivative of the state,
- $\mathbf{a}(\mathbf{x})$ is the system model function,
- \mathbf{G} is the noise shaping matrix and
- \mathbf{w} is the white noise entering the system.

After linearisation, this function reads:

$$\delta \dot{\mathbf{x}} = \mathbf{A} \delta \mathbf{x} + \mathbf{G} \mathbf{w} \quad (2.60)$$

$$\delta \dot{\mathbf{x}} = \dot{\mathbf{x}} - \mathbf{g}(\mathbf{x}_0) \quad (2.61)$$

$$\delta \mathbf{x} = \mathbf{x} - \mathbf{x}_0 \quad (2.62)$$

$$A_{ij} = \frac{\partial a_i(\mathbf{x}_0)}{x_j} \quad (2.63)$$

where \mathbf{A} is the Jacobian matrix of the function \mathbf{a} and \mathbf{x}_0 is the linearisation point. The solution to the differential equation 2.60 reads:

$$\begin{aligned} \delta \mathbf{x}(t) &= e^{(t-t_0)\mathbf{A}} \delta \mathbf{x}(t_0) + \int_{t_0}^t e^{(t'-t_0)\mathbf{A}} \mathbf{G} \mathbf{w}(t') dt' \\ &= e^{(t-t_0)\mathbf{A}} \delta \mathbf{x}(t_0) + \mathbf{u} \end{aligned} \quad (2.64)$$

Assuming that \mathbf{w} is a stationary white noise process and that all three components have the same standard deviation, variance-covariance propagation can be applied to obtain the variance-covariance of the propagated state:

$$\mathbf{U} = \int_{t_0}^t e^{(t'-t_0)\mathbf{A}} \mathbf{G} \mathbf{I}_3 \sigma_w^2 \mathbf{I}_3 \mathbf{G}^T \left(e^{(t'-t_0)\mathbf{A}} \right)^T dt' \quad (2.65)$$

where \mathbf{U} is the Kalman filter process noise (see Eq. 2.45) and σ_w^2 is the noise variance. Integration

of this equation leads to an analytical formula for \mathbf{U} :

$$\mathbf{U} = \sigma_w^2 \begin{pmatrix} \mathbf{\Theta} & \mathbf{\Omega} \\ \mathbf{\Theta}^T & \Delta t \mathbf{I}_3 \end{pmatrix} \quad (2.66)$$

$$\mathbf{\Theta} = \frac{\Delta t^3}{12} \begin{pmatrix} q_1^2 + q_2^2 + q_3^2 & -q_0 q_1 & -q_0 q_2 & -q_0 q_3 \\ -q_0 q_1 & q_0^2 + q_2^2 + q_3^2 & -q_1 q_2 & -q_1 q_3 \\ -q_0 q_2 & -q_1 q_2 & q_0^2 + q_1^2 + q_3^2 & -q_2 q_3 \\ -q_0 q_3 & -q_1 q_3 & -q_2 q_3 & q_0^2 + q_1^2 + q_2^2 \end{pmatrix} \quad (2.67)$$

$$\mathbf{\Omega} = \frac{\Delta t^2}{4} \begin{pmatrix} -q_1 & -q_2 & -q_3 \\ q_0 & q_3 & -q_2 \\ -q_3 & q_0 & q_1 \\ q_2 & -q_1 & q_0 \end{pmatrix} \quad (2.68)$$

where Δt is the time interval between two epochs and q_i is the i^{th} element of the quaternion. The stochastic model of the double-difference observations \mathbf{V} is simply obtained after application of variance-covariance propagation:

$$\mathbf{V} = \mathbf{D} \mathbf{Q}_{ll} \mathbf{D}^T \quad (2.69)$$

where \mathbf{D} is the differencing operator leading to double-difference observations and \mathbf{Q}_{ll} is the variance-covariance matrix of the zero-difference observations. If equal weighting of all observations is assumed, Eq. 2.69 becomes:

$$\mathbf{V} = \mathbf{D} \mathbf{I}_n \sigma_p^2 \mathbf{I}_n \mathbf{D}^T \quad (2.70)$$

where σ_p^2 is the zero-difference observation variance and n is the number of zero-difference observations.

2.9 Paper I – GNSS Attitude Determination with Non-Synchronized Receivers and Short Baselines Onboard a Spacecraft

The first paper presents a summary of the algorithm for attitude determination as well as results obtained from synthetic data and from a validation conducted with signal simulator data. It was published in *GPS Solutions*, Volume 21, Issue 4, pp. 1605–1617, October 2017 (first online 18 may 2017) with the title *GNSS Attitude Determination with Non-Synchronized Receivers and Short Baselines Onboard a Spacecraft*.

2.9.1 Abstract

A new algorithm for GNSS attitude determination is presented. It is based on a Kalman filter which uses GNSS phase measurements as input. A rigorous approach for the combination of data from several baselines in the Kalman filter is presented.

Because the u-blox receivers used in this study do not perform clock steering, the measurements must be extrapolated to a common epoch. Therefore, an extrapolation term is derived. It ranges from -6 to $+6$ m, which shows that a proper extrapolation is crucial.

The article presents a validation based on both, a synthetic data study and a signal simulator study. Both studies demonstrated the good performance and the validity of the approach. This is an important contribution to attitude determination in space with receivers without clock steering. The filter formulation including a derivation of the process noise is of general interest in the context of attitude determination.

2.9.2 Author's contribution

The following section attempts to give a summary of the author's contribution to paper I (Willi and Rothacher, 2017). The author's contribution is summarized in Table 2.9.1. The theoretical developments as well as the implementation in Matlab were nearly exclusively carried out by the author. This includes the development of a quaternion maths library, routines for reading the observations, for double differencing, for parameter estimation, for ambiguity resolution, for orbit interpolation and routines for the Kalman filter.

The generation of synthetic data was done by the author using Bernese. For the signal simulator study, a processing pipeline including a RINEX parser for binary u-blox UBX files was developed. Standard RINEX parsers for UBX files could not be used, as the receivers used within this study are equipped with a customized firmware.

2.9.3 Relevance to the field

The algorithm was originally designed especially for the real-time needs of the CubETH spacecraft. The developed algorithm, especially the extrapolation part, is a novelty. The paper published in *GPS Solutions* is nicely complementary to the literature available, as it presents a full framework for attitude determination, including a clean parametrisation with quaternions and the corresponding filter formulation and a stochastic model.

Table 2.9.1 : Summary of the author's contribution to paper I – GNSS Attitude Determination with Non-Synchronized Receivers and Short Baselines Onboard a Spacecraft.

	Original idea	Measurements, data generation	Theoretical developments	Software implementation	Computation, data processing
General GNSS routines				80%	
Extrapolation of the measurements	80%		100%	100%	
Quaternion parametrisation	100%		100%	100%	
Filter formulation	60%		100%	100%	
Synthetic data study	50%	100%			100%
Simulator data study	50%	33%			100%
Editorial work	90%				

2.10 Outlook

Unfortunately, the CubETH project was not continued, giving us no opportunity to pursue the development of the algorithm. The present work is a solid base. It could easily be enhanced with outlier detection, a robust initialization and a more powerful ambiguity resolution algorithm. These three topics were extensively studied in the past and do not represent novel scientific issues.

The next step after the synchronisation of the receivers is the modelling of the Phase Centre Calibrations (PCC). Because of the short baselines, any uncorrected PCV has a huge impact on the accuracy. This topic is addressed in the next chapters.

Chapter 3

GNSS Antenna Calibration

GNSS antennas are a key factor in GNSS measurements. Antennas transform incoming electromagnetic signals into voltage. They are an essential part of any Satellite Navigation System, as they are the interface between the GNSS signals and the receiver. A very good introduction to GNSS antennas is provided in Maqsood et al. (2017) and in Rao et al. (2013).

Antennas are not perfect and are therefore subject to errors. When measuring coordinates with a GNSS antenna, the coordinates refer to a mechanical point on the antenna, the Antenna Reference Point (ARP). Usually, the intersection of the lowest horizontal surface of the antenna with the vertical symmetry axis is defined as ARP. An updated list of the ARP for the most common antennas including technical drawings is provided by the antenna working group (AGW) of the International GNSS Service (IGS).¹

The electronic centre of the antenna is not located in the ARP. Therefore, Phase Centre Offsets (PCO) were introduced. The PCO is the vector from the ARP to the so-called Mean Phase Centre (MPC). The MPC is a purely conventional point, as the measurement locations of the incoming electromagnetic waves never meet in a single point. First theoretical considerations for interferometric baseline measurements were made already at the end of the seventies (Counselman and Shapiro, 1979). Very soon, phase centre calibrations were studied, attempted and achieved (Sims, 1985; Geiger, 1988; Tranquilla and Colpitts, 1989).

The result of a successful calibration is a map of the so-called Phase Centre Variations (PCV), which are corrections that are added on top of the PCO. PCV are typically in the range of several millimetres (Rothacher, 2001), but can reach centimetre level for miniaturized low-cost antennas. Although this nomenclature is a bit confusing, as the MPC is arbitrary and the PCV directly depends on the chosen PCO, this convention is still widely used in the antenna calibration community after its introduction in the early nineties (Geiger, 1990). Nowadays, the term Phase Centre Correction (PCC) should be used to designate calibrations that include PCO and PCV.

¹Antenna information file of the IGS AWG, <ftp://igs.org/pub/station/general/antenna.gra>.

The present chapter describes antenna calibration in general, the parametrisation of PCC and the underlying estimation theory. Chapter 4 presents the relative field calibration approach tailored to the calibration of attitude determination systems. Robot specific questions are addressed in Chapter 5, followed by Chapter 6 on absolute field calibrations using a robot.

3.1 Definitions

Within the present document, following nomenclature is adopted.

Phase Centre Correction (PCC) is the total correction to be applied to the measured range in order to obtain the coordinates of the Antenna Reference Point (ARP). The PCC is divided into:

- i. The **Phase Centre Offset (PCO)**, which is the vector from the ARP to the Mean Phase Centre (MPC), an arbitrary point and
- ii. The **Phase Centre Variation (PCV)**, which is the actual direction dependent correction function.

Generally, the MPC is chosen in such a way that the PCV is minimized. However, various different conventions exist (see for instance in Dach et al. 2015, pp. 404–405). The obtained MPC is dependent on the weighing of the observations and on the elevation cut-off angle. Therefore, the PCC is the only meaningful quantity. The comparison of two or several antenna calibrations should always be based on a comparison of the PCC. Figure 3.1.1 illustrates the relationship between the different quantities.

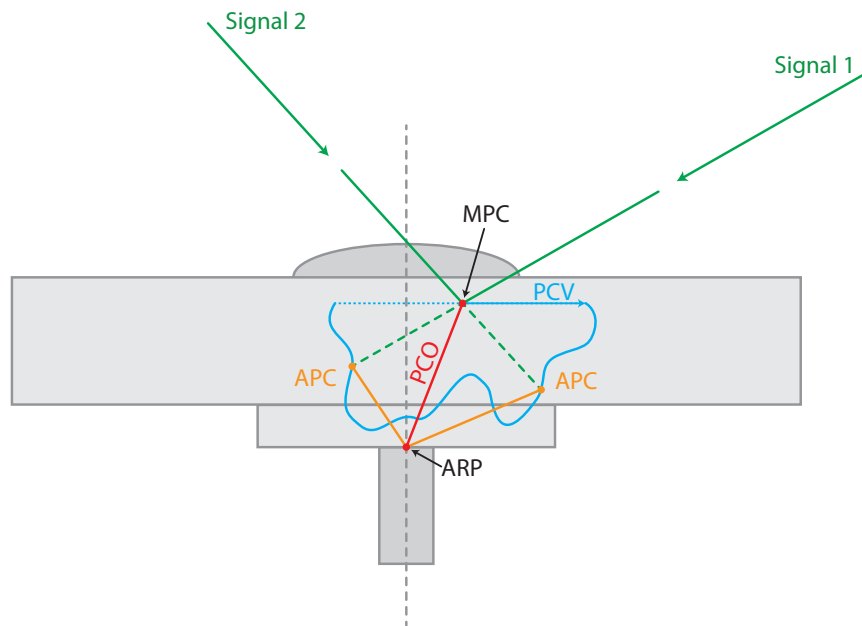


Figure 3.1.1 : Illustration of the relevant quantities in antenna calibration. The Antenna Reference Point (ARP) is the mechanical reference of the antenna. The Phase Centre Offset (PCO) is the vector from the ARP to the Mean Phase Centre (MPC). The MPC is purely conventional and can be arbitrarily chosen. The actual direction dependent correction, the Phase Centre Variation (PCV), is added on top of the PCO, leading to the Apparent Phase Centre (APC). The Phase Centre Correction is the projection of the vector from the ARP to the APC (drawn in orange) onto the line-of-sight.

3.2 State of the art

Antenna calibration procedures can be divided into three categories: (Görres et al., 2006; Rothacher, 2001)

- i. Relative field calibration.
- ii. Absolute calibration:
 - a. Anechoic chamber calibration.
 - b. Absolute field calibration using a robot.

Antenna calibrations are performed routinely worldwide by a dozen of groups. German institutions were particularly active in GNSS antenna calibration. A GNSS antenna calibration workshop was held annually in Germany from 1999 to 2009.² Nowadays, German institutions are still leading in this field, as is shown in the following sections. German speaking practitioner can find general information on antenna calibrations in Görres et al. (2018).

Various studies show that the results from different techniques agree well for the first GPS frequency (L1), typically below the millimetre level, but some improvements are possible for GPS L2 (Görres et al., 2006; Bilich et al., 2012).

The repeatability within each technique is very well documented for robot calibrations (Schmitz et al., 2002; Wübbena et al., 2003) and for anechoic chamber measurements (Zeimetz and Kuhlmann, 2008).

3.2.1 Relative field calibration

In relative field calibration (Rothacher et al., 1995), a short baseline is set up and data is collected over a period of at least one day. The first antenna of the baseline is the reference antenna. It can either have perfectly known PCC or arbitrarily been set to zero. The second antenna of the baseline is the uncalibrated antenna. During the estimation, a PCC function is fit through the residuals, resulting in estimates of the station coordinates and of the PCC.

In order to decorrelate the PCO from the station coordinates, the antenna can be rotated around its vertical axis of symmetry. Typically, four sessions with four different azimuths are recorded, every session lasting for one hour. The vertical component of the PCO will still correlate to 100% with the station height and needs to be constrained to a known value. This value can be determined with terrestrial surveying methods (levelling). Alternatively, all three components of the station position can be surveyed and fixed. In this case, only the PCC are set up as parameters. The antenna still needs to be rotated, in order to probe the entire antenna hemisphere and thus filling the north or the south hole respectively. These are the sections of the sky which are never occupied by any GNSS satellite due to the inclination of the GNSS orbits.

²GNSS antenna workshops, University of Bonn, 10.03.2019, <https://www.gib.uni-bonn.de/team/lehrbeauftragte/bgoerres/antennen-workshops>

The relative field calibration method is illustrated in Chapter 4 based on the very specific use-case of a GNSS attitude determination system.

3.2.2 Anechoic chamber calibration

In anechoic chamber measurements (Sims, 1985; Tranquilla and Colpitts, 1989; Schupler et al., 1994; Zeimet, 2010), the GNSS antenna is set up in an anechoic chamber together with a signal source. The signal is received by the antenna and interfered with the original signal, leading to a measurement of the phase shifts. Either the antenna is rotated or the sender is moved in order to scan the antenna hemisphere. This will produce a map of phase shifts. Anechoic chamber measurements are not affected by multipath and realise a very pure form of antenna calibration. In return, the infrastructure is very demanding and the synchronisation of all the equipment is difficult to achieve.

Currently, the University of Bonn is the only institution having been approved by the IGS to deliver chamber calibrations.³

3.2.3 Absolute field calibration

Absolute field calibrations use a device to rotate the antenna around at least two axes. Calibrations currently being undertaken make use of 2-axis robots (Bilich and Mader, 2010) or robots with five or more axes (Wübbena et al., 2000; Menge, 2003; Kersten, 2014; Riddell et al., 2015; Hu et al., 2015). The actuator rotates the antenna into different orientations, and therefore decorrelates the PCC from the station coordinates.

Furthermore, the rotation allows to sample the antenna hemisphere much more efficiently. As a consequence, an elevation mask can be applied. All low-elevation signals, for instance below 20 degrees elevation, are removed. Because the antenna is inclined towards all possible directions by the robotic arm, reliable data can be collected even for low elevations in the antenna specific coordinate system. In other words, the entire antenna hemisphere is sampled. As the calibration procedure does not rely on low elevations anymore, multipath is mitigated.

The most sophisticated systems use a robot with five or more axes. The advantage is that the coordinates of the antenna can be kept fixed during the calibration. The first robotic calibration system was developed by the University of Hanover and the German company Geo++[®] GmbH (Wübbena et al., 2000; Menge, 2003; Dillner, 2008; Kersten, 2014). These two institutions and the Landeskabriereinrichtung of the Senatsverwaltung für Stadtentwicklung Berlin are the only institutions performing robot type calibrations and being currently approved by the IGS AWG.³

Other groups are currently setting up robotic calibration systems with six axes as well, namely Wuhan University (Hu et al., 2015), Geoscience Australia (Riddell et al., 2015) and the

³Readme file of the IGS AWG, 27.11.2018, ftp://igs.org/pub/station/general/antenna_README.pdf.

US American National Geodetic Survey (NGS; Bilich et al., 2018). The system developed at ETH Zurich and related scientific questions are discussed in Chapter 6.

3.3 Phase Centre Correction Model

A GNSS phase observation reads (Hauschild, 2017a):

$$P_A^i = \mathbf{e}_A^{i\top} (\mathbf{x}^i - \mathbf{x}_{A,\text{MPC}}) + c \delta t_A - c \delta t^i + \lambda N_A^i + \text{PCV}_A^i + v_A^i \quad (3.1)$$

where

P_A^i	is the carrier phase observation between antenna A and satellite i ,
\mathbf{e}_A^i	is the line-of-sight vector,
\mathbf{x}^i	is the GNSS satellite position at signal emission,
$\mathbf{x}_{A,\text{MPC}}$	is the position of the receiver antenna MPC at signal reception,
c	is the speed of light,
δt_A	is the receiver clock error,
δt^i	is the satellite clock error,
λ	is the carrier wavelength,
N_A^i	is the integer phase ambiguity,
PCV_A^i	is the PCV and
v_A^i	is the zero-difference observation noise.

Atmospheric delays (ionosphere and troposphere) and relativistic corrections were neglected in this latest equation. The PCV in Eq. 3.1 is modelled as an azimuth and zenith angle dependent correction as follows:

$$\text{PCV}_A^i = \text{PCV}_A(\alpha^i, z^i) \quad (3.2)$$

where α^i is the azimuth angle of the GNSS satellite in the antenna-fixed coordinate system and z^i is the zenith angle. The coordinates of the conventional MPC are obtained after application of the PCO to the geometrical reference of the antenna, the ARP, as follows:

$$\mathbf{x}_{\text{MPC}} = \mathbf{x}_{\text{ARP}} + \mathbf{PCO} \quad (3.3)$$

where \mathbf{x}_{ARP} is the position of the ARP and \mathbf{PCO} is the PCO vector. Substitution of Eq. 3.3 into Eq. 3.1 and rearranging leads to:

$$P_A^i = \mathbf{e}_A^{i\top} (\mathbf{x}^i - \mathbf{x}_{A,\text{ARP}}) + c \delta t_A - c \delta t^i + \lambda N_A^i + \text{PCV}_A^i - \mathbf{e}_A^{i\top} \mathbf{PCO} + v_A^i \quad (3.4)$$

The PCV and the PCO term can be grouped into one term, the PCC. The total correction

applied on top of the raw measurements is not affected:

$$\text{PCC}_A^i = \text{PCV}_A^i - \mathbf{e}^{i\top} \mathbf{PCO} \quad (3.5)$$

where PCC_A^i is the total range correction or PCC and \mathbf{e}^i is the line-of-sight (LOS; positively pointing towards the GNSS spacecraft). The negative sign in Eq.3.5 emerges due to the ANTEX sign convention (Rothacher and Schmid, 2010) and the choice of the direction of \mathbf{e}^i . A PCV can always be transformed to any other PCO by the following relation:

$$\text{PCV}'_A(\alpha^i, z^i) = \text{PCV}_A(\alpha^i, z^i) + \mathbf{e}^{i\top} (\mathbf{PCO}' - \mathbf{PCO}) \quad (3.6)$$

where $\text{PCV}'_A(\alpha^i, z^i)$ is the PCV belonging to the offsets \mathbf{PCO}' and $\text{PCV}_A(\alpha^i, z^i)$ is the PCV belonging to the offsets \mathbf{PCO} . In both cases, the total PCC is identical. PCV and PCO must always be used consistently.

3.4 Phase Centre Parametrisations

Grid parametrisations with piecewise linear interpolation between the grid points and spherical harmonics are the two most common types of PCC parametrisations. The different methods will shortly be discussed hereafter.

3.4.1 Grid parametrisation

The PCC is represented as a regular grid covering the antenna hemisphere. A typical resolution for an antenna pattern is 5 times 5 degrees. PCC values are available in a look-up table for every point in the grid. The number of parameters equals:

$$n_{\text{parameters}} = \left(\frac{90}{\Delta z} + 1 \right) \frac{360}{\Delta \alpha} \quad [\text{deg}] \quad (3.7)$$

where $n_{\text{parameters}}$ is the number of grid points, Δz is the vertical resolution in degrees and $\Delta \alpha$ is the azimuthal resolution in degrees.

In the estimation process, the grid has to be constrained, because its constant part correlates with the receiver clock (as can be seen for instance in Eq. 2.24). One way to make the system regular is to constrain the PCC values at zenith to zero. This is very convenient, as the zenith values have to be constrained in any case, as all points located in the zenith have the same value. This operation reduces the degree of freedom of the system, leading to a final degree of freedom of:

$$n_{\text{parameters}} = \frac{90}{\Delta z} \cdot \frac{360}{\Delta \alpha} \quad [\text{deg}] \quad (3.8)$$

In the case of the standard resolution of 5 degrees times 5 degrees, this represents 1296 parameters.

The PCC between the grid points are obtained after two linear interpolations, one in zenith angle and one in azimuth. These two linear interpolations, combined into one equation, read:

$$\begin{aligned} \text{PCC}(\alpha_0, z_0) &= w_1 \text{PCC}(\alpha_i, z_i) + w_2 \text{PCC}(\alpha_{i+1}, z_i) \\ &\quad + w_3 \text{PCC}(\alpha_i, z_{i+1}) + w_4 \text{PCC}(\alpha_{i+1}, z_{i+1}) \end{aligned} \quad (3.9)$$

$$w_1 = 1 - r_\alpha - r_z + r_\alpha r_z \quad (3.10)$$

$$w_2 = r_\alpha - r_\alpha r_z \quad (3.11)$$

$$w_3 = r_z - r_\alpha r_z \quad (3.12)$$

$$w_4 = r_\alpha r_z \quad (3.13)$$

$$r_\alpha = \frac{\alpha_0 - \alpha_i}{\alpha_{i+1} - \alpha_i} \quad (3.14)$$

$$r_z = \frac{z_0 - z_i}{z_{i+1} - z_i} \quad (3.15)$$

where $\text{PCC}(\alpha_0, z_0)$ is the interpolated PCC and $\alpha_i, z_i, \alpha_{i+1}$ and z_{i+1} are the coordinates of the grid points (see Figure 3.4.1). This formulation is equivalent to performing two linear interpolations, one in azimuth and one in zenith angle.

The drawback of this approach is the large distortions that appear close to zenith. The grid parametrisation is inherently a representation of values on a plane. In contrast, spherical harmonics are perfectly suited to represent scalar values on a sphere and should therefore be preferred, if no evidence speaks against it.

3.4.2 Grid partial derivatives

After omission of the arguments α and z , Eq. 3.9 reads:

$$\text{PCC} = w_1 \text{PCC}_1 + w_2 \text{PCC}_2 + w_3 \text{PCC}_3 + w_4 \text{PCC}_4 \quad (3.16)$$

The partial derivatives are trivial:

$$\frac{\partial \text{PCC}}{\partial \text{PCC}_1} = w_1 \quad (3.17)$$

$$\frac{\partial \text{PCC}}{\partial \text{PCC}_2} = w_2 \quad (3.18)$$

$$\frac{\partial \text{PCC}}{\partial \text{PCC}_3} = w_3 \quad (3.19)$$

$$\frac{\partial \text{PCC}}{\partial \text{PCC}_4} = w_4 \quad (3.20)$$

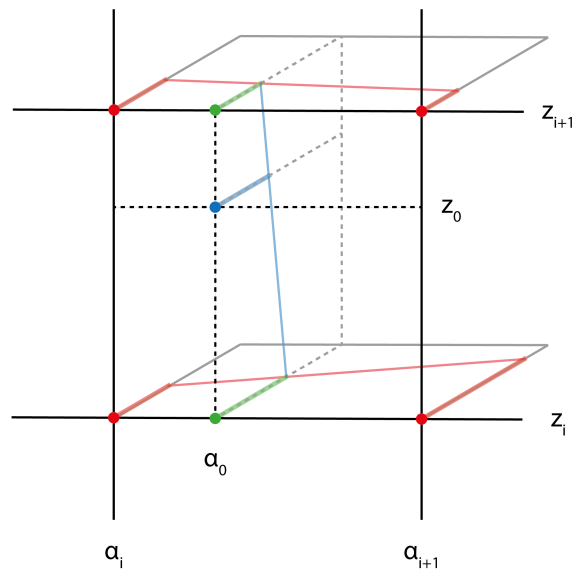


Figure 3.4.1 : Principle of the grid interpolation. The actual parameters are the values at the grid intersection points, marked in red. An interpolation along the azimuth (resulting in the green values) is followed by an interpolation along the zenith, resulting in the value at the requested azimuth and elevation (in blue). Source: Willi et al. (2018a).

3.4.3 Spherical harmonics parametrisation

The phase centre correction, expressed as spherical harmonics, read as:

$$\text{PCC}(\alpha^i, z^i) = \sum_{n=0}^{n_{max}} \sum_{m=0}^n \tilde{P}_{nm}(\cos z^i) \left(a_{nm} \cos(m \alpha^i) + b_{nm} \sin(m \alpha^i) \right) \quad (3.21)$$

where

- n is the degree and
- m is the order of the spherical harmonics series,
- \tilde{P}_{nm} are the normalized associated Legendre polynomials,
- a_{nm} are the spherical harmonics cosine coefficients and
- b_{nm} are the spherical harmonics sine coefficients.

The typical resolution for spherical harmonics PCC is degree and order 8 or degree and order 12. The total number of parameter equals:

$$n_{\text{parameters}} = (n + 1)(m + 1) \quad (3.22)$$

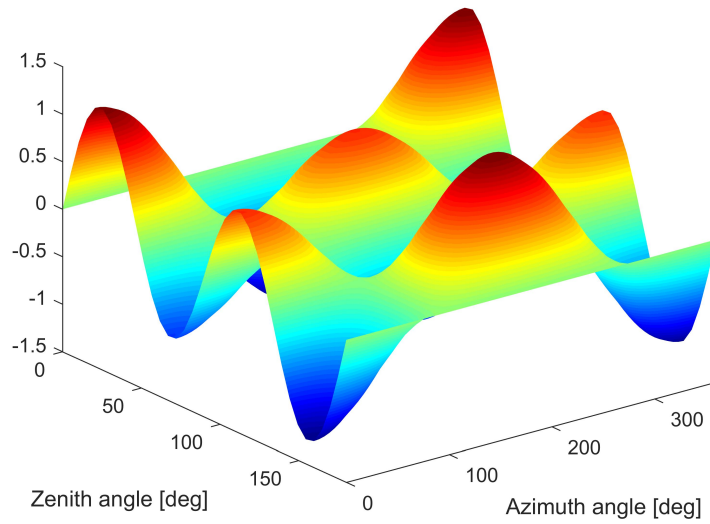
This count excludes all coefficients b_{n0} , because their contribution equals zero, as $\sin 0 = 0$. Exactly as in the case of the grid parametrisation, the inversion of the unconstrained system will lead to singularities. The absolute term a_{00} correlates with the receiver clock parameter and is constrained to zero (see Figure 3.4.2). The parameters a_{10} , a_{11} and b_{11} fully correlate with the PCO components. Therefore, no explicit PCO parameters are necessary in the PCC model.

Because no measurements are available for the lower hemisphere of the antenna, a symmetry assumption has to be made. If symmetry is assumed between the upper and the lower antenna hemisphere, all coefficients that represent a function with an odd number of zeros between $z = 0$ deg and $z = 180$ deg along z (called odd coefficients hereafter) have to be constrained to zero. This is the case if $n - m$ is odd (see Figure 3.4.2). Figure 3.4.3 illustrates odd and even coefficients of spherical harmonics.

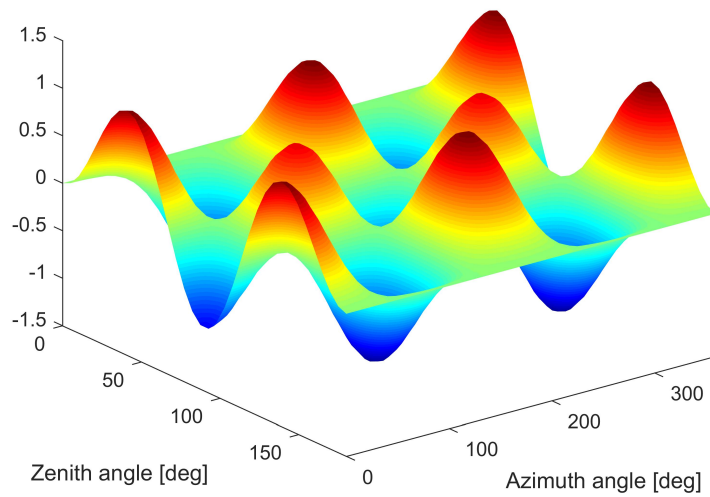
Assuming that $n = m$ and that all odd coefficients but a_{10} , a_{11} and b_{11} are constrained to zero, the total number of parameters reads (Willi et al., 2018a):

$$n_{\text{parameters}} = \frac{(n + 2)(n + 1)}{2} \quad (3.23)$$

This leads to 91 parameters for a degree and order 12 expansion and 45 parameters for a degree and order 8 spherical harmonics expansion. Compared to a grid parametrisation, the number of parameters is reduced. This reduction occurs at the cost of a lower resolution: A degree and order 12 spherical harmonics has a resolution of about 15 degrees, as $\tilde{P}_{12,0}$ has twelve zeros along z , which ranges from 0 to 180 degrees and $\cos(m \alpha)$ and $\sin(m \alpha)$ have 24 zeros along α , which ranges from 0 to 360 degrees.



(a) coefficient $a_{41} = 1$



(b) coefficient $a_{42} = 1$

Figure 3.4.3 : Illustration of the contribution of an odd spherical harmonics coefficient (a) and an even coefficient (b). Odd functions create fields with no symmetry with respect to the equator (zenith angle of 90 deg), whereas even functions create equatorial symmetry.

3.4.4 Spherical harmonics partial derivatives

Since the spherical harmonics expansion is a linear function of the coefficients (see Eq. 3.21), the partial derivatives simply read:

$$\frac{\partial \text{PCC}(\alpha^i, z^i)}{\partial a_{nm}} = \tilde{P}_{nm}(\cos z^i) \cos(m \alpha^i) \quad (3.24)$$

$$\frac{\partial \text{PCC}(\alpha^i, z^i)}{\partial b_{nm}} = \tilde{P}_{nm}(\cos z^i) \sin(m \alpha^i) \quad (3.25)$$

3.5 Multi-GNSS requirements

PCC are frequency-dependent. All current GNSS transmit ranging signals at different frequencies. Thus, an independent calibration is generated for each frequency transmitted. The frequencies of the GNSS included in RINEX 3.03 (RINEX Working Group and RTCM-SC104, 2015) are presented in Table 3.5.1.

Traditionally, calibration institutes have generated calibrations for GPS L1, GPS L2, GLONASS G1 and GLONASS G2.⁴

Since the new GPS L5 and the Galileo E5a signals are in the vicinity of the GPS L2 signal (see Figure 3.5.1), a first approximation is to assume GPS L2 patterns for GPS L5 and for Galileo E5a measurements. Unfortunately, no L5/E5a robot calibrations are available yet, as no institution is providing those. However, Geo++[®] announced an upgrade to Galileo calibrations for 2019.⁵ Individual chamber calibrations, which include all frequencies, are available for several antennas of the European Permanent Network⁶ (EPN) and the IGS network⁷.

FDMA signals are a particular challenge for PCC calibration, because every satellite in view has another frequency. As the PCC is modelled as frequency-dependent correction function, in principle each satellite has a different PCC.

Wübbena et al. (2006) present a method to deal with the frequency changes within the GLONASS signals. Basically, the PCC difference between GPS L1 and GLONASS G1 is used to linearly extrapolate the GLONASS PCC for slot number $k = 0$ to any other GLONASS frequency within the GLONASS G1 signal. The same procedure is applied for GPS L2 and GLONASS G2. Frequency dependent PCC within a GNSS signal is not foreseen in the ANTEX format version 1.4 (Rothacher and Schmid, 2010).

The frequency range within GLONASS G1 and GLONASS G2 are small compared to the

⁴As of November 2018, the official PCV file used by the IGS is igs14.atx available on <ftp://igs.org/pub/station/general>. For receiver antennas, solely GPS L1, GPS L2, GLONASS G1 and GLONASS G2 calibrations are available in this file.

⁵IGS AWG mail 508 from 15.11.2018 by Michael Moore, available at www.igs.org/mail for registered users.

⁶Which kind of antenna calibration is available for EPN stations can be checked under http://epncb.oma.be/_networkdata/stationlist.php.

⁷Oral communication during the AWG splinter meeting, 31.10.2018, IGS Workshop, Wuhan, China.

general spread of the GNSS frequencies. The difference between the highest and the lowest frequencies is approximately 7.3 MHz within the GLONASS G1 signal and 5.7 MHz within GLONASS G2, assuming slot numbers between $k = -7$ and $k = 6$. Therefore, the estimation of a unique PCC at the GLONASS centre frequency (slot number $k = 0$) seems to be a reasonable approximation.

3.6 Validation strategies

In order to verify the performance of any calibration system, validations are essential. In principle, relative and absolute field calibrations can be validated in a similar manner. The following methods require an important logistical effort. It would make no sense to carry out such ambitious validations for a relative antenna calibration.

These methods are:

- i. A validation on very short baselines is conducted. The baselines are surveyed and therefore, a ground truth is available. The comparison is conducted either on the coordinate level or on the observation residual level. This kind of validation is documented in (Kallio et al., 2018).
- ii. A so-called ‘ring calibration’ is conducted. This implies that the same antenna is shipped to several calibration institutions and the results are compared at the PCC level.

Strategy (i) is difficult to carry out and requires a test field with as many pillars as antennas and a sufficient number of multi-GNSS receivers. Antenna types should be mixed, in order to investigate the behaviour of antennas with mixed equipment. A ground truth not only for the height but also for the position of every pillar would strengthen the validation compared to the method presented in Kallio et al. (2018). However, a full 3D ground truth at a precision of 0.1 mm is cumbersome and difficult to achieve. Strategy (ii) is complementary to approach (i). As no ground truth is available, no absolute statement can be derived from a ring calibration. However, the consistency between different calibration facilities is of uppermost importance, especially, if PCC from different facilities are used together in a GNSS solution.

Table 3.5.1 : Centre frequencies of the current GNSS according to the RINEX 3.03 standard (RINEX Working Group and RTCM-SC104, 2015). ¹ The frequencies of the GLONASS FDMA signals G1 and G2 are dependent on the satellite slot number k . The slot numbers range from $k = -7$ to $k = 6$; ² E5 is the E5a+E5b AltBOC signal.

	Signal	RINEX 3 signal code	Frequency [MHz]
GPS	L1	1	1575.42
	L2	2	1227.6
	L5	5	1176.45
GLONASS	G1 ¹	1	$1602 + \frac{9}{16} k$
	G2 ¹	2	$1246 + \frac{7}{16} k$
	G3	3	1202.025
Galileo	E1	1	1575.42
	E5a	5	1176.45
	E5b	7	1207.14
	E5 ²	8	1191.795
	E6	6	1278.75
SBAS	L1	1	1575.42
	L2	5	1176.45
BeiDou	B1	2	1561.098
	B2	7	1207.14
	B3	6	1268.52
QZSS	L1	1	1575.42
	L2	2	1227.6
	L5	5	1176.45
	LEX	6	1278.75
IRNSS	L5	5	1176.45
	S	9	2492.028

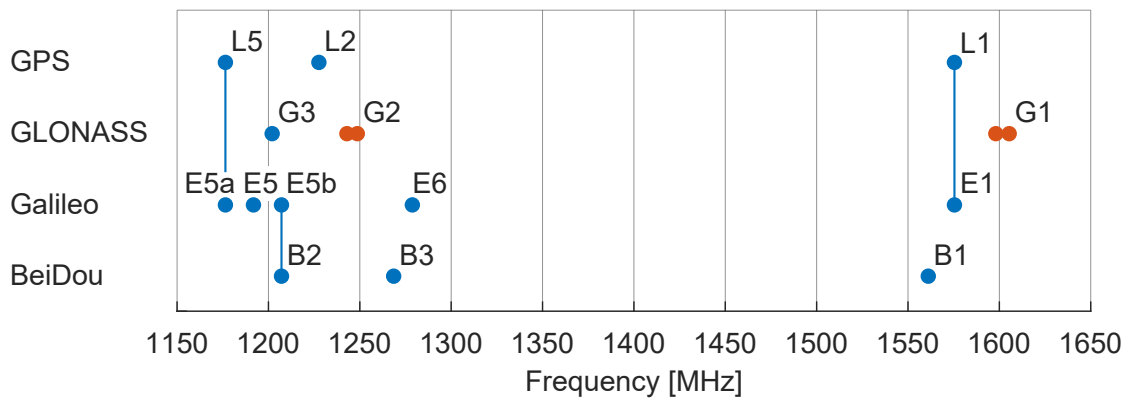


Figure 3.5.1 : Graphical overview of the frequencies of the main four GNSS. FDMA signals are displayed in orange with two dots, marking the highest and the lowest frequency assigned. CDMA signals are displayed in blue. L1 and E1 are compatible, as well as L5 and E5a and E5b and B2 (see blue lines). The other signals do not match each other.

Chapter 4

Relative GNSS antennas field calibrations

In relative field calibration, a GNSS antenna is set up in the field together with a reference station. A PCC function can be estimated with the collected GNSS data. The result is a calibration relative to the reference antenna, thus the name ‘relative calibration’. Depending on the latitude of the experimental site, some portions of the antenna hemisphere are not sampled by any data (this is the so-called north or south hole), preventing the estimation of azimuthal variations of the PCC. To solve this issue, data is acquired with several different antenna orientations. This rotation of the antenna has three effects:

- i. Enhanced sampling of the antenna hemisphere (filling of the north or south hole).
- ii. Multipath mitigation.
- iii. Separation of the horizontal PCO from the station coordinates, as illustrated in Figure 4.0.1.

The relative field calibration was extensively used in the past (Rothacher et al., 1995). However, its application decreased because of following limitations:

- i. The obtained calibration is dependent on the reference antenna (thus the name ‘relative calibration’).
- ii. Multipath is not prevented from affecting the results.
- iii. The method is not able to separate the height component of the PCO from the station height.
- iv. The method is not well suited to provide reliable PCC for low elevations.

Nowadays, the use of the relative field calibration is limited to validation campaigns, as for instance shown in Kallio et al. (2018).

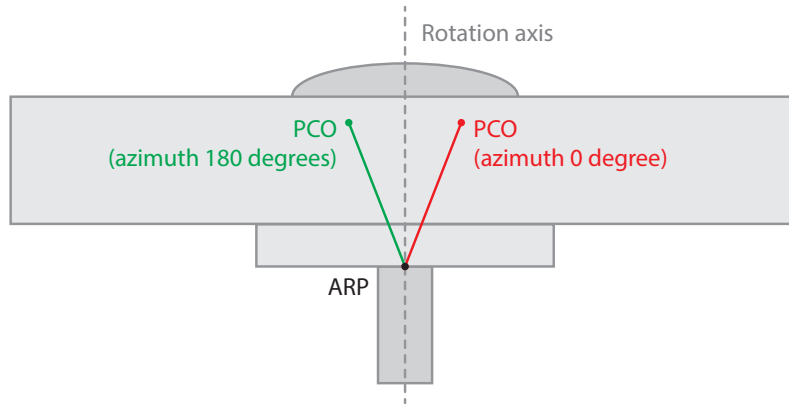


Figure 4.0.1 : The principle of PCO estimation in relative field calibration. The horizontal components of the coordinates can be decorrelated from the horizontal offset by rotating the antenna around its vertical axis. Measurement with more different azimuths (for instance, 0 deg, 90 deg, 180 deg and 270 deg) further enhance the PCO estimation.

4.1 Observation equation

A GNSS phase observation reads (Hauschild, 2017a):

$$P_A^i = \mathbf{e}_A^{i\top} (\mathbf{x}^i - \mathbf{x}_{A,ARP}) + c \delta t_A - c \delta t^i + \lambda N_A^i + T_A^i + I_A^i + \text{PCC}_A^i + W_A^i + v_A^i \quad (4.1)$$

where

- P_A^i is the carrier phase observation between antenna A and satellite i ,
- \mathbf{e}_A^i is the line-of-sight vector,
- \mathbf{x}^i is the GNSS satellite position at signal emission,
- $\mathbf{x}_{A,ARP}$ is the position of the receiver antenna ARP at signal reception,
- c is the speed of light,
- δt_A is the receiver clock error,
- δt^i is the satellite clock error,
- λ is the carrier wavelength,
- N_A^i is the integer phase ambiguity,
- T_A^i is the tropospheric delay,
- I_A^i is the ionospheric delay,
- PCC_A^i is the PCC,
- W_A^i is the phase wind-up and
- v_A^i is the zero-difference observation noise.

In so-called double-differences (Hauschild, 2017b), measurements from two stations to two satellites are differenced against each another:

$$\begin{aligned} P_{AB}^{ij} &= (P_B^j - P_A^j) - (P_B^i - P_A^i) \\ &= P_B^j - P_A^j - P_B^i + P_A^i \end{aligned} \quad (4.2)$$

where P_{AB}^{ij} is the double-difference phase observation. In this differencing process, the receiver clock error as well as the satellite clock error is eliminated.¹ This can be seen by substitution of Eq. 4.1 into Eq. 4.2. On short baselines, the tropospheric and ionospheric delays are highly correlated between both stations. Therefore, it can be assumed that they vanish on double-difference level. Assuming antenna rotations only around the antenna vertical axis, the phase wind-up is identical to all observations of an antenna and therefore eliminated by the differencing process as well. After simplification, the double-difference reads:

$$\begin{aligned} P_{AB}^{ij} &= \rho_{AB}^{ij} + \lambda N_{AB}^{ij} + \text{PCC}_B(\alpha_B^j, z_B^j) - \text{PCC}_B(\alpha_B^i, z_B^i) \\ &\quad - \text{PCC}_A(\alpha_A^j, z_A^j) + \text{PCC}_A(\alpha_A^i, z_A^i) + v_{AB}^{ij} \end{aligned} \quad (4.3)$$

where

- ρ_{AB}^{ij} is the double-difference geometry term,
- N_{AB}^{ij} is the double-difference phase ambiguity,
- α is the azimuth of a satellite as seen from the station,
- z is the zenith angle of a satellite as seen from the station and
- v_{AB}^{ij} is the double-difference observation noise.

As can easily be seen from Eq. 4.3, the PCC of the antenna to be calibrated (which is the parameter of interest) is fully correlated with the PCC of the reference antenna: any mismodelling of the reference PCC will lead to a bias in the PCC estimation. The conclusion is that the estimation of PCC on the double-difference level leads to relative PCC estimates.

4.2 Relative calibration of an attitude estimation platform

Although its limitations, relative antenna calibration has some appreciable advantages:

- i. The set up is very easy.
- ii. Virtually no infrastructure is needed.

¹The satellite clock of satellite i is only completely eliminated, if the signal emission time of P_A^i is identical to the signal emission time of P_B^i . This is the case for synchronised receivers on short baselines. Otherwise, the double-difference is still affected by the differential satellite clock error. The differential satellite clock error is the difference in satellite clock between the two emission times. It is due to the drift of the satellite clock.

Therefore, the relative field calibration method is well suited for a first study of the PCC of the CubETH satellite model.

In the very specific case of an attitude determination platform, all antennas of the platform can be calibrated together in a unique field experiment. Figure 4.2.1 shows the implemented processing pipeline for a case with four antennas on a common platform. The Bernese GNSS Software V5.2 (Dach et al., 2015) was used for the processing.

The first step of the processing is to convert the RINEX data to Bernese observation files (see Figure 4.2.2). This step can be carried out individually for every file. One additional nearby antenna serves as common reference.

In a second step, baselines are formed and processed within every session (see Figure 4.2.3). Each antenna observation file is differenced against the reference antenna observation file. A standard processing pipeline leads to one normal equation system per antenna to be calibrated and per session.

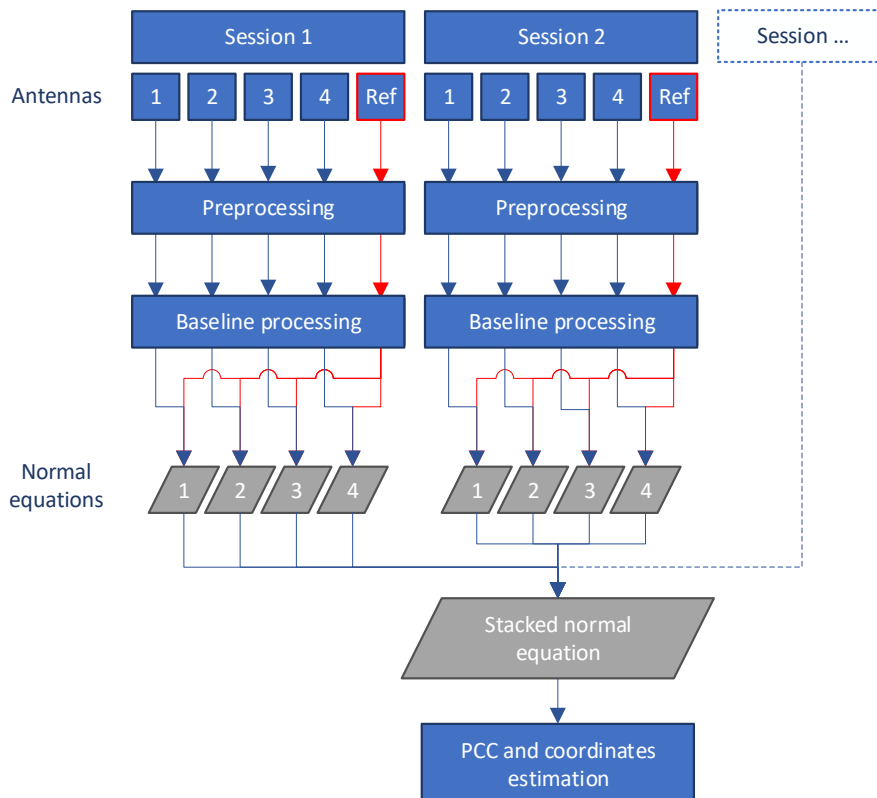


Figure 4.2.1 : Summary of the processing of relative field calibrations. Antennas 1 to 4 designate the antennas which are to be calibrated and Ref designates the reference antenna. Every session results in one normal equation per antenna to be calibrated. The NEQ are stacked before inversion. The NEQ system parameters are summarized in Table 4.2.1.

The parameters present in the normal equation system after ambiguity resolution and after stacking are shown in Table 4.2.1. The number of parameters does not increase with increasing number of sessions. A unique set of station coordinates is set up for all sessions. The resulting PCO are relative to the centre of rotation, which is identical to the estimated common station coordinates. This principle is schematised for two antennas and two sessions in Figure 4.2.4. A session-wise estimation of station coordinates is not possible, as the PCO fully correlates with the station coordinates.

The rotation around a vertical axis decorrelates the horizontal station coordinates from the horizontal PCO. The station height in contrary is constrained to the average height of all four antennas, as it remains fully correlated with the PCO in up direction. Other rotations, for instance around the x- or y-axis are necessary to decorrelate the height components as well.

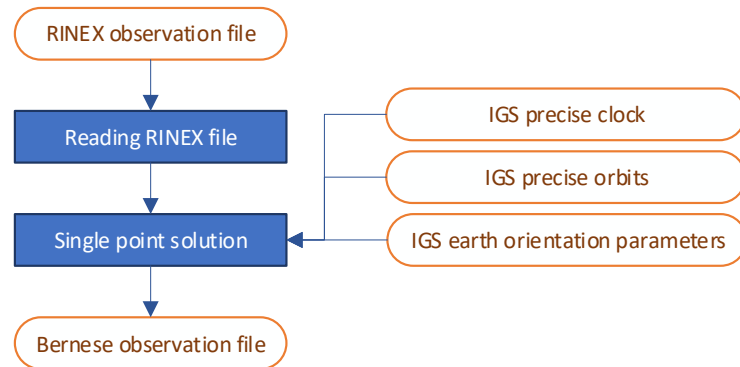


Figure 4.2.2 : Preprocessing of the observations. This step is carried out individually for every antenna and every session. The Single Point Positioning (SPP) is performed for receiver clock synchronisation.

Table 4.2.1 : Relative field calibration NEQ parameters after ambiguity resolution. The number of PCV parameters corresponds to a degree and order 8 spherical harmonics expansion. The receiver clock parameters have vanished on double-difference level.

Parameter	Number of parameters
Centre of rotation coordinates X, Y, Z	3
PCC antenna 1	3 PCO + 42 PCV
PCC antenna 2	3 PCO + 42 PCV
PCC antenna 3	3 PCO + 42 PCV
PCC antenna 4	3 PCO + 42 PCV

For implementation reasons (for instance the support of PCV in the NEQ handling program of Bernese) it is necessary to first estimate PCO and station coordinates. In a second iteration, the PCO and the station coordinates are constrained to the estimated values and only PCV are set up. This can be done separately for every baseline (but including all sessions). The results are equivalent to the results that are obtained if all parameters are set up in one estimation process. Differences might occur if the PCV is considered separately, but the PCC is identical in both cases.

4.3 Paper II – GNSS Antenna Phase Center Variation Calibration for Attitude Determination on Short Baselines

The second paper presents the results obtained from antenna field calibrations and its application to an attitude determination system. It was originally published in *Proceedings of the 30th International Technical Meeting of The Satellite Division of the Institute of Navigation (ION GNSS+ 2017)*, Portland, Oregon, September 2017, pp. 3997–4010 with the title *GNSS Antenna Phase Center Variation Calibration for Attitude Determination on Short Baselines*. This paper was published after peer-review. Upon the recommendation of the session chairs, the same article was submitted to the Journal of Navigation.

4.3.1 Abstract

A mock-up model of the CubETH satellite and an attitude determination platform are calibrated. The mock-up model of the satellite is equipped with four 18 x 18 mm² passive ceramic patch antennas. The baseline lengths range from 5.7 cm to 6.5 cm. The experimental platform was equipped with Trimble Bullet III low-cost geodetic antennas. Both systems are calibrated in a field campaign using the approach presented above.

The first conclusion from the field calibration is that a massive shrinking of the electric baseline lengths compared to the nominal baselines (from the mechanical centre of an antenna to the mechanical centre of the other antenna) of the satellite model takes place: They measure 4.8 cm, 5.6 cm and 4.3 cm instead of 5.7 cm, 6.5 cm and 5.7 cm.

A simulator data study proved these corrections to be essential in order to correctly estimate the attitude of a spacecraft. Otherwise, a systematic bias is present in the estimates of the attitude. Because of the short baselines, the bias in yaw is up to 14 degrees if no correction is applied.

In the field calibration, significant PCV were obtained for the ceramic patch antennas. The corrections range up to 26 mm. The corrections are highly non-symmetrical. Further tests with the attitude determination platform showed that the PCV is mainly dependent on the position of the antenna on the ground plane and not the antenna itself. An experiment with permuted antennas allowed this conclusion to be drawn.

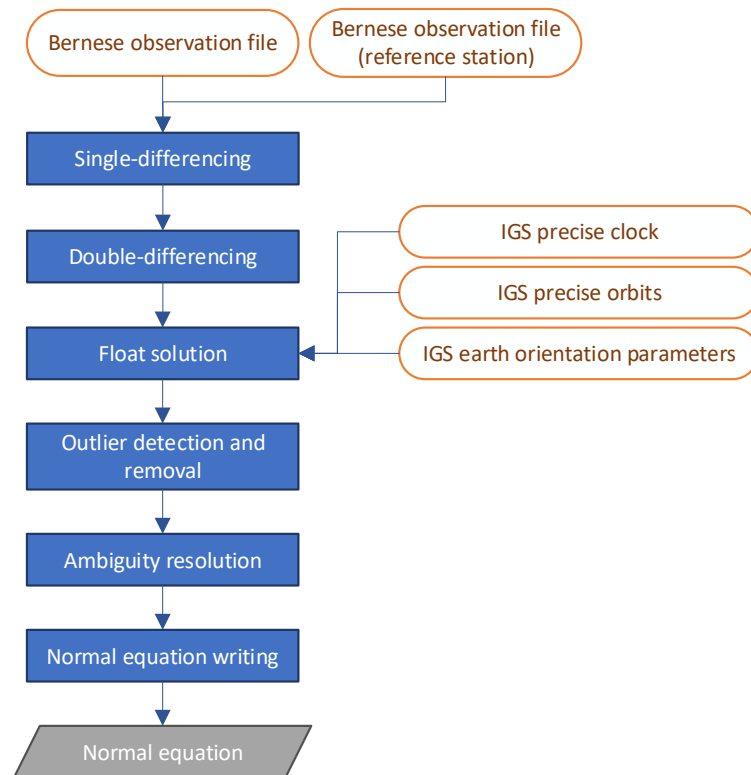


Figure 4.2.3 : Baseline processing of the observations. A baseline is formed between the reference antenna and every antenna of the attitude determination system. At the end, a normal equation is written for every baseline and every session.

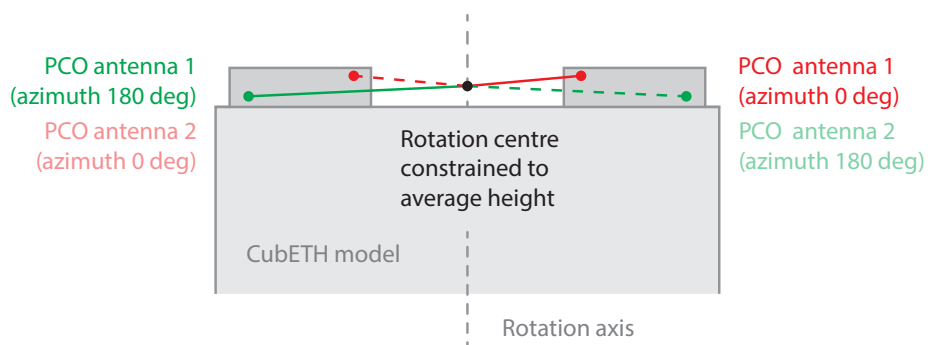


Figure 4.2.4 : Principle of PCO estimation on CubETH. The height component of the PCO cannot be separated from the height of the station coordinates solely with rotations around a vertical axis. To overcome this singularity, the height of the station is constrained to the average height of the antennas.

The PCV obtained in the field experiment with the Trimble Bullet III on the experimental platform range from -20 mm to 15 mm. A real data validation proved that the estimated PCO and PCV are meaningful, as they increase the accuracy of attitude determination from 6 degrees without PCC to 4.5 degrees Root Mean Square Error (RMSE) with PCC.

4.3.2 Author's contribution

The following section attempts to give a summary of the author's contribution to paper II (Willi et al., 2017). The author's contribution is summarized in Table 4.3.1. The main implementation task was the development of a processing pipeline in Bernese. The specificity of the data, 1 Hz single-frequency, had to be taken into account and the software options had to be set accordingly. This task was cumbersome but necessary for a clean processing.

The theoretical developments and the implementation of the calibration procedure presented above were mainly undertaken by the author. The simulation study is built upon the developments presented in paper I and only small modifications were necessary. Beside the main developments, the author developed many additional tools for handling, editing and visualising PCC files.

4.3.3 Relevance to the field

Although antenna calibration has been studied extensively, no literature is available about calibration of low-cost antennas by the GNSS community. This paper is among the first studies investigating this topic. The paper presents strong evidence for mutual coupling of the antennas. It was shown that the mutual coupling must be taken account in the PCC estimation process.

An easy to carry out relative field calibration method is developed and presented. The novelty consists in the calibration of an entire system for attitude determination instead of individual antennas. The paper clearly shows the necessity of antenna calibration, especially for such short baselines.

4.4 Outlook

The Relative antenna calibration method gives a first insight into the expected magnitude of the PCC for a small satellite. However, according to experience, the relative field calibration method is prone to errors due to multipath. The implemented method does not allow a clean assessment of multipath, neither its mitigation.

For these reasons, an absolute field calibration using a robotic arm is targeted. Such an approach has the potential to significantly enhance the results. The implementation of an absolute field calibration is presented in the next chapters.

Table 4.3.1 : Summary of the author's contribution to paper II – GNSS Antenna Phase Center Variation Calibration for Attitude Determination on Short Baselines.

	Original idea	Measurements, data generation	Theoretical developments	Software implementation	Computation, data processing
Development of the processing pipeline in Bernese	20%		90%	100%	
Calibration campaign	90%	90%			100%
Synthetic data study	80%	100%			100%
Validation study	80%	80%			100%
Analysis of the results				90%	100%
Editorial work	90%				

Chapter 5

Robot geometry

Six-axis robots have some appreciable advantages over robots with less axes in the context of antenna calibration. Five-axis robots lack one degree of freedom. Because the 6th axis is omitted compared to six-axis robots, rotations around the antenna vertical axis are not possible. Robots with two axes for instance do not allow to keep the antenna coordinates fixed while changing its orientation. Six-axis robots have six degrees of freedom and are therefore best suited for antenna calibration.

Among serial manipulator arms with six axes, the serial manipulator with an ortho-parallel basis and a spherical wrist is the most common one (Brandstötter et al., 2014). An example for such a robot is given in Figure 5.0.1. The underlying kinematic equations as well as an enhanced kinematic model, allowing for the calibration of the robot, are presented in this chapter.

5.1 Definitions

In this Chapter, following terminology is applied:

The **world coordinate system** is any global reference frame, for instance WGS84.

The **topocentric coordinate system** is the East, North, Up system with respect to the reference ellipsoid. This system is approximately parallel to the Local Level Frame (LLF), which is aligned to the local gravity field. The convention East, North, Up instead of North, East, Up is chosen in order to have a right-hand coordinate system.

The **robot (base or root) coordinate system** is a coordinate system attached to the base of the robot (see Figure 5.1.2).

The **flange coordinate system** is a coordinate system attached to the flange of the robot (see Figure 5.1.2).

The **tool coordinate system** is a coordinate system attached to the tool mounted on the robot flange. For instance, if a welding equipment is mounted on the robot flange, the tool coordinate system is centred at the welding flame and the x-axis of the coordinate system is aligned with the flame. This coordinate system is meant to facilitate the computation of



Figure 5.0.1 : KUKA Agilus KR 6 R900 sixx mounted on the roof of the Institute of Geodesy and Photogrammetry (IGP) at ETH Zurich. The robot is performing a GNSS antenna calibration. The aluminium plate serves as interface between the four bolts inserted into the concrete foundation and the robot base. The white antenna in the back is used as reference station.

poses and trajectories if a tool is attached to the robot. The relationship between the different coordinate systems is shown in Figure 5.1.3.

The **robot flange** is the mechanical interface between the robot and any tool. Mathematically, if referred to it as a point, the robot flange is the intersection between the last axis and the surface of the flange.

The **pose** of the robot is the position and the orientation of the flange of the robot with respect to the robot base. The pose can be given either in X, Y, Z, A, B and C or in angular values for all axes. In the first case, KUKA applies the following convention:

$$\mathbf{R}_{t \leftarrow r} = (\mathbf{R}_{r \leftarrow t})^T = \mathbf{R}_1(C) \mathbf{R}_2(B) \mathbf{R}_3(A) \quad (5.1)$$

where

- $\mathbf{R}_{t \leftarrow r}$ is the rotation from the robot coordinate system to the tool coordinate system,
- \mathbf{R}_i are the rotation matrices according to Eqs. 2.4 to 2.6 and
- A, B, C are the three angles used by KUKA to describe the orientation of a point.

The **posture** is the topology of the robot, for instance shoulder up or shoulder down. Figure 5.1.1 shows two postures of the same pose. The same posture can be identified for different poses. For instance, if the robot goes to point A and then to a different point B without changing its topology, these are different poses but the same posture.

The **pose repeatability** is the ability of the robot to reach the same pose in the same posture several times (Willi and Guillaume, 2019) as precisely as possible. The standard deviation of the positions is a quantitative measure for this ability.

The **precision of the robot** is the ability to precisely reach given coordinates with varying orientations (Willi and Guillaume, 2019). The standard deviation is a quantitative indicator for this ability.

The **accuracy of the robot** designates its ability to reach any pose in any posture with the best accuracy. The Root Mean Square Error (RMSE) best quantifies this ability.

5.2 KUKA Agilus KR 6 R900 sixx

The KUKA Agilus KR 6 R900 sixx is a small six-axis serial manipulator. The main technical data are shown in Table 5.2.1. The whole set-up comprises:

- i. The robotic arm,
- ii. the robot controller (manufacturer provided),
- iii. a SmartPad (manufacturer provided) which acts basically as control panel for the controller and
- iv. an optional notebook computer to run custom software.

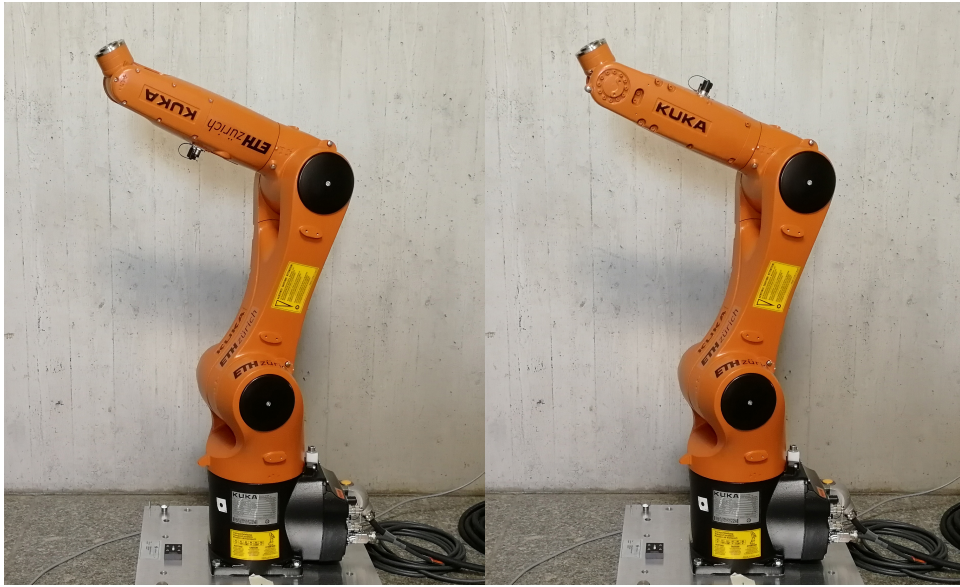


Figure 5.1.1 : The KUKA robot in two different postures but in the same pose (position and orientation of the flange).

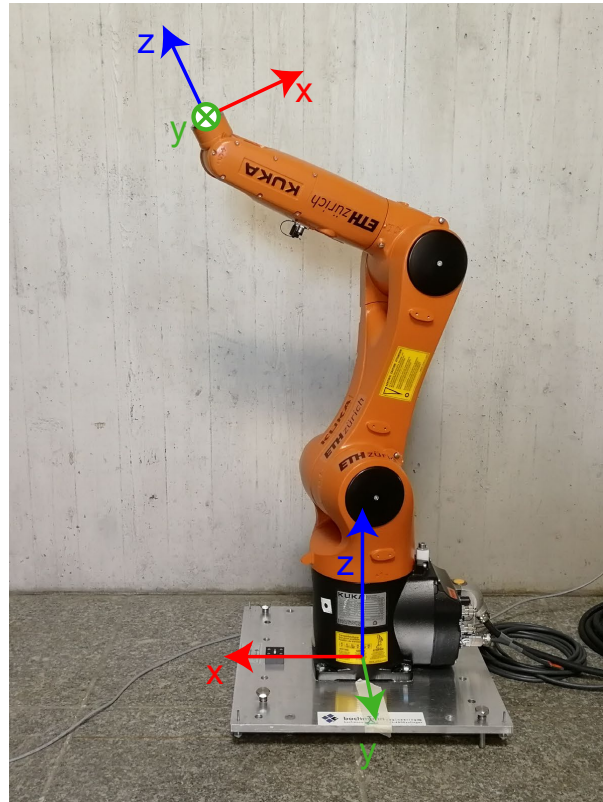


Figure 5.1.2 : Robot (base) coordinate system and flange coordinate system. The orientation of the flange coordinate system depends on the angular position of the last axis. Source: Willi and Guillaume (2019).

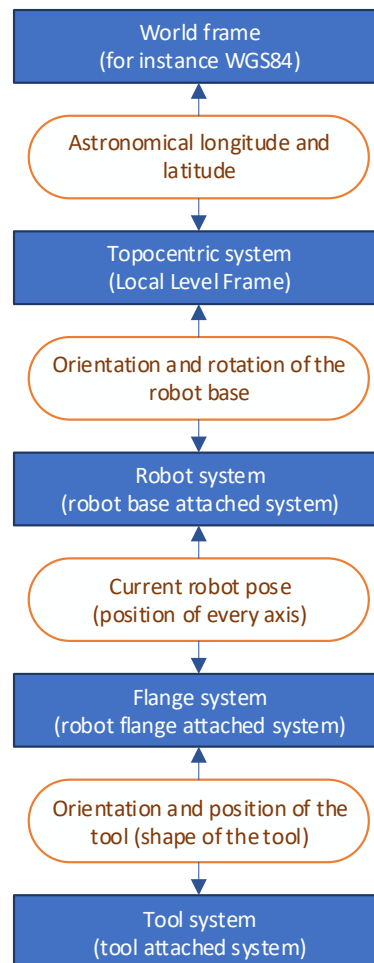


Figure 5.1.3 : Overview of the different coordinate systems and of the transformations between each of the coordinate systems.

The components but the robotic arm are depicted in Figure 5.2.1. The interface which allows to interact with the controller by UDP and XML is called RobotSensorInterface (RSI). A custom software was developed for this specific task of interacting with the robot controller. It is called QKuka and is written in C++. The overall scheme is presented in Figure 5.2.2. Implementation details are given in the next section.

5.3 QKuka control software

A software called QKuka was developed to interact with the controller of the robotic arm. It is written in C++ and runs on a standard laptop. The communication with the controller is based on User Data Protocol (UDP) and Extensible Markup Language (XML). Figure 5.3.1 is an example for a file sent by the controller. The ‘IPOC’ integer which is contained in this message must be returned within a specified time frame, typically 100 milliseconds. If this is not the case, the robot executes an emergency stop. An example for an answer returning this ‘IPOC’ is displayed in Figure 5.3.2.

As soon as they are received, the XML files are interpreted within a program running on the robot controller (see Figure 5.3.3). A program running on the controller executes the required actions, for instance steering the tool of the robotic arm to a certain position.

5.4 Robot Kinematics

Forward kinematics is the task of computing the coordinates and the attitude of the flange (or of the tool) from angular values for every of the six axes whereas inverse kinematics is the inverse task. In general, no analytical solution to inverse kinematics is available. In some special cases, analytical solutions can be derived from geometrical thoughts.

Robots with a configuration similar to the KUKA Agilus KR 6 are said to have an ortho-parallel basis and a spherical wrist. The ortho-parallel basis consists of two parallel axes (axes 2 and 3) mounted on a first, perpendicular axis. In case of the spherical wrist, the last three axes

Table 5.2.1 : Size, weight, accuracy and operation temperature range of the KUKA KR 6 R900 sixx (Kuka, 2018).

Axes	6
Operation volume	2.85 m ²
Operation radius	901.5 mm
Maximum payload	6 kg
Weight	52 kg
Pose repeatability	0.03 mm
Operation temperature	+5°C to +45°C

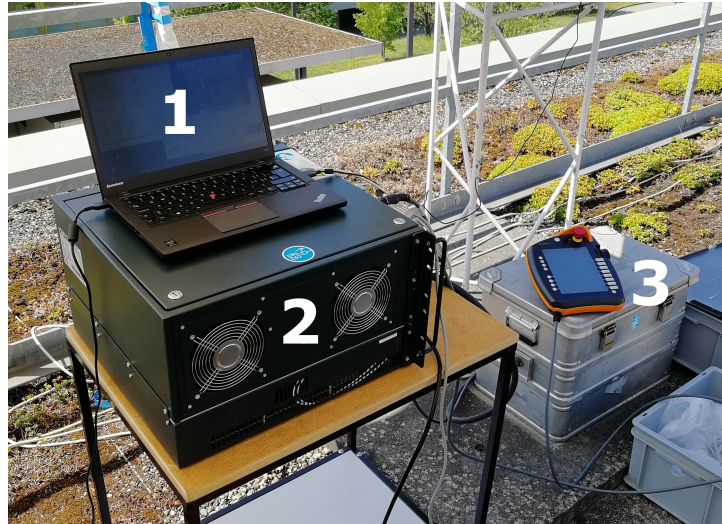


Figure 5.2.1 : KUKA control equipment consisting of a standard notebook computer (1), the KUKA controller (2) and the KUKA SmartPad (3). The notebook computer is used to run a custom software. The interface is based on a network protocol called UDP and uses XML files.

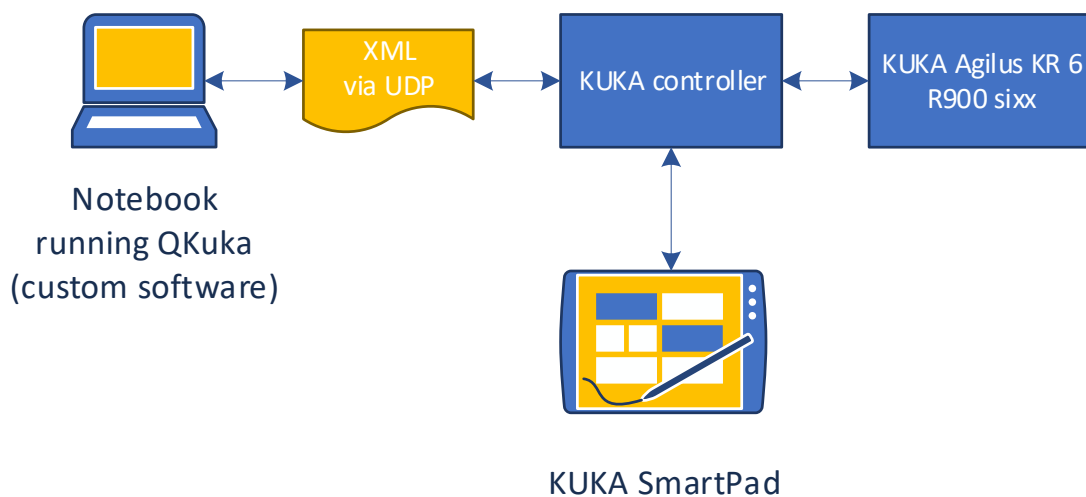


Figure 5.2.2 : Interface between the robotic arm, the controller, the SmartPad and QKuka.

<Rob Type="KUKA">	1
<RIst X="625.00043" Y="0.00000" Z="889.99976"	2
A="179.78603" B="89.99429" C="179.78603"/>	3
<AIPos A1="0.00000" A2="-77.16124" A3="75.60643"	4
A4="0.00000" A5="1.56052" A6="-0.00002"/>	5
<Delay D="1"/>	6
<IINA>1</IINA>	7
<IPOC>896032</IPOC>	8
</Rob>	9

Figure 5.3.1 : Example for a message sent by the robot controller. It contains the current position of the tool (X, Y, Z), the Euler angles of the tool orientation (A, B, C) and the angular readings of axes A1 to A6 as well as the integer 'IPOC' and the current delay.

<Sen Type="ImFree">	1
<EStr></EStr>	2
<RKorr X="625.00" Y="0.00" Z="890.00"	3
A="0.00" B="90.00" C="0.00"/>	4
<TYPE>0</TYPE>	5
<IOUT>1</IOUT>	6
<IPOC>896032</IPOC>	7
</Sen>	8

Figure 5.3.2 : Example for a message sent to the robot controller. It contains a position and orientation instruction for the tool (X, Y, Z, A, B and C) and two integers (TYPE and IOUT) as well as the mandatory ‘IPOC’.

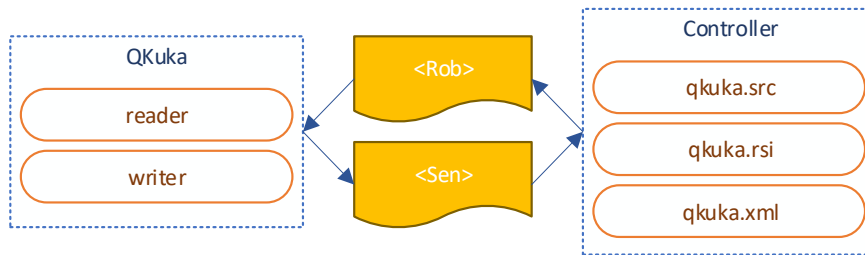


Figure 5.3.3 : Details of the exchange of XML messages. A program (*qkuka.src*) is running on the controller and executes predefined actions. The actual reading of the XML file is achieved in *qkuka.rsi*, based on the format description of the XML file, which is contained in *qkuka.xml*.

(axes 4 to 6) intersect in one point. The consequence is very pleasant, as this property allows to separate the coordinate computation part from the attitude determination part. The following developments are based on Brandstötter et al. (2014). As shown by the authors, this kind of robots can be parametrized by only seven parameters. The values of the parameters for the present case are given in Table 5.4.1. The six non-zero parameters are shown in Figure 5.4.1. Figure 5.4.2 should convince the reader that all links and joints are in one plane and that $b = 0$. The axes one to three control the coordinates, whereas the axes four to six control the attitude of the flange. The variables θ_1 to θ_6 are the angles of rotation of every axis and therefore our control variables.

5.4.1 Forward kinematics (Brandstötter et al., 2014)

The task of computing the position and the attitude of the flange of the robot or the tool mounted on the robot flange, given the angle of every axis, is called forward kinematics. The point C is the intersection of the last three axes (see also Figure 5.4.1). The coordinates \mathbf{c} of the

Table 5.4.1 : The seven geometrical parameters of the KUKA Agilus KR 6 R900 sixx. b is equal to zero as all the links and joints are in one plane for this type of robot.

Parameter	Value [mm]
a_1	25
a_2	-35
b	0
d_1	400
d_2	455
d_3	420
d_4	80

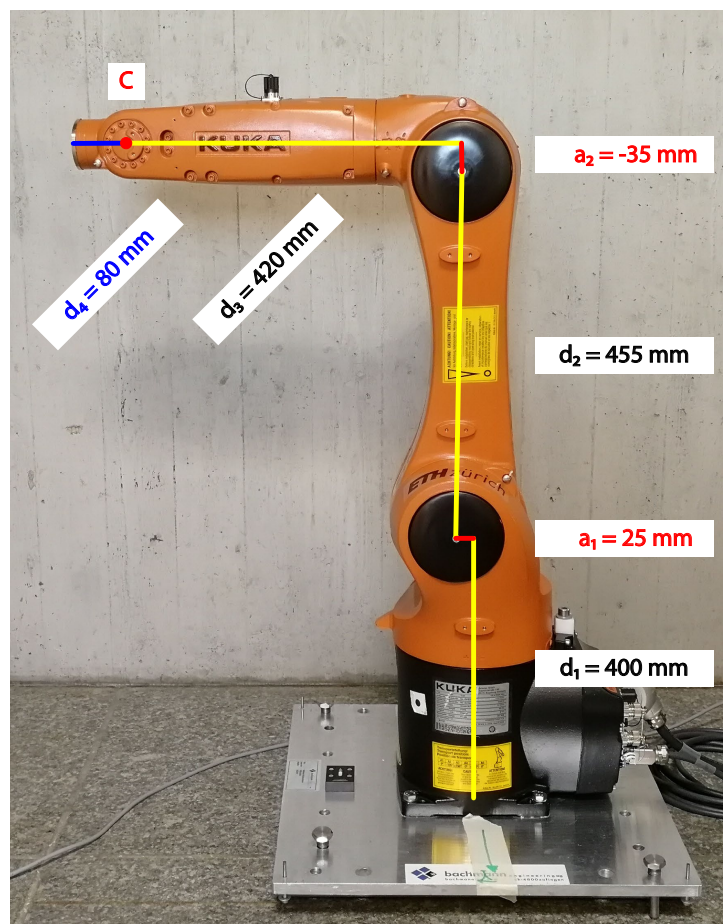


Figure 5.4.1 : The six non-zero geometrical parameters of the KUKA Agilus KR 6 R900 sixx. The robot x-axis is on the left, the y-axis is pointing towards the reader. The red dot shows the point C, which is the intersection of the last three axes.



Figure 5.4.2 : Front view of the KUKA Agilus KR 6 R900 sixx. It can easily be seen that all links and joints are in one plane.

point C in the robot coordinate system are given by:

$$\mathbf{c} = \begin{pmatrix} \cos \theta_1 & -\sin \theta_1 & 0 \\ \sin \theta_1 & \cos \theta_1 & 0 \\ 0 & 0 & 1 \end{pmatrix} \mathbf{c}' + \begin{pmatrix} 0 \\ 0 \\ d_1 \end{pmatrix} \quad (5.2)$$

with

$$\mathbf{c}' = \begin{pmatrix} d_2 \sin \theta_2 + k \sin(\theta_2 + \theta_3 + \phi_3) + a_1 \\ b \\ d_2 \cos \theta_2 + k \cos(\theta_2 + \theta_3 + \phi_3) \end{pmatrix} \quad (5.3)$$

and with

$$\phi_3 = \arctan \frac{a_2}{d_3} \quad (5.4)$$

$$k = \sqrt{a_2^2 + d_3^2} \quad (5.5)$$

where

- \mathbf{c} is the set of coordinates, given in the robot coordinate system, of the intersection of the last three axes,
- θ_i is the angular reading of axis i ,
- \mathbf{c}' is an auxiliary point,
- ϕ_3 is an auxiliary variable and
- k is an auxiliary variable as well.

The final coordinates of the flange are computed using the attitude of the flange and the length of the last articulation:

$$\mathbf{u} = \mathbf{c} + d_4 \mathbf{R}_{r \leftarrow f} \begin{pmatrix} 0 \\ 0 \\ 1 \end{pmatrix} \quad (5.6)$$

with \mathbf{u} being the coordinates of the flange. The angles four to six control the attitude of the flange. The final attitude is the product of the attitude up to the point C and the attitude of the last three axis.

$$\mathbf{R}_{r \leftarrow f} = \mathbf{R}_{r \leftarrow c} \mathbf{R}_{c \leftarrow f} \quad (5.7)$$

$$\mathbf{R}_{c \leftarrow f} = \begin{pmatrix} c_{\theta_4} c_{\theta_5} c_{\theta_6} - s_{\theta_4} s(\theta_6) & -c_{\theta_4} c_{\theta_5} s_{\theta_6} - s_{\theta_4} c_{\theta_6} & c_{\theta_4} s_{\theta_5} \\ s_{\theta_4} c_{\theta_5} c_{\theta_6} + c_{\theta_4} s_{\theta_6} & -s_{\theta_4} c_{\theta_5} s_{\theta_6} + c_{\theta_4} c_{\theta_6} & s_{\theta_4} s_{\theta_5} \\ -s_{\theta_5} c_{\theta_6} & s_{\theta_5} s_{\theta_6} & c_{\theta_5} \end{pmatrix} \quad (5.8)$$

$$\mathbf{R}_{r \leftarrow c} = \begin{pmatrix} c_{\theta_1} c_{\theta_2} c_{\theta_3} - c_{\theta_1} s_{\theta_2} s_{\theta_3} & -s_{\theta_1} & c_{\theta_1} c_{\theta_2} s_{\theta_3} + c_{\theta_1} s_{\theta_2} c_{\theta_3} \\ s_{\theta_1} c_{\theta_2} c_{\theta_3} - s_{\theta_1} s_{\theta_2} s_{\theta_3} & c_{\theta_1} & s_{\theta_1} c_{\theta_2} s_{\theta_3} + s_{\theta_1} s_{\theta_2} c_{\theta_3} \\ -s_{\theta_2} c_{\theta_3} - c_{\theta_2} s_{\theta_3} & 0 & -s_{\theta_2} s_{\theta_3} + c_{\theta_2} c_{\theta_3} \end{pmatrix} \quad (5.9)$$

where

- $\mathbf{R}_{r \leftarrow f}$ is the rotation from the flange attached system to the the robot system,
- $\mathbf{R}_{r \leftarrow c}$ is the rotation from the system associated with the point C to the robot coordinate system,
- $\mathbf{R}_{c \leftarrow f}$ is the rotation from the flange system to the system associated with point C,
- s_{θ_i} is the sine of θ_i and
- c_{θ_i} is the cosine of θ_i .

The separation, mentioned earlier, between the attitude computation and the coordinate computation is well reflected by the fact that $\mathbf{R}_{r \leftarrow c}$ only depends on θ_1 to θ_3 and $\mathbf{R}_{c \leftarrow f}$ only depends on θ_4 to θ_6 .

In order to comply with the KUKA convention, following operations have to be performed:

$$\theta_1 = -\theta'_1 \quad (5.10)$$

$$\theta_2 = \theta'_2 + \frac{\pi}{2} \quad (5.11)$$

$$\theta_4 = -\theta'_4 \quad (5.12)$$

$$\theta_6 = -\theta'_6 \quad (5.13)$$

with θ'_i being the angles used by the KUKA controller (see also Figure 5.4.3).

If the tool is affected by an offset, an additional transformation leads to the coordinates of the tool in the robot coordinate system:

$$\mathbf{R}_{r \leftarrow t} = \mathbf{R}_{r \leftarrow f} \mathbf{R}_{f \leftarrow t} \quad (5.14)$$

$$\mathbf{t} = \mathbf{u} + t''_z \mathbf{R}_{r \leftarrow t} \begin{pmatrix} 0 \\ 0 \\ 1 \end{pmatrix} + t''_x \mathbf{R}_{r \leftarrow t} \begin{pmatrix} 1 \\ 0 \\ 0 \end{pmatrix} + t''_y \mathbf{R}_{r \leftarrow t} \begin{pmatrix} 0 \\ 1 \\ 0 \end{pmatrix} \quad (5.15)$$

Where

- \mathbf{t} is the set of coordinates of the tool (in the robot coordinate system),
- t''_x is the tool offset in x (in the tool system),
- t''_y is the tool offset in y (in the tool system),
- t''_z is the tool offset in z (in the tool system) and
- $\mathbf{R}_{f \leftarrow t}$ is the rotation from the tool system to the flange system.

Frequently, tools do have an offset in z- but not in x- and y-direction. This is the reason for

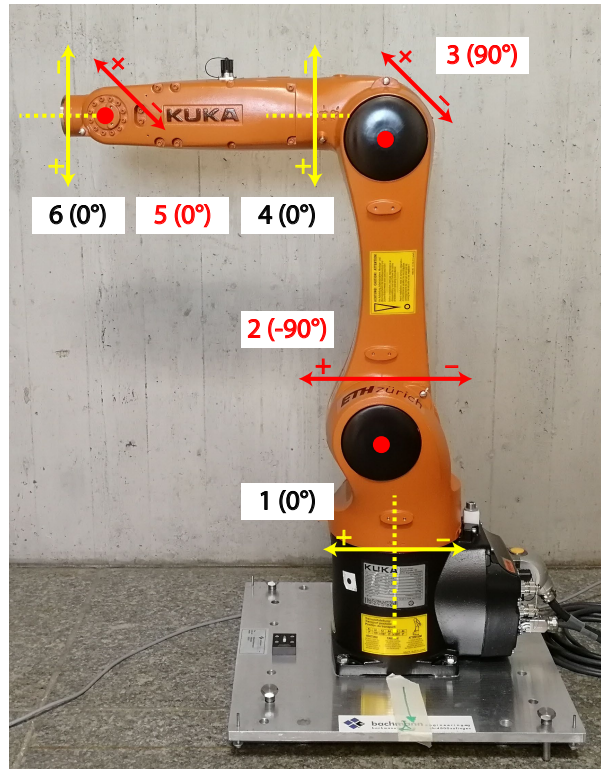


Figure 5.4.3 : The KUKA angle convention for θ_1 to θ_6 . Axes shown in yellow are parallel to the image plane, red axes are out of plane. Source: Willi and Guillaume (2019).

the non-alphabetic order in Eq. 5.15. Typically, $\mathbf{R}_{f \leftarrow t}$ is either an identity matrix (as in the case of antenna calibrations) or its values are calibrated and therefore known. It can be expressed as an Euler sequence:

$$\mathbf{R}_{t \leftarrow f} = (\mathbf{R}_{f \leftarrow t})^T = \mathbf{R}_1(\gamma'') \mathbf{R}_2(\beta'') \mathbf{R}_3(\alpha'') \quad (5.16)$$

where α'' , β'' and γ'' are the tool yaw, pitch and roll angles. The final results of the algorithm are the coordinates of the tool \mathbf{t} and its orientation $\mathbf{R}_{r \leftarrow t}$ in the robot coordinate system.

5.4.2 Inverse kinematics (Brandstötter et al., 2014)

Unsurprisingly, inverse kinematics is more complicated than forward kinematics. This tasks consist of computing the angles θ_1 to θ_6 given the position and attitude of the tool. Again, the problem can be solved in two parts. The coordinates of the tool \mathbf{t} and its orientation $\mathbf{R}_{r \leftarrow t}$ are the input variables:

$$\mathbf{u} = \mathbf{t} - t''_z \mathbf{R}_{r \leftarrow t} \begin{pmatrix} 0 \\ 0 \\ 1 \end{pmatrix} - t''_x \mathbf{R}_{r \leftarrow t} \begin{pmatrix} 1 \\ 0 \\ 0 \end{pmatrix} - t''_y \mathbf{R}_{r \leftarrow t} \begin{pmatrix} 0 \\ 1 \\ 0 \end{pmatrix} \quad (5.17)$$

$$\mathbf{R}_{r \leftarrow f} = \mathbf{R}_{r \leftarrow t} \mathbf{R}_{t \leftarrow f} = \mathbf{R}_{r \leftarrow t} (\mathbf{R}_{f \leftarrow t})^T \quad (5.18)$$

$$\mathbf{c} = \mathbf{u} - d_4 \mathbf{R}_{r \leftarrow f} \begin{pmatrix} 0 \\ 0 \\ 1 \end{pmatrix} \quad (5.19)$$

where

- \mathbf{u} is the set of coordinates of the flange in the robot system,
- \mathbf{t} is the set of coordinates of the tool in the robot system,
- t''_x is the tool offset in x in the tool system,
- t''_y is the tool offset in y in the tool system,
- t''_z is the tool offset in z in the tool system,
- $\mathbf{R}_{r \leftarrow t}$ is the rotation from the tool system to the robot system,
- $\mathbf{R}_{r \leftarrow f}$ is the rotation from the flange system to the robot system and
- \mathbf{c} is the set of coordinates of the intersection of the last tree axis.

Once the coordinates \mathbf{c} of the point C have been computed, they can be used to retrieve the angular values of the first three axes. Eight different solutions exist. The eight possible postures for a given pose are displayed in Figures 5.4.4 and 5.4.5. The solutions one to four for θ_1 to θ_3 read:

$$\theta_{1,1} = \text{atan2}(c_2, c_1) - \text{atan2}(b, h_1 + a_1) \quad (5.20)$$

$$\theta_{1,2} = \theta_{1,1} \quad (5.21)$$

$$\theta_{1,3} = \text{atan2}(c_2, c_1) + \text{atan2}(b, h_1 + a_1) - \pi \quad (5.22)$$

$$\theta_{1,4} = \theta_{1,3} \quad (5.23)$$

$$\theta_{2,1} = -\arccos \frac{s_1^2 + d_2^2 - k^2}{2 s_1 d_2} + \text{atan2}(h_1, c_3 - d_1) \quad (5.24)$$

$$\theta_{2,2} = \arccos \frac{s_1^2 + d_2^2 - k^2}{2 s_1 d_2} + \text{atan2}(h_1, c_3 - d_1) \quad (5.25)$$

$$\theta_{2,3} = -\arccos \frac{s_2^2 + d_2^2 - k^2}{2 s_2 d_2} - \text{atan2}(h_1 + 2 a_1, c_3 - d_1) \quad (5.26)$$

$$\theta_{2,4} = \arccos \frac{s_2^2 + d_2^2 - k^2}{2 s_2 d_2} - \text{atan2}(h_1 + 2 a_1, c_3 - d_1) \quad (5.27)$$

$$\theta_{3,1} = \arccos \frac{s_1^2 - d_2^2 - k^2}{2 d_2 k} - \text{atan2}(a_2, d_3) \quad (5.28)$$

$$\theta_{3,2} = -\arccos \frac{s_1^2 - d_2^2 - k^2}{2 d_2 k} - \text{atan2}(a_2, d_3) \quad (5.29)$$

$$\theta_{3,3} = \arccos \frac{s_2^2 - d_2^2 - k^2}{2 d_2 k} - \text{atan2}(a_2, d_3) \quad (5.30)$$

$$\theta_{3,4} = -\arccos \frac{s_2^2 - d_2^2 - k^2}{2 d_2 k} - \text{atan2}(a_2, d_3) \quad (5.31)$$

where $\theta_{i,j}$ is the j^{th} solution of θ_i and c_i is the i^{th} component of \mathbf{c} . The additional variables h_1 ,

s_1 , s_2 and k are defined as follows:

$$h_1 = \sqrt{c_1^2 + c_2^2 - b^2} - a_1 \quad (5.32)$$

$$s_1 = \sqrt{h_1^2 + (c_3 - d_1)^2} \quad (5.33)$$

$$s_2 = \sqrt{(h_1 + 2a_1)^2 + (c_3 - d_1)^2} \quad (5.34)$$

$$k = \sqrt{a_2^2 + d_3^2} \quad (5.35)$$

The solutions five to eight for θ_1 to θ_3 are identical to solutions one to four for these three angles:

$$\theta_{i,j} = \theta_{i,j+4} \quad i \in [1, 2, 3], j \in [1, 2, 3, 4] \quad (5.36)$$

Eq. 5.36 can easily be verified by comparing Figure 5.4.4 to Figure 5.4.5. The solutions for the angles θ_4 to θ_6 read:

$$\theta_{4,j} = \text{atan2}(R_{23} h_{3,j} - R_{13} h_{2,j}, R_{13} h_{3,j} h_{5,j} + R_{23} h_{2,j} h_{5,j} - R_{33} h_{4,j}) \quad (5.37)$$

$$\theta_{4,j+4} = \theta_{4,j} + \pi \quad (5.38)$$

$$\theta_{5,j} = \text{atan2}\left(\sqrt{1 - h_{6,j}^2}, h_{6,j}\right) \quad (5.39)$$

$$\theta_{5,j+4} = -\theta_{5,j} \quad (5.40)$$

$$\begin{aligned} \theta_{6,j} = \text{atan2}(R_{12} h_{3,j} h_{4,j} + R_{22} h_{2,j} h_{4,j} + R_{32} h_{5,j}, \\ -R_{11} h_{3,j} h_{4,j} - R_{21} h_{2,j} h_{4,j} - R_{31} h_{5,j}) \end{aligned} \quad (5.41)$$

$$\theta_{6,j+4} = \theta_{6,j} - \pi \quad (5.42)$$

where R_{mn} are the elements of $\mathbf{R}_{r \leftarrow f}$ from Eq. 5.18 and $j \in [1, 2, 3, 4]$. The auxiliary variables $h_{2,j}$ to $h_{6,j}$ are defined as follows:

$$h_{2,j} = \sin \theta_{1,j} \quad (5.43)$$

$$h_{3,j} = \cos \theta_{1,j} \quad (5.44)$$

$$h_{4,j} = \sin(\theta_{2,j} + \theta_{3,j}) \quad (5.45)$$

$$h_{5,j} = \cos(\theta_{2,j} + \theta_{3,j}) \quad (5.46)$$

$$h_{6,j} = R_{13} h_{3,j} h_{4,j} + R_{23} h_{2,j} h_{4,j} + R_{33} h_{5,j} \quad (5.47)$$

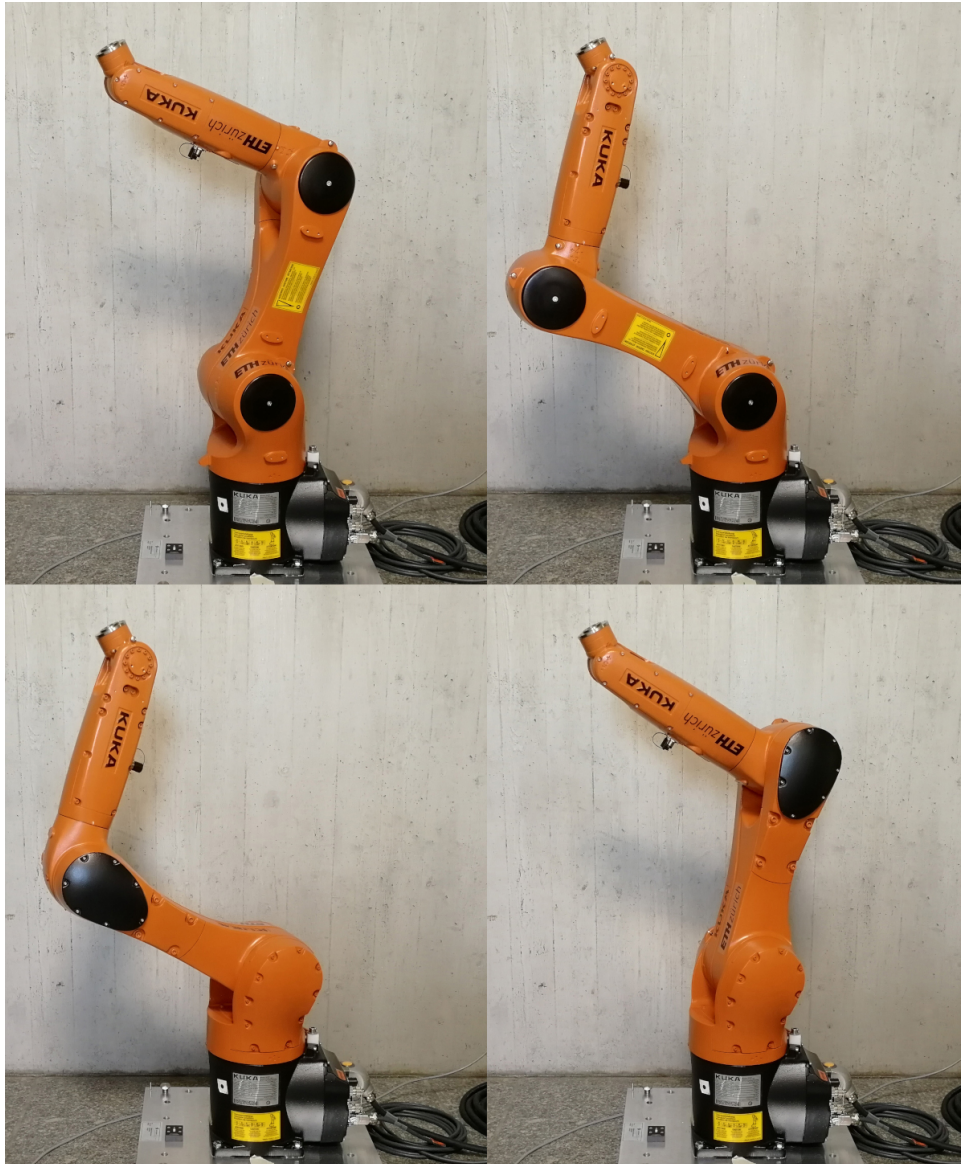


Figure 5.4.4 : View of the postures one to four ($j \in [1, 2, 3, 4]$), from left to right, for a given pose.
Source: Willi and Guillaume (2019).

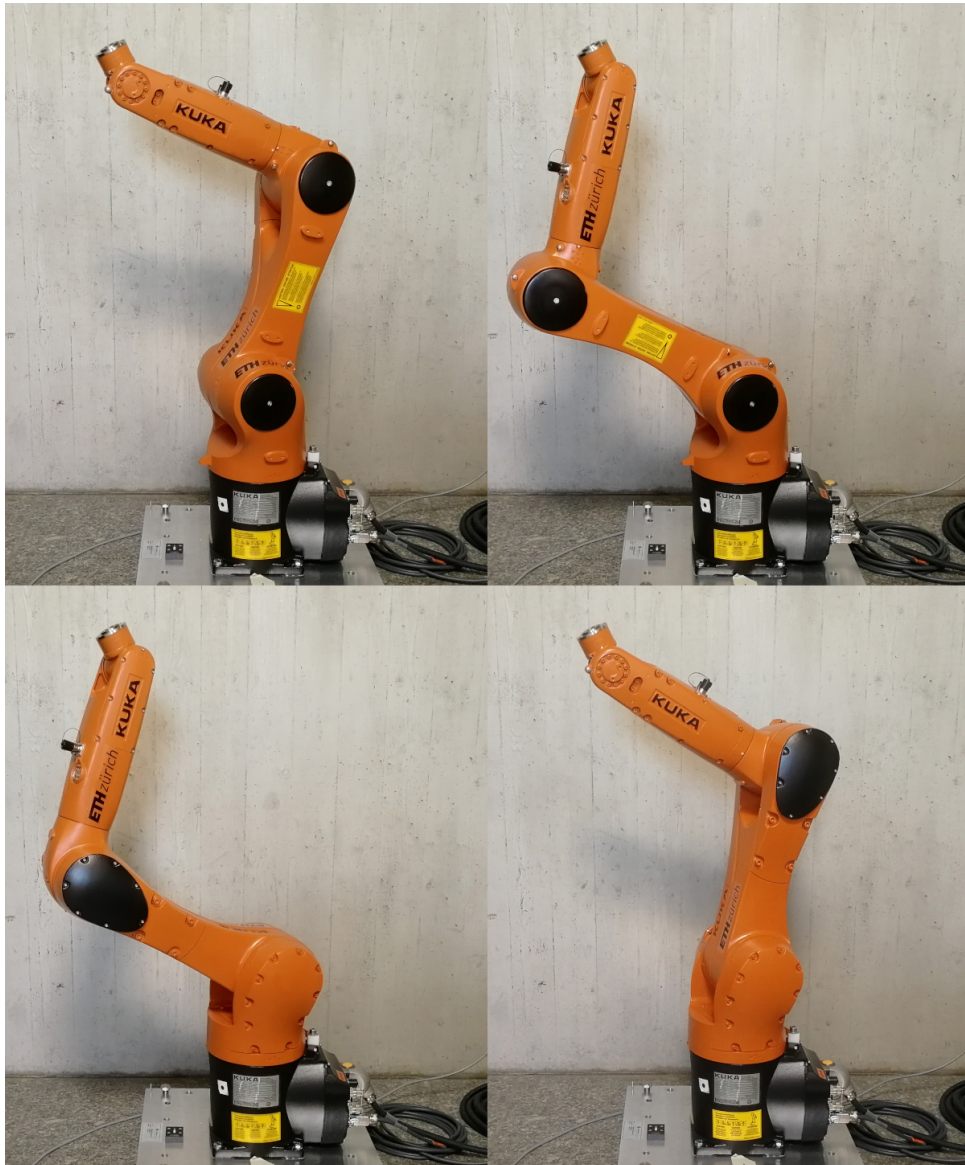


Figure 5.4.5 : View of the postures five to eight ($j \in [5, 6, 7, 8]$), from left to right, for a given pose.

In order to match the KUKA sign and offset conventions, following changes must be performed:

$$\theta'_1 = -\theta_1 \quad (5.48)$$

$$\theta'_2 = \theta_2 - \frac{\pi}{2} \quad (5.49)$$

$$\theta'_4 = -\theta_4 \quad (5.50)$$

$$\theta'_6 = -\theta_6 \quad (5.51)$$

where θ'_i denotes the KUKA angle convention and θ_i denotes the angles as computed by the present algorithm.

5.5 Enhanced kinematic model

Every robot is affected by errors, as the actual geometry does not perfectly fit the nominal geometry. In the same way as axis errors affect theodolites, axis errors also affect an industrial robot: orthogonal axes are not necessarily perfectly orthogonal and parallel axes are not necessarily perfectly parallel.

Furthermore, the dimensions do not necessarily fit the nominal values: the robot's arms can be slightly longer or shorter than indicated in the data-sheet. Finally, the axis angles can be affected by offsets. The first kind of errors cannot be modelled by the kinematic model presented in Section 5.4.1. Therefore, the so-called Denavit-Hartenberg (DH) convention is used (Corke, 2017; Hollerbach et al., 2016).

5.5.1 State of the art

Kinematic robot models based on DH parameters or a similar parametrisation are widely used (Schröder, 1999; Motta, 2006; Hollerbach et al., 2016). The different robot calibration models are very well discussed in (Schröder et al., 1997). Most typically, laser trackers are used for the calibration. Nubiola and Bonev (2013) and Allman et al. (2018) are good examples for robot calibrations using laser trackers. Typically, accuracies of 0.2 mm to 0.4 mm are obtained after calibration of the robot (Nubiola and Bonev, 2013; Allman et al., 2018).

Menge (2003) and Kersten (2014) present a calibration model for a robot with five axes. The subject of the calibration is a robot used for GNSS PCC estimation. The model comprises 20 parameters, including parameters for the joint elasticity. The accuracy of the calibrated robot is 0.2 to 0.3 mm. The measurements were performed with theodolites in the first case and with a laser tracker in the second case.

5.5.2 Denavit-Hartenberg parametrisation

The basic idea is to represent every axis of the robot as a coordinate transformation in 3 dimensions. In principle, this would require three translational parameters and three rotational

parameters. By adroitly attaching the coordinate systems to every axis, the number of parameters can be reduced to four: two rotation angles and two translation. The principle is schematised in Figure 5.5.1.

The first rotational parameter Θ is the angle between two subsequent x-axes. It is the control variable and therefore the final angle reading from the robot. The signs were chosen to match the KUKA convention. α is the angle between two successive y-axes and is 0 for parallel axes. The length of a link is denoted by a and the lateral offset of a joint is denoted by d . The DH parameters for the KUKA Agilus KR 6 R900 sixx are given in Table 5.5.1 and the non-zero parameters are depicted in Figure 5.5.2. The addition of $\delta\Theta$ is necessary to comply with the KUKA convention.

Using DH parameters, the coordinates and the orientation of the flange read as a homogeneous transformation matrix:

$$\mathbf{T} = \prod_{i=0}^6 \mathbf{T}_i = \left(\begin{array}{ccc|c} \mathbf{R}_{r \leftarrow f} & & & \mathbf{u} \\ \hline 0 & 0 & 0 & 1 \end{array} \right) \quad (5.52)$$

where

- \mathbf{T} is the homogeneous transformation matrix of the flange,
- \mathbf{T}_i is the transformation associated with joint and link i ,
- $\mathbf{R}_{r \leftarrow f}$ is the rotation from the flange system to the robot system and
- \mathbf{u} is the coordinates of the flange.

With $i \in [1, 2, 3, 4, 5, 6]$. The individual transformations are functions of the DH parameters:

$$\mathbf{T}_i = \begin{pmatrix} \cos(\Theta_i + \delta\Theta_i) & -\sin(\Theta_i + \delta\Theta_i) \cos \alpha_i & \sin(\Theta_i + \delta\Theta_i) \sin \alpha_i & a_i \cos(\Theta_i + \delta\Theta_i) \\ \sin(\Theta_i + \delta\Theta_i) & \cos(\Theta_i + \delta\Theta_i) \cos \alpha_i & -\cos(\Theta_i + \delta\Theta_i) \sin \alpha_i & a_i \sin(\Theta_i + \delta\Theta_i) \\ 0 & \sin \alpha_i & \cos \alpha_i & d_i \\ 0 & 0 & 0 & 1 \end{pmatrix} \quad (5.53)$$

Table 5.5.1 : DH parameters for the KUKA Agilus KR 6 R900 sixx.

	Θ [rad]	$\delta\Theta$ [rad]	α [rad]	\mathbf{a} [mm]	\mathbf{d} [mm]
1	$-\theta_1$	0	$\pi/2$	25	400
2	$-\theta_2$	0	0	455	0
3	$-\theta_3$	$\pi/2$	$-\pi/2$	35	0
4	θ_4	0	$\pi/2$	0	-420
5	$-\theta_5$	0	$-\pi/2$	0	0
6	θ_6	π	π	0	-80

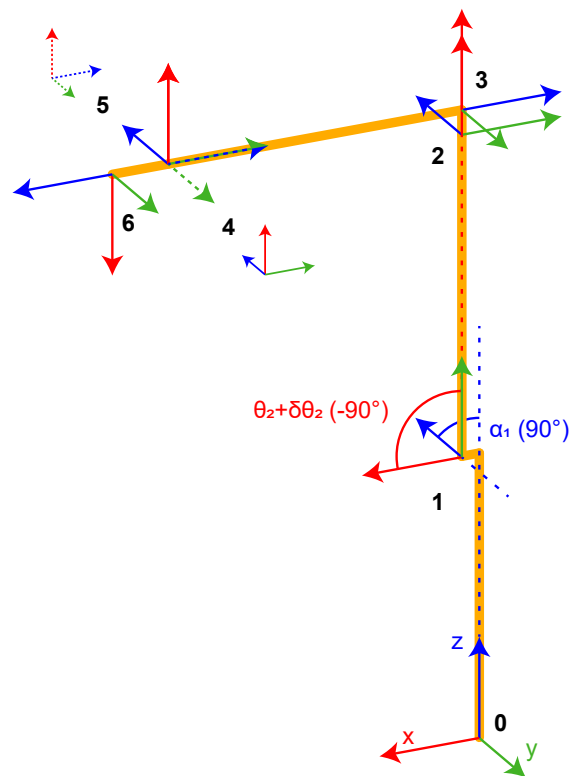


Figure 5.5.1 : Application of the DH convention to a robot with the same configuration as the KUKA Agilus KR 6 R900 sixx. A coordinate system is attached to every joint. Its z-axis is collinear with the joint axis. Each joint and link pair is represented by four parameters. The angle between two successive x-axes is called Θ and the angle between to successive z-axes is α . Source: Willi and Guillaume (2019).

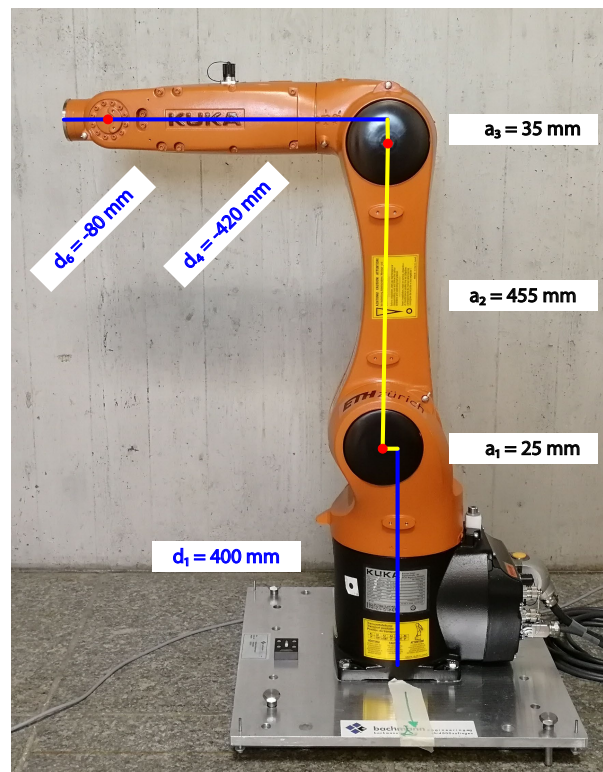


Figure 5.5.2 : The non-zero DH length parameters (a and d) of the KUKA Agilus KR 6 R900 sixx.
Source: Willi and Guillaume (2019).

If \mathbf{T}_0 is equal to the identity matrix, the obtained coordinates are in the robot coordinate system. To obtain coordinates in an other frame, \mathbf{T}_0 can be initialized as follows:

$$\mathbf{T}_0 = \left(\begin{array}{ccc|c} & & & t'_x \\ & \mathbf{R}_{w \leftarrow r} & & t'_y \\ & & & t'_z \\ \hline 0 & 0 & 0 & 1 \end{array} \right) \quad (5.54)$$

where $\mathbf{R}_{w \leftarrow r}$ is the rotation matrix from the robot system to the world system (e.g. a topocentric system) and t'_x , t'_y and t'_z are the offsets and therefore equal to the coordinates of the robot in the world frame. This rotation can be expressed as Euler sequence:

$$\mathbf{R}_{r \leftarrow w} = (\mathbf{R}_{w \leftarrow r})^T = \mathbf{R}_1(\gamma') \mathbf{R}_2(\beta') \mathbf{R}_3(\alpha') \quad (5.55)$$

where α' , β' and γ' are the yaw, pitch and roll angles of the robot in the world coordinate system¹. The convention for the rotation matrices is the same as in Eqs. 2.4 to 2.6. If desired, the tool orientation and the tool offsets can be applied on top of this transformation exactly as shown in Eqs. 5.14 and 5.15

5.5.3 Calibration model

Based on the developments of the previous chapter, a model with 36 parameters was defined. The parameters are listed in Table 5.5.3. In order to decorrelate all parameters from each other, measurements well distributed in the whole operation space of the robot would be needed. The tool orientation can only be estimated if the attitude of the tool is observed. This is for instance the case, if three or more targets are mount on the robot flange.

In general, it is not necessary to fully decorrelate the parameters. If a calibration is meant to be used only over a confined part of the robot operation space, a reduced calibration can be conducted. In general, the calibration will be valid at least in the vicinity of the measurement points. In the specific case of GNSS antenna calibrations, a reduced sequence was found to work well.

5.5.4 Model limitations

The current implementation has several limitations, namely:

- i. Temperature dependency is not modelled,
- ii. joint elasticity is not modelled and
- iii. the non-linearity of axis six is not modelled.

¹Note that in the software QKuka the opposite convention is used: $\mathbf{R}_{w \leftarrow r} = \mathbf{R}_1(\gamma') \mathbf{R}_2(\beta') \mathbf{R}_3(\alpha')$.

Table 5.5.3 : KUKA DH calibration model parameters. Source: Willi and Guillaume (2019).

1 to 6	$\delta\Theta_1$ to $\delta\Theta_6$	Axis angle offsets
7 to 12	α_1 to α_6	DH parameters α
13 to 18	a_1 to a_6	DH parameters a
19 to 24	d_1 to d_6	DH parameters d
25 to 27	t''_x, t''_y, t''_z	Tool offsets in x, y and z
28 to 30	$\alpha'', \beta'', \gamma''$	Tool orientation as Euler sequence
31 to 33	t'_x, t'_y, t'_z	Robot coordinates in the world frame
34 to 36	α', β', γ'	Robot orientation in the world frame as Euler sequence

The latter two effects are well studied and presented in the literature. Nubiola and Bonev (2013) included a stiffness model and a non-linearity model for axis six and obtained excellent results. Inclusion of these two models is expected to enhance the accuracy of the calibrated robot. The non-linearity model parameters can be estimated only if the orientation of the tool is observed as well. This requires a laser tracker with a probe for six degrees of freedom.

The temperature dependence is more difficult to model. Theoretical considerations and simulations lead to the conclusion that the temperature dependence can be neglected if using a small robot and if high precision and not high accuracy is targeted (Willi and Guillaume, 2019). However, further experiments are necessary to verify this assumption. A possible approach to deal with temperature changes is to include temperature dependent DH parameters, as suggested by Bilich et al. (2018).

5.6 Paper III – Calibration of a Six-Axis Robot for GNSS Antenna Phase Center Estimation

The third paper presents a novel method for the calibration of a six-axis robot. The paper was submitted to the *Journal of Surveying Engineering* with the title *Calibration of a Six-Axis Robot for GNSS Antenna Phase Center Estimation*. The article is in review.

5.6.1 Abstract

A new method for the calibration of a six-axis robot is presented. Using a kinematic model of the robot based on its geometry, we were able to increase the precision of the positioning from about 0.5 mm to below 0.1 mm. The kinematic robot model is based on the Denavit-Hartenberg convention. The main innovation consists in using a micro-triangulation system which allows to perform the calibration of the robot on site.

Unlike standard calibrations based on similar models, our approach uses the exact sequence of robot positions that is used for GNSS antenna calibrations. The result is a very efficient and highly automatic calibration procedure, although its applicability is limited to the exact same case of GNSS antenna calibrations.

5.6.2 Author's contribution

This subsection summarises the author's contribution to paper III. The main work packages include the theoretical developments of the kinematic model, the derivation of the parametrisation, the implementation of an estimation software in Matlab and the implementation of the correction model in the control software of the robot.

The experimental part includes the data acquisition and the data processing. It should be mentioned that a substantial part of the data acquisition was accomplished by students. Table 5.6.1 quantifies the proportion of work carried out by the main author.

5.6.3 Relevance to the field

Robot calibrations based on DH models are present in the literature. The use of a calibration sequence which is tailored to GNSS antenna calibration, in combination with the optical micro-triangulation, however, is a novelty. The developed method is a very efficient means of calibrating a robot in the field. Therefore, it is of real benefit for the antenna calibration community, which relies on well-calibrated robots.

5.7 Outlook

With the successful calibration, the robot is ready to be used for absolute antenna calibrations (see Chapter 6). The use of the robot in the field, together with periodic recalibration, will help to answer the open research questions. Namely:

- i. How is the long-term stability of the calibration?
- ii. How do temperature variations influence the DH parameters?

Further data will help to improve the understanding of the underlying processes and finally improve the kinematic robot models.

Table 5.6.1 : Summary of the author's contribution to paper III – Calibration of a Six-Axis Robot for GNSS Antenna Phase Center Estimation.

	Original idea	Measurements, data generation	Theoretical developments	Software implementation	Computation, data processing
Derivation of the DH parametrisation			100%		
Development of a kinematic model and an estimation strategy	100%		100%		
Model implementation in Matlab and in C++				100%	
Measurement campaigns	25%				
Processing of the micro-triangulation					0%
Estimation of the parameters and analysis					100%
Editorial work	80%				

Chapter 6

Absolute GNSS antenna field calibration

Absolute field calibrations represent an enhancement of relative field calibration. Introducing rotations around axes other than the antenna vertical axis allows to decorrelate all three components of the PCO from the station coordinates. The other main advantages of absolute field calibration over relative field calibration are:

- i. The probing of the antenna hemisphere can be controlled by choosing appropriate rotations, for instance by choosing a large inclination of the antenna,
- ii. multipath can potentially be mitigated and
- iii. the calibration result is independent from the calibration of the reference antenna.

Time-differenced GNSS observations fulfil requirement (ii) and (iii), unlike double-differenced or single-differenced observations. This approach is presented in the following section.

6.1 Time-differencing mode

In principle, two differencing modes in time are imaginable:

- i. Differences over a sidereal day and
- ii. Differences over only a few seconds.

The first absolute field calibrations were performed using differences over a sidereal day (Wübbena et al., 1997; Menge, 2003). As the GPS constellations repeats after a sidereal day, the same multipath is expected to repeat as well. This technique does not apply to other GNSS with other repeat periods. The drawback of this method is the very long calibration time of at least a sidereal day plus the duration of the measurements on the second day. However, the measurements on the first day do not necessarily need to cover 24 hours.

In the second differencing mode, a robotic manipulator is used to perform very fast rotations. Multipath is a time varying quantity. Differencing epochs that are very close to each other

eliminates the multipath fraction which is common to both epochs. In order to have a reasonable correlation, the time between epochs should not exceed a few seconds. Multipath from the ground has a rate of $1.73 h \cdot 10^{-4}$ m/s, where h is the antenna height over ground (Braasch, 2017, p. 447); The multipath change (and thus the error in time-differences) already exceeds a millimetre after five seconds. Objects located closer to the antenna (for instance the measurement pillar) will have faster multipath rates and thus, their multipath contribution will not be eliminated in the time-differencing process.

6.2 Triple-difference observation equation

A GNSS phase observation reads (Hauschild, 2017a):

$$P_A^i = \mathbf{e}_A^{i\top} (\mathbf{x}^i - \mathbf{x}_{A,ARP}) + c \delta t_A - c \delta t^i + \lambda N_A^i + T_A^i + I_A^i + PCC_A^i + W_A^i + v_A^i \quad (6.1)$$

where

P_A^i	is the carrier phase observation between antenna A and satellite i ,
\mathbf{e}_A^i	is the line-of-sight vector,
\mathbf{x}^i	is the GNSS satellite position at signal emission,
$\mathbf{x}_{A,ARP}$	is the position of the receiver antenna ARP at signal reception,
c	is the speed of light,
δt_A	is the receiver clock error,
δt^i	is the satellite clock error,
λ	is the carrier wavelength,
N_A^i	is the integer phase ambiguity,
T_A^i	is the tropospheric delay,
I_A^i	is ionospheric delay,
PCC_A^i	is the PCC,
W_A^i	is the phase wind-up and
v_A^i	is zero-difference observation noise.

The phase wind-up is modelled according to Wu et al. (1993). Triple-differences involve eight measurements, as two satellites are observed from two stations at two epochs (Hauschild, 2017b):

$$\begin{aligned} P_{AB,t_1t_2}^{ij} &= \left((P_B^j - P_A^j) - (P_B^i - P_A^i) \right)_{t_2} - \left((P_B^j - P_A^j) - (P_B^i - P_A^i) \right)_{t_1} \\ &= \left(P_B^j - P_A^j - P_B^i + P_A^i \right)_{t_2} - \left(P_B^j - P_A^j - P_B^i + P_A^i \right)_{t_1} \end{aligned} \quad (6.2)$$

where $P_{AB,t_1t_2}^{ij}$ is the triple-difference involving epochs t_1 and t_2 . After substitution of Eq. 6.1

into Eq. 6.2 and simplification, the triple-difference reads:

$$\begin{aligned}
 P_{AB,t_1t_2}^{ij} = & \left(\rho_{B,t_2}^j - \rho_{A,t_2}^j - \rho_{B,t_2}^i + \rho_{A,t_2}^i \right) - \left(\rho_{B,t_1}^j - \rho_{A,t_1}^j - \rho_{B,t_1}^i + \rho_{A,t_1}^i \right) \\
 & + \left(N_{B,t_2}^j - N_{A,t_2}^j - N_{B,t_2}^i + N_{A,t_2}^i \right) - \left(N_{B,t_1}^j - N_{A,t_1}^j - N_{B,t_1}^i + N_{A,t_1}^i \right) \\
 & + \left(PCC_B(\alpha_{B,t_2}^j, z_{B,t_2}^j) - PCC_A(\alpha_{A,t_2}^j, z_{A,t_2}^j) \right. \\
 & \quad \left. - PCC_B(\alpha_{B,t_2}^i, z_{B,t_2}^i) + PCC_A(\alpha_{A,t_2}^i, z_{A,t_2}^i) \right) \\
 & - \left(PCC_B(\alpha_{B,t_1}^j, z_{B,t_1}^j) - PCC_A(\alpha_{A,t_1}^j, z_{A,t_1}^j) \right. \\
 & \quad \left. - PCC_B(\alpha_{B,t_1}^i, z_{B,t_1}^i) + PCC_A(\alpha_{A,t_1}^i, z_{A,t_1}^i) \right) \\
 & + \left(W_{B,t_2}^j - W_{A,t_2}^j - W_{B,t_2}^i + W_{A,t_2}^i \right) - \left(W_{B,t_1}^j - W_{A,t_1}^j - W_{B,t_1}^i + W_{A,t_1}^i \right) \\
 & + v_{AB,t_1t_2}^{ij}
 \end{aligned} \tag{6.3}$$

where

- ρ is the respective geometrical term,
- $v_{AB,t_1t_2}^{ij}$ is the triple-difference observation noise,
- α is the azimuth of the GNSS satellite and
- z is the zenith angle of a GNSS satellite as seen from the station.

The triple-difference observation noise is $2\sqrt{2}$ times larger than the zero-difference observation noise (assuming that all observations have the same standard deviation and are uncorrelated). Assuming a short baseline, the ionospheric and the tropospheric delays are strongly reduced already on station single-difference level, together with the satellite clock error (Hauschild, 2017b, p. 594). Receiver clock errors vanish at double-difference level (Hauschild, 2017b, p. 597).

Assuming that the interval between the two epochs is very small, further simplifications can be introduced:

- i. In the absence of cycle slips, the ambiguity term is constant in time, thus:
 - a. N_{B,t_1}^j equals N_{B,t_2}^j ,
 - b. N_{A,t_1}^j equals N_{A,t_2}^j ,
 - c. N_{B,t_1}^i equals N_{B,t_2}^i and
 - d. N_{A,t_1}^i equals N_{A,t_2}^i .
- ii. Because the reference antenna B does not rotate, its phase wind-up is almost constant over short time intervals. Therefore:
 - a. W_{B,t_1}^i equals W_{B,t_2}^i and
 - b. W_{B,t_1}^j equals W_{B,t_2}^j .
- iii. The apparent positions of the GNSS satellites change very slowly. Therefore:

- a. α_{B,t_1}^i equals α_{B,t_2}^i ,
- b. α_{B,t_1}^j equals α_{B,t_2}^j ,
- c. z_{B,t_1}^i equals z_{B,t_2}^i and
- d. z_{B,t_1}^j equals z_{B,t_2}^j ,

practically leading to the elimination of the PCC of the reference antenna.

Introducing these simplifications into Eq. 6.3 leads to the following, final expression:

$$\begin{aligned}
P_{AB,t_1t_2}^{ij} = & \rho_{AB,t_1t_2}^{ij} - PCC_A(\alpha_{A,t_2}^j, z_{A,t_2}^j) + PCC_A(\alpha_{A,t_2}^i, z_{A,t_2}^i) \\
& - PCC_A(\alpha_{A,t_1}^j, z_{A,t_1}^j) + PCC_A(\alpha_{A,t_1}^i, z_{A,t_1}^i) \\
& - W_{A,t_2}^j + W_{A,t_2}^i - W_{A,t_1}^j + W_{A,t_1}^i + v_{AB,t_1t_2}^{ij}
\end{aligned} \tag{6.4}$$

where $\rho_{AB,t_1t_2}^{ij}$ is the triple-difference geometry term. The geometry term can easily be modelled using broadcast or precise satellite orbits and approximate station coordinates. The phase wind-up is modelled according to Wu et al. (1993). Even though the phase wind-up and the PCC of the reference antenna nearly vanish on triple-difference level, the modelled corrections are applied in the processing software.

6.3 Absolute character of triple-difference antenna calibration

The last remaining deterministic signal component in Eq. 6.4 is the PCC. The PCC of the reference antenna has vanished, leading to a truly absolute estimation of PCC. If the reference antenna PCC is still present in the observation equation, the calibration cannot be said to be truly ‘absolute’ (see also Bilich and Mader, 2010, p. 1371).

This independence on the reference PCC of the triple-differences is illustrated with the help of a use case. A sequence of 4042 orientations and a precise orbit file from 22.8.2018 have been used to generate synthetic observations. Biases were added on the reference station during the data generation process. The data was then processed with double-difference as well as triple-difference algorithms. As can be seen in Table 6.3.1, the triple-difference is much less sensitive to biases like the modelled PCC of the reference antenna. Even a very long calibration sequence of over 4000 orientations is not able to eliminate the bias which is due to the omission of the reference PCC, if double-differences are used. An error of up to 0.3 mm is the consequence. If a five times larger PCC bias is applied, the difference between double-differences and triple-differences becomes more obvious. In this case, the error on the estimated PCC amounts to over 1.5 mm for the double-difference approach, while the triple-difference approach leads to a PCC with only 0.16 mm maximal error.

Table 6.3.1 : Results from a study on PCC biases conducted with synthetic data. Biases were added to the data during the data generation process. During the estimation process, the biases were not modelled. The results show a different sensitivity of the processing based on triple-differences (TD) compared to the processing based on double-differences (DD). In the first case, a PCO bias of 10 cm was added to the reference station. In the second case, the PCC of the ‘SEPCHOKE_B3E6 SPKE’ antenna (IGS type mean value) was added to the reference station. In the last case, a bias corresponding to five times the PCC of the ‘SEPCHOKE_B3E6 SPKE’ antenna (IGS type mean value) was added to the reference. The table holds the Root Mean Square error (RMSE), the minimal error (Min.) and the maximal error (Max.) of the estimated PCC.

[mm]		RMSE	Min.	Max.
PCO bias (100 mm)	TD	0.03	-0.09	0.12
	DD	0.03	-0.06	0.15
PCC bias I (80 mm)	TD	0.03	-0.08	0.11
	DD	0.08	-0.32	0.26
PCC bias II (400 mm)	TD	0.03	-0.16	0.08
	DD	0.34	-1.61	1.13

Of course, the pure access to the PCC of the antenna to be calibrated has a cost, namely a higher noise level of triple-differences compared to double-differences. As eight observations are involved in a triple-difference, the standard deviation of one observation is $2\sqrt{2}$ times higher than the standard deviation of a zero-difference observation (in the case of uncorrelated observations with equal weight). Nevertheless, triple-differences should always be preferred if:

- i. The goal is to obtain unbiased estimates of the PCC and if
- ii. enough measurements are available to reduce the variance of the estimates to a reasonable level.

6.4 Rotation sequence

During the calibration, a point within the antenna, for instance the nominal GPS L1 phase centre, is kept fixed in space. The nominal coordinates of the chosen point do not change during the calibration. A fixed rotation point has following advantages:

- i. The dynamics of the antenna is reduced. Therefore, dynamics induced tracking loop responses are reduced and
- ii. beside the tilt, the antenna is stationary with respect to its environment. Thus, the change in the multipath pattern is reduced.

The algorithm for the generation of the rotation sequence is displayed in Figure 6.4.1. First, a regular grid in azimuth and elevation is formed. This grid describes in which direction and by which angle the antenna is tilted. This step and all subsequent steps are illustrated in Figure 6.4.2. In a second step, a common rotation is applied to all normal vectors. The goal of this additional rotation is to avoid pointing towards the north hole. In step three, the sequence is randomized. Finally, rotations around the inclined antenna z-axis are added.

The randomisation of the rotation sequence is the key to successful antenna calibration. Randomisation ensures that time correlated effects do not systematically bias the estimation of the PCC. Another key factor is a good mixture between rotations around the antenna z-axis and rotations around the two other axes.

Rotations around the antenna z-axis do not change the orientation of the antenna gain pattern with respect to the site, because the gain pattern of geodetic antennas is typically highly symmetrical. However, rotations around the z-axis do not add information about the zenithal behaviour of the PCC. They strengthen the observability of azimuth variations of the PCC. This is illustrated in Figure 6.4.3. Two or three different rotations of the antenna z-axis for each orientation is a reasonable choice.

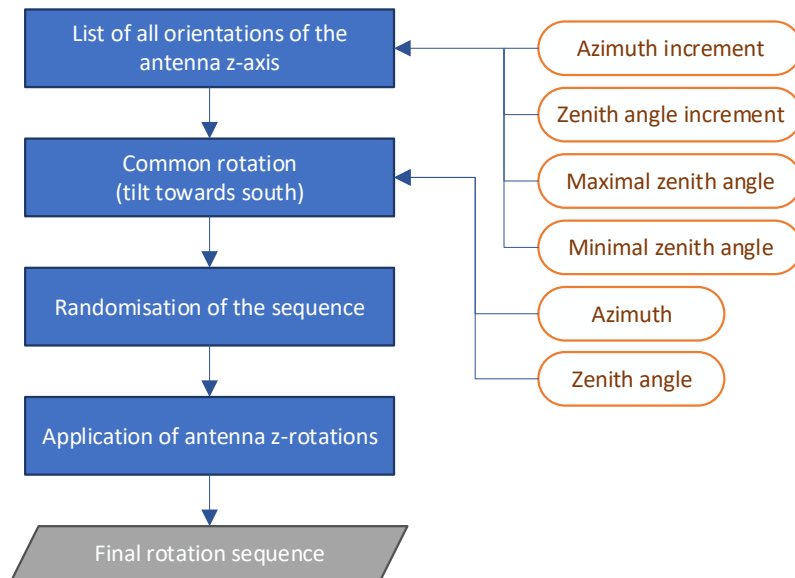


Figure 6.4.1 : Flowchart of the algorithm for the generation of the randomized rotation sequence.

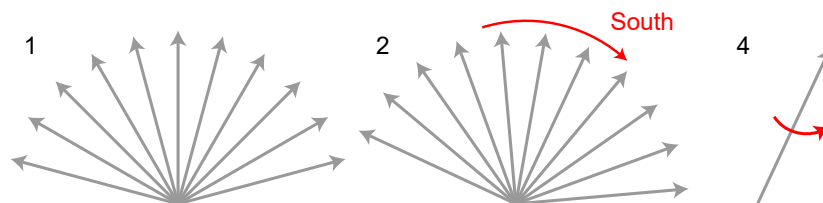


Figure 6.4.2 : Algorithm for the generation of the randomized rotation sequence. In 1, all orientations for the antenna z-axis are set up. In 2, the space of all rotations is tilted towards south, in order to avoid the north-hole. Pointing towards the north-hole unnecessarily reduces the number of observations. In 3 (not shown), the order of the sequence is randomized. Finally, in 4, rotations around the antenna z-axis are added.

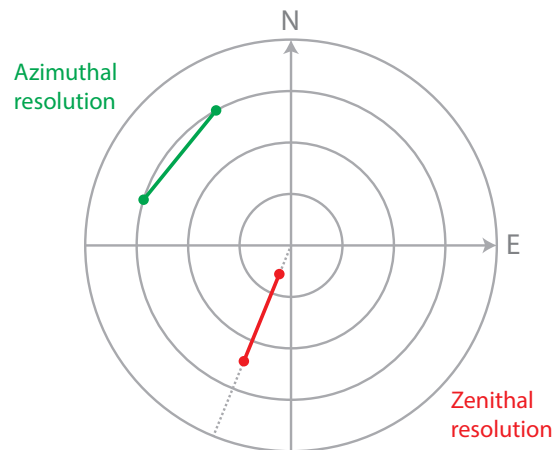


Figure 6.4.3 : Skyplot illustrating azimuthal and zenithal resolution. Azimuthal information is added by rotating the antenna around the antenna z-axis. In this case, only the azimuth satellite changes. Information on the zenithal variability of the PCC is obtained by applying rotations around the antenna x- or y-axis (or both), in order to change the elevation of the GNSS satellite.

6.5 Receiver dynamical stress

As pointed out in Häberling (2015), receiver suffer from dynamical stress in high dynamical situations. The rotation around the nominal phase centre theoretically reduces the dynamics during the change of orientation of the antenna. Only the PCC rate remains. However, the KUKA robot does not perform trajectory control between two stationary positions. In fact, all axes are driven linearly. This might induced a small dynamics. Within the frame of this thesis, receiver dynamical stress was not given particular attention. From the comparisons of the results obtained with various signals on the same frequency, it is obvious that the GPS L2W signals, which are derived from the encrypted P-code, lead to absurd results. These measurements have an inertia of several seconds and can therefore not be used for antenna calibration purposes.¹ More information on the signal structure is found in Teunissen and Montenbruck (2017), more information on GNSS receiver architecture is found in Kaplan and Hegarty (2017).

For most of the calibrations, Septentrio PolaRx 5 receivers with the default setting were used.

¹Personal communication from Septentrio at the ION GNSS+ 2018 conference, 24–28 September 2018, Miami.

6.6 Differencing strategy

Two requirements drive the differencing strategy:

- i. The triple-difference observations should be algebraically uncorrelated. This allows a sequential parameter estimation process (normal equation stacking) and
- ii. the time interval between two epochs being differentiated against each other should be small.

A sequence fulfilling these requirements is displayed in Figure 6.6.1. Half of the measurements taken at orientation k are differentiated against half of the measurements taken at orientation $k+1$. The measurements acquired during the robot motion are discarded. Those measurements can be taken into account, provided that the robot motion is sufficiently well-known between two stationary positions and provided that the dynamics of the robot does not lead to dynamical stress tracking errors.

In case of an odd number of measurement epochs, one epoch is discarded. The number of epochs finally taken into account is dependent on:

- i. The sampling rate of the receiver,
- ii. the duration of the stationary position of the robot and
- iii. the timing accuracy of the robot, which is less accurate than the timing accuracy of the GNSS receivers.

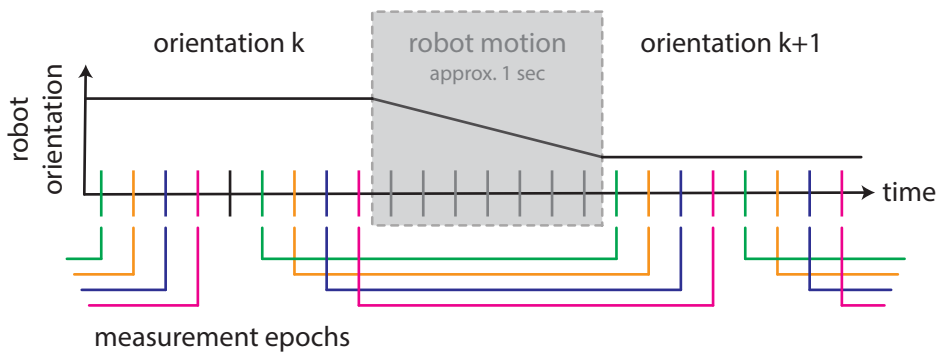


Figure 6.6.1 : Differencing strategy avoiding algebraic correlation between the triple-differences. Source: (Willi et al., 2018a).

6.7 Processing pipeline

A summary of the processing pipeline, which is implemented in Matlab, is presented in Figure 6.7.1. The pipeline uses the following input data:

- i. GNSS observations:
 - a. A RINEX observation file from the reference station and
 - b. a RINEX observation file from the antenna to be calibrated.
- ii. A file with the start time and the end time of each orientation (robot attitude file),
- iii. a configuration file (see Table 6.7.1) and
- iv. precise GNSS products:
 - a. Precise GNSS orbits,
 - b. precise GNSS clocks and
 - c. a RINEX navigation file for the ionospheric correction parameters.

The configuration file contains all options for the processing, for instance the signal for which to generate a calibration. Its content is shown in Table 6.7.1. After data reading and automatic download of precise products, a Single Point Positioning (SPP) solution is computed. The Centre for Orbit Determination in Europe (CODE; Prange et al., 2017) is one example for a facility offering precise orbits and clocks.² The SPP solution uses the GPS user algorithm from the GPS ICD 200 (2015) and the ionospheric model coefficients from a concatenated RINEX navigation file. This file is available, for instance, at NASA’s Crustal Dynamics Data Information System (CCDIS).³ The main goal of this processing step is to provide a receiver clock estimate with respect to GPS time, which is necessary for the alignment of the measurements.

The alignment part consists of a loop establishing the time correspondence between the GNSS observations from the reference station, the GNSS observations from the antenna to be calibrated and the robot orientations, according to the scheme presented in Section 6.6 and in Figure 6.6.1. The result is a list of simultaneous GNSS observations from both, the reference station and the antenna to be calibrated, labeled with the orientation of the robot at that exact moment.

The actual PCC estimation is achieved in the main computation loop, based on triple-differences generated according to Section 6.2. The observation equation is set up, the derivatives are computed and the normal equation matrix is populated. This operation is performed sequentially and all normal equations are summed up. The inversion of the accumulated normal equations leads to the final estimation of the PCC.

²<http://ftp.aiub.unibe.ch>

³<ftp://cddis.gsfc.nasa.gov/gnss/data/daily>. The daily concatenated navigation files containing the coefficients are named *brdcDOY0.YYn* with DOY being the day of the year and YY being the two digit year.

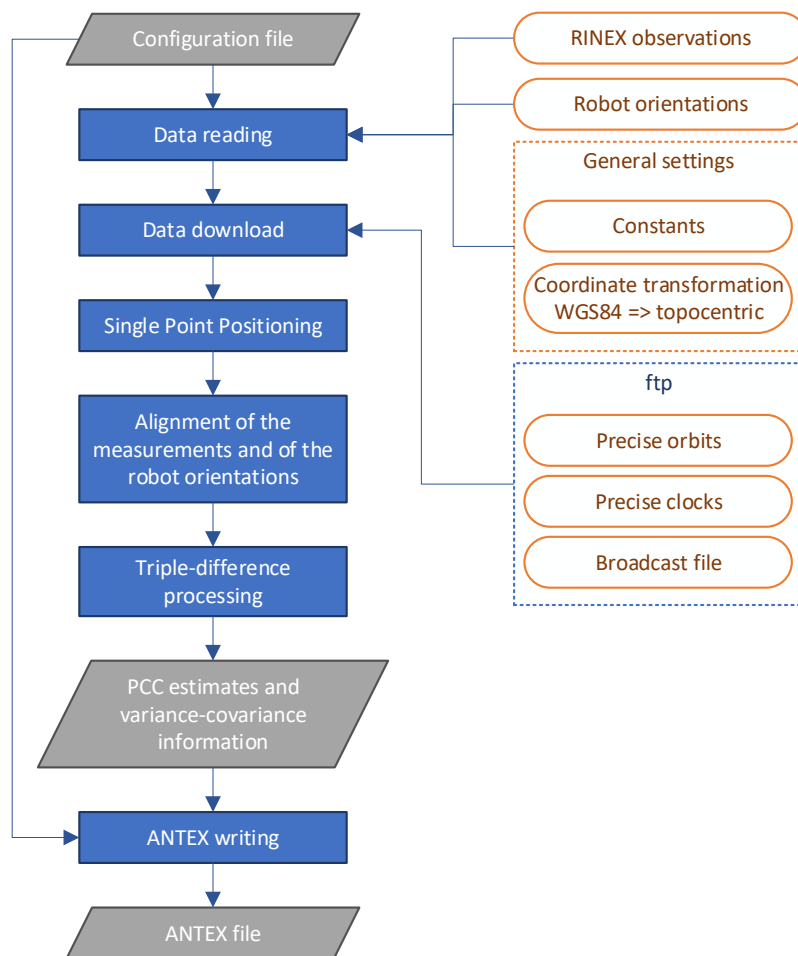


Figure 6.7.1 : Overview of the processing of the GNSS observations for PCC estimation.

Table 6.7.1 : Configuration options for PCC estimation. As suggested by the entry ‘Reference PCC’, the PCC of the reference antenna are applied, even though they nearly vanish on triple-difference-level.

Option	Description	E.g.
Folder	Path to data folder	
Campaign	Name of the campaign for file naming	
Save path	Path for all result files	
Date	Date of the processing	
RINEX	Input GNSS observation files	
Attitude	Input file of robot orientations	
Type	Type of the antenna to be calibrated	
Serial	Serial number of the antenna	
Offset to ARP	X, Y and Z Offset of the ARP in the robot tool system in mm	
System 1	GNSS used for Single Point Positioning	GPS
Signal 1	Signal used for Single Point Positioning	C1C
System 2	GNSS to be calibrated	Galileo
Signal 2	Signal to be calibrated	L5Q
Pseudorange 2	Pseudorange associated with the above signal	C5Q
Resolution	Degree and order of the spherical harmonics expansion	8
Reference PCC	Path to the ANTEX file of the reference antenna	
Reference type	Type of the reference antenna	
Reference serial	Serial number of the reference antenna	
Robot coordinates	Approximated coordinates (in the topocentric frame) which were kept fix during the calibration	
Reference station coordinates	Approximated coordinates of the reference station	
Coordinate weight	Standard deviation of the reference coordinates in metres. The coordinates are introduced as pseudo-observations	
Elevation mask	Minimum elevation in the topocentric reference frame	
Grid	Optional estimation of PCC with the grid parametrisation	
Grid resolution	Spacing of the grid in azimuth and elevation	
Simulation	Optional simulation ability	

All parameters are originally set up in the normal equation. The singular parameters, for instance the spherical harmonics coefficients representing anti-symmetry (see section 3.4.3) are hard-constrained to zero. The relative coordinates of the antenna to be calibrated (or more accurately, the coordinates of the rotation point) with respect to the reference antenna are introduced as pseudo-observation (soft-constrain). If a spherical harmonics parametrisation is chosen, the PCO is not explicitly set up, as it is implicitly already contained in the spherical harmonics series (see section 3.4.3).

The configuration file is needed a second time in order to generate the ANTEX file. In the case of PCC parametrisation as spherical harmonics, the spherical harmonics are evaluated at a regular spacing (typically 5 degrees). The best-fit PCO is estimated and subtracted from the grid. The resulting grid is written into the ANTEX file instead of spherical harmonics coefficients, as ANTEX does not support a spherical harmonics representation. If necessary for conventional reasons, a best-fit PCO can be estimated and subtracted from the PCV before the ANTEX file is written.

6.8 Paper IV – Absolute GNSS Antenna Phase Center Calibration with a Robot

The forth paper presents preliminary results obtained with the new robot calibration system. It was originally published in *Proceedings of the 31st International Technical Meeting of The Satellite Division of the Institute of Navigation (ION GNSS+ 2018), Miami, Florida, September 2018, pp. 3909–3926* with the title *Absolute GNSS Antenna Phase Center Calibration with a Robot*. This paper was published after peer-review.

6.8.1 Abstract

Paper IV presents preliminary results obtained with the GNSS receiver antenna calibration facility. A robotic arm brings the GNSS antenna to be calibrated into various orientations. The acquired data is processed using data from a nearby reference station and a triple-difference approach.

The system is described in detail, including a description of the rotation sequence and the processing strategy. The authors demonstrated the ability of the system to estimate meaningful PCC for GPS L1. The estimated PCC are statistically significant. First results show that the estimated PCC are mostly insensitive to changes in the elevation cut-off angle. Repeatability tests revealed a repeatability of the PCC at the order of 0.6 mm Root Mean Square (RMS), using calibration sequences of only 40 minutes.

Although only GPS L1 results are presented, the system is ready to estimate PCC for any Code Division Multiple Access (CDMA) signal.

6.8.2 Author's contribution

The following section gives a summary of the author's contribution to paper IV (Willi et al., 2018a). The idea of using a robot for PCC estimation is not new. However, a substantial amount of work was necessary, as the system at ETH Zurich was developed from scratch.

The theoretical developments focused on the parametrisation of PCC and the parameter estimation process, whereas the implementation effort was mostly spent on commissioning the robot, writing the interface from the robot to the control computer, implementation of the triple-difference processing approach and development of the entire processing pipeline, from raw GNSS data to ANTEX.

Table 6.8.1 holds a summary of the author's proportional contribution to the mentioned peer-review publication.

6.8.3 Relevance to the field

No group has yet demonstrably developed a system performing field calibration of GNSS receiver antennas for the new Galileo signals (E5a, E5b, E5, E6). With the present publication, the validity of our approach is demonstrated and an important step towards a full Galileo calibrations is achieved. Potentially, any other CDMA signal can be calibrated as well.

The calibration of GNSS receiver antennas for E5a is an important gap in the scientific GNSS community. The European GNSS Agency released PCC for the spacecraft (European GNSS Service Centre, 2018). However, this precious feature can only be fully exploited once the ground network of receiving antennas is properly calibrated. Our contribution is a significant step in that direction. Eventually, this could lead to a better estimate of the system scale, as a lack in receiver and satellite PCC seems to be the primary factor currently preventing GNSS to provide an independent scale to the International Terrestrial Reference Frame (ITRF; Altamimi and Collilieux, 2009).

6.9 Pending publication

Extended results, including GPS L5 and Galileo E5 PCC and a validation campaign on short baselines, are available since recently. A part of these results was presented at the IGS Workshop 2018 in Wuhan, China.⁴ A publication in a scientific journal with the full results is in preparation.

The short baseline experiment was conducted on the roof of the institute (see Figure 6.9.1). Four antennas were set up on four pillars in four sessions, permuting the antennas after every session. The distance between the stations is about 5 m. The duration of the sessions was at least 24 h. The station coordinates were precisely surveyed before and after the experiment, resulting in ground-truth coordinates with an accuracy of 0.2 mm. The acquired data was

⁴The presentations will be available online at www.igs.org/presents.

Table 6.8.1 : Summary of the author's contribution to paper IV – Absolute GNSS Antenna Phase Center Calibration with a Robot.

	Original idea	Measurements, data generation	Theoretical developments	Software implementation	Computation, data processing
Commissioning of the robot		70%			
C++ interface to the robot	90%			90%	
PCC parametrisation			90%		
Robot rotation sequence	95%			100%	
Triple-difference processing	95%		80%	90%	
ANTEX related software implementations				90%	
Conduction of calibrations		50%			
PCC analysis				100%	
Editorial work	70%				

processed with the Bernese GNSS Software V5.2 (Dach et al., 2015). The six possible baselines were processed individually, using one system and one frequency at a time. The north, east and up residuals per baseline and per session were then reported on the plots.

Figure 6.9.2 shows the results for Galileo E1, Figure 6.9.3 for Galileo E5. The upper parts of the plot holds the results obtained with the individual ETH Zurich PCC, the lower part the results obtained with a mix between individual Geo++[®] calibrations and IGS type-mean PCC (see Table 6.9.1). As no Galileo E5 reference PCC are available, GPS L2 is used. It can be seen that the ETH Zurich calibration significantly reduces the spread and the systematic bias in the coordinate domain. The main limitation of the experiment lies in the fact that individual reference calibrations are available for two antennas of the same type and for no other antenna. However, in order to see interesting effects, a mix of various antenna types with individual calibrations would be of highest interest. Additionally, the up component in the lower part of Figure 6.9.3 shows an unexpected behaviour: the spread of this component is much smaller than the spread of the north and the east components. This effect is not explained yet.

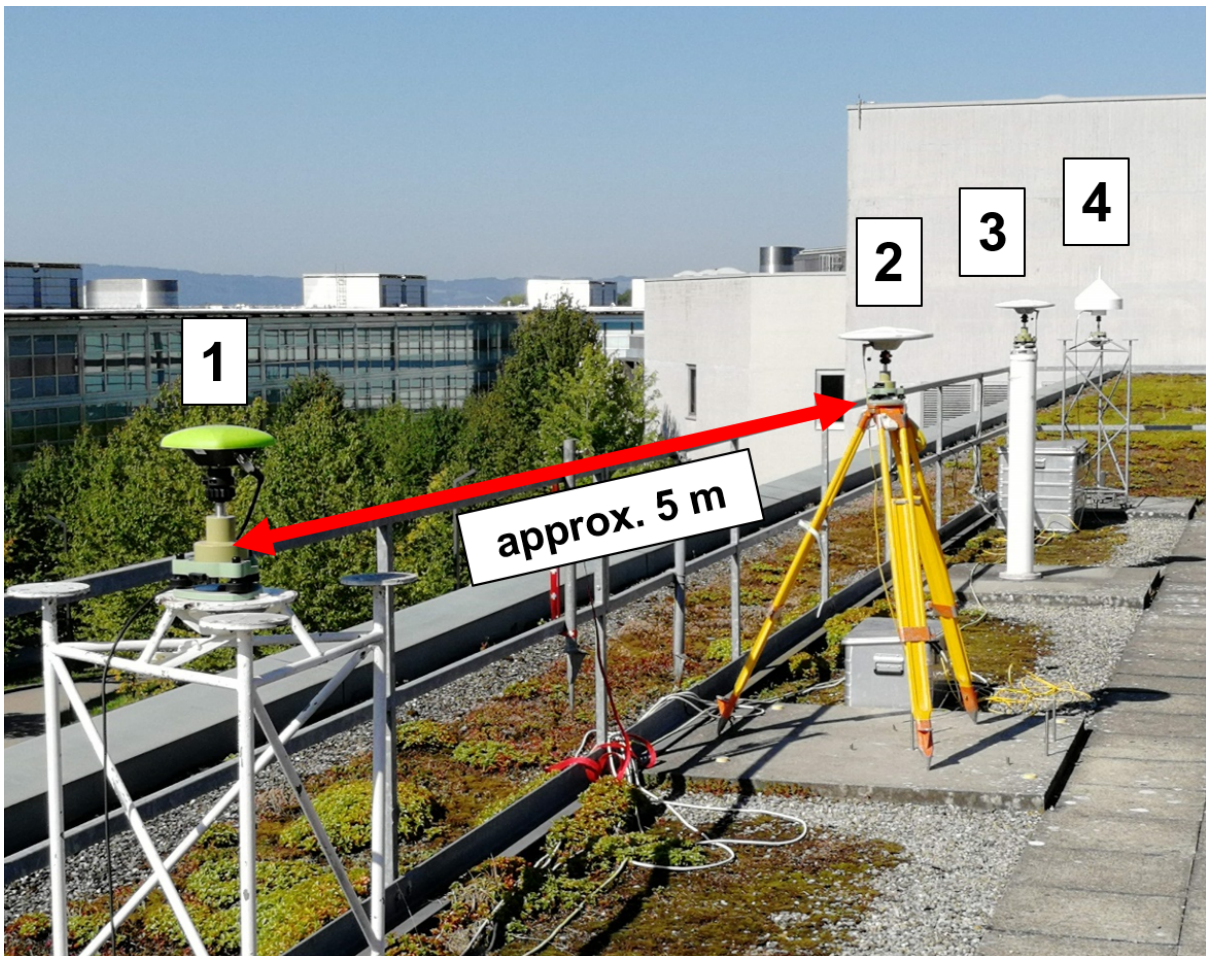


Figure 6.9.1 : Set-up for the short baseline calibration.

Table 6.9.1 : Antennas used in the short baseline validation.

Antenna	Calibration type
JAV_GRANT-G3T	IGS type-mean PCC
SEPCHOKE_B3E6	IGS type-mean PCC
TRM57971.00	Individual Geo++ [®] PCC
TRM57971.00	Individual Geo++ [®] PCC

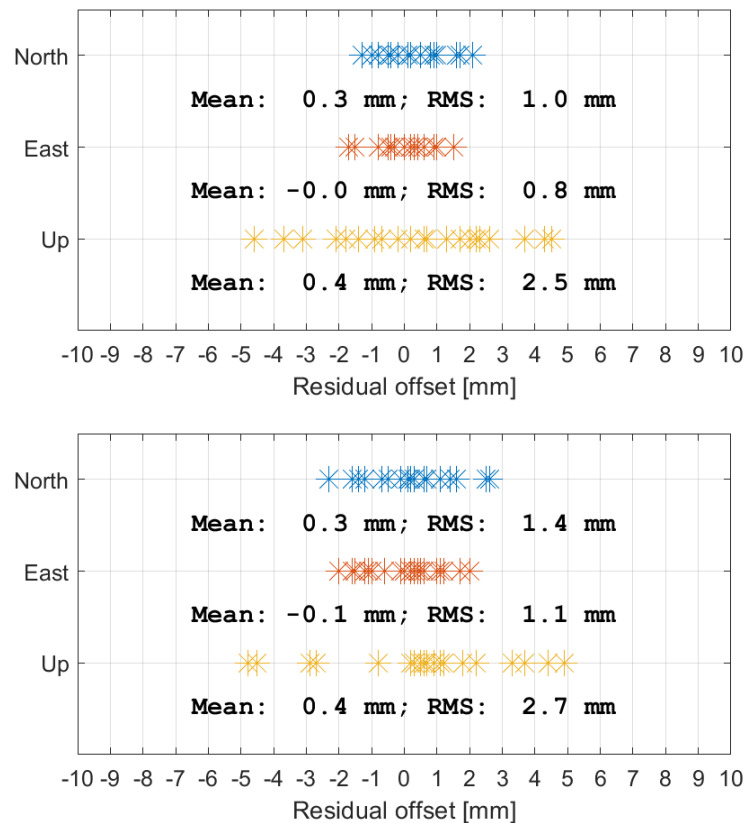


Figure 6.9.2 : Coordinate residuals of all baseline used within the short baseline validation. The relative coordinates were estimated using Galileo E1 only. The upper plot shows the results obtained using the ETH Zurich patterns, the lower plot shows the results using Geo++[®] individual calibrations (two antennas) and IGS type-mean calibrations (two antennas).

6.10 Outlook

The future effort will focus on further validation. The implementation of Frequency Division Multiple Access Signals (FDMA) is foreseen as well.

Multipath will remain a big challenge. Software Defined Radio (SDR) GNSS receivers (also called software receivers) are a very efficient way of quantifying and mitigating multipath propagation errors. Efforts should be put in utilizing SDR GNSS receivers for GNSS antenna calibration. SDR GNSS receivers allow to investigate dynamical stress errors and multipath on the receiver tracking loop level. This is the key for an efficient quantification and mitigation of multipath.

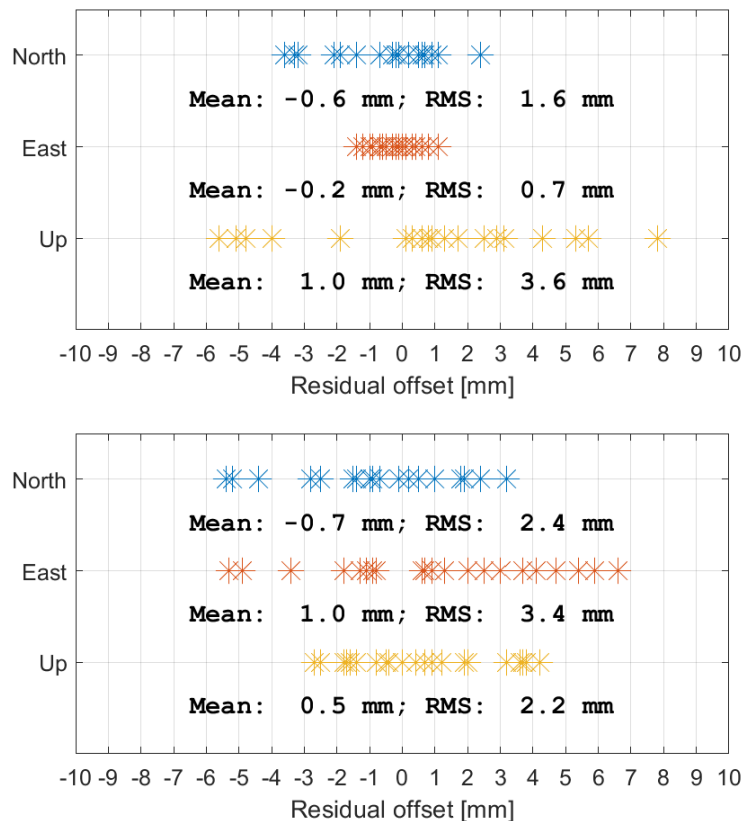


Figure 6.9.3 : Coordinate residuals of all baseline used within the short baseline validation. The relative coordinates were estimated using Galileo E5 only. The upper plot shows the results obtained using the ETH Zurich patterns, the lower plot shows the results using Geo++[®] individual calibrations (two antennas) and IGS type-mean calibrations (two antennas).

Chapter 7

Conclusions and outlook

This doctoral thesis started with the study of the attitude onboard a spacecraft with baselines of less than 10 cm. In a first step, the synchronisation of the receivers on a software level was investigated. The result is an algorithm for the extrapolation of the measurements, which was published in *GPS Solutions* (Willi and Rothacher, 2017). The algorithm was validated with a synthetic data study and a signal simulator study.

The insights from the first studies led to further investigations on the Phase Centre Corrections (PCC) of antennas in the vicinity of each other. A relative field calibration was set up. It allowed to calibrate a model of the CubETH satellite and a GNSS attitude determination platform with low-cost geodetic antennas at 15 cm distance from each other. The final results were published in the *ION GNSS proceedings 2017* (Willi et al., 2017) and in *Navigation* (Willi et al., 2018b). They included a synthetic data study and a validation with real data. We showed that the correction of the PCC is of tremendous importance on short baselines. Furthermore, we demonstrated that mutual coupling affects antennas and that this effect must be taken into account when performing PCC estimation.

Although the relative field calibration was suited to calibrate the GNSS attitude determination system, it has fundamental weaknesses. The delay in the CubETH project triggered a reorientation of the present doctoral thesis. The main focus was moved away from GNSS attitude determination, towards absolute GNSS antenna calibration. Within a short time, an operational, absolute field calibration system for GNSS antennas was developed from scratch. This includes the commissioning and the calibration of the industrial KUKA robot, which is documented in Willi and Guillaume (2019).

Preliminary results obtained with the new calibration system were presented at the *ION GNSS+ 2018* (Willi et al., 2018a). The system obtained the attention of the international community at the *IGS Workshop 2018* in Wuhan, China, as being the first absolute field calibration system able to produce calibrations for the new Galileo signals.

The need for high-accuracy, multi-GNSS antenna calibration is going to increase in the future. Properly calibrated antennas are a central element of permanent station networks. The full

strength of a multi-GNSS processing can only be exploited, if multi-GNSS antenna calibrations are available for ground antennas. Eventually, calibrated GNSS antennas will help to better quantify and assess socially relevant changes in the environment, as sea level rise.

The need for calibrated low-cost antennas might rapidly increase as well. The 21st century is already marked by the automation of transportation. Autonomous cars are the most prominent example. GNSS will be one of the technologies used for the positioning of autonomous vehicles. Due to significant advances in kinematic positioning, Phase Centre Corrections (PCC) of GNSS antennas already tend to become the limiting factor in low-cost GNSS positioning.

Finally, well-calibrated antennas might be a key to further advances in Precise Point Positioning (PPP). A remarkable progress was achieved in the convergence time of PPP and in PPP ambiguity resolution. PPP will sooner or later run into limitations due to the PCC of the receiver antenna. Here again, precise multi-GNSS and multi-frequency calibrations will help to reach the accuracy, which is inherent to PPP.

Bibliography

REMARK: if not stated otherwise, the links in the bibliography were checked on 12 December 2018.

Aghili F and Salerno A (2013) Driftless 3-D Attitude Determination and Positioning of Mobile Robots By Integration of IMU With Two RTK GPSs. *IEEE/ASME Transactions on Mechatronics*, 18(1):21–31. URL <https://doi.org/10.1109/TMECH.2011.2161485>.

Allman M, Novotny D and Gordon J (2018) Calibration of a 6-Axis Serial Robotic Arm Mounted to a Moveable Base at the National Institute of Standards and Technology. In *Proceedings of the 35th Annual Coordinate Metrology Society Conference 2018*, p. 12. Orlando, FL, USA.

Altamimi Z and Collilieux X (2009) IGS contribution to the ITRF. *Journal of Geodesy*, 83(3-4):375–383. URL <https://doi.org/10.1007/s00190-008-0294-x>.

Arbinger C and Enderle W (2000) Spacecraft Attitude Determination using a Combination of GPS Attitude Sensor and Star Sensor Measurements. In *Proceedings of the 13th International Technical Meeting of the Satellite Division of The Institute of Navigation (ION GPS 2000)*, pp. 2634–2642. Salt Lake City, UT, USA. URL <https://www.ion.org/publications/abstract.cfm?articleID=1692>.

Bilich A and Mader GL (2010) GNSS absolute antenna calibration at the national geodetic survey. In *Proceedings of the 23rd International Technical Meeting of The Satellite Division of the Institute of Navigation (ION GNSS 2010)*, pp. 1369–1377. Portland, OR, USA. URL <https://www.ion.org/publications/abstract.cfm?articleID=9251>.

Bilich A, Schmitz M, Görres B, Zeimetz P, Mader G and Wübbena G (2012) Three-method absolute antenna calibration comparison (oral presentation). In *IGS Workshop 2012*. Olsztyn, Poland. URL <http://www.igs.org/assets/video/Poland%202012%20-%20P09%20Bilich%20PR59.mp4>.

Bilich A, Erickson B and Geoghegan C (2018) 6-axis robot for absolute antenna calibration at the US National Geodetic Survey (poster). In *IGS Workshop 2018*. Wuhan, Hubei, China.

- Braasch MS (2017) Multipath. In Teunissen PJG and Montenbruck O (eds.) *Springer Handbook of Global Navigation Satellite Systems*, pp. 443–468. Springer International Publishing, Cham, Germany. ISBN 978-3-319-42928-1. URL https://doi.org/10.1007/978-3-319-42928-1_15.
- Brandstötter M, Angerer A and Hofbaur M (2014) An analytical solution of the inverse kinematics problem of industrial serial manipulators with an ortho-parallel basis and a spherical wrist (Revised Version). In *Proceedings of the Austrian Robotics Workshop 2014*, pp. 7–11. Linz, Austria.
- Cannon ME and Sun H (1996) Experimental assessment of a non-dedicated GPS receiver system for airborne attitude determination. *ISPRS Journal of Photogrammetry and Remote Sensing*, 51(2):99–108. URL [https://doi.org/10.1016/0924-2716\(96\)00011-6](https://doi.org/10.1016/0924-2716(96)00011-6).
- Chen W and Qin H (2012) New method for single epoch, single frequency land vehicle attitude determination using low-end GPS receiver. *GPS Solutions*, 16(3):329–338. URL <https://doi.org/10.1007/s10291-011-0234-8>.
- Cohen CE (1992) *Attitude Determination Using GPS, Development of an All Solid-State Guidance, Navigation, and Control Sensor for Air and Space Vehicles Based on the Global Positioning System*. Doctoral Thesis, Stanford University, Stanford, CA, USA. URL <https://web.stanford.edu/group/scpnt/gpslab/pubs/theses/ClarkCohenThesis92.pdf>.
- Cohen CE, Lightsey EG, Parkinson BW and Feess WA (1994) Space flight tests of attitude determination using GPS. *International Journal of Satellite Communications*, 12(5):427–433. URL <https://doi.org/10.1002/sat.4600120504>.
- Corke P (2017) Robot Arm Kinematics. In *Robotics, Vision and Control*, vol. 118 of *Springer Tracts in Advanced Robotics*, pp. 193–228. Springer International Publishing, Cham. ISBN 978-3-319-54413-7. URL https://doi.org/10.1007/978-3-319-54413-7_7.
- Counselman CC and Shapiro II (1979) Miniature interferometer terminals for earth surveying. *Bulletin Géodésique*, 53(2):139–163. URL <https://doi.org/10.1007/BF02521086>.
- Dach R, Lutz S, Walser P and Fridez P (eds.) (2015) *Bernese GNSS Software Version 5.2*. Astronomical Institute, University of Bern, Bern, Switzerland. URL <https://doi.org/10.7892/boris.72297>.
- Diebel J (2006) Representing attitude: Euler angles, unit quaternions, and rotation vectors. *Tech. rep.*, Stanford University, Stanford, CA, USA.
- Dilßner F (2008) *Zum Einfluss des Antennenumfeldes auf die hochpräzise GNSS-Positionsbestimmung*. Doctoral Thesis, Leibniz University Hanover, Hanover,

- Germany. URL <https://www.tib.eu/de/suchen/id/TIBKAT%3A583144810/Zum-Einfluss-des-Antennenfeldes-auf-die-hochpr%C3%A4zise/>.
- European GNSS Service Centre (2018) Galileo Satellite Metadata | European GNSS Service Centre (webpage). URL <https://www.gsc-europa.eu/support-to-developers/galileo-satellite-metadata>.
- Farrell JL, Stuelpnagel JC, Wessner RH, Velman JR and Brook JE (1966) A least squares estimate of satellite attitude (Grace Wahba). *Siam Review*, 8(3):384–386. URL <https://doi.org/10.1137/1008080>.
- Geiger A (1988) Modeling of Phase Center Variation and its Influence on GPS-Positioning. In Groten E and Strauss R (eds.) *GPS-Techniques Applied to Geodesy and Surveying*, pp. 210–222. Springer Berlin Heidelberg, Berlin, Heidelberg. ISBN 978-3-540-45962-0. URL <https://doi.org/10.1007/BFb0011339>.
- Geiger A (1990) Influence of Phase Center Variations on the Combination of different Antenna Types. In *Proceedings of the Second International Symposium on Precise Positioning with the Global Positioning System*, pp. 466–476. The Canadian Institute of Surveying and Mapping, Ottawa, Canada. ISBN 0-919088-40-6.
- Giorgi G (2017) Attitude Determination. In Teunissen PJG and Montenbruck O (eds.) *Springer Handbook of Global Navigation Satellite Systems*, pp. 781–809. Springer International Publishing, Cham, Germany. ISBN 978-3-319-42928-1. URL https://doi.org/10.1007/978-3-319-42928-1_27.
- Giorgi G, Teunissen PJG and Gourlay TP (2012) Instantaneous Global Navigation Satellite System (GNSS)-Based Attitude Determination for Maritime Applications. *IEEE Journal of Oceanic Engineering*, 37(3):348–362. URL <https://doi.org/10.1109/JOE.2012.2191996>.
- Görres B, Campbell J, Becker M and Siemes M (2006) Absolute calibration of GPS antennas: laboratory results and comparison with field and robot techniques. *GPS Solutions*, 10(2):136–145. URL <https://doi.org/10.1007/s10291-005-0015-3>.
- Görres B, Kersten T, Schön S, Zimmermann F and Wanninger L (2018) Berücksichtigung von Antennenkorrekturen bei GNSS-Anwendungen. *DVW-Merkblatt 1-2018*, Gesellschaft für Geodäsie, Geoinformation und Landmanagement e.V., Bühlertal, Germany. URL https://www.dvw.de/sites/default/files/news_termine/dateianhang/2018/01_DVW-Merkblatt_Antennenkorrekturen-GNSS_2018.pdf.
- Häberling S (2015) *Theoretical and practical aspects of high-rate GNSS geodetic observations*. Doctoral Thesis, ETH Zurich, Zurich, Switzerland. URL <https://doi.org/10.3929/ethz-a-010592866>.

- Hauschild A (2017a) Basic Observation Equations. In Teunissen PJG and Montenbruck O (eds.) *Springer Handbook of Global Navigation Satellite Systems*, pp. 561–582. Springer International Publishing, Cham, Germany. ISBN 978-3-319-42928-1. URL https://doi.org/10.1007/978-3-319-42928-1_19.
- Hauschild A (2017b) Combinations of Observations. In Teunissen PJG and Montenbruck O (eds.) *Springer Handbook of Global Navigation Satellite Systems*, pp. 583–604. Springer International Publishing, Cham, Germany. ISBN 978-3-319-42928-1. URL https://doi.org/10.1007/978-3-319-42928-1_20.
- Hollenstein C, Männel B, Serantoni E, Scherer L, Rothacher M, Kehl P and Ivanov A (2014) Concepts and Testing of Low-cost GNSS Receivers for CubeSat Orbit and Attitude Determination. In *Proceedings of the 7th European Navigation Conference (navitec 2014)*. Noordwijk, Netherlands.
- Hollerbach J, Khalil W and Gautier M (2016) Model Identification. In Siciliano B and Khatib O (eds.) *Springer Handbook of Robotics*, pp. 113–138. Springer International Publishing, Cham. ISBN 978-3-319-32552-1. URL https://doi.org/10.1007/978-3-319-32552-1_6.
- Hu Z, Zhao Q, Chen G, Wang G, Dai Z and Li T (2015) First Results of Field Absolute Calibration of the GPS Receiver Antenna at Wuhan University. *Sensors*, 15(11):28717–28731. URL <https://doi.org/10.3390/s151128717>.
- IS-GPS-200 (2015) Global Positioning Systems Directorate, Systems Engineering & Integration Interface Specification IS-GPS-200. *Tech. rep.*, Global Positioning Systems Directorate, United States Air Force, USA. URL https://www.gps.gov/technical/icwg/IRN-IS-200H-001+002+003_rollup.pdf.
- Jekeli C (2001) Coordinate Frames and Transformations. In *Inertial Navigation Systems with Geodetic Applications*. Walter de Gruyter, Berlin, Germany. ISBN 978-3-11-080023-4. URL <https://doi.org/10.1515/9783110800234.1>.
- Kallio U, Koivula H, Lahtinen S, Nikkonen V and Poutanen M (2018) Validating and comparing GNSS antenna calibrations. *Journal of Geodesy*. URL <https://doi.org/10.1007/s00190-018-1134-2>.
- Kaplan ED and Hegarty C (eds.) (2017) *Understanding GPS/GNSS: principles and applications*. GNSS Technology and Applications Series. Artech House, Boston, MA, USA, third edn. ISBN 978-1-63081-058-0.
- Kersten T (2014) *Bestimmung von Codephasen-Variationen bei GNSS-Empfangsantennen und deren Einfluss auf Positionierung, Navigation und Zeitübertragung*. Doctoral Thesis, Leibniz University Hanover, Hanover, Germany. URL <https://doi.org/10.15488/4003>.

- Kim D and Langley RB (2007) GPS RTK-based attitude determination for the e-POP platform onboard the Canadian CASSIOPE spacecraft in low earth orbit. In *Time Nav'07 (ENC GNSS 2007)*. Geneva, Switzerland.
- Kuka (2018) KUKA KR AGILUS sixx Specification. *Tech. rep.*, KUKA Deutschland GmbH, Augsburg, Germany.
- Maqsood M, Gao S and Montenbruck O (2017) Antennas. In Teunissen PJG and Montenbruck O (eds.) *Springer Handbook of Global Navigation Satellite Systems*, pp. 505–534. Springer International Publishing, Cham, Germany. ISBN 978-3-319-42928-1. URL https://doi.org/10.1007/978-3-319-42928-1_17.
- Menge F (2003) *Zur Kalibrierung der Phasenzentrumsvariationen von GPS Antennen für die hochpräzise Positionsbestimmung*. Doctoral Thesis, Leibniz University Hanover, Hanover, Germany. URL <https://www.tib.eu/de/suchen/id/TIBKAT%3A381885593/Zur-Kalibrierung-der-Phasenzentrumsvariationen/>.
- Motta J (2006) Robot Calibration: Modeling Measurement and Applications. In Kin-Huat L (ed.) *Industrial Robotics: Programming, Simulation and Applications*. IntechOpen Limited, London, UK. ISBN 3-86611-286-6. URL <https://doi.org/10.5772/4894>.
- Nadarajah N, Teunissen PJG and Buist PJ (2012) Attitude determination of LEO satellites using an array of GNSS sensors. In *15th International Conference on Information Fusion*, pp. 1066–1072. IEEE, Singapore, Singapore. ISBN 978-0-9824438-4-2. URL http://ieeexplore.ieee.org/xpls/abs_all.jsp?arnumber=6289927.
- Nubiola A and Bonev IA (2013) Absolute calibration of an ABB IRB 1600 robot using a laser tracker. *Robotics and Computer-Integrated Manufacturing*, 29(1):236–245. URL <https://doi.org/10.1016/j.rcim.2012.06.004>.
- Park C and Teunissen PJG (2003) A new carrier phase ambiguity estimation for GNSS attitude determination systems. In *Proceedings of international GPS/GNSS symposium*. Tokyo, Japan. URL <https://gnss.curtin.edu.au/wp-content/uploads/sites/21/2016/04/Park2003new.pdf>.
- Petit G and Luzum B (eds.) (2010) *IERS Conventions*, vol. 36 of *IERS Technical Note*. Verlag des Bundesamts für Kartographie und Geodäsie, Frankfurt am Main, Germany. URL <http://www.iers.org/TN36>.
- Prange L, Orliac E, Dach R, Arnold D, Beutler G, Schaer S and Jäggi A (2017) CODE's five-system orbit and clock solution—the challenges of multi-GNSS data analysis. *Journal of Geodesy*, 91(4):345–360. URL <https://doi.org/10.1007/s00190-016-0968-8>.

BIBLIOGRAPHY

- Rao BR, Kunysz W, Fante R and McDonald K (2013) *GPS/GNSS antennas*. GNSS technology and applications series. Artech House, Boston, MA, USA. ISBN 978-1-59693-150-3.
- Riddell A, Moore M and Hu G (2015) Geoscience Australia's GNSS antenna calibration facility: Initial results. In *Proceedings of IGNSS Symposium 2015 (IGNSS2015)*. Surfers Paradise, QLD, Australia.
- RINEX Working Group and RTCM-SC104 (2015) RINEX, The Receiver Independent Exchange Format, Version 3.03. *Tech. rep.*, International GNSS Service (IGS) and Radio Technical Commission for Maritime Services Special Committee 104 (RTCM-SC104), Pasadena, CA, USA. URL <ftp://igs.org/pub/data/format/rinex303.pdf>.
- Rothacher M (2001) Comparison of absolute and relative antenna phase center variations. *GPS solutions*, 4(4):55–60. URL <https://doi.org/10.1007/PL00012867>.
- Rothacher M and Schmid R (2010) ANTEX: The antenna exchange format version 1.4. *Tech. rep.*, International GNSS Service, Pasadena, CA, USA. URL <ftp://igs.org/pub/station/general/antex14.txt>.
- Rothacher M, Schaer S, Mervart L and Beutler G (1995) Determination of antenna phase center variations using GPS data. In Gendt G and Dick G (eds.) *Special Topics and New Directions, Workshop Proceedings. IGS Workshop*, pp. 205–220. Potsdam, Germany.
- Sabatini R, Rodríguez L, Kaharkar A, Bartel C and Shaid T (2012) Carrier-phase GNSS attitude determination and control system for unmanned aerial vehicle applications. *ARPJ Journal of Systems and Software*, 2(11):297–322. ISSN 2222-9833.
- Schmitz M, Wübbena G and Boettcher G (2002) Tests of phase center variations of various GPS antennas, and some results. *GPS Solutions*, 6(1-2):18–27. URL <https://doi.org/10.1007/s10291-002-0008-4>.
- Schröer K (1999) Precision and Calibration. In Nof SY (ed.) *Handbook of Industrial Robotics*, pp. 795–810. John Wiley & Sons, Inc., Hoboken, NJ, USA. ISBN 978-0-470-17250-6. URL <https://doi.org/10.1002/9780470172506.ch39>.
- Schröer K, Albright SL and Grethlein M (1997) Complete, minimal and model-continuous kinematic models for robot calibration. *Robotics and Computer-Integrated Manufacturing*, 13(1):73–85. URL [https://doi.org/10.1016/S0736-5845\(96\)00025-7](https://doi.org/10.1016/S0736-5845(96)00025-7).
- Schupler BR, Allshouse RL and Clark TA (1994) Signal characteristics of GPS user antennas. *Navigation*, 41(3):276–296. URL <https://doi.org/10.1002/j.2161-4296.1994.tb01881.x>.
- Sims ML (1985) Phase center variation in the geodetic TI4100 GPS receiver system's conical spiral antenna. In *Proceedings of the first International Symposium on Precise Positioning with the Global Positioning System*, pp. 227–244. Rockville, MD, US.

- Teunissen PJG (1995) The least-squares ambiguity decorrelation adjustment: a method for fast GPS integer ambiguity estimation. *Journal of Geodesy*, 70(1-2):65–82. URL <https://doi.org/10.1007/BF00863419>.
- Teunissen PJG (2010) Integer least-squares theory for the GNSS compass. *Journal of Geodesy*, 84(7):433–447. URL <https://doi.org/10.1007/s00190-010-0380-8>.
- Teunissen PJG (2017) Carrier Phase Integer Ambiguity Resolution. In Teunissen PJG and Montenbruck O (eds.) *Springer Handbook of Global Navigation Satellite Systems*, pp. 661–685. Springer International Publishing, Cham, Germany. ISBN 978-3-319-42928-1. URL https://doi.org/10.1007/978-3-319-42928-1_23.
- Teunissen PJG and Montenbruck O (eds.) (2017) *Springer Handbook of Global Navigation Satellite Systems*. Springer International Publishing, Cham, Germany. ISBN 978-3-319-42928-1. URL <https://doi.org/10.1007/978-3-319-42928-1>.
- Teunissen PJG, Giorgi G and Buist PJ (2011) Testing of a new single-frequency GNSS carrier phase attitude determination method: land, ship and aircraft experiments. *GPS Solutions*, 15(1):15–28. URL <https://doi.org/10.1007/s10291-010-0164-x>.
- Tranquilla JM and Colpitts BG (1989) GPS Antenna Design Characteristics for High-Precision Applications. *Journal of Surveying Engineering*, 115(1):2–14. URL [https://doi.org/10.1061/\(ASCE\)0733-9453\(1989\)115:1\(2\)](https://doi.org/10.1061/(ASCE)0733-9453(1989)115:1(2)).
- u-blox (2014) u-blox M8 Receiver Description. *Tech. rep.*, u-blox AG, Thalwil, Switzerland.
- Um J and Lightsey EG (2001) GPS Attitude Determination for the SOAR Experiment. *Navigation*, 48(3):180–194. URL <https://doi.org/10.1002/j.2161-4296.2001.tb00241.x>.
- Van Graas F and Braasch M (1991) GPS Interferometric Attitude and Heading Determination: Initial Flight Test Results. *Navigation*, 38(4):297–316. URL <https://doi.org/10.1002/j.2161-4296.1991.tb01864.x>.
- Welch G and Bishop G (2006) An Introduction to the Kalman Filter. 2006. *Tech. rep.*, University of North Carolina, Chapel Hill, NC, USA.
- Willi D and Guillaume S (2019) Calibration of a Six-Axis Robot for GNSS Antenna Phase Center Estimation. *Journal of Surveying Engineering*. ISSN 1943-5428. In review.
- Willi D and Rothacher M (2017) GNSS attitude determination with non-synchronized receivers and short baselines onboard a spacecraft. *GPS Solutions*, 21(4):1605–1617. URL <https://doi.org/10.1007/s10291-017-0639-0>.
- Willi D, Meindl M, Xu H and Rothacher M (2017) GNSS Antenna Phase Center Variation Calibration for Attitude Determination on Short Baselines. In *30th International Technical*

- Meeting of The Satellite Division of the Institute of Navigation (ION GNSS+ 2017)*, pp. 3997–4010. Portland, OR, USA. URL <https://www.ion.org/publications/abstract.cfm?articleID=15411>.
- Willi D, Koch D, Meindl M and Rothacher M (2018a) Absolute GNSS Antenna Phase Center Calibration with a Robot. In *Proceedings of the 31st International Technical Meeting of The Satellite Division of the Institute of Navigation (ION GNSS+ 2018)*, pp. 3909 – 3926. Miami, FL, USA. URL <https://www.ion.org/publications/abstract.cfm?articleID=16040>.
- Willi D, Meindl M, Xu H and Rothacher M (2018b) GNSS Antenna Phase Center Variation Calibration for Attitude Determination on Short Baselines. *Navigation*. URL <https://doi.org/10.1002/navi.273>.
- Wu J, Wu S, Hajj G, Bertiger W and Lichten S (1993) Effects of antenna orientation on GPS carrier phase. *Manuscripta geodetica*, 18:91–98.
- Wübbena G, Schmitz M, Menge F, Seeber G and Völksen C (1997) A New Approach for Field Calibration of Absolute GPS Antenna Phase Center Variations. *Navigation*, 44(2):247–255. URL <https://doi.org/10.1002/j.2161-4296.1997.tb02346.x>.
- Wübbena G, Schmitz M, Menge F, Böder V and Seeber G (2000) Automated absolute field calibration of GPS antennas in real-time. In *Proceedings of the 13th International Technical Meeting of the Satellite Division of The Institute of Navigation (ION GPS 2000)*, pp. 2512–2522. Salt Lake City, UT, USA. URL <https://www.ion.org/publications/abstract.cfm?articleID=1675>.
- Wübbena G, Schmitz M and Boettcher G (2003) Analyse umfangreicher Messreihen von GPS Antennen PCV aus absoluten Roboter-Feldkalibrierungen seit Januar 2000 (oral presentation). In *5th GPS Antenna Workshop*. Frankfurt am Main, Germany.
- Wübbena G, Schmitz M, Boettcher G and Schumann C (2006) Absolute GNSS antenna calibration with a robot: repeatability of phase variations, calibration of GLONASS and determination of carrier-to-noise pattern (oral presentation). In Springer T, Gendt G and Dow J (eds.) *The International GNSS Service (IGS): Perspectives and Visions for 2010 and Beyond. Proceedings of the IGS Workshop 2006*. Darmstadt, Germany. URL ftp://igs.org/pub/resource/pubs/06_darmstadt/IGS%20Presentations%20PDF/10_1_Schmitz.pdf.
- Zeimetz P (2010) *Zur Entwicklung und Bewertung der absoluten GNSS-Antennenkalibrierung im HF-Labor*. Doctoral Thesis, University Bonn, Bonn, Germany. URL <hss.ulb.uni-bonn.de/2010/2212/2212.pdf>.
- Zeimetz P and Kuhlmann H (2008) On the accuracy of absolute GNSS antenna calibration and the conception of a new anechoic chamber. In *Proceedings of the FIG Working*

Week 2008. Stockholm, Sweden. URL http://fig.net/resources/proceedings/fig_proceedings/fig2008/papers/ts05g/ts05g_01_zeimetz_kuhlmann_2901.pdf.

Zhang J, Zhang K, Grenfell R and Deakin R (2006) GPS Satellite Velocity and Acceleration Determination using the Broadcast Ephemeris. *Journal of Navigation*, 59(02):293. URL <https://doi.org/10.1017/S0373463306003638>.

Ziebart M and Cross P (2003) LEO GPS attitude determination algorithm for a micro-satellite using boom-arm deployed antennas. *GPS Solutions*, 6(4):242–256. URL <https://doi.org/10.1007/s10291-002-0023-5>.

Appendix A

Paper I

Title	GNSS Attitude Determination with Non-Synchronized Receivers and Short Baselines Onboard a Spacecraft
Authors	Daniel WILLI, Markus ROTHACHER
Journal	GPS Solutions
DOI	10.1007/s10291-017-0639-0
Received	13 December 2016
Accepted	08 May 2017
First Online	18 May 2017

Printed with permission from Springer Nature (license number 4466520432841).

GNSS attitude determination with non-synchronized receivers and short baselines onboard a spacecraft

Daniel Willi, Markus Rothacher
daniel.willi@geod.baug.ethz.ch
markus.rothacher@geod.baug.ethz.ch
ETH Zurich
Institute of Geodesy and Photogrammetry
Robert-Gnehm-Weg 15
8093 Zürich
Switzerland

Abstract A new algorithm for Global Navigation Satellite System (GNSS) attitude determination onboard a spacecraft was developed. A distinct feature of the algorithm is the extrapolation of the measurements to a common epoch within a Kalman filter. The necessity for the extrapolation arises from the usage of non-synchronized low-cost receivers. The extrapolation terms typically range from -6 m to $+6$ m for u-blox receivers. Thus, no solution can be obtained without a proper extrapolation. A validation was carried out with synthetic data as well as with signal simulator data. The algorithm delivers an attitude estimation with an accuracy below one degree for three orthogonal baselines of 10 cm length. In conclusion, the algorithm is proven to work, offering a very efficient method of attitude determination onboard a spacecraft.

Keywords

Attitude determination, quaternion, Kalman filter, low earth orbit, spacecraft, satellite

Introduction

The knowledge of the orbit and the attitude of a spacecraft is crucial to many applications, such as telecommunication or remote sensing. The utilization of Global Positioning System (GPS) receivers onboard spacecraft started in 1982 with the launch of the Landsat-4 satellite (Birmingham et al. 1983). Since then, many missions used Global Navigation Satellite Systems (GNSS), establishing this approach as one of the standard techniques for orbit determination. If three or more GNSS antennas are placed on a spacecraft, forming at least two baselines, attitude determination becomes possible. A few missions already used GNSS for attitude determination, such as RADCAL in 1993 (Cohen et al. 1994) or the SOAR experiment on the Space Shuttle Atlantis (Um and Lightsey 2001). Although having some appreciable advantages, such as being free from drift and being autonomous, employment of GNSS attitude determination is limited by the size, mass and power consumption of the receivers as well by its modest accuracy compared to other sensors used on spacecraft (Arbinger and Enderle 2000). Besides space applications, GNSS attitude determination is widely studied and used, often in combination with inertial sensors, namely for terrestrial applications (Chen and

Qin 2012, Aghili and Salerno 2013), on ships (Giorgi et al. 2012), onboard aircrafts (Graas and Braasch 1991, Cannon and Sun 1996) or for unmanned aerial vehicles (Sabatini et al. 2012).

Recently, a trend towards small satellites and miniaturization of components can be observed (Montenbruck et al. 2008). The satellite project CubETH (Ivanov et al. 2015) reflects this evolution. CubETH will fly in a low earth orbit (LEO) between 400 km and 500 km height with a speed of approximately 8 km/s. The single unit CubeSat is of $10 \times 10 \times 10 \text{ cm}^3$ size (CubeSat Design Specification 2015) and equipped with five GNSS antennas (Figure 1), each connected to two u-blox GNSS receivers. Hence, the spacecraft is equipped with ten u-blox receivers. Four antennas are located on the zenith-pointing face of the cube, forming two orthogonal baselines of 5.6 cm and 6.5 cm and a diagonal baseline of 8.6 cm length. The fifth antenna is side-looking and serves experimental purposes, as the study of the decay in signal strength of low elevation satellites. This set-up allows the determination of the attitude. The main difference to past missions lies in the highly non-synchronized receivers used. The measurements of each receiver are triggered by the 1 kHz signal of its internal oscillator (u-blox M8 Receiver Description 2016), leading to an actual measurement epoch within a time window of approximately 1 ms around nominal GPS time. Therefore, an extrapolation procedure for observations was developed. Without extrapolation, no solution can be obtained, as the corrections typically range from -6 m to $+6 \text{ m}$ for u-blox receivers.

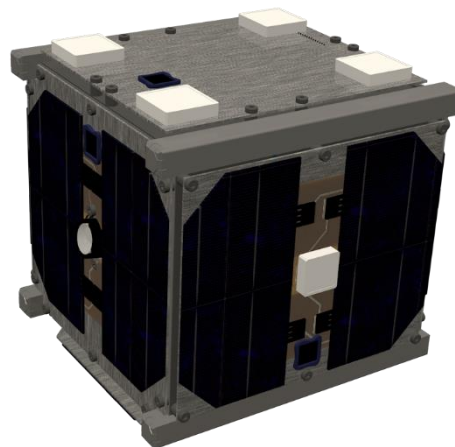


Fig. 1 Model of the Swiss nano-satellite CubETH. The spacecraft measures $10 \times 10 \times 10 \text{ cm}^3$. The four white patches on the upper face are the main GNSS antennas. The white patch on the side is the experimental side-looking antenna.

In the first part, we describe in detail the algorithm for onboard real-time attitude determination. In the second part, two distinct validation cases are shown. The results were obtained with synthetic data in the first case and with signal simulator data in the second case. Synthetic data was generated with the Bernese GNSS Software (Dach et al. 2015). Signal simulator data was obtained using a Spirent GNSS Signal Generator with two radio-frequency outputs and space-enabled u-blox M8 receivers. Both, the synthetic and the simulator data set were post-processed with a prototype of the attitude determination algorithm and compared to a ground truth.

Attitude determination algorithm

The first part of this section is a brief introduction to the principle of GNSS attitude determination. It is followed by a summary of the Kalman filter equations and a description of the attitude filter algorithm. This description includes details on the state vector, the dynamical model, the observation equation and the stochastic model.

Principle of attitude determination

GNSS attitude determination is based on the interferometric principle shown in Figure 2. A range difference r involving two receivers and a GNSS satellite can be expressed as the projection of the baseline vector \mathbf{b} onto the normalized line-of-sight (LOS) vector \mathbf{e} :

$$r = \mathbf{e}_{\text{world}}^T \mathbf{R}_{\text{world} \leftarrow \text{body}} \mathbf{b}_{\text{body}} + v \quad (1)$$

The baseline vector \mathbf{b} is expressed in the spacecraft body frame and the LOS vector \mathbf{e} in a world frame, e.g. the inertial frame. The rotation matrix $\mathbf{R}_{\text{world} \leftarrow \text{body}} \in \text{SO}(3)$, relating these two coordinate systems to each other, is an orthogonal matrix, thus $\mathbf{R}^T \mathbf{R} = \mathbf{I}$. v is the measurement noise and follows a normal distribution with zero mean and standard deviation σ . For the sake of simplicity, the subscripts indicating the reference frame are omitted in all further developments. The optimal attitude is obtained after minimization of:

$$L(\mathbf{R}) = \sum_k \sum_i \frac{1}{\sigma^2} \left(r_{ki} - (\mathbf{e}^i)^T \mathbf{R} \mathbf{b}_k \right)^2 \quad (2)$$

where L is the cost function, k is the index of the baseline and i is the GNSS satellite index. The minimization of (2) is often also referred to as Wahba's problem (Farrell et al. 1966). Besides the classical iterative least-squares solution, a number of analytical solutions to this problem exist, see for instance Cohen (1992) or Crassidis and Markley (1997).

Attitude determination algorithm

The attitude is estimated within an extended Kalman filter. The processing sequence is shown in Figure 3. The initialization consists of solving phase ambiguities and baseline coordinates. Using the baseline coordinates, an initial value for the attitude is computed. An additional ambiguity resolution is necessary to solve phase ambiguities which were not present in the last filter update, e.g. due to a new satellite becoming visible. Since the attitude is known at this point and for short baselines, this step is trivial. The Kalman filter (Welch and Bishop 2006) consists of a prediction part, the so-called time update, and a correction part, the measurement update. For the sake of completeness, the following paragraphs briefly summarize the main filter equations.

A process function f links two temporally successive, true state vectors x_s and x_{s-1} :

$$\begin{aligned} x_s &= f(x_{s-1}) + u_{s-1} \\ u_{s-1} &\sim N(0, U_{s-1}) \end{aligned} \quad (3)$$

where u_{s-1} is the normally distributed process noise with zero mean and variance-covariance U_{s-1} . A similar relation holds for the observations:

$$\begin{aligned} z_s &= h(x_s) + v_s \\ v_s &\sim N(0, V_s) \end{aligned} \quad (4)$$

where z_s is the observation vector at time-step s , h is the observation function and x_s is the true state. v_s is the normally distributed measurement noise with zero mean and variance-covariance V_s .

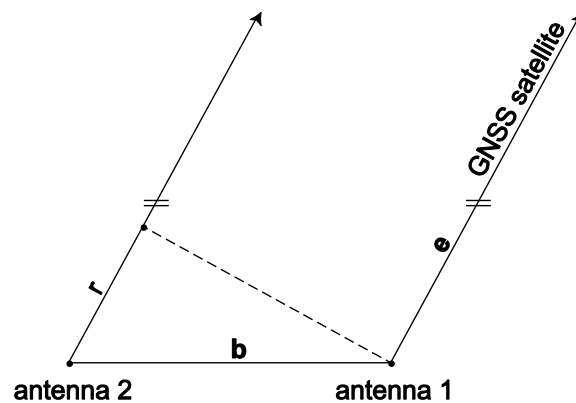


Fig. 2 Principle of interferometric attitude determination. r is a range difference between antenna 1 and 2 and b is the baseline between those two antennas. For very short baselines, the two line-of-sight vectors to one GNSS satellite can be assumed to be parallel.

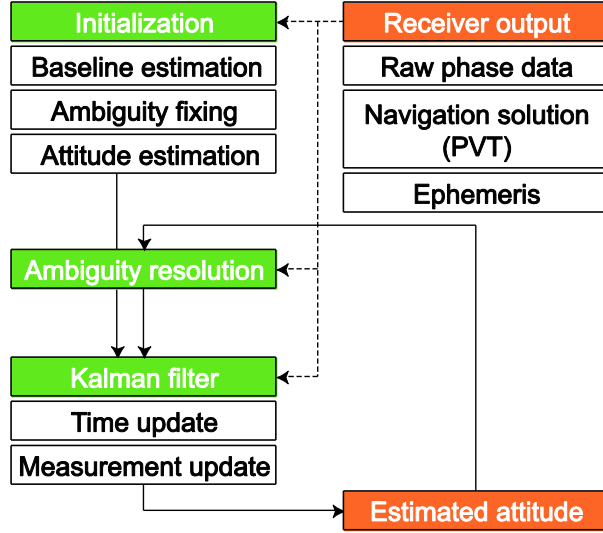


Fig. 3 Attitude determination flow chart. The algorithm is autonomous and, besides the phase data, relies only on the receiver position, velocity and time (PVT) output and the ephemeris. The core of the algorithm is an extended Kalman filter, running on double-difference level.

The filter time update is given by:

$$\hat{\mathbf{x}}_s^- = \mathbf{f}(\hat{\mathbf{x}}_{s-1}) \quad (5)$$

$$\mathbf{P}_s^- = \mathbf{A}_{s-1} \mathbf{P}_{s-1} \mathbf{A}_{s-1}^T + \mathbf{U}_{s-1} \quad (6)$$

where $\hat{\mathbf{x}}_s^-$ with variance-covariance \mathbf{P}_s^- is the predicted state at time-step s , and $\hat{\mathbf{x}}_{s-1}$ with variance-covariance \mathbf{P}_{s-1} is the corrected state of the previous step. \mathbf{A}_{s-1} is the Jacobian matrix of \mathbf{f} with respect to \mathbf{x} evaluated at the time-step $s - 1$.

The filter measurement update is given by:

$$\mathbf{K}_s = \mathbf{P}_s^- \mathbf{H}_s^T (\mathbf{H}_s \mathbf{P}_s^- \mathbf{H}_s^T + \mathbf{V}_s)^{-1} \quad (7)$$

$$\hat{\mathbf{x}}_s = \hat{\mathbf{x}}_s^- + \mathbf{K}_s (\mathbf{z}_s - \mathbf{h}(\hat{\mathbf{x}}_s^-)) \quad (8)$$

$$\mathbf{P}_s = (\mathbf{I} - \mathbf{K}_s \mathbf{H}_s) \mathbf{P}_s^- \quad (9)$$

where \mathbf{K}_s is the Kalman gain, and \mathbf{H}_s is the Jacobian matrix of \mathbf{h} with respect to \mathbf{x} evaluated at the time-step s . $\hat{\mathbf{x}}_s$ with variance-covariance \mathbf{P}_s is the estimated state and consequently the result of the algorithm.

State vector

The state vector consists of a quaternion \mathbf{q} representing the attitude and the angular velocity vector $\boldsymbol{\omega}$:

$$\mathbf{x} = \begin{pmatrix} \mathbf{q} \\ \boldsymbol{\omega} \end{pmatrix} \quad (10)$$

Neither phase ambiguities nor clock errors are part of the filter state. The velocity vector and the unit quaternion are defined as follows,

$$\mathbf{q} = (q_0 \quad q_1 \quad q_2 \quad q_3)^T = \begin{pmatrix} \cos\left(\frac{\alpha}{2}\right) \\ \sin\left(\frac{\alpha}{2}\right) \mathbf{n} \end{pmatrix} \quad (11)$$

$$\boldsymbol{\omega} = (\omega_1 \quad \omega_2 \quad \omega_3)^T \quad (12)$$

where α is the rotation angle and \mathbf{n} is the unit vector representing the rotation axis. q_0 is the scalar part of the quaternion. A discussion of the different attitude representations can be found in Diebel (2006). The most widely used attitude representation is based on Euler angles. Euler angles are easy to interpret, e.g. the Euler sequence 1-2-3 which represents roll, pitch and yaw, but are not free of singularities. Unit quaternions are a valid alternative, although no intuitive interpretation of quaternions is possible. The norm of a quaternion reads as:

$$q = \sqrt{q_0^2 + q_1^2 + q_2^2 + q_3^2} \quad (13)$$

Within the algorithm, the quaternion is normalized after the time and the measurement updates, since only quaternions with unity norm represent pure rotations.

Dynamical model

The state is propagated assuming a constant rotation rate. This assumption holds as the cube exhibits a high degree of symmetry. Therefore, the three axes of inertia will have similar values and the spacecraft will be subject to no or negligible precession. Disturbing torques such as air drag are small because of the symmetrical shape of the satellite, and can be neglected. External torques, e.g. steering torques from the satellite's attitude control system, are not included to keep the attitude determination independent from any other satellite subsystem. Moreover, additional parameters in the state generally blur the parameter estimation and seem to lead to good results only with proper force and torque models (Ward and Axelrad 1997). The state propagation (3) is given by:

$$\mathbf{x}_s = \mathbf{x}_{s-1} + (t_s - t_{s-1}) \dot{\mathbf{x}}_{s-1} = \begin{pmatrix} \mathbf{q} \\ \boldsymbol{\omega} \end{pmatrix}_{s-1} + (t_s - t_{s-1}) \begin{pmatrix} \dot{\mathbf{q}} \\ \mathbf{0} \end{pmatrix}_{s-1} = \mathbf{f}(\mathbf{x}_{s-1}) \quad (14)$$

where $\dot{\mathbf{q}}$ is a vector which is composed of the time derivatives of the four quaternion elements and $(t_s - t_{s-1})$ is the time difference between time-step s and $s - 1$. The quaternion derivatives are a function of the quaternion and the angular velocity:

$$\dot{\mathbf{q}}(\mathbf{q}, \boldsymbol{\omega}) = (\dot{q}_0 \quad \dot{q}_1 \quad \dot{q}_2 \quad \dot{q}_3)^T = \frac{1}{2} \mathbf{T}(\mathbf{q})^T \boldsymbol{\omega} \quad (15)$$

$$\mathbf{T}(\mathbf{q}) = \begin{pmatrix} -q_1 & q_0 & -q_3 & q_2 \\ -q_2 & q_3 & q_0 & -q_1 \\ -q_3 & -q_2 & q_1 & q_0 \end{pmatrix} \quad (16)$$

with $\mathbf{T}(\mathbf{q})$ being the quaternion rate matrix. Further details on mathematics with quaternions can be found in Diebel (2006).

Observation equation

Let P be a GNSS carrier phase observation onboard a spacecraft,

$$P_A^i = \mathbf{e}_A^{i\top} (\mathbf{X}^i(t_A - \tau_A) - \mathbf{X}_{\text{LEO}}(t_A) - \mathbf{R}(t_A) \mathbf{X}_A) + c \delta t_A - c \delta t^i + \lambda N_A^i + I_A^i + \Phi_A^i + v_A^i \quad (17)$$

where \mathbf{e}_A^i is the normalized LOS vector, \mathbf{X}^i is the GNSS satellite position in the world frame, t_A is the time of signal reception, τ_A is the signal travel time, \mathbf{X}_{LEO} is the position of the spacecraft in the world frame, \mathbf{R} is the attitude matrix, \mathbf{X}_A is the position of the receiving antenna in the body frame (including the mean phase offset), c is the speed of light, δt_A and δt^i are the receiver and satellite clock errors, λ is the carrier wavelength, N_A^i is the integer phase ambiguity, I_A^i is the ionospheric signal delay, Φ_A^i is the phase center variation (PCV) correction which is a function of the azimuth and the elevation angle of the incoming signal, and v_A^i is the Gaussian white noise affecting the measurements.

The single-difference between receivers reads as:

$$P_{AB}^i = P_A^i - P_B^i = \mathbf{e}_A^{i\top} (\mathbf{X}^i(t_A - \tau_A) - \mathbf{X}_{\text{LEO}}(t_A) - \mathbf{R}(t_A) \mathbf{X}_A) - \mathbf{e}_B^{i\top} (\mathbf{X}^i(t_B - \tau_B) - \mathbf{X}_{\text{LEO}}(t_B) - \mathbf{R}(t_B) \mathbf{X}_B) + c \delta t_{AB} + \lambda N_{AB}^i + I_{AB}^i + \Phi_{AB}^i + v_{AB}^i \quad (18)$$

where δt_{AB} is the single-difference clock error, N_{AB}^i is the single-difference phase ambiguity, I_{AB}^i is the differential ionospheric delay, Φ_{AB}^i is the single-difference PCV correction, and v_{AB}^i is the single-difference noise term.

Since the baseline is very small, the ionospheric delays experienced by both receivers are identical and $I_{AB}^i \approx 0$. Moreover, the two LOS vectors can be assumed to be parallel. Therefore, $\mathbf{e}_A^i = \mathbf{e}_B^i = \mathbf{e}^i$. Since the rotation velocity of the spacecraft is expected to be small, $\mathbf{R}(t_A) = \mathbf{R}(t_B) = \mathbf{R}$ is a valid assumption; an angular velocity of 1 rad/sec would only induce a maximal range error of 0.1 mm, assuming the distance from the center of mass to the antenna is 10 cm. Introducing these simplifications into (18) leads to:

$$P_{AB}^i = \mathbf{e}^{i\top} \mathbf{R} \mathbf{b}_{AB} + E_{AB}^i + c \delta t_{AB} + \lambda N_{AB}^i + \Phi_{AB}^i + v_{AB}^i \quad (19)$$

$$\mathbf{b}_{AB} = \mathbf{X}_B - \mathbf{X}_A \quad (20)$$

$$E_{AB}^i = \mathbf{e}^{i\top} [\mathbf{X}^i(t_A - \tau_A) - \mathbf{X}^i(t_B - \tau_B) - \mathbf{X}_{\text{LEO}}(t_A) + \mathbf{X}_{\text{LEO}}(t_B)] \quad (21)$$

where \mathbf{b}_{AB} is the baseline vector, E_{AB}^i is the extrapolation term, and τ is the signal travel time. The extrapolation term arises because the two receivers measure at the 1 kHz clock tick which is closest to the nominal epoch (u-blox M8 Receiver Description 2016). The extrapolation term typically reaches values between -6 m and $+6$ m for u-blox receivers. Figure 4 shows the values of E_{AB}^i for an example case with a u-blox receiver. From the magnitude of the corrections, it is obvious that no solution can be obtained if this effect is not taken into account. The difference between the two measurement epochs $t_A - t_B$ can reach values up

to 1 ms. In this time interval, a spacecraft in LEO moves by about 8 m. Consequently, $\tau_A^i \neq \tau_B^i$. The position of the LEO spacecraft can be expressed as a second order Taylor series:

$$\mathbf{X}_{\text{LEO}}(t_{\text{nom}} + \Delta t) = \mathbf{X}_{\text{LEO}}(t_{\text{nom}}) + \Delta t \dot{\mathbf{X}}_{\text{LEO}}(t_{\text{nom}}) + \frac{1}{2} \Delta t^2 \ddot{\mathbf{X}}_{\text{LEO}}(t_{\text{nom}}) \quad (22)$$

where t_{nom} is the nominal measurement epoch, $\Delta t = t - t_{\text{nom}}$ is the difference between the nominal and the actual measurement epoch, $\dot{\mathbf{X}}_{\text{LEO}}$ is the velocity of the LEO spacecraft and $\ddot{\mathbf{X}}_{\text{LEO}}$ is its acceleration. $\dot{\mathbf{X}}_{\text{LEO}}$ as well as Δt are delivered by the u-blox receivers as part of the position, velocity and time (PVT) output, which is the result of a Kalman filter process. The velocity accuracy is better than 0.1 m/s (Hollenstein et al. 2014) and the time estimation is typically accurate to 50 ns. The acceleration is approximated with sufficient accuracy by the Kepler term:

$$\ddot{\mathbf{X}}(\mathbf{X}) = -\frac{GM}{X^3} \mathbf{X} \quad (23)$$

where G is the gravitational constant and M is the mass of the earth. The position of a GNSS satellite can be expressed as a second order Taylor series as well:

$$\mathbf{X}^i(t_{\text{nom}} + \Delta t - \tau^i) = \mathbf{X}^i(t_{\text{nom}} - \tau_{\text{nom}}^i + \Delta t - \delta\tau^i) = \mathbf{X}^i(t_{\text{nom}} - \tau_{\text{nom}}^i) + (\Delta t - \delta\tau^i) \dot{\mathbf{X}}^i(t_{\text{nom}} - \tau_{\text{nom}}^i) + \frac{1}{2} (\Delta t - \delta\tau^i)^2 \ddot{\mathbf{X}}^i(t_{\text{nom}} - \tau_{\text{nom}}^i) \quad (24)$$

$$\delta\tau^i = \tau^i - \tau_{\text{nom}}^i = \frac{1}{c} \mathbf{e}^{i\text{T}} \Delta t (\dot{\mathbf{X}}^i - \dot{\mathbf{X}}_{\text{LEO}}) \quad (25)$$

where $\dot{\mathbf{X}}^i$ is the velocity of the GNSS satellite i and $\ddot{\mathbf{X}}^i$ is its acceleration. Compared to (22), an additional term $\delta\tau$ appears in order to account for the change in signal travel time, which is due to the change in range. $\delta\tau$ is approximated by a first order development, as in (25). A first order development is completely sufficient, as the acceleration of a GPS satellite is approximately 0.6 m/s^2 . Neglecting this term leads to errors smaller than a micrometer within a microsecond. Thus, the second order term in (24) is solely relevant for tests with simulated, noise free data. From (25) it is obvious that the change in light travel time δ cannot exceed $4 \cdot 10^{-8} \text{ s}$ in a microsecond, as a GPS satellite travels with approximately 4 km/s and a spacecraft in LEO with approximately 8 km/s.

In the case of GPS, the velocity of the satellites is obtained by taking the time derivative of the user algorithm for the ephemeris computation (Remondi 2004). The acceleration of the satellites is computed with (23). Substitution of (22) and (24) into (21) leads to the final expression for the extrapolation term:

$$E_{AB}^i = \mathbf{e}^{i\text{T}} \left[(\Delta t_A - \delta\tau_A^i - (\Delta t_B - \delta\tau_B^i)) \dot{\mathbf{X}}^i + \frac{1}{2} \left((\Delta t_A - \delta\tau_A^i)^2 - (\Delta t_B - \delta\tau_B^i)^2 \right) \ddot{\mathbf{X}}^i - (\Delta t_A - \Delta t_B) \dot{\mathbf{X}}_{\text{LEO}} - \frac{1}{2} (\Delta t_A^2 - \Delta t_B^2) \ddot{\mathbf{X}}_{\text{LEO}} \right] \quad (26)$$

Literature indicates that estimation procedures based on single-differences lead to better results than procedures based on double-differences (Um and Lightsey 2001). This might be the case, if the clock error has well predictable dynamics. The unstable oscillator of the u-blox receiver, however, cannot be properly modeled. Therefore, no benefit is expected from using

single-differences, whereas the number of parameters is reduced in the case of double-difference observations:

$$P_{AB}^{ij} = P_{AB}^i - P_{AB}^j = (\mathbf{e}^i - \mathbf{e}^j)^T \mathbf{R}(\mathbf{x}) \mathbf{b}_{AB} + E_{AB}^{ij} + \lambda N_{AB}^{ij} + \Phi_{AB}^{ij} + v_{AB}^{ij} = h(\mathbf{x}) + v_{AB}^{ij} \quad (27)$$

$$\mathbf{R}(\mathbf{x}) = \begin{pmatrix} q_0^2 + q_1^2 - q_2^2 - q_3^2 & 2q_1q_2 + 2q_0q_3 & 2q_1q_3 - 2q_0q_2 \\ 2q_1q_2 - 2q_0q_3 & q_0^2 - q_1^2 + q_2^2 - q_3^2 & 2q_2q_3 + 2q_0q_1 \\ 2q_1q_3 + 2q_0q_2 & 2q_2q_3 - 2q_0q_1 & q_0^2 - q_1^2 - q_2^2 + q_3^2 \end{pmatrix} \quad (28)$$

where P_{AB}^{ij} is a double-difference phase observation, $E_{AB}^{ij} = E_{AB}^i - E_{AB}^j$ is the double-difference extrapolation term, N_{AB}^{ij} is the double-difference phase ambiguity, Φ_{AB}^{ij} is the double-difference PCV correction, and v_{AB}^{ij} is the normally distributed, zero mean, double-difference measurement error. $h(\mathbf{x})$ was introduced to emphasize the connection to (4). $\mathbf{R}(\mathbf{x})$ is quaternion rotation matrix (Diebel 2006) and allows to express the attitude as function of the state \mathbf{x} .

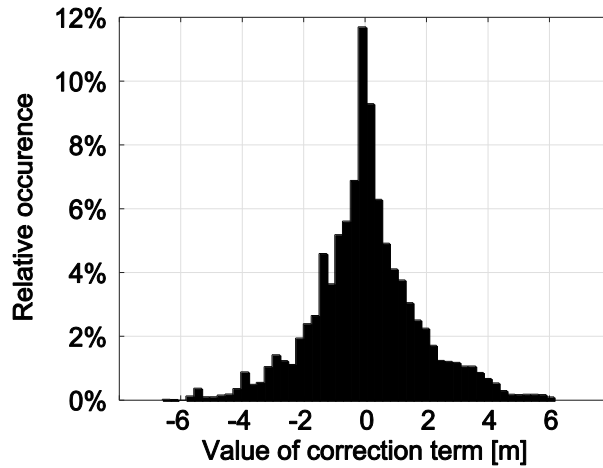


Fig. 4 Histogram of the correction terms E_{AB}^i for data set 2 (see next section) with u-blox receivers. The values range from -6 m to $+6$ m. Without the correction term, no proper solution can be obtained.

The linearization of (27) and (28) around the linearization point \mathbf{x}_0 leads to the final form of the observation equation:

$$\mathbf{z} = \mathbf{h}(\mathbf{x}_0) + 2 (\mathbf{e}^i - \mathbf{e}^j)^T \begin{pmatrix} n_1 & n_3 & -n_4 & n_2 \\ n_2 & n_4 & n_3 & -n_1 \\ n_4 & -n_2 & n_1 & n_3 \end{pmatrix} (\mathbf{x} - \mathbf{x}_0) + \mathbf{v} = \mathbf{H} (\mathbf{x} - \mathbf{x}_0) + \mathbf{v}$$

$$n_1 = b_x q_0 + b_y q_3 - b_z q_2$$

$$n_2 = b_y q_0 - b_x q_3 + b_z q_1$$

$$n_3 = b_x q_1 + b_y q_2 + b_z q_3$$

$$n_4 = b_x q_2 - b_y q_1 + b_z q_0 \quad (29)$$

where b_x , b_y and b_z are the components of the baseline vector \mathbf{b} . \mathbf{H} is the Jacobian matrix of \mathbf{h} and emphasizes the relation to (7), (8) and (9).

Stochastic model

The stochastic behavior of the propagation is theoretically given by (3). However, the process noise variance-covariance matrix \mathbf{U} is unknown. Assuming that the noise enters the system only through the rotation rates, the state-space equation of the system reads as:

$$\dot{\mathbf{x}}(t) = \begin{pmatrix} \dot{\mathbf{q}}(t) \\ \dot{\boldsymbol{\omega}}(t) \end{pmatrix} = \mathbf{g}(\mathbf{x}(t)) + \mathbf{G} \mathbf{w}(t) = \begin{pmatrix} \dot{\mathbf{q}}(\mathbf{q}(t), \boldsymbol{\omega}(t)) \\ \mathbf{0} \end{pmatrix} + \begin{pmatrix} \mathbf{0}_{4 \times 3} \\ \mathbf{I}_3 \end{pmatrix} \begin{pmatrix} w_1(t) \\ w_2(t) \\ w_3(t) \end{pmatrix} \quad (30)$$

where $\dot{\mathbf{x}}$ is the time derivative of the state and \mathbf{w} the white noise affecting the rotation rates. This equation can be written compactly in its linearized form:

$$\dot{\mathbf{x}} = \mathbf{g}(\mathbf{x}_0) + \left. \frac{\partial \mathbf{g}}{\partial \mathbf{x}} \right|_{\mathbf{x}_0} (\mathbf{x} - \mathbf{x}_0) + \mathbf{G} \mathbf{w} \quad (31)$$

where \mathbf{x}_0 is the linearization point. Introducing $\delta \mathbf{x} = \mathbf{x} - \mathbf{x}_0$, $\delta \dot{\mathbf{x}} = \dot{\mathbf{x}} - \mathbf{g}(\mathbf{x}_0)$ and renaming the Jacobian matrix to \mathbf{F} leads to following expression:

$$\delta \dot{\mathbf{x}} = \mathbf{F} \delta \mathbf{x} + \mathbf{G} \mathbf{w} \quad (32)$$

The solution to this differential equation reads:

$$\delta \mathbf{x}(t) = e^{(t-t_0)\mathbf{F}} \delta \mathbf{x}(t_0) + \int_{t_0}^t e^{(t'-t_0)\mathbf{F}} \mathbf{G} \mathbf{w}(t') dt' = \mathbf{A} \delta \mathbf{x} + \mathbf{u} \quad (33)$$

Assuming that w_1 , w_2 and w_3 all have the same variance σ_w^2 , variance propagation leads to an expression for the variance-covariance of \mathbf{u} , which is the process noise variance-covariance:

$$\mathbf{U} = \int_{t_0}^t e^{(t'-t_0)\mathbf{F}} \mathbf{G} \mathbf{I}_3 \sigma_w^2 \mathbf{I}_3 \mathbf{G}^T (e^{(t-t_0)\mathbf{F}})^T dt' \quad (34)$$

After integration and setting $\Delta t = t - t_0$, this expression leads to an analytical expression for \mathbf{U} :

$$\mathbf{U} = \sigma_w^2 \begin{pmatrix} \mathbf{\Theta} & \mathbf{\Omega} \\ \mathbf{\Omega}^T & \Delta t \mathbf{I}_3 \end{pmatrix}$$

$$\mathbf{\Theta} = \frac{\Delta t^3}{12} \begin{pmatrix} q_1^2 + q_2^2 + q_3^2 & -q_0 q_1 & -q_0 q_2 & -q_0 q_3 \\ -q_0 q_1 & q_0^2 + q_2^2 + q_3^2 & -q_1 q_2 & -q_1 q_3 \\ -q_0 q_2 & -q_1 q_2 & q_0^2 + q_1^2 + q_3^2 & -q_2 q_3 \\ -q_0 q_3 & -q_1 q_3 & -q_2 q_3 & q_0^2 + q_1^2 + q_2^2 \end{pmatrix}$$

$$\mathbf{\Omega} = \frac{\Delta t^2}{4} \begin{pmatrix} -q_1 & -q_2 & -q_3 \\ q_0 & q_3 & -q_2 \\ -q_3 & q_0 & q_1 \\ q_2 & -q_1 & q_0 \end{pmatrix} \quad (35)$$

The stochastic model of the double-difference observations is obtained after variance propagation. Let \mathbf{D} be a differencing operator which forms double-difference measurements out of n undifferenced measurements. The measurement variance-covariance matrix \mathbf{V} reads:

$$\mathbf{V} = \mathbf{D} \mathbf{I}_n \sigma_p^2 \mathbf{I}_n \mathbf{D}^T \quad (36)$$

where σ_p^2 is the variance of a undifferenced phase observation.

Initialization

The initialization process is based on a baseline-wise search. Instead of introducing the attitude into the observation equation, the baseline coordinates in the world frame are solved for (see also equation 27):

$$P_{AB}^{ij} = (\mathbf{e}^i - \mathbf{e}^j)^T \mathbf{B}_{AB} + E_{AB}^{ij} + \lambda N_{AB}^{ij} + \Phi_{AB}^{ij} + v_{AB}^{ij} \quad (37)$$

where \mathbf{B} is the baseline-vector in the world frame. A first approximation \tilde{N}_{AB}^{ij} for the phase ambiguity N_{AB}^{ij} is obtained by setting the baseline coordinates to zero ($\mathbf{B}_{AB} = \mathbf{0}$). This method is only valid for baselines shorter than $\lambda/2$. After omitting the error term, the equation reads as:

$$\tilde{N}_{AB}^{ij} = \lambda^{-1} (P_{AB}^{ij} - E_{AB}^{ij}) \quad (38)$$

This value is rounded and used as initial guess for the unknown integer phase ambiguity. The correct phase ambiguity is searched for in a search space consisting of the guess plus minus one cycle. As the baseline is shorter than one wavelength, the true ambiguity must lie in the interval $[-1, 1]$ (Graas and Braasch 1991). A baseline solution is computed for each set in this search space. The ambiguity set with the lowest root mean square error is selected, and the ratio between the best and the second-best set serves as validation criterion.

The chosen ambiguity resolution approach is suitable for baselines up to 1 m length if the search space is widened accordingly (Graas and Braasch 1991). Depending on the processing power and the real-time requirements, an alternative ambiguity resolution process will be needed for longer baselines. The LAMBDA method (Teunissen 1995) is widely used, very efficient and leads to high ambiguity resolution success rates. The LAMBDA method can be extended to take advantage of the known baseline length (Teunissen 2007, 2009). As demonstrated by Teunissen et al. (2011), this method leads to very high ambiguity resolution rates, even in situations with high dynamics and baselines of several meters.

Validation

The following section presents preliminary results obtained with the new algorithm. Two data sets with moving baselines on a LEO spacecraft were processed with a prototype of the attitude determination filter: (i) synthetic data generated with the Bernese GNSS Software Version 5.2 and (ii) GNSS signal simulator data. In both cases, orbital conditions were simulated, leading to a high velocity of the receiver and allowing to test the main feature of the algorithm, the extrapolation of the measurements within the filter. The effect of noise on the initialization is also investigated.

It is visible from (27) that, besides the extrapolation term and the phase ambiguity, the PCV have the largest effect on the accuracy of a GNSS attitude determination system. Calibrated antennas are therefore required to obtain valid results. In the simulation, no PCV were introduced. The interested reader is referred to Rothacher et al. (1995) for further information regarding the determination of PCV. Using the algorithm with real data but omitting to correct the PCV will lead to a degradation in accuracy.

Data set 1 – synthetic data

Synthetic GNSS data was simulated using the Bernese GNSS Software V5.2 (Dach et al. 2015). Table 1 summarizes the main simulation parameters. A conservative value of 5 mm was chosen for the standard deviation of a phase observation. A realistic baseline configuration, corresponding to the CubETH set-up, was simulated. The three baselines form a "Z", therefore the first and the last baseline have the same relative coordinates. The spacecraft attitude is conservative as well, since the yaw rate is higher than the expected rotation speed. Since emphasis was on the investigation of the synchronization, unusually high receiver clock errors of up to 0.01 second were introduced. Satellite clock corrections were not applied, as this effect is expected to be negligible on the double-difference level. Similarly, no ionosphere was modeled, as its effect is also negligible on very short baselines.

Table 1 Main simulation parameters for data set 1 - synthetic data.

Data type	Synthetic GPS L1 carrier phase data	
Simulator	Bernese GNSS Software V5.2	
Orbit	Type	Near circular LEO
	Height	450 km
	Inclination	89°
GPS constellation	True constellation of year 2012 day 359	
Spacecraft attitude	Roll	-5°
	Pitch	+5°
	Yaw	+1°/sec rate
Receiver clock error	Receiver 1	0.01 sec
	Receiver 2	0.01 sec
	Receiver 3	-0.01 sec
	Receiver 4	0.005 sec
Ionosphere	No ionospheric path delay modelled	
Antenna coordinates	Antenna coordinates in the body frame [cm]	$\begin{pmatrix} 2.85 \\ 3.25 \\ -5 \end{pmatrix}, \begin{pmatrix} -2.85 \\ 3.25 \\ -5 \end{pmatrix}, \begin{pmatrix} 2.85 \\ -3.25 \\ -5 \end{pmatrix}, \begin{pmatrix} -2.85 \\ -3.25 \\ -5 \end{pmatrix}$
Baseline coordinates*	Baseline coordinates in the body frame [cm]	$\begin{pmatrix} -5.7 \\ 0 \\ 0 \end{pmatrix}, \begin{pmatrix} 5.7 \\ -6.5 \\ 0 \end{pmatrix}, \begin{pmatrix} -5.7 \\ 0 \\ 0 \end{pmatrix}$
Sampling rate	1 Hz	
Length of the data set	57 min 50 sec	

* Due to changes in the design, the baseline lengths differ by 1 mm from the values given in the introduction. The values in the introduction correspond to the current CubETH mission state.

Results obtained with synthetic data

The following results were obtained using broadcast ephemeris for the GPS satellites and a SP3 file (Hilla 2010) for the LEO satellite positions and velocities. The initialization part was removed from the results. The filter reaches initialization after one epoch and converges after five epochs. Figure 5 displays all four quaternions of the estimated state. The estimation is bias-free. The 2σ (95% error quantile) formal error, displayed in red, fits the actual error and therefore indicates a good agreement between the stochastic model and the data. The periodic change in the formal error is due to the changing attitude, as each quaternion element has a different weight in the adjustment. The jumps are explained by changes in the observation geometry, when GPS satellites appear or disappear. The measurement noise and process noise parameters are summarized in Table 2. The value of 6 mm for σ_p was determined empirically from the data and is in good accordance with the actual standard deviation of the synthetic data (compare with Table 1).

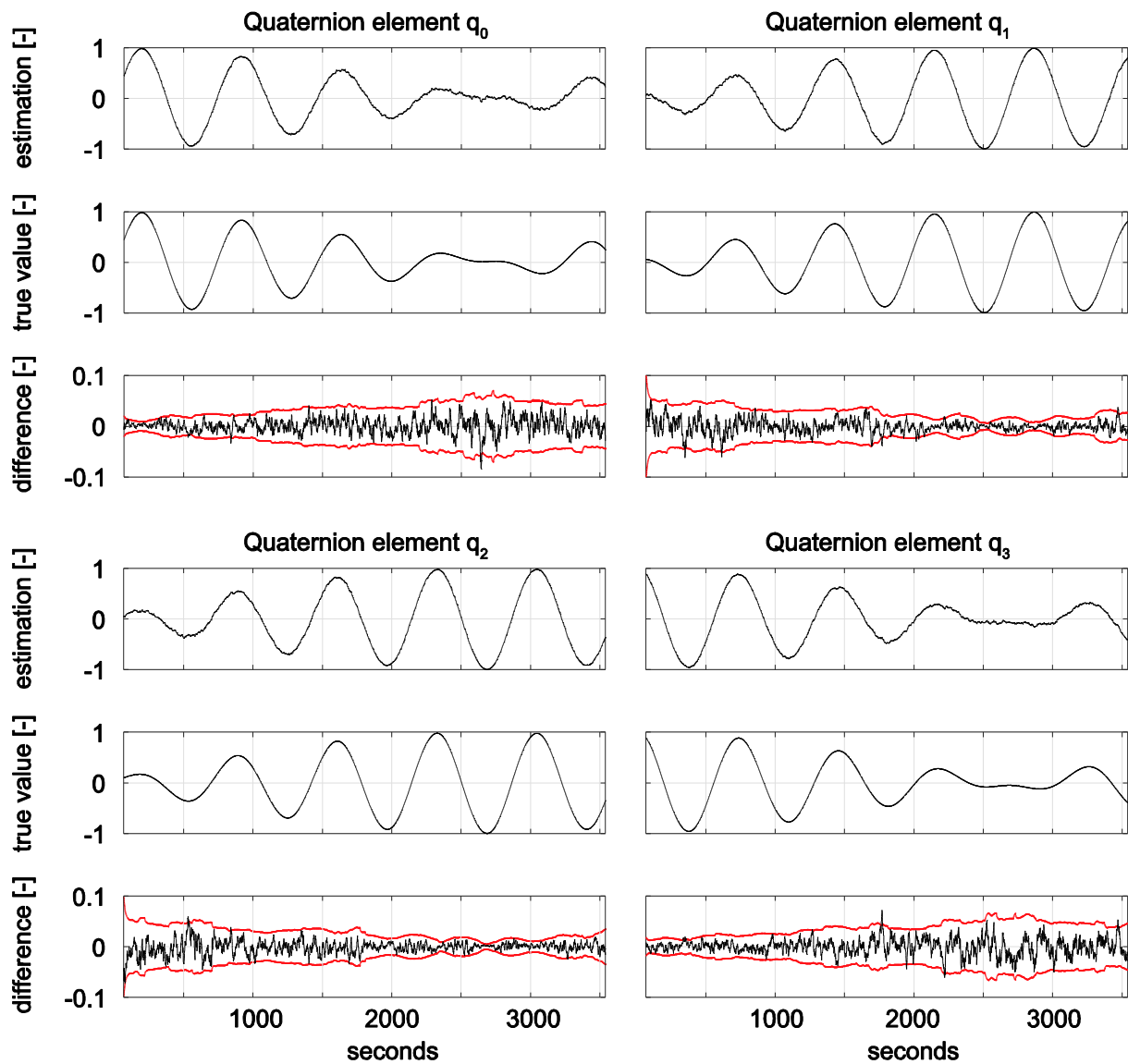


Fig. 5 Result of the attitude determination with data set 1. The plots show the four quaternion elements q_0 to q_3 . The upper plot of each element is the filter estimation; the second plot displays the true value while the last plot is the difference. The red lines are the $\pm 2\sigma$ or 95% quantile and indicate that the formal errors are in good agreement with the actual errors. The quaternion elements as well as the formal errors change as a function of attitude.

Table 2 Summary of the stochastic filter parameters for data set 1

σ_p^2	36 mm ²
σ_w^2	10 ⁻⁶ s ⁻³

Figure 6 offers a better picture for interpretation. It shows the difference between the true attitude and the estimated attitude in Euler angles. The Euler sequence (1,2,3) was chosen, which corresponds to roll, pitch and yaw (Diebel 2006). All three components are centered and free of systematic errors. The uncertainty in height, typically two to three times larger than the uncertainty in position, affects roll and pitch. Therefore, the estimation of the yaw angle is about two to three times more precise than the estimation of roll and pitch. A summary is given in Table 3.

Table 3 Mean and Root Mean Square (RMS) values of roll, pitch and yaw, and absolute error for data set 1

	Mean [deg]	RMS [deg]
Roll	0.28	2.20
Pitch	-0.20	2.11
Yaw	-0.04	0.88
Absolute error	2.85	3.17

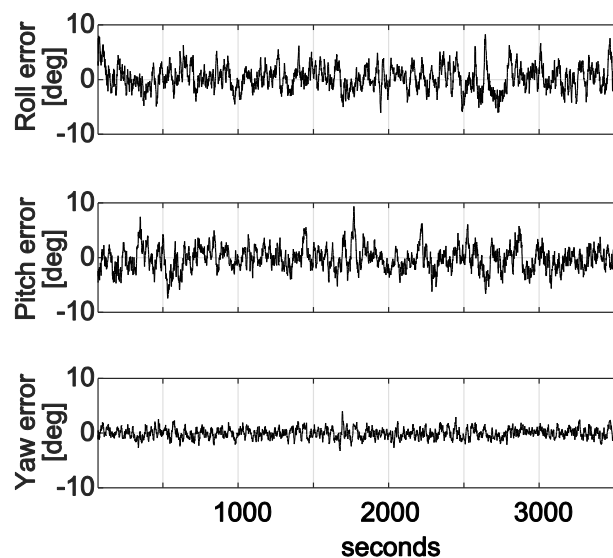


Fig. 6 Difference between the true attitude and the estimated attitude for data set 1 (synthetic data). The rotation is expressed in roll, pitch and yaw angles. The yaw component is about 2.5 times more accurate, because the geometric weakness typically affecting the height enters the roll and pitch angles.

Impact of noise on the attitude estimation

In order to study the impact of noise on the estimation of the attitude, data sets with the same configuration as data set 1 but with different noise levels were produced. These additional data sets have a length of 24 min and 40 sec, all other parameters are identical to those in Table 1. The ambiguity resolution and the filter convergence process were investigated separately (see next section). Therefore, the filter was initialized with the true attitude and the true phase ambiguities were introduced.

The results are shown in Figure 7 and summarized in Table 4. The experiment with 5 mm measurement noise confirms the results of the previous section. The small difference is explained by the data set length, which is different in the two cases. Unsurprisingly, the absolute error increases with increasing noise. However, the increase is not linear. This is expected because of the filter process and the associated dynamical model. A second order polynomial model is well-suited to represent this relation. The coefficients of the second order polynomials and their accuracies are shown in Table 5. An accuracy of 1 degree or better would require a measurement noise smaller than 1 mm on a Cube satellite. Even with an unrealistically high noise level of 30 mm, the algorithm delivers reliable attitude information.

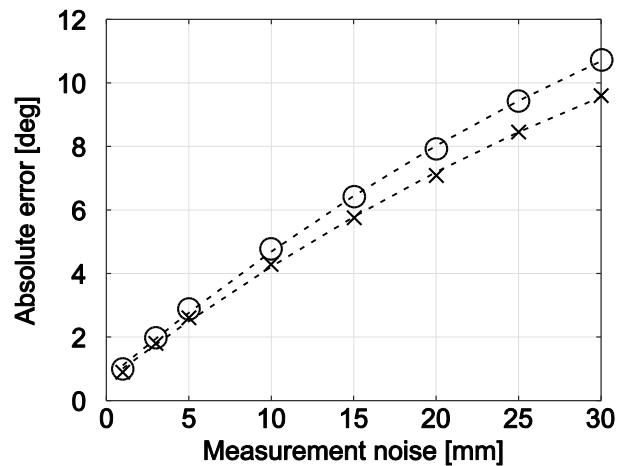


Fig. 7 Relation between the measurement noise and the absolute error of the attitude determination. The mean error is indicated by crosses, the RMS error by circles. The dashed lines show the second order polynomial fit.

Table 4 Mean and RMS of the absolute error (great-circle distance) for data set 1, but with different noise levels.

Measurement noise (σ)	Absolute error (great-circle distance)	
	Mean [deg]	RMS [deg]
1 mm	0.88	0.98
3 mm	1.80	1.99
5 mm	2.60	2.87
10 mm	4.29	4.76
15 mm	5.75	6.41
20 mm	7.10	7.92
25 mm	8.44	9.44
30 mm	9.61	10.73

Table 5 Relationship between the measurement noise and absolute error of the attitude determination. Results of the second order polynomial fit $y = a \sigma^2 + b \sigma + c$.

	Mean	RMS
a ($\pm 1\sigma$)	$-0.0031 \pm 0.0004 \text{ deg/mm}^2$	$-0.0034 \pm 0.0004 \text{ deg/mm}^2$
b ($\pm 1\sigma$)	$0.3901 \pm 0.0137 \text{ deg/mm}$	$0.4347 \pm 0.0138 \text{ deg/mm}$
c ($\pm 1\sigma$)	$0.6202 \pm 0.0797 \text{ deg}$	$0.6760 \pm 0.0801 \text{ deg}$

Impact of noise on the ambiguity resolution

Figure 8 shows the baseline-wise ambiguity resolution success rate for the data sets with variable noise level used in the previous section. The distance between the antennas was introduced as pseudo-observation in the adjustment to enhance the estimation process. The ambiguity resolution success rate is over 95% even with 15 mm measurement noise on the phase observations. This is easily explained by the short baseline length. Only unrealistically high noise levels of over 20 mm affect the ambiguity resolution.

A more sophisticated ambiguity resolution strategy seems unnecessary under these circumstances. This hypothesis needs to be verified with real data, which can potentially be affected by outliers. The main advantage of instantaneous ambiguity resolution is the fact that it is not affected by undetected cycle slips.

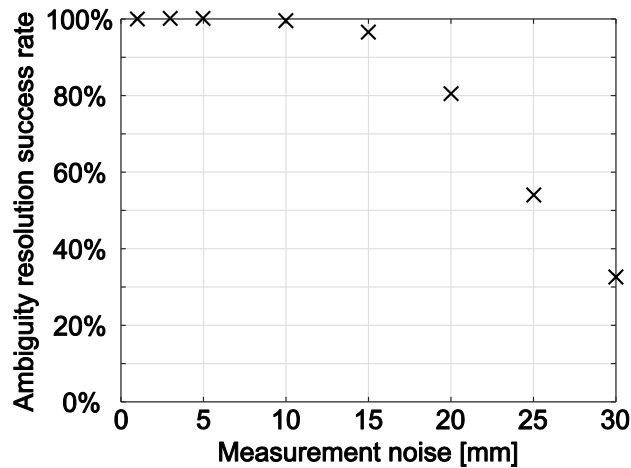


Fig. 8 Success rate of baseline-wise ambiguity resolution. The data set has the same configuration as data set 1, but other noise levels (noise standard deviation of 1 mm, 3 mm, 5 mm, 10 mm, 15 mm, 20 mm, 25 mm and 30 mm). Ambiguity resolution is considered successful, if the ambiguity set candidate with the smallest RMS residuals corresponds to the reference ambiguity set. Up to a noise level of 15 mm, the success rate lies over 95%.

Data set 2 – signal simulator data

Table 6 summarizes the main parameters of the signal simulator data set. The Spirent simulator consists of a signal generator and its associated software (Simgen Software User Manual 2012). The signal generator has two radio-frequency (RF) outputs, allowing to simulate differential positioning over baselines. Each of the two RF outputs was connected to a u-blox NEO-M8 receiver, receiver A and B (Figure 9). Speed and height limits, included in the receiver to avoid military usage, were removed from the receiver firmware to enable operability in space. Three successive simulator runs were undertaken, resulting in three independent and uncorrelated baselines, as shown in Table 7. These baselines were combined in the Kalman filter to obtain one attitude estimation. This set-up is identical to the case where six receivers are located on the spacecraft. The results are similar to those obtained with only four receivers, since all correlations, respectively the absence of correlation, are properly taken into account (see equation 36).

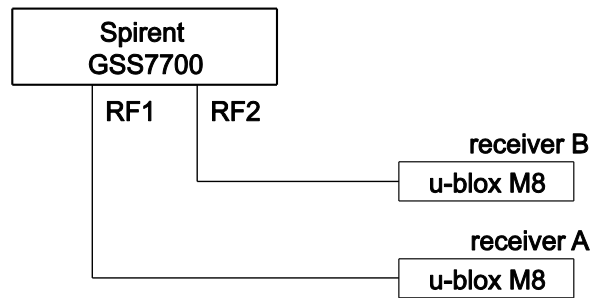


Fig. 9 Signal simulator set-up. Each radio-frequency (RF) output is connected to the corresponding receiver by a coaxial cable.

Table 6 Main simulation parameters for data set 2 – signal simulator data

Data type	Signal simulator data	
Simulator	Spirent GSS7700 GNSS Signal Simulator	
Receiver	u-blox NEO-M8 (u-blox M8 Receiver Description 2016), single-frequency, low-cost, multi-GNSS receiver with custom, space-enabled firmware	
Orbit	Type	Near circular LEO
	Height	450 km
	Inclination	98.7°
GPS constellation	YUMA almanac of GPS week 1669 (YUMA almanac 2016)	
Spacecraft attitude	Roll	0°
	Pitch	0°
	Yaw	0°
Ionosphere	No ionospheric path delay simulated	
Measurement noise	Actual receiver measurement noise	
Length of the data set	1 h 36 min 40 sec	

Table 7 Summary of the three simulator runs. For each run, receiver (A) and (B) were connected to the simulator. Each of the three runs generated an independent (uncorrelated) baseline.

Simulator run	Baseline number	Simulator radio frequency output (RF)	Receiver connected to corresponding RF output	Antenna coordinates in the body frame [cm]
Run 1	Baseline 1	RF output 1	u-blox NEO M8 (A)	0,0,0
		RF output 2	u-blox NEO M8 (B)	0,0,10
Run 2	Baseline 2	RF output 1	u-blox NEO M8 (A)	0,0,0
		RF output 2	u-blox NEO M8 (B)	10,0,0
Run 3	Baseline 3	RF output 1	u-blox NEO M8 (A)	0,0,0
		RF output 2	u-blox NEO M8 (B)	0,10,0

Results obtained with signal simulator data

The following results were obtained using the same almanac which was fed into the signal simulator. Receiver positions and velocities were obtained directly from the u-blox PVT estimate. The initialization part was removed from the results. The filter reaches initialization within one epoch and converges within five seconds after the initialization. Figure 10 shows the difference between the true attitude and the estimated attitude in Euler angles. Table 8 gives a summary of the results. In contrast to the results in data set 1, all three components show a similar precision. This is due to the improved observation geometry, with three orthogonal baselines. Again, the data is free of any systematic error. The precision is much higher than in data set 1 because the observation noise is smaller (approximately by a factor 3) and the geometry is improved (approximately 1.5 times longer baselines). Therefore, a RMS ratio of about 4.5 between data set 1 and data set 2 is expected. The actual ratio is 4.46 and fits the theoretical value. The stochastic filter parameters are displayed in Table 9. σ_w is identical for both data sets. This is expected, since in both cases the spacecraft has constant rotation rates in the orbital system but not in the inertial frame. The process noise has to be sufficiently large to allow for changing rotation rates in the inertial frame, which is the case with the empirically selected value.

Figure 11 shows the absolute error of the estimated attitude. The absolute error is the great-circle distance between the true attitude and the estimated attitude. Therefore, it has no sign. The absolute error is smaller than the sum of the errors on the three Euler angles. The filter is well performing and delivers an attitude with an average error below one degree (see also Table 8), compared to an accuracy around 3 degrees for data set 1 (see Table 3). The maximal error in the data set is 2.5 degrees.

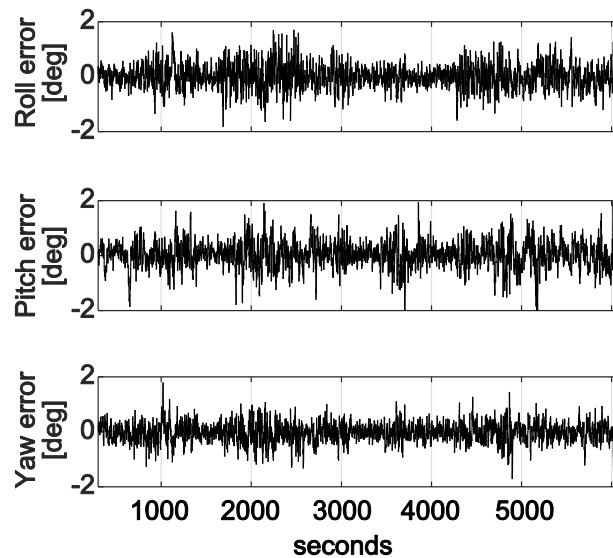


Fig. 10 Difference between the true attitude and the estimated attitude for data set 2 (signal simulator data). The rotation is expressed in roll, pitch and yaw angles. All three components have a similar accuracy, which is expected with three orthogonal baselines.

Table 8 Mean and Root Mean Square (RMS) values of roll, pitch and yaw, and absolute error for data set 2

	Mean [deg]	RMS [deg]
Roll	0.01	0.41
Pitch	0.03	0.47
Yaw	-0.02	0.34
Absolute error	0.62	0.71

Table 9 Summary of the stochastic filter parameters for data set 2

σ_p^2	4 mm ²
σ_w^2	10 ⁻⁶ s ⁻³

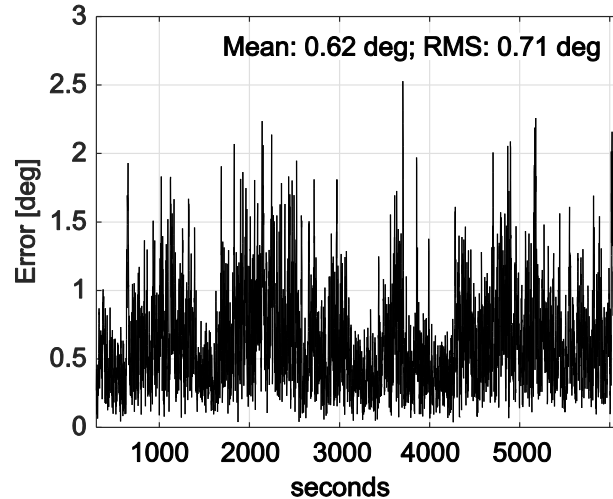


Fig. 11 Overall accuracy of the attitude determination with data set 2. The mean deviation lies below 1 degree. The maximal error is around 2.5 degrees.

Conclusions and outlook

A new algorithm for attitude determination with non-synchronized receivers was presented in great detail. It was shown that the extrapolation is crucial to obtain an attitude solution. The algorithm was tested with synthetic data as well as with signal simulator data. Due to the predictable dynamics of the spacecraft, the filter performs very well. The overall accuracy lies well below five degrees for data set 1 and below one degree for data set 2. Additional inquiries showed that the algorithm is able to deliver a robust attitude estimation, even if the observations are affected by high noise levels.

All results show the expected pattern: with the original CubETH antenna configuration of data set 1, the yaw component is about 2.5 times more accurate than the roll and pitch components. This roll and pitch degradation vanishes, if the observation geometry is improved, as in data set 2. The attitude estimation shows no systematic errors. Therefore, the algorithm and especially the extrapolation of the measurements based on the receiver PVT solution is proven to work very well. As no ground data is used to run the filter, it fulfills the requirement of an autonomous onboard filter for real-time processing, for instance onboard a Cube satellite.

PCV have a considerable impact on the accuracy of a GNSS attitude determination with short baselines. The quality and the stability of the PCV calibrations for small patch antennas, as on CubETH, is only insufficiently known. PCV are currently under investigation at the Institute of Geodesy and Photogrammetry. Up to now, the application of the presented algorithm is limited to applications with well-calibrated antennas. As soon as flight data is available, in-flight calibration of the antennas can be attempted.

The presented algorithm is potentially of high interest, since it provides a very efficient method for attitude determination onboard a spacecraft. Typical star trackers for small satellites have a mass of several hundreds of grams, a power consumption of about 1 W and

an accuracy better than half an arc minute (Gebre-Egziabher et al. 2016). U-blox receivers require only 63 mW and have a mass of 1.6 g (u-blox M8 Product Summary 2016). Therefore, they present an excellent mean of attitude determination, if no high accuracy is needed, e.g. as back-up sensor or as primary sensor in energy-save-mode. Since no synchronization between the receivers is needed, the set-up of an attitude determination system is theoretically as simple as putting receivers and corresponding antennas at every corner of the spacecraft. The method can easily be adapted to different baseline geometries and to longer baselines, if the ambiguity resolution process is adapted accordingly. The presented approach is suitable for baselines up to 1 meter.

Acknowledgment

We would like to thank Dr. Oliver Montenbruck and Markus Markgraf at DLR for providing access to the GNSS Signal Simulator and for the great support during the data acquisition. This work was supported by ETH Research Grant ETH-43 14-2.

Bibliography

- Aghili F, Salerno A (2013) Driftless 3-D Attitude Determination and Positioning of Mobile Robots By Integration of IMU With Two RTK GPSs. *IEEE/ASME Transactions on Mechatronics* 18(1):21–31
- Arbinger C, Enderle W (2000) Spacecraft attitude determination using a combination of GPS attitude sensor and star sensor measurements. *Proc. ION GPS 2000, Institute of Navigation, Salt Lake City, Utah, USA, September 19 – 22, 2634 – 2642.*
- Birmingham WP, Miller BL, Stein WL (1983) Experimental results of using the GPS for Landsat 4 onboard navigation. *Navigation* 30(3):244–251.
- Cannon ME, Sun H (1996) Experimental assessment of a non-dedicated GPS receiver system for airborne attitude determination. *ISPRS journal of photogrammetry and remote sensing* 51(2):99–108
- Chen W, Qin H (2012) New method for single epoch, single frequency land vehicle attitude determination using low-end GPS receiver. *GPS Solutions* 16(3):329–338
- Cohen CE (1992) Attitude determination using GPS. Dissertation, Department of Aeronautics and Astronautics, Stanford University.
- Cohen CE, Lightsey EG, Parkinson BW, Feess WA (1994) Space flight tests of attitude determination using GPS. *International Journal of Satellite Communications* 12:427-433
- Crassidis JL, Markley FL (1997) New algorithm for attitude determination using Global Positioning System signals. *Journal of Guidance, Control, and Dynamics* 20:891–896

CubeSat Design Specification (2015) Revision 13 – Updated 4-6-2015.

<http://www.cubesat.org/resources/>.

Dach R, Lutz S, Walser P, Fridez P (eds.) (2015) Bernese GNSS Software Version 5.2. Software user manual, Astronomical Institute, University of Bern.

Diebel J (2006) Representing Attitude: Euler Angles, Unit Quaternions, and Rotation Vectors. Technical Report, Stanford University.

<https://www.astro.rug.nl/software/kapteyn/downloads/attitude.pdf>.

Farrell JL, Stuelpnagel JC, Wessner RH, Velman JR, Brook JE (1966) A least squares estimate of satellite attitude (Grace Wahba). *Siam Review*, 8:384–386

Gebre-Egziabher D, Hisamoto CS, Sheikh SI (2016) Small Satellite Attitude Determination. In: Fourati H, Belkhiat DEC, Iniewski K (eds) *Multisensor Attitude Estimation: Fundamental Concepts and Applications*, CRC Press, pp. 427–444.

Giorgi G, Teunissen PJG, Gourlay TP (2012) Instantaneous Global Navigation Satellite System (GNSS)-Based Attitude Determination for Maritime Applications. *IEEE Journal of Oceanic Engineering* 37(3): 348–362

Graas F, Braasch M (1991) GPS interferometric attitude and heading determination: Initial flight test results. *Navigation* 38(4):297–316

Hilla S (2010) The Extended Standard Product 3 Orbit Format (SP3-c).

<ftp://igs.org/pub/data/format/sp3c.txt>.

Hollenstein Ch, Männel B, Serantoni E, Scherer L, Rothacher M, Kehl P, Ivanov A (2014) Concepts and Testing of Low-cost GNSS Receivers for CubeSat Orbit and Attitude Determination. In *Proceedings of NAVITEC*, Noordwijk, Netherlands.

Ivanov AB, et al. (2015) CubETH: Nano-Satellite Mission for Orbit and Attitude Determination Using Low-Cost GNSS Receivers. IAC-15,B4.4.5. In *66th International Astronautical Congress*, Jerusalem, Israel.

Montenbruck O, Markgraf M, Garcia-Fernandez M, Helm A (2008) GPS for microsatellites – status and perspectives. In: Sandau R, Röser HP, Valenzuela A (eds) *Small Satellites for Earth Observation*. Springer, Berlin, pp. 165-174

Remondi BW (2004) Computing satellite velocity using the broadcast ephemeris. *GPS Solutions* 8(3):181-183. doi:10.1007/s10291-004-0094-6

Rothacher M, Schaer S, Mervart L, Beutler G (1995) Determination of antenna phase center variations using GPS data. In Gendt G, Dick G (eds) *Special Topics and New Directions, 1995 IGS Workshop*. Potsdam, pp. 205-220.

Sabatini R, Rodriguez L, Kaharkar A, Bartel C, Shaid T (2012) Carrier-phase GNSS attitude determination and control system for unmanned aerial vehicle applications. *ARPN Journal of Systems and Software* 2(11):297–322

- Simgen Software User Manual (2012) Spirent Communication plc, Devon, United Kingdom.
- Teunissen PJG (1995) The least-squares ambiguity decorrelation adjustment: a method for fast GPS integer ambiguity estimation. *Journal of Geodesy*, 70(1):65–82
- Teunissen PJG (2007) The LAMBDA method for the GNSS compass. *Art Satellites* 41:89–103
- Teunissen PJG (2009) Integer least squares theory for the GNSS Compass. *J Geod* 84(7):433-447. doi: 10.1007/s00190-010-0380-8
- Teunissen PJG, Giorgi G, Buist PJ (2011) Testing of a new single-frequency GNSS carrier phase attitude determination method: land, ship and aircraft experiments. *GPS Solutions* 15(1):15-28. doi:10.1007/s10291-010-0164-x
- Um J, Lightsey EG (2001) GPS attitude determination for the SOAR experiment. *Navigation* 48(3):181-194
- u-blox M8 Product Summary (2016) R04. u-blox, Thalwil, Switzerland. <https://www.u-blox.com/en/product/neo-m8-series>.
- u-blox M8 Receiver Description (2016) v15.00-19.00, 22.00, R11. u-blox, Thalwil, Switzerland.
- Ward LM, Axelrad P (1997) A Combined Filter for GPS-Based Attitude and Baseline Estimation. *Navigation* 44(2):195–214
- Welch G, Bishop G (2006) An Introduction to the Kalman Filter. University of North Carolina. https://www.cs.unc.edu/~welch/media/pdf/kalman_intro.pdf.
- YUMA almanac (2016) United States Coast Guard, GPS NANUs, Almanac & OPS Advisories. <http://www.navcen.uscg.gov/?pageName=gpsAlmanacs>.

Appendix B

Paper II

Title	GNSS Antenna Phase Center Variation Calibration for Attitude Determination on Short Baselines
Authors	Daniel WILLI, Michael MEINDL, Hui XU, Markus ROTHACHER
Proceedings	Proceedings of the 30th International Technical Meeting of The Satellite Division of the Institute of Navigation (ION GNSS+ 2017), September 25 - 29, 2017, Oregon Convention Center, Portland, Oregon
Pages	3997 – 4010
Link	www.ion.org/publications/abstract.cfm?articleID=15411
Peer review	Yes

Upon recommendation of the session chair, this article was submitted to Navigation:

Journal	Navigation
DOI	10.1002/navi.273
Received	23 November 2017
Accepted	30 August 2018
First Online	07 December 2018

The attached version is the first version submitted to Navigation, which has an identical content than the final version of the ION GNSS+ version. The reprint of this document is in agreement with the Copyright Transfer Agreement signed on 12 November 2018 with Wiley Periodicals.

GNSS Antenna Phase Center Variation Calibration for Attitude Determination on Short Baselines

Daniel Willi, Michael Meindl, Hui Xu, Markus Rothacher, *Institute of Geodesy and Photogrammetry, ETH Zürich*

BIOGRAPHIES

Daniel Willi is Ph.D. student at the Institute of Geodesy and Photogrammetry, ETH Zurich. He holds a Master degree in Geomatics Engineering from ETH Zurich. His research interests are GNSS attitude determination and precise orbit determination for low earth orbiters.

Michael Meindl works as a senior scientist at the Institute of Geodesy and Photogrammetry at ETH Zurich. He was heavily involved in the development of the scientific Bernese GNSS Software becoming an expert on GNSS modelling and algorithms. His research interests cover modelling the atmosphere, ambiguity resolution, orbit determination, reference frames, and the consistent combination of different satellite systems. In his current position he is responsible for the scientific payload of the small satellite mission CubETH.

Hui Xu is Academic Guest of Mathematical and Physical Geodesy at ETH Zurich in 2016. She works in Beijing satellite control center for 16 years. She was heavily involved in the operations of Sinosat-1, Sinosat-2, Sinosat-3 and Sinosat-6. Her expertise is comprised of satellite communications, communications satellite payload and user management, satellite operations, ground station calibrations, etc. For many years she was deputy chief of Beijing satellite control center. She presently serves in technology application center of Beijing satellite communication and control center.

Markus Rothacher is Professor of Mathematical and Physical Geodesy at ETH Zurich. His research interests comprise high-precision GNSS applications, space geodesy, satellite missions, orbit determination, and earth rotation. For many years he was Chair of the Global Geodetic Observing System (GGOS) and Analysis Coordinator of the IERS. He presently serves on the Galileo Science Advisory Committee (GSAC) of ESA.

ABSTRACT

Relative antenna field calibrations were carried out for two attitude determination setups with antennas located within a wavelength of each other. Four Amotech ceramic patch antennas and three Trimble Bullet III antennas were used. The obtained phase patterns are highly heterogeneous and asymmetrical.

These patterns were applied to a simulation of attitude determination onboard a spacecraft in low Earth orbit, using synthetic GNSS data. The analysis revealed the importance of the proper correction of phase center variations.

Finally, a field data validation was carried out. The root mean square error of the estimated attitude for a platform with three antennas located within 15 cm of each other, could be reduced from over 6 degrees to 4.5 degrees.

A step towards more precise attitude determination on very short baselines was done, but additional efforts are required. Especially the temporal stability of the phase patterns of low-cost antennas remains questionable.

INTRODUCTION

Precise knowledge of the orbit and the attitude of a spacecraft is crucial to many applications, such as broadcasting, weather forecasting or Earth observation. With the development of the Global Positioning System (GPS), a new technology became available for orbit and attitude determination. In 1982, the first spacecraft equipped with a GPS receiver, Landsat-4, was launched (Birmingham et al. 1983). Since then, Global Navigation Satellite Systems (GNSS) became a standard technique for orbit determination of satellites in low Earth orbits (LEO). If several antennas are mounted on a spacecraft, attitude determination is possible. This technique was employed, e.g., on the spacecraft RADCAL in 1993 (Cohen et al. 1994) or onboard the Space Shuttle Atlantis (Um and Lightsey 2001).

The cube satellite mission CubETH (Ivanov et al. 2015) is a good illustration for two recent trends in modern spaceflight: miniaturization and usage of commercial off-the-shelf (COTS) components. The project aims at using low-cost COTS receivers on a $10 \times 10 \times 10 \text{ cm}^3$ spacecraft for orbit and attitude determination. To this end, the satellite is equipped with four GNSS antennas on its zenith looking face forming three baselines shorter than 10 cm. An additional experimental antenna is located on the side. Each antenna is connected to two low-cost receivers manufactured by u-blox. The main challenges arise from the fact that (i) the receivers do not run on a common oscillator and that (ii) extremely small patch antennas on a common ground plane are used. The first issue was addressed in a previous publication (Willi and Rothacher 2017) whereas the second issue will be discussed hereafter. Small patch antennas are especially challenging, as they are expected to have large phase center variations (PCV) which bias the estimation of the position and the attitude from GNSS phase observations. PCV calibration has been studied extensively in the past. Antenna calibrations have been carried out since the very beginning of GPS, for instance by Sims (1985). Nowadays, antenna calibrations are routinely performed and calibrated antennas are widely used (Schmitz et al. 2002). However, a lack of knowledge exists regarding the behavior of low-cost antennas in general and in particular regarding systems of low-cost antennas placed within a wavelength of each other. These aspects will be studied in this paper and applied to attitude determination on very short baselines.

After a brief theoretical introduction to GNSS attitude determination and PCV estimation, an approach for the relative field calibration of antenna systems will be presented. Calibration-results for both, a model of the CubETH satellite and an experimental platform are shown in the second part. The calibration of the experimental platform was repeated after permutation of the antennas, in order to investigate the main contributors to PCV in antenna systems. In the last section, the effect of PCV on attitude determination on-board a spacecraft is studied with synthetic data and validated with a real data test case.

GOVERNING EQUATIONS

GNSS attitude determination is based on the interferometric model as depicted in Figure 1:

$$\Delta r = \mathbf{e}_{\text{world}}^T \mathbf{R}_{\text{world} \leftarrow \text{body}} \mathbf{b}_{\text{body}} + v \quad (1)$$

Δr is the range difference and therefore the actual observable, \mathbf{e} is the length line-of-sight (LOS) unit vector from the receiver to the GNSS satellite in the world frame, \mathbf{R} is the unknown orthogonal attitude matrix, \mathbf{b} is the baseline vector known in the body frame, and v is the measurement noise. In the following developments, the subscript indicating the reference frame is omitted for the sake of readability. Usually, the attitude matrix is obtained after an optimization procedure, combining all available GNSS measurements. The objective function L is:

$$L(\mathbf{R}) = \sum_k \sum_i \frac{1}{\sigma_{ki}^2} (\Delta r_{ki} - (\mathbf{e}^i)^T \mathbf{R} \mathbf{b}_k)^2 \quad (2)$$

where k is an index running over all baselines, i is an index indicating the GNSS satellite, and σ_{ki}^2 is the variance of the range difference observation Δr_{ki} .

Typically, very precise carrier phase measurements P_A^i are used for attitude determination:

$$P_A^i = \mathbf{e}_A^{i\top} (\mathbf{X}^i - \mathbf{X} - \mathbf{R} \mathbf{x}_A) + c \delta t_A - c \delta t^i + \lambda N_A^i + \Phi_A^i + I_A^i + v_A^i \quad (3)$$

P_A^i is a phase measurement from antenna A to the GNSS satellite i , \mathbf{X}^i is the position, at signal emission time, of the emitting antenna located on the GNSS spacecraft, \mathbf{X} is the position of a reference point, for instance the position of the center of mass of the LEO spacecraft, at signal reception time, \mathbf{x}_A is the position (in the body frame) of the mean phase center of the receiving antenna with respect to the reference point, c is the speed of light, δt_A is the receiver clock error, δt^i is the GNSS satellite clock error, λ is the carrier phase wavelength, N_A^i is the integer phase ambiguity, Φ_A^i is the PCV correction, I_A^i is the ionospheric signal delay, and v_A^i is the observation noise. The position of the mean phase center can be split into two parts:

$$\mathbf{x}_A = \mathbf{x}_{ARP,A} + \mathbf{PCO}_A \quad (4)$$

Where $\mathbf{x}_{ARP,A}$ is the position of the antenna reference point (ARP) in the body frame and \mathbf{PCO}_A is the phase center offset (PCO). As the baselines are short compared to the distance between the GNSS satellite and the LEO spacecraft, $\mathbf{e}_A^i = \mathbf{e}_B^i$ is a valid assumption. Moreover, the differential ionospheric signal delay vanishes. Introducing $\mathbf{b}_{AB} = \mathbf{x}_B - \mathbf{x}_A$, a single-difference between two phase observations reads as:

$$P_{AB}^i = P_A^i - P_B^i = \mathbf{e}^{i\top} \mathbf{R} \mathbf{b}_{AB} + E_{AB}^i + c \delta t_{AB} + \lambda N_{AB}^i + \Phi_{AB}^i + v_{AB}^i \quad (5)$$

P_{AB}^i is a single-difference carrier phase measurement between antennas A and B , E_{AB}^i is a synchronisation term which arises from the unsynchronised receivers (Willi and Rothacher 2017), δt_{AB} is the differential clock error, N_{AB}^i is the single-difference integer phase ambiguity, Φ_{AB}^i is the differential PCV correction and v_{AB}^i is the single-difference noise. Note that the two PCO are now implicitly contained in \mathbf{b}_{AB} .

The PCV correction term is a function of the azimuth angle α and zenith angle z of the incoming signal. Two parametrizations are possible with respect to α and z , either a piecewise-linear approach or spherical harmonics functions:

$$\Phi_A^i = \Phi_A^i(\alpha, z) = \sum_{n=1}^{n_{max}} \sum_{m=0}^n \tilde{P}_{nm}(\cos z) (a_{nm} \cos m\alpha + b_{nm} \sin m\alpha) \quad (6)$$

where α is the azimuth angle of the incoming signal (in the antenna system), z is the angle between the antenna normal vector and the LOS of the incoming signal, \tilde{P}_{nm} is the normalized associated Legendre polynomial of degree n and order m , and a_{nm} and b_{nm} are the coefficients to be estimated. The coefficient a_{00} correlates with the clock and the ambiguity term and is therefore not estimated.

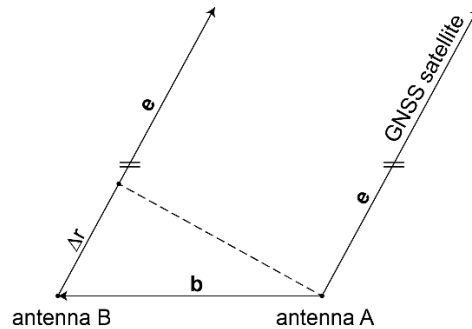


Fig. 1 Principle of interferometric attitude determination. Δr is a range difference between antenna A and B and \mathbf{b} is the baseline between those two antennas. For very short baselines, the two line-of-sight vectors to one GNSS satellite can be assumed to be parallel.

PCO AND PCV ESTIMATION

Three main classes of GNSS antenna calibration have been developed in the past: (i) absolute calibrations obtained with anechoic chamber measurements, (ii) absolute field measurements and (iii) relative field measurements.

In the case of absolute chamber measurements (i), the antenna is placed within an anechoic chamber and fed with a signal, either from a signal generator or from a GNSS repeater (Sims 1985, Tranquilla and Colpitts 1989, Schupler et al. 1994). Then, either the antenna is rotated or the source is moved, in order to measure phase variations for various elevations and azimuths.

In absolute field calibrations (ii), time-differences with a change in the antenna orientation between the two measurements involved in the time-difference are used. The main challenge is the elimination of multipath. In order to do so, either differences between subsequent sidereal days are taken (Wübbena et al. 1997), expecting the multipath to be identical when the GPS constellation repeats, or differences over a very short time-span are used (Wübbena et al. 2000), expecting the multipath to be highly correlated in time. In the latter case, a robot is used to perform fast and precise rotations of the antenna.

In relative field calibrations (iii), a very short baseline is setup and a differential processing is carried out. All baseline-length dependent errors, as atmospheric delays, ionospheric delays, and orbital errors are practically eliminated in the differencing process. The PCV model is fit to the data in order to minimize the observation residuals in a least squares sense. This calibration method provides a pattern which is relative to the second antenna involved in the baseline. (Rothacher et al. 1995)

Rothacher (2001) compared calibration values obtained with these three methods. In general, all three methods deliver comparable and reliable results, if carried out properly. Both absolute methods have the advantage to be practically free of multipath. Moreover, they deliver reliable calibration values for low elevations (in principle also for negative elevations). Field calibrations might be preferred, as real data is tracked with real equipment, but the need for a precise and fast robot is a considerable burden. On the other hand, the relative field calibration has the advantage that it is carried out more easily, but suffers from multipath.

Calibration procedure

A relative field calibration procedure for attitude systems was developed. The presented approach does not need any particular hardware except for a GNSS reference antenna and receiver. The impact of multipath on the results will be discussed later in this section.

For every antenna within the system, two to four sessions of 24 h of GNSS data were recorded. Between the sessions, the antennas were rotated by 90 degrees to cover the azimuths 0 degrees, 90 degrees, 180 degrees and 270 degrees, or by 180 degrees to cover two azimuths. Rotation of the antennas serves two goals: (i) without rotation, a part of the antenna phase pattern will never be probed by any satellite, due to north and south holes caused by the 55° inclination of the GPS orbits (Zurich is located at latitude 47.4° north), and (ii) the rotation decorrelates the PCO in north and east from the coordinates of the center of rotation of the antenna setup. Furthermore, rotation of the antenna mitigates the effect of multipath.

The data was post-processed with the Bernese GNSS Software V5.2 (Dach et al. 2015). A GNSS station of the Swiss GNSS Permanent Network AGNES (Automated GNSS Network for Switzerland 2017) served as reference station. The slant distance to the reference was 23.5 m. An absolute field calibration obtained by a robot was available for this antenna and used in the processing.

For every antenna of the attitude determination system, the processing based on double-differences included following steps:

- Preprocessing of the data (outlier elimination, cycle slip detection),
- Computation of a session-wise, static, ambiguity float solution using the reference station,
- Quality check and outlier detection based on the float solution,
- Ambiguity resolution and computation of a session-wise, static solution using the reference station,

- Writing of normal equations, introducing the previously resolved ambiguities and including PCO as unknown parameters.

This process resulted in two to 16 normal equation systems, depending on the number of antennas and the number of sessions processed together. In the example depicted in Figure 2, 16 normal equations are the result, as four antennas and four sessions (with four different azimuths) are processed together. The normal equations are then combined to estimate one set of coordinates (corresponding to the center of rotation) and PCO in north, east and up directions for every antenna. Within this process, the height of the center of rotation has been constrained to the mean value obtained from the baseline-wise solutions. This is necessary, as the PCO estimates in up direction and the station height cannot be separated. As a consequence, the PCO and PCV of the calibrated antennas are consistent to each other, but a common height offset to the reference antenna remains unknown. External height information would be needed to determine this height offset to the reference antenna. Once the coordinates of the center of rotation and the PCO are estimated, this information is introduced into the adjustment and PCV corrections are estimated. The spherical harmonics approach was preferred, as the number of unknowns is reduced for a similar resolution.

Calibration Setup

A calibration was undertaken with two different setups: (i) a model of the satellite (see Figure 2a) equipped with four passive L1 Amotech A18-4135920-AMT04 ceramic patch antennas (Amotech datasheet 2017) measuring 18 x 18 mm² and (ii) the experimental platform with three active L1 Trimble Bullet III antennas (Trimble Bullet III Datasheet 2015) shown in Figure 2b. The latter has the advantage of being modular: the antennas can be swapped to other positions or removed from the setup. In both cases, the length of all baselines is shorter than one GPS L1 wavelength. On the satellite model (i), the orthogonal baselines have a length of 6.5 cm and 5.7 cm and on the experimental platform (ii) all three baselines measure 15 cm.



Fig. 2 a) A model of CubETH during measurements for the PCV calibration. Four antennas are located on a common ground plane on the upper face. The side antenna (not used) is visible on the right side. Each antenna is connected to a u-blox GNSS receiver. **b)** Experimental setup for antenna attitude system calibration. The aluminum plate can be oriented with the help of the telescope. The three antennas of the type Trimble Bullet III can be freely turned and swapped to another location.

In both cases, u-blox receivers were used. As the Amotech antenna is passive, the cable length between the antenna and the receiver should not exceed 10 cm. Therefore, customized loggers, as visible at the bottom of Figure 2a, were used. These loggers are equipped with u-blox NEO 7 receivers (u-blox 7 Data Sheet 2014). The receiver's firmware was modified by u-blox in order to enable the output of raw GNSS data. In the case of the platform (ii), u-blox M8T evaluation kits were employed (u-blox EVK-M8T User Guide 2016). The latter output raw data per default.

Calibration Results

The first result obtained with the satellite model is the shrinking of the baselines. The mean PCO derived from the calibration procedure form baselines of 4.8 cm, 5.6 cm and 4.3 cm in length instead of 5.7 cm, 6.5 cm and 5.7 cm between the ARP. In this example, the baselines have been formed sequentially (antenna 2 minus antenna 1, and so on).

The PCV patterns obtained after calibration of the satellite model are shown in Figure 3. A spherical harmonics model of degree and order 8 was estimated. The overall observation noise (reduced to an L1 phase observation at zenith) is 5 mm. This value is surprisingly high but reflects the performance of the ceramic patch antennas on the satellite. Most terms of the spherical harmonics expansion are significant to $\pm 2\sigma$. The PCV corrections range from -8 mm to 26 mm. The standard deviation of the pattern lies below 1 millimeter in average and linearly increases from zenith to horizon. It reaches 3 mm at maximum. This standard deviation was obtained based on a full variance-covariance propagation. Therefore, all major structures seen in the patterns are significantly present in the data. Visual inspection of the patterns show large differences between each antenna and the absence of symmetry around the axis of the spacecraft (which is the point in between all for antennas). When looking at each individual antenna, again, no symmetry is apparent. A typical geodetic-grade antenna, for comparison, is expected to show PCV in the millimeter range and in the lower centimeter range for low elevations (Rothacher 2001).

The lower part of Figure 3 shows the estimated multipath for each individual antenna. Every session, with azimuth 0, 90, 180 and 270 degree, was processed separately and PCV corrections were estimated. Subsequently, the patterns were rotated back to make the north holes coincide and the mean value of the four patterns was formed. The result is a measure of the multipath, as the pattern will be averaged due to the four different rotations of the antenna. As the north hole is not sensed by any data, this region does not show meaningful results. Visual inspection shows that the magnitude of the multipath is lower than the magnitude of the PCV for antennas 1, 3 and 4. This information gives us confidence in the fact, that the patterns are only marginally influenced by multipath. The multipath pattern of antenna 2 shows magnitudes similar to the PCV corrections. The multipath pattern, after a rotation of 180 degrees, partly coincides with the PCV. The PCV corrections at low elevations might therefore be affected by multipath.

From these results, the hypothesis arose that the pattern is mainly dependent on the position of the antenna within the ground plane and not on the antenna itself. In order to verify this hypothesis, a calibration was conducted with the second setup (as seen in Figure 2b). The result of the calibration is displayed in Figure 4. Compared to the first setup, the quality of the measurements is improved. The overall observation noise is 2.6 mm. The PCV values range from -20 mm to 15 mm, which is a slightly smaller range than in the previous case. Visual inspection leads to the same conclusion as before; there is neither overall symmetry nor any symmetry for each individual antenna. In a second step, the same setup was calibrated again, but the antennas were permuted counterclockwise. The obtained patterns are depicted in Figure 5. They look surprisingly similar to the patterns before permutation of the antennas. For instance, the pattern of Antenna 3 in Figure 4 is very similar to the pattern of Antenna 2 in Figure 5. Table 1 shows the RMS of the differences between the PCV with and without permutation. When considering the permutation, the RMS is divided by two, making obvious that the pattern is more strongly dependent on its position on the ground plane than on the individual antenna.

Again, these results have to be interpreted with care due to possible pollution by multipath. The lower part of Figure 4 shows the multipath patterns. In this case, the multipath has magnitudes similar to the PCV. This is presumably due to the fact, that only data for two azimuths (0 and 180 degrees) is available for this setup. Keeping in mind that the rotation of the antennas during the determination of the PCV mitigates multipath, the results remain valid, but additional measurements would be necessary to definitively answer the question if the pattern is due to the close field (the influence of the other antennas) or the far field (classical multipath). In any case, the antenna exemplar plays little role, which is the main conclusion of this experiment.

Table 1 RMS of the differences in the PCV corrections with and without permutation.

	Figure 4	Figure 5	RMS [mm]
Antenna	1	2	2.54
Antenna	2	3	3.01
Antenna	3	1	2.23
Antenna	1	1	4.79
Antenna	2	2	5.54
Antenna	3	3	6.12

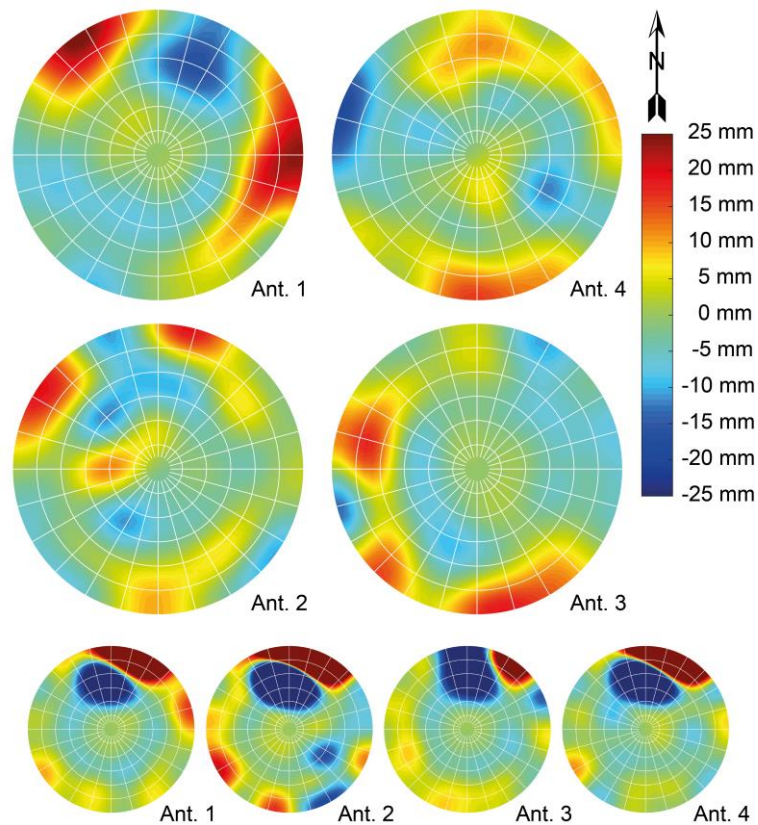


Fig. 3 Estimated PCV patterns for the satellite model shown in Figure 2a. The grid has a spacing of 15 degrees and the center of each Figure is the antenna normal vector. The PCV patterns are shown in the same manner as they are located on the model of the spacecraft. The lower row shows the multipath patterns for the four antennas.

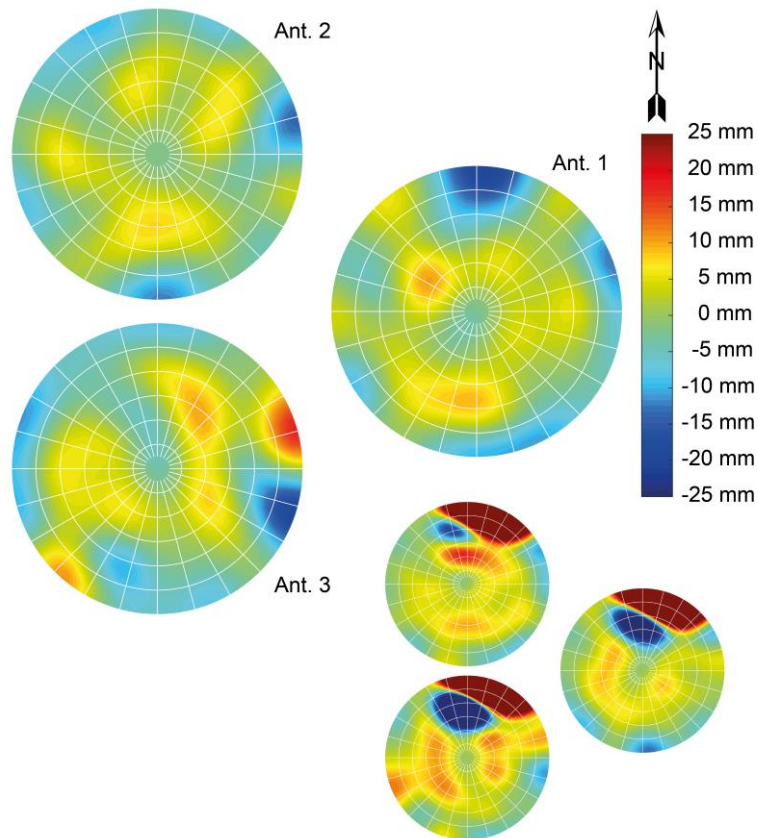


Fig. 4 Estimated PCV patterns for the experimental platform shown in Figure 2b. The grid has a spacing of 15 degrees and the center of each Figure is the antenna normal vector. The PCV patterns are shown in the same manner as they are located on the platform. The lower triangle shows the multipath patterns for the three antennas.

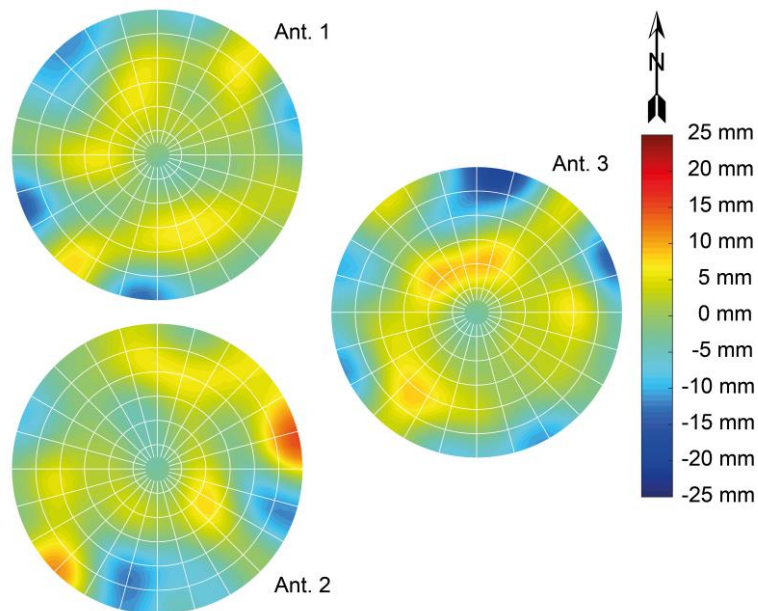


Fig. 5 Estimated PCV patterns for the experimental platform shown in Figure 2b, after permuting the antennas counterclockwise (1 -> 2, 2 -> 3, 3 -> 1). The grid has a spacing of 15 degrees and the center of each Figure is the antenna normal vector.

SIMULATION STUDY

In order to investigate the impact of the PCO and the PCV on the attitude estimation, a simulation with synthetic data was conducted. Data was generated with the Bernese GNSS Software V5.2 for four receivers on a spacecraft in a near circular, near polar LEO. Table 2 summarizes the main simulation parameters. During this process, four individual PCV and their PCO were introduced and applied to the simulated measurements. The PCV and the PCO were obtained in a field calibration (see previous section) with a model of the CubETH satellite (see Figure 2a). This data was then processed in a Kalman filter (Willi and Rothacher 2017). In *run 0*, a zero test was performed: the PCV which were used in the simulation were introduced in the filter and corrected for. In *run 1*, only the corrections of the ARP by the PCO were applied, but no PCV corrections. In *run 2*, neither the PCO nor the PCV were applied. Solely the ARP were used.

Results

A summary of the errors for *run 0*, which is the zero-test, is given in Table 3. The mean and the root mean square errors lie below 3 degrees. This value is comparable to results previously obtained (Willi and Rothacher 2017). The absolute error is the great circle distance between the ground truth and the estimation. This value can easily be computed, as the attitude can be represented as a point on a unit sphere.

The roll, pitch and yaw components are centered around zero. Roll and pitch have a similar precision of about 1.9 degrees. The yaw component is about twice as accurate. An uncertainty in height, as present in GNSS for geometrical reasons, does not affect the estimate of the yaw component. For this reason, the yaw component is more precise than the other two. Figure 6 shows the time series for roll, pitch and yaw and illustrates this statements.

As the PCV corrections are omitted, the accuracy of the attitude determination is degraded (Table 3). This is a typical case, as often only PCO are known, but no PCV. The increase in error is expected, as the PCV corrections show very large values, of up to 2.5 cm. The absolute error lies above 10 degrees. The roll, pitch and yaw components show RMS errors of about 9 degrees, 8 degrees and 4 degrees. Interestingly, the yaw component is not centered around zero anymore. This indicates an asymmetry in the PCV. The time series for roll, pitch and yaw are shown in Figure 7. Comparison with Figure 6 reveals that the time series are now time correlated.

Unsurprisingly, the accuracy is further deteriorated when omitting the correction of the PCO (Table 3). In this last scenario, the ARP are introduced in the filter. The absolute error increases to 30 degrees and the RMS error of roll, pitch and yaw now lies between 15 and 20 degrees. The yaw is clearly affected by an offset. This can be explained by the difference between the ARP and the ARP corrected for the PCO. A 2D Helmert transformation (Welsch et al. 2000) between the ARP alone, *as used in run 2*, and the ARP corrected for the PCO, reveals a rotation of 11 degrees +/- 4.5 degrees. This explains the bias in yaw.

Impact on the ambiguity resolution

The impact of neglecting the PCO and PCV corrections on the ambiguity resolution success rate was investigated as well. The results are summarized in Table 4. Single epoch ambiguity resolution was attempted for each of the first 1000 epochs in every run. An ambiguity resolution success rate of 100% was obtained in all three cases. The ambiguity validation ratio, which is the ratio between the RMS of the residuals of the second best and the RMS of the residuals of the best ambiguity candidate set, decreased from *run 0* to *run 1* and from *run 1* to *run 2*. This decrease is expected, since a degradation in the float solution produces a degradation of ambiguity resolution (Odijk and Teunissen 2008). This results shows that the initialization procedure of the filter can be carried out without PCV corrections, as the ambiguity resolution is robust with respect to missing PCV corrections. This is crucial, as at the time of initialization, no a priori information on the attitude is available.

Table 2 Main simulation parameters for data set 1 - synthetic data.

Data type	Synthetic GPS L1 carrier phase data	
Simulator	Bernese GNSS Software V5.2	
Orbit	Near circular LEO, 450 km height, 89 degree inclined	
GPS constellation	True constellation of year 2012 day 359	
Spacecraft attitude	Roll of -5 degrees, pitch of +5 degrees and yaw rate of +1 degree per sec	
PCV	Four individually estimated PCV for the four Amotech A18-4135920-AMT04	
Baselines	Mean phase centers* in the body frame [cm]	$\begin{pmatrix} 1.50 \\ -2.56 \\ -0.14 \end{pmatrix}, \begin{pmatrix} -3.25 \\ -2.14 \\ 0.14 \end{pmatrix}, \begin{pmatrix} -1.20 \\ 3.35 \\ -0.56 \end{pmatrix}, \begin{pmatrix} 2.91 \\ 3.45 \\ 0.48 \end{pmatrix}$
	Baselines	Antenna 1 – Antenna 2 Antenna 2 – Antenna 3 Antenna 3 – Antenna 4
	Length of baselines*	4.8 cm, 5.9 cm, 4.2 cm
Observations	5 mm standard deviation, 1 Hz data rate, 57 min and 50 sec length	

*the values are slightly different from those given in the previous chapter, as the calibration procedure was refined. The study was conducted with the old values, the previous section shows the final results.

Table 3 Mean and RMS errors in attitude determination for *run 0*, *run 1* and *run 2*

[degrees]	Run 0 (PCO and PCV applied)		Run 1 (PCO applied, PCV not applied)		Run 2 (PCO and PCV not applied)	
	Mean	RMS	Mean	RMS	Mean	RMS
Absolute error	2.45	2.81	11.53	12.98	29.77	31.44
Roll	-0.04	1.87	0.59	9.04	0.61	19.89
Pitch	0.08	1.94	-0.17	8.32	-3.94	20.00
Yaw	0.06	0.83	3.36	4.55	14.37	15.11

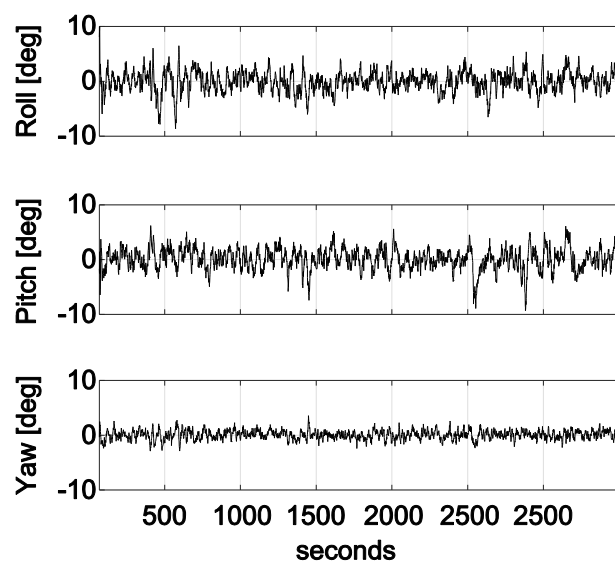


Fig. 6 Roll, pitch and yaw error for *run 0* (PCO and PCV correction applied).

VALIDATION WITH REAL DATA

The importance of PCV corrections has been demonstrated in the last section through a simulation study. In the present section, a real data experiment is undertaken, in order to validate the presented approach in a realistic environment. The test was carried out with a subset of the data which was collected to carry out the calibration. Although the validation uses data which has entered the calibration process, this approach is valid; the calibration was carried out using a static processing strategy with more than 24 h of data and thus eliminating all short periodic effects, whereas for the validation, a 1 Hz kinematic processing is performed. The dataset was acquired on April 10, 2017, from 08:54:40 (GPS time) to 23:59:59, with the platform shown in Figure 2b and three u-blox NEO M8T receivers.

Results

Again, three runs were performed. In *run 0*, PCO as well as PCV corrections were applied. This run is expected to deliver the best results. In *run 1*, only PCO were applied, but no PCV corrections. *Run 2* was performed introducing solely the theoretical (mechanical) phase centers into the filter prototype. In order not to bias the results, the same process noise and measurement noise settings were applied to all three runs. L1 carrier phase measurements were the only observables used in the filter. No outlier detection was performed. Phase ambiguities were solved for beforehand and introduced as fixed values.

The results of this comparative study are displayed in Table 5. Unsurprisingly, the accuracy of the attitude determination worsens with decreasing modelling accuracy. The mean error and the RMS lie below 5 degrees for *run 0* and increase to over 6 degrees for *run 2*. The roll, pitch and yaw angle series for *run 0* and *run 2* are shown in Figure 8.

The decrease in accuracy is less spectacular than in the simulation study. This is easily explained by the smaller magnitude of the patterns of the ensemble of the three Trimble Bullet III antennas compared to the patch antennas on the satellite model. The PCO are much smaller; a 2D Helmert transformation between the ARP and the ARP corrected by the PCO reveals a shift in x of 1.4 mm, a shift in y of -6.5 mm, a rotation of -1.7 degrees and a scale of 1.018. Furthermore, the experimental platform has significantly longer baselines than the satellite model, making it less sensitive to neglecting PCV corrections.

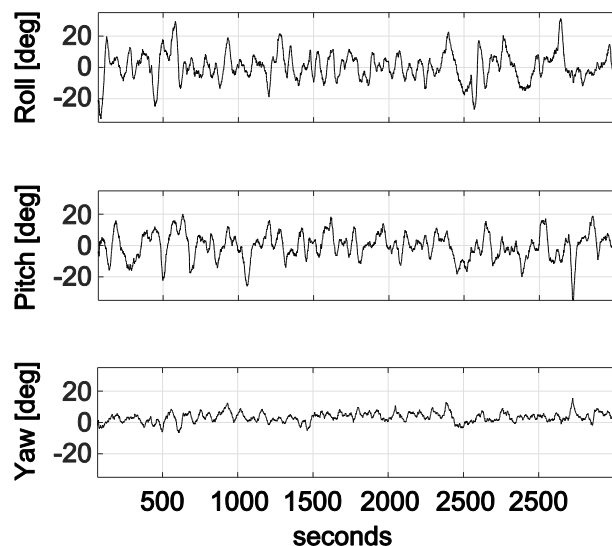


Fig. 7 Roll, pitch and yaw error for run 1 (PCO applied, PCV not applied).

Table 4 Ambiguity resolution success rate and ambiguity validation ratio for the three runs.

	Ambiguity resolution success rate	Ambiguity validation ratio		
		Mean	Quantiles	
			25%	75%
<i>Run 0</i> (PCO and PCV applied)	100%	6.87	5.50	7.78
<i>Run 1</i> (PCO applied, PCV not applied)	100%	4.84	3.68	5.61
<i>Run 2</i> (PCO and PCV not applied)	100%	4.57	3.53	5.23

Table 5 Mean and RMS errors for *run 0*, *run 1* and *run 2*

	<i>Run 0</i> (PCO and PCV applied)		<i>Run 1</i> (PCO applied, PCV not applied)		<i>Run 2</i> (PCO and PCV not applied)	
	Mean	RMS	Mean	RMS	Mean	RMS
[degrees]						
Absolute error	4.04	4.53	5.09	5.87	5.50	6.33
Roll	0.37	2.92	1.13	3.65	1.23	3.98
Pitch	-0.96	3.30	-0.89	4.42	-1.08	4.61
Yaw	0.21	1.08	0.08	1.29	1.14	1.76

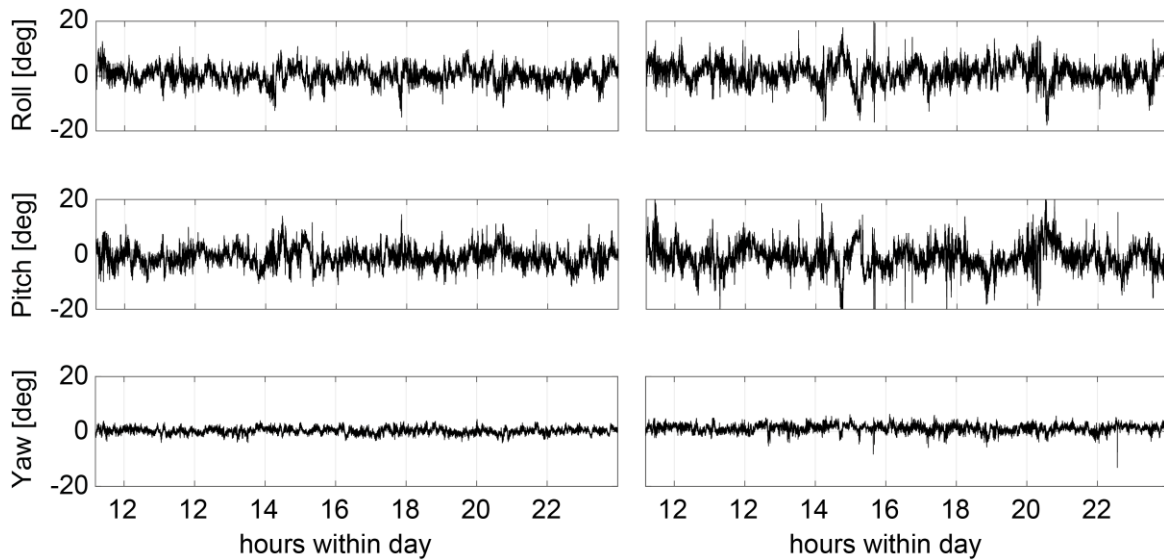


Fig. 8 Time series of roll, pitch and yaw errors for *run 0* (on the left) and *run 2* (on the right). The maximal errors are 15, 15 and 4 degrees for *run 0* and 21, 30 and 4 degrees for *run 2*.

CONCLUSIONS AND OUTLOOK

Relative antenna field calibrations for attitude determination systems with very short baselines were successfully obtained. The calibration of the satellite model showed unexpected large PCV. Permutation of the antennas on the experimental platform revealed that the antenna pattern is not only driven by the antenna itself, but mainly by its location on the ground plane. The chosen field calibration suffers from multipath and additional investigations are required to assess its impact on PCV.

A simulation study showed the importance of proper calibration values in the attitude estimation process on a small spacecraft. In the case of CubETH, the mean error decreased from around 30 degrees to below 3 degrees when the phase center offset and the phase center variations were correctly calibrated and applied. The ambiguity resolution process however is robust; ambiguities can be fixed without the need to apply antenna corrections.

Finally, a real data validation was performed. It demonstrated the feasibility of attitude determination with very short baselines and showed the importance of antenna calibration in a realistic scenario. The root mean square error could be reduced from 6.33 degrees to 4.53 degrees on a platform with three baselines of 15 cm.

These preliminary results are very encouraging, but many questions remain open. A step towards a more precise attitude determination system was made, but the accuracy inherent to the system has probably not been reached yet. It would be extremely valuable to compare the relative calibrations either to robot or to anechoic chamber measurements. This would also allow to definitively quantify the effect of multipath on the current procedure.

Moreover, additional investigations are necessary to better characterize phase patterns of antenna systems and especially low-cost antennas. The present work showed that ceramic patch antennas have extremely variable patterns. It is questionable, whether classical phase center variation models are well suited to reflect this behavior and whether the calibrations are stable in time. The final question is whether these calibrations are applicable to a spacecraft actually orbiting the Earth. Flight data which is expected for beginning of 2018 might give the answer.

ACKNOWLEDGMENTS

We would like to thank Robert Presl for the great hardware support, which was essential for the realization of the present study. This work was supported by ETH Research Grant ETH-43 14-2.

REFERENCES

Amotech datasheet (2017)

[http://www.amotech.co.kr/Data/uploads/antenna/01%20GPS%20Antenna/GPS_Glonass/Datasheet_A18-4135920-AMT04\(Rev_0\).pdf](http://www.amotech.co.kr/Data/uploads/antenna/01%20GPS%20Antenna/GPS_Glonass/Datasheet_A18-4135920-AMT04(Rev_0).pdf), accessed 13.06.2017

Automated GNSS Network for Switzerland (2017) <http://pnac.swisstopo.admin.ch/pages/en/agnes.html>, accessed 13.06.2017

Birmingham WP, Miller BL, Stein WL (1983) Experimental results of using the GPS for Landsat 4 onboard navigation. *Navigation* 30(3):244–251

Cohen CE, Lightsey EG, Parkinson BW, Feess WA (1994) Space flight tests of attitude determination using GPS. *International Journal of Satellite Communications* 12:427-433

Dach R, Lutz S, Walser P, Fridez P (eds.) (2015) Bernese GNSS Software Version 5.2. Software user manual, Astronomical Institute, University of Bern

Ivanov AB, Masson LA, Rossi S, Belloni F, Mullin N, Wiesendanger R, Rothacher M, Hollenstein C, Männel B, Willi D, Fisler M, Fleischmann P, Mathis H, Klaper M, Joss M, Styger E (2015) CubETH: Nano-Satellite Mission for Orbit

and Attitude Determination Using Low-Cost GNSS Receivers. IAC-15,B4.4.5 . In 66th International Astronautical Congress, Jerusalem, Israel

Odiik D, Teunissen PJG (2008) ADOP in closed form for a hierarchy of multi-frequency single-baseline GNSS models. *J Geod*, 82(8):473-492

Rothacher M (2001) Comparison of absolute and relative antenna phase center variations. *GPS Sol*, 4(4):55-60

Rothacher M, Schaer S, Mervart L, Beutler G (1995) Determination of antenna phase center variations using GPS data. In Gendt G, Dick G (Eds) *Special Topics and New Directions, 1995 IGS Workshop*. Potsdam, Germany, pp. 205–220

Schmitz M, Wübbena G, Boettcher G (2002) Tests of phase center variations of various GPS antennas, and some results. *GPS Sol*, 6:18–27

Schupler BR, Allshouse RL, Clark TA (1994) Signal characteristics of GPS user antennas. *Navigation*, 41(3):276–296

Sims ML (1985) Phase center variation in the geodetic TI4100 GPS receiver system's conical spiral antenna. In *Proceedings of the first International Symposium on Precise Positioning with the Global Positioning System*, Rockville, Maryland, USA, pp. 227–244.

Tranquilla JM, Colpitts BG (1989) GPS antenna design characteristics for high-precision applications. *Journal of Surveying Engineering*, 115(1):2–14

Trimble Bullet III Datasheet (2015) Trimble Bullet™ III GPS Antenna – Datasheet. Trimble Limited, Sunnyvale, California, USA. http://trl.trimble.com/docushare/dsweb/Get/Document-8420/Bullet-III_DS.pdf, accessed 13.06.2017

u-blox 7 Data Sheet (2014) R07. u-blox, Thalwil, Switzerland. https://www.u-blox.com/sites/default/files/products/documents/NEO-7_DataSheet_%28UBX-13003830%29.pdf, accessed 13.06.2017

u-blox EVK-M8T User Guide (2016) R04. u-blox, Thalwil, Switzerland. https://www.u-blox.com/sites/default/files/products/documents/EVK-M8T_UserGuide_%28UBX-14041540%29.pdf, accessed 13.06.2017

Um J, Lightsey EG (2001) GPS attitude determination for the SOAR experiment. *Navigation* 48(3):181-194

Welsch W, Heunecke O, Kuhlmann H (2000) *Auswertung geodätischer Überwachungsmessungen*. Wichmann Verlag, Heidelberg, Germany.

Willi D, Rothacher M (2017) GNSS attitude determination with non-synchronized receivers and short baselines onboard a spacecraft. *GPS Sol*, submitted

Wübbena G, Schmitz M, Menge F, Böder V, Seeber G (2000) Automated absolute field calibration of GPS antennas in real-time. In *Proceedings of the International Technical Meeting, ION GPS-00*, Salt Lake City, Utah, USA.

Wübbena G, Schmitz M, Menge F, Seeber G, Völksen C (1997) A New Approach for Field Calibration of Absolute GPS Antenna Phase Center Variations. *Navigation*, 44(2):247–255

Appendix C

Paper III

Title	Calibration of a Six-Axis Robot for GNSS Antenna Phase Center Estimation
Authors	Daniel WILLI, Sébastien GUILLAUME
Journal	Journal of Surveying Engineering
Manuscript	SUENG-934R1
Status	Submitted, in review

The reprint is allowed according to the American Society of Civil Engineers Publication Policies.¹. This was confirmed by Leslie Connelly (e-mail from 4 December 2018).

¹<https://ascelibrary.org/doi/pdf/10.1061/9780784479018.ch03>

CALIBRATION OF A SIX-AXIS ROBOT FOR GNSS ANTENNA PHASE CENTER ESTIMATION

Daniel Willi¹ and Sébastien Guillaume²

¹PhD student , ETH Zurich , Institute of Geodesy and Photogrammetry (IGP) , E-mail: daniel.willi@geod.baug.ethz.ch

²Dr. , ETH Zurich , Institute of Geodesy and Photogrammetry (IGP)

ABSTRACT

We show that the scatter of the coordinates of the tool of an uncalibrated KUKA Agilus KR 6 R900 sixx lies between 0.5 to 0.7 mm if the same point is approached several times, but with different tool orientations. In order to use the robot for GNSS antenna calibration, the standard deviation of the coordinates must lie below 0.1 mm. We developed a calibration procedure based on the optical micro-triangulation system QDaedalus and a kinematic model of the robot. The proposed calibration is easy to carry out and highly automatic. Several measurement campaigns including a validation demonstrated that the calibration reduces the standard deviation of the coordinates to below 0.1 mm, making the robot suitable to use for GNSS antenna calibrations.

INTRODUCTION

The Institute for Geodesy and Photogrammetry (IGP) at ETH Zurich acquired a six-axis industrial robot of type KUKA Agilus KR 6 R900 sixx (Kuka 2018, see Figure 1), with the goal to perform calibrations of Global Satellite Navigation System (GNSS) antennas. The robot is used to position the antenna in various orientations, while an arbitrary point of the antenna is kept fixed in space. The purpose of the rotation of the antenna is to cover the entire antenna hemisphere with observations and to decorrelate the antenna dependent effects from the site dependent effects, for instance multipath (Willi et al., 2018). Therefore, at least two rotations axes are required. Calibrations have been performed with two-axis robots in the past (Bilich and Mader, 2010), but five- or six-axis robots are theoretically superior. They allow to keep an arbitrary point of the antenna fixed in space, in opposition to two-axis robots. The advantage is that the nominal coordinates of the GNSS antenna to be calibrate remain unchanged during the GNSS antenna calibration, ensuring a constant nominal observation geometry.

The de facto standard for GNSS antenna calibrations is the German company Geo++ (Wübbena et al., 2000; Schmitz et al., 2002). Geo++ uses a 5-axes robot. Their system was developed in collaboration by the Institut für Erdmessung (IfE) at the Leibniz University Hanover, which still uses

the system (Menge, 2003; Kersten, 2014). The Geo++/IfE system is in use in the State Surveying Agency of Berlin in Germany (Landeskalibriereinrichtung, <https://www.stadtentwicklung.berlin.de/geoinformation/landesvermessung/landeskalibriereinrichtung/index.shtml>) and in Australia (Riddell et al., 2015). The National Geodetic Survey (NGS) recently acquired a six-axes robot KUKA KR60 HA (Bilich et al., 2018). Wuhan University develops a system for antenna calibration as well (Hu et al., 2015), apparently using a robot with 5 or 6 axes.

Accuracy requirement

According to the manufacturer, the repeatability of the KUKA robot is 0.03 mm (Kuka, 2018), but no indications about the accuracy or the precision is provided. The term robot postures designates the configuration in which the robot is, for instance elbow up or elbow down. Serial manipulators with ortho-parallel basis and a spherical wrist, as the KUKA Agilus KR 6 R900 sixx, have eight different postures to reach the same point with the same tool orientation (Brandstötter et al., 2014). Throughout this paper, we will use the term repeatability for the quantity which measures the ability of the robot to reach the same coordinates, with the same orientation and the same posture; precision will be used to quantify the ability of the robot to reach the same coordinates with the same posture, but with different orientations (this is the ability needed for antenna calibration); and finally, accuracy will be employed to quantify the ability of the robot to reach any point in any orientation and any of the eight posture.

In order to be suitable for GNSS antenna calibration, the precision of the positioning of the robot should be 0.1 mm (standard deviation). The accuracy does not matter, since the GNSS observations will be time-differentiated. Therefore, only the ability of the robot to reach the same coordinates but with various orientations is of interest, best represented by the standard deviation of the positions. Since a millimeter-level accuracy is targeted for the GNSS antenna calibration, the standard deviation of the robot positioning should be an order of magnitude smaller, namely 0.1 mm. The requirement of an accuracy of 1 mm or better for antenna calibration is motivated by the phase noise of GNSS measurements, which is typically around 1 mm (Teunissen and Montenbruck, 2017, p. 579). Accordingly, antenna calibrations are exchanged using the ANTEX format (Rothacher and Schmid, 2010), which provides a resolution of 0.1 mm.

State of the art in robot calibration

The Geo++ robot is calibrated using a micro-triangulation measurement system (Menge, 2003). The calibrated robot reaches an accuracy of 0.2 to 0.3 mm and includes joint elasticity coefficients. The NGS robot was individually calibrated at the factory, which should result in an accuracy of 0.2 mm. The on-site accuracy was not verified yet (Bilich et al., 2018).

Calibration of industrial robot is a standard procedure in industry (Schröer, 1999; Siciliano and Khatib, 2008). The fit of a kinematic model into reference measurements is common to nearly all calibrations. Schröer et al. (1997) presents a good overview on various kinematic models. Examples of measurement techniques include laser tracker (Allman et al., 2018) or vision based systems (Motta et al., 2001). Some authors do also model the elasticity of some joints of the robot and backlash effects, e.g. Nubiola and Bonev (2013). Most of the authors make use of the so called Denavit-Hartenberg convention (which will be introduced in the next section). The quality improvement depends on how close the robot corresponds to the nominal geometry. After calibration, most publications mention an accuracy around 0.1 mm, which represents an improvement by up to one order of magnitude.

Outline

A robot calibration achieving the targeted precision of 0.1 mm in the whole robot operation space would be very cumbersome and unnecessary in the context of antenna calibration with a robot. Therefore, we propose a novel method specifically designed for the calibration of a robotic arm used for GNSS antenna calibration. The principle is to use the exact same sequence for the calibration of the KUKA robot as will be used later to calibrate GNSS antennas. This approach requires some adaptations in the mathematical model, which are presented in the next section. In the second section, the robot calibration procedure is presented, followed by an introduction to the optical micro-triangulation system used within this study. The results section is preceded by the description of the calibration and validation campaigns.

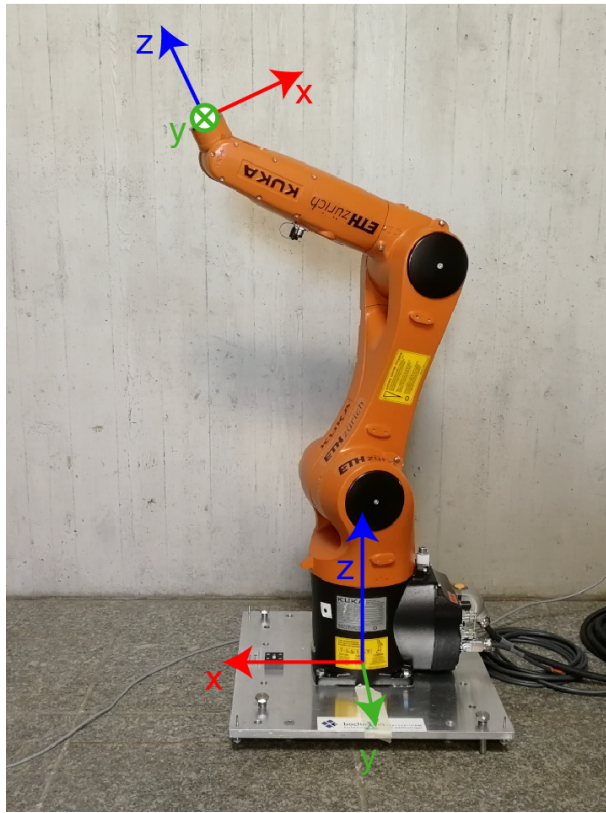


Fig. 1. Industrial robot KUKA Agilus KR 6 R900 sixx, mounted on an aluminum plate allowing to mount it on the roof of the Institute and to handle the robotic arm more easily. Handles can be attached to both side of the plate. The coordinate system at the base of the robot is the robot coordinate system. It is centered at the intersection of the first axis and the bottom of the robot base. The coordinate system at the robot flange is the tool coordinate system. It is centered at the robot flange. The origin and the orientation of the tool coordinate system is a function of the angular position of the six axes of the robot.

KINEMATIC MODEL OF THE ROBOT

In the following section, three different coordinate systems will be referred to: world coordinates (or world frame), robot coordinates (or robot frame) and tool coordinates (or tool frame). The world coordinate system can be any global or local coordinate system. World coordinates are independent of the robot. Examples for world coordinates can be WGS84 or the local level frame. In the present case, it was chosen to work in a local level frame. Robot coordinates refer to a coordinate system which is attached to the base of the robot (see Figure 1). The robot coordinate system is centered at the intersection of the first robot axis and the bottom of the robot base. The tool coordinate system is attached to the flange of robot and centered at the intersection of axis six and the surface of the flange (see Figure 1). The coordinate transformation from the world coordinate system to the robot coordinate system will describe where and with which orientation the robot is mounted. The coordinate transformation between the robot coordinate system and the tool coordinate system is a useful parameter when trying to control the robot, because it is a function of the angular positions of the six robot axes.

Forward kinematics is the task of computing the coordinate transformation between the robot coordinate system and the tool coordinate system from the angles of each axis. This transformation can be represented as homogeneous transformation, as it comprises three rotations and three translations. Every individual link and joint pair can be modeled as a homogeneous coordinate transformation as well. The transformation from the robot base system to the tool system is then simply the product of the individual transformations.

In principle, three translation parameters and three rotation parameters would be required for every link and joint pair, but by attaching the successive coordinate frames in a certain manner, this can be broken down to two rotations and two translations, the so called Denavit-Hartenberg (DH) parameters (Corke, 2017). Figure 2 shows the position of all six coordinate system of the KUKA: The Z axis is always parallel to the rotation axis of the joint, θ is the rotation around the Z axis and α is the rotation around X. The non-zero length parameters a and d and the angle conventions are shown in Figure 3. The full DH parameter set for the KUKA Agilus KR 6 R900 sixx, derived from this previous illustrations, is summarized in Table 1. If these parameters are used to compute the position of the tool out of the angular readings output by the KUKA controller, the obtained coordinates are identical to the coordinates output by the KUKA controller. This indicates that the KUKA controller uses the nominal geometry for internal computations.

More detailed information about how to derive the parameters for this kind of robot can be found in various online resources (P. Corke, “Denavit-Hartenberg notation for common robots”, http://www.petercorke.com/doc/rtb_dh.pdf, 2014; F. Abelbeck, “Koordinatentransformation nach Denavit-Hartenberg am Beispiel eines KUKA KR16”, https://abelbeck.files.wordpress.com/2015/11/uebung_dh-trafo_300dpi.pdf, 2008).

The steering variable Θ is the angular reading of the robot. The signs were adapted in order to fit the KUKA convention. The angle offsets read $\delta\Theta$. Again, there are needed for conventional reasons. The angle between two successive axes is α . This angle equals 0 if the two axes are parallel. The length of a link is represented by a and the link offset is represented by d . With this

model, the coordinates and the attitude of the flange read:

$$\mathbf{T} = \prod_{i=0}^6 \mathbf{T}_i = \left(\begin{array}{ccc|c} \mathbf{R}_{w \leftarrow f} & & & \mathbf{u}_w \\ \hline 0 & 0 & 0 & 1 \end{array} \right) \quad (1)$$

Where \mathbf{T} is the homogeneous transformation matrix, \mathbf{T}_i is the homogeneous transformation associated to link and joint i , $\mathbf{R}_{w \leftarrow f}$ is the rotation matrix from the coordinate system attached to the flange (denoted with f) to the world frame (denoted with w) and \mathbf{u}_w is the coordinates of the center of the flange, expressed in world coordinates. For $i \in [1, 2, 3, 4, 5, 6]$, \mathbf{T}_i reads:

$$\mathbf{T}_i = \left(\begin{array}{cccc|c} \cos(\Theta_i + \delta\Theta_i) & -\sin(\Theta_i + \delta\Theta_i) \cos \alpha_i & \sin(\Theta_i + \delta\Theta_i) \sin \alpha_i & a_i \cos(\Theta_i + \delta\Theta_i) & \\ \sin(\Theta_i + \delta\Theta_i) & \cos(\Theta_i + \delta\Theta_i) \cos \alpha_i & -\cos(\Theta_i + \delta\Theta_i) \sin \alpha_i & a_i \sin(\Theta_i + \delta\Theta_i) & \\ 0 & \sin \alpha_i & \cos \alpha_i & d_i & \\ 0 & 0 & 0 & 1 & \end{array} \right) \quad (2)$$

The parameters in this equation are the DH parameters. The values of the DH parameters can be found in Table 1. The transformation matrix from robot centered coordinates to world coordinates is \mathbf{T}_0 . If it is set to the identity matrix, the coordinates obtained from Eq. 1 lie in the coordinate system attached to the origin of the robot. To obtain coordinates in the world frame, \mathbf{T}_0 is set to:

$$\mathbf{T}_0 = \left(\begin{array}{ccc|c} & & & t'_x \\ \mathbf{R}_{w \leftarrow r} & & & t'_y \\ & & & t'_z \\ \hline 0 & 0 & 0 & 1 \end{array} \right) \quad (3)$$

Where $\mathbf{R}_{w \leftarrow r}$ is the rotation matrix rotating from the robot coordinate frame to the world coordinate frame and t'_x , t'_y and t'_z are the position of the robot in the world coordinate frame. The rotation matrix can be obtained from an Euler angle sequence:

$$\mathbf{R}_{w \leftarrow r} = \mathbf{R}_1(\gamma') \mathbf{R}_2(\beta') \mathbf{R}_3(\alpha') \quad (4)$$

With α' , β' and γ' being the Euler angles of the robot in the world frame. Typically, a tool is mounted on the robot flange. The coordinates of the tool are obtained after an additional step:

$$\mathbf{t} = \mathbf{u}_w + \mathbf{R}_{w \leftarrow t} \begin{pmatrix} t_x \\ t_y \\ t_z \end{pmatrix} \quad (5)$$

Where t_x , t_y and t_z are the tool offsets in the tool frame and $\mathbf{R}_{w \leftarrow t}$ is the tool orientation. Again, the tool orientation matrix could be obtained from an Euler sequence as in Eq. 4.

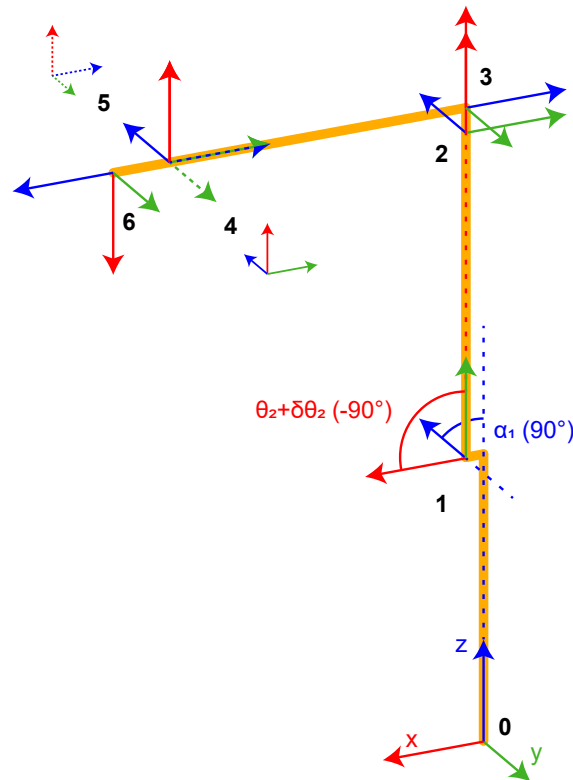


Fig. 2. Position of the six link coordinate systems in the DH convention applied to the KUKA Agilus KR 6 R900 sixx. The Z axis is always parallel to the rotation axis of the joint. The rotation around the X axis between the coordinate system 0 and 1 is represented by α_1 , the rotation around the Z axis between the coordinate system 1 and 2 is represented by $\theta_2 + \delta\theta_2$. The term $\delta\theta_2$ is present for conventional reasons. The coordinate transformation between coordinate system 0 and coordinate 6 is the result of the direct kinematics. Inverse kinematics consists of finding θ_1 to θ_6 if the coordinate transformation is given.

Table 1. Nominal DH parameters for the KUKA Agilus KR 6 R900 sixx. The parameters are derived from the geometry of the robot, which can be found in [Kuka \(2018\)](#)

	Θ [rad]	$\delta\Theta$ [rad]	α [rad]	a [mm]	d [mm]
1	$-\theta_1$	0	$\pi/2$	25	400
2	$-\theta_2$	0	0	455	0
3	$-\theta_3$	$\pi/2$	$-\pi/2$	35	0
4	θ_4	0	$\pi/2$	0	-420
5	$-\theta_5$	0	$-\pi/2$	0	0
6	θ_6	π	π	0	-80

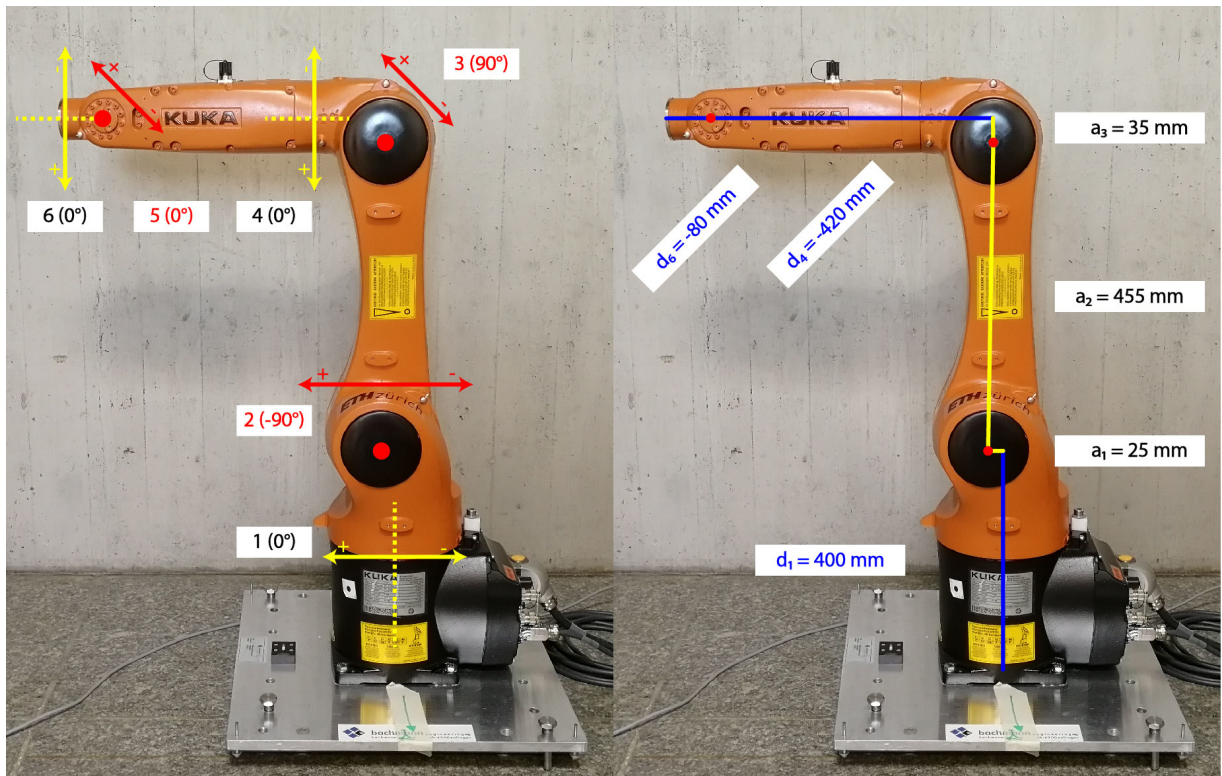


Fig. 3. Angle conventions (left) and non-zero DH length parameters (right) of the KUKA robot.

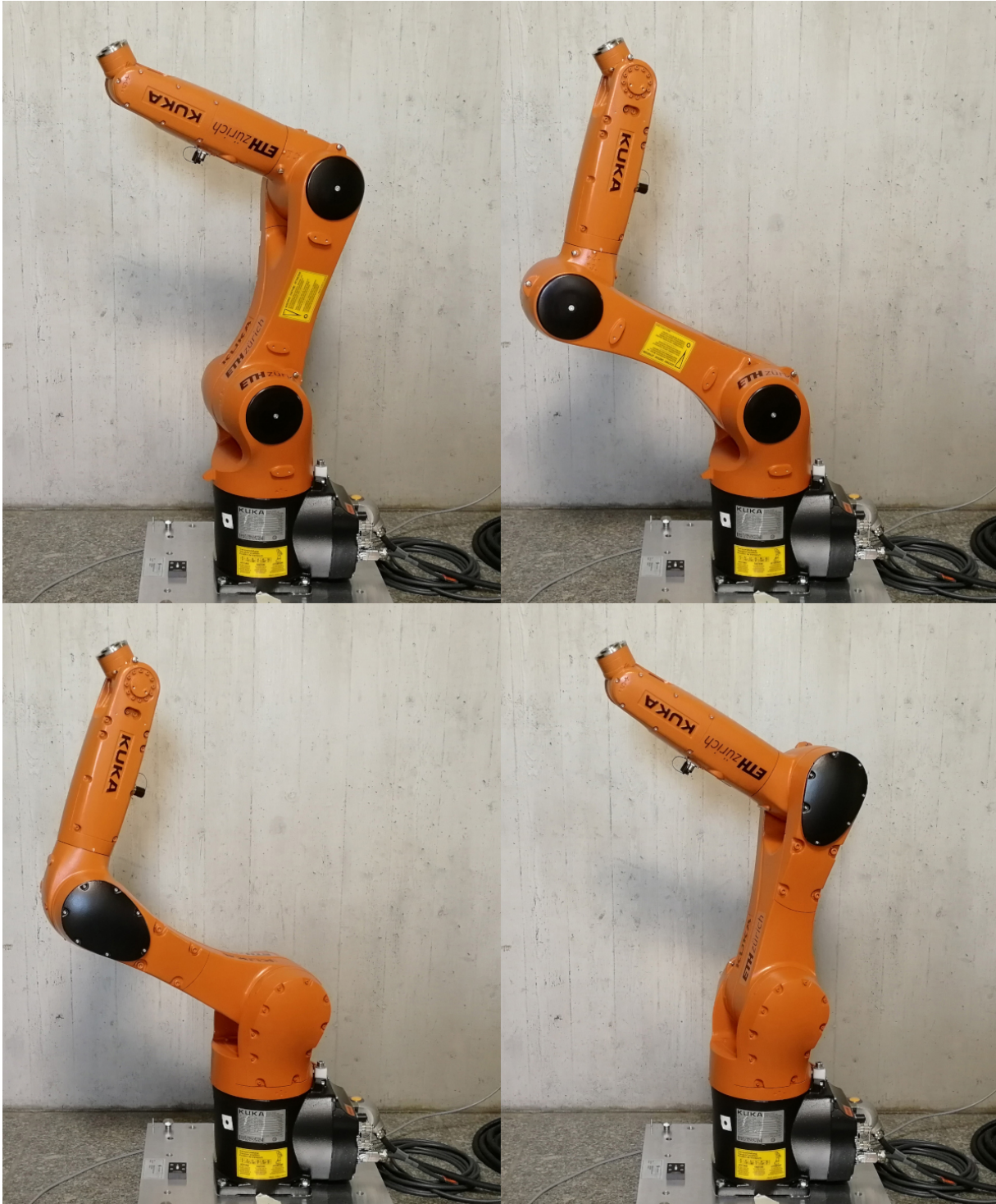


Fig. 4. Four of the eight possible postures to reach the same point with the same tool orientation.

ROBOT CALIBRATION PROCEDURE

A robot calibration procedure was developed specifically for the present application. The robot calibration is based on the estimation of geometrical parameters of the KUKA robot. The values given in Table 1 represent the nominal values that can be derived from the data sheet of the KUKA (Kuka, 2018). As the geometry of the robot does not perfectly correspond to the nominal geometry, these parameters are subject to errors. The actual value of these parameters must be estimated in the robot calibration procedure, additionally to the position and orientation of the robot in the world coordinate frame. Therefore, an adjustment was performed to estimate these 36 parameters. The list of estimated parameters is given in Table 3.

Main robot calibration sequence

The robot calibration sequence consists of 1440 different orientations and results from a grid with 7.5 degree steps in azimuth and 5 degree steps in zenith angle from 0 degrees (the antenna is horizontal) to 70 degrees. During the sequence, the coordinates of the tool are kept constant at the nominal value of $(-364.9\text{mm}, 163.9\text{mm}, 1120\text{mm})$ in the robot coordinate system. The coordinates of this point fixed in space could be arbitrary, but they are chosen in order to reduce the overall movement every axis has to perform to run through the whole sequence. The tool offset in z of 83 mm serves as approximation and was measured with a ruler. This sequence is identical to the sequence which is used during the calibration of GNSS antennas. The order of the orientations is randomized in order to avoid any effects correlated in time. During the robot calibration, the angle readings of the KUKA are recorded by the robot control system and the coordinates of the tool are measured with the image-based micro-triangulation system QDaedalus, described in the next section. The use of the same sequence as for the calibration of GNSS antennas makes the robot calibration very efficient. However, a full decorrelation of all DH parameters will not be reached. Therefore, the robot calibration obtained in that way is valid only to correct a rotation sequence consisting of the exact same points (same coordinate, same posture, but various orientations).

Robot position and orientation

In addition to the main sequence, eight positions distributed in all four quadrants are measured. Otherwise, the orientation of the robot in the world frame would be singular and could not be estimated. In principle, three points would be sufficient to estimate the orientation of the robot, but eight points are preferred because they are well distributed in the operation space of the robot. The coordinates of the eight positions are given in Table 4. These eight points are used to estimate parameters 31 to 36. From now on, α' , β' and γ' are taken over from this first estimation and constrained to the estimated values in every consecutive step. This is necessary, as the eight additional points are not introduced in the next processing steps anymore. The term $\delta\Theta_1$ was constrained to zero as well, as it correlates with the orientation of the robot in the world frame and therefore with α' . The parameters t'_x , t'_y and t'_z are still present however, and will absorb any offset between the actual calibration sequence consisting of 1440 points and the eight additional points.

The separation of the main robot calibration sequence from the estimation of the robot position and orientation leads to much more flexibility. If the robot is installed permanently at a location, the estimation of the position and the orientation needs to be performed only sporadically, whereas the estimation of the DH parameters with the main sequence should be performed more often. Our calibration strategy offers the flexibility to do so.

Temperature effects and robot elasticity

Temperature variations are expected to have an impact on the robot. A simulation was conducted assuming a thermal expansion coefficient of $20 \cdot 10^{-6} \text{ K}^{-1}$ and a temperature difference of 20 degrees for all links of the robot. The results are displayed in Table 2. The simulation reveals the presence of a systematic bias of nearly 0.5 mm in Z but no significant increase of the standard deviation. Therefore, the thermal dilatation can safely be neglected, keeping in mind that an important temperature change during the sequence would still have an effect. The general insensitivity is explained by the small dimensions of the robot and the limited variety of movements executed during the main robot calibration sequence.

Drift in the offset (or the zero reading) of the angular readings is a well known phenomenon from total stations. However, there is no obvious relation between the temperature and the offset. The design of this study does not allow to investigate such effects. Therefore, no temperature dependent offset drift was assumed. Only a study in a climate chamber would allow to study this effect in more detail.

Some authors included models for the elasticity of the robot joints in their parametrizations (Nubiola and Bonev, 2013). The impact of joint elasticity in the context of GNSS antenna calibration is expected to be very small, because the robot is used to execute always the same position, with a change in orientation only. The second axis, for instance, is only operated in a range from -78 deg to -114 deg during the chosen main calibration sequence. Furthermore, changes in the mass of the robot payload (the mass of the GNSS antenna during GNSS antenna calibration) are expected to have an impact mainly on the accuracy, but not on the precision. Therefore, the hypothesis is emitted that the robot joint elasticity can be neglected.

Constraining and regularization

Several robot calibration parameters correlate with each other. As the goal of the whole procedure is to obtain a small variance of the positions, parameters correlating with the absolute position of the robot are not of direct interest. The tool offsets t_x , t_y and t_z strongly correlate with a_6 , α_6 and d_6 respectively. Singularities were avoided by constraining these three tool offsets to fixed values. The procedure for offset estimation is presented in the next section. The tool orientation (α , β and γ) is never observed, as the tool consists of a single point. Therefore, the tool orientation was constrained to zero as well. In summary, the parameters 7, 25 to 30 and 34 to 36 (see Table 3) are constrained and 26 parameters are estimated. With the chosen geometry, it is not possible to fully decorrelate all remaining parameters from each other, as the robot is kept in the same pose all the time. A posture is a way to reach a certain position with a given orientation. Six-axis robots have eight possible postures to reach a the same point, as is illustrated in Figure 4. Changing posture during the GNSS antenna calibration is not desired because of the antenna cable (our experience shows that changes of twist of the cable) and in order to keep the travel time between two orientations as succinct as possible. Keeping in mind that a full decorrelation is not of interest, as the goal of the procedure is to reduce the variance of the positions and not to obtain robot parameters, this method provides a very efficient way to reach this goal. Being unable to fully decorrelate the parameters, a regularization was added by introducing the nominal parameters as pseudo-observations with the weights shown in Table 5. The weights were chosen to reflect the expected mechanical uncertainty, for instance 0.1 mm for length parameters. Empirical tests confirmed this choice.

Table 2. Standard deviation (STD) and Root Mean Square (RMS) error of the robot positions acquired on 18.4.2018 without and with a simulated dilatation of all links assuming a thermal expansion coefficient of $20 \cdot 10^{-6} \text{ K}^{-1}$ and a temperature difference of 20 degrees. Temperature change leads to a bias but does not significantly increase the scatter of the measurements.

	X [mm]	Y [mm]	Z [mm]
STD Reference	0.095	0.096	0.064
STD Reference + 20 deg	0.095	0.096	0.064
RMS Reference	0.095	0.096	0.064
RMS Reference + 20 deg	0.130	0.153	0.428

Table 3. KUKA robot calibration model parameters.

1 to 6	$\delta\Theta_1$ to $\delta\Theta_6$	Axis angle offsets
7 to 12	α_1 to α_6	DH parameters α
13 to 18	a_1 to a_6	DH parameters a
19 to 24	d_1 to d_6	DH parameters d
25 to 27	t_x, t_y, t_z	Tool offsets in x, y and z
28 to 30	α, β, γ	Tool orientation as Euler sequence
31 to 33	t'_x, t'_y, t'_z	Robot coordinates in the world frame
34 to 36	α', β', γ'	Robot orientation in the world frame as Euler sequence

Table 4. List of the 8 additional points measured to estimate the orientation and the coordinates of the robot in the world frame.

	x [mm]	y [mm]	z [mm]
1 (5)	400	400	900 (1100)
2 (6)	-400	400	900 (1100)
3 (7)	400	-400	900 (1100)
4 (8)	-400	-400	900 (1100)

Table 5. Weights for the regularization.

parameter	weight	unit
$\delta\Theta$	10^{-2}	rad
α	10^{-3}	rad
a	10^{-1}	mm
d	10^{-1}	mm
t'_x, t'_y, t'_z	1	mm

MEASUREMENT SET-UP

The image-based micro-triangulation system QDaedalus (Guillaume et al., 2012; Bürki et al., 2010) was used for the determination of precise 3D coordinates (see Figure 5). It consists of two total stations of the type Leica TCRP 1201 placed approximately at two meters distance from the robot. Two stations are sufficient, but in principle every additional station would enhance the observation geometry. The total stations have an angular accuracy of 0.3 mgon. The eyepiece of the total stations was removed and replaced by a CCD-sensor. The target, which is mounted on the robot, consists of a 5 mm sphere (see Figure 6). The sphere is illuminated by an LED from its inside. On both stations, coaxial images are acquired with a rate of 20 Hz. A sphere matching algorithm extracts the center of the spheres (see Figure 7) with an accuracy better than a tenth of a pixel (Guillaume et al., 2012). A pixel on the CCD-sensor corresponds to four arc-seconds, which corresponds to 0.1 mm at five meters. Through an affine transformation, these image coordinates are related to horizontal and zenith angles. Both stations are synchronized with GPS time and connected to a local network. On the master computer, the 3D line intersection is performed in real-time in order to compute the 3D coordinates of the center of the sphere. The real-time processing drastically reduces the amount of data that has to be stored. The result is a time-series of the sphere coordinates. Before the measurements, the instruments are calibrated with the on-board calibration program, in order to determine the instrumental errors (compensator error, vertical index error and collimation error). After calibration of the instruments, measurements in only one face (one telescope position) are automatically corrected for the instrumental errors. The set-up is finalized by estimating the coordinates and the orientation of both stations. In the present case, the high accuracy geodetic reference network (local accuracy of 0.1 mm) of the roof of the Institute has been used. This network is our realization of the world frame. The optical targets of the high precision network are marked in red in Figure 5. Because of the small size of the network (2 to 3 m and one point further away for orientation), a standard model for atmospheric refraction (coefficient of refraction of 0.13) is fully sufficient. The observations are processed in a geodetic adjustment software. Because both stations measured the same reference points for the estimation of their coordinates and orientation, and because these parameters were estimated within the same adjustment, the relative position of the two theodolites with respect to each other is very well defined (better than 0.1 mm).

Interaction with the robot

Once the robot and the QDaedalus system are set-up, the robot calibration is fully autonomous and needs no interaction. Because the target sphere shows only very small movements, it stays always in the field of view of the theodolites (1 deg, 3.5 cm at 2 m distance) and no theodolite telescope motion is required. During the robot movements, the sphere might briefly be lost, but the measurement continue as soon as the sphere is visible again by the two total stations. The computer controlling the robot is synchronized over an internet time-server (accuracy better than 1 ms) and writes out the start and the end time of every static position. This information is used in postprocessing to align the QDaedalus measurements and the angular readings of the robot. As every static position is maintained for 1 second, the whole robot calibration lasts less than 1 hour.

Offset estimation

The offset of the tool needs to be determined beforehand, as mentioned in the previous section. In order to do so, the tool is brought in line with a QDaedalus station, as in Figure 8. Both, the horizontal and the vertical angles are measured with the QDaedalus, before the tool is dismount from the robot and rotated by 180 degrees. The angles are measured again, and half the angle difference multiplied by the distance leads to the offset of the tool. The offset in Z was measured with a slide gauge.

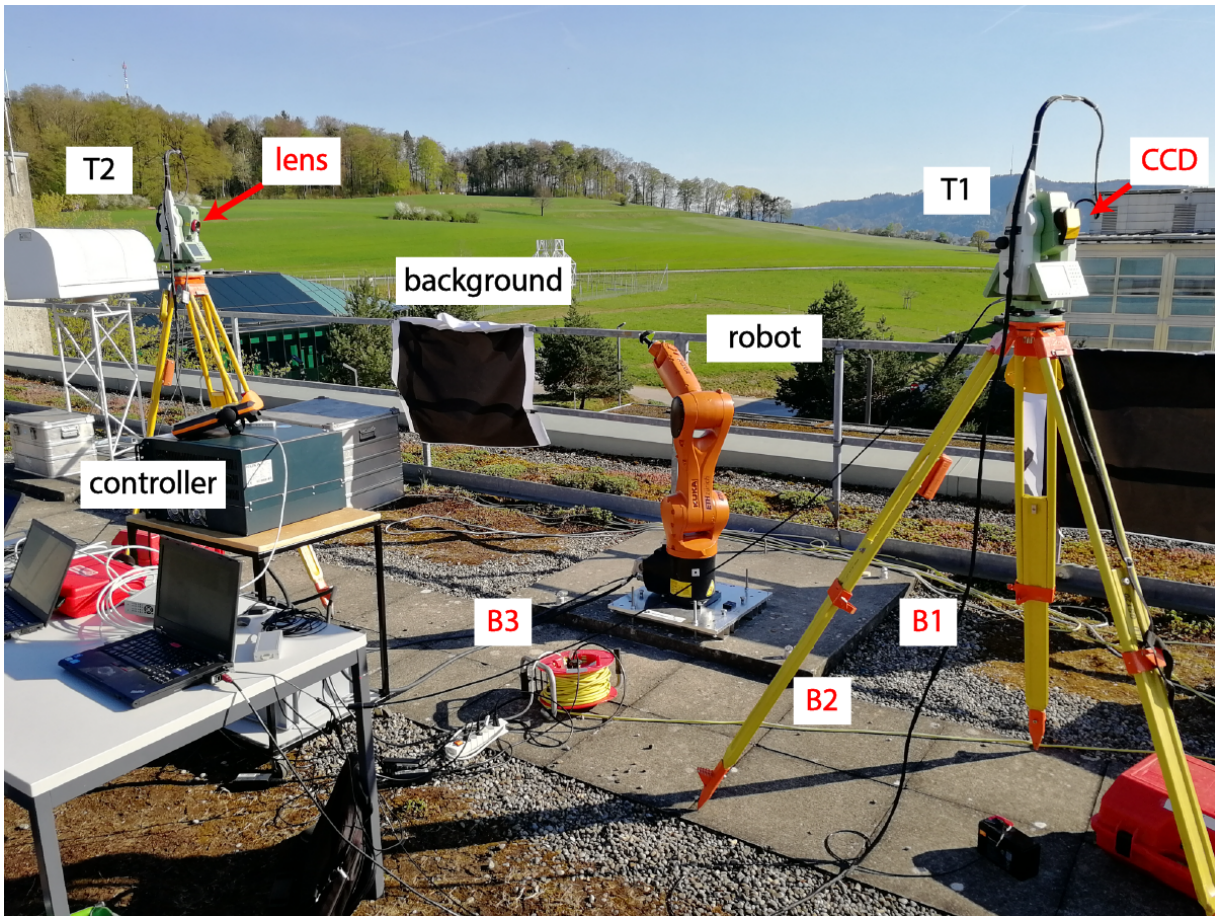


Fig. 5. Optical micro-triangulation system QDaedalus. The picture shows the two theodolites (T1 and T2), the housing of the CCD sensor installed instead of the theodolite's eyepiece, the converging lens, the black screen for enhanced contrast in the images which leads to better matching in sunny conditions, the controller and three of the reference points (B1 to B3) of the high precision network. Other reference points are located all over the Institute's roof. The picture was taken during the robot calibration sequence and the robot is in one of the 1440 orientations.



Fig. 6. Illuminated spherical target mounted on the robot. The picture was taken during the offset calibration.

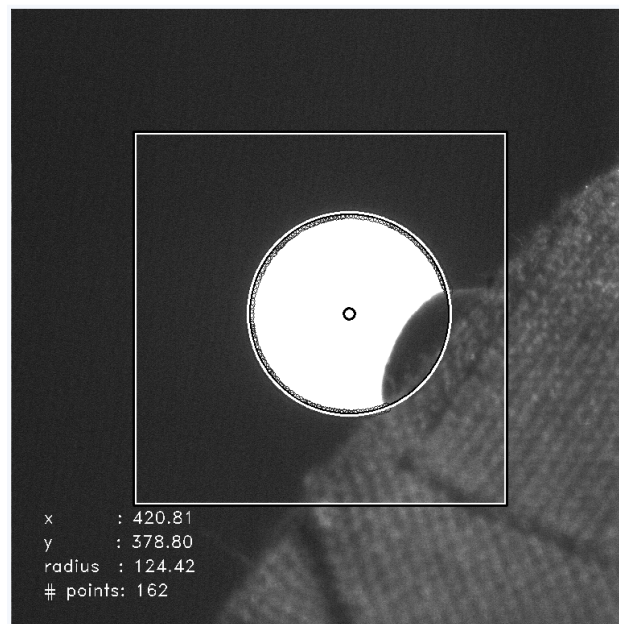


Fig. 7. Sub-pixel accurate extraction of the sphere in the gray-scale image which was acquired by the CCD camera through the telescope of the theodolite.

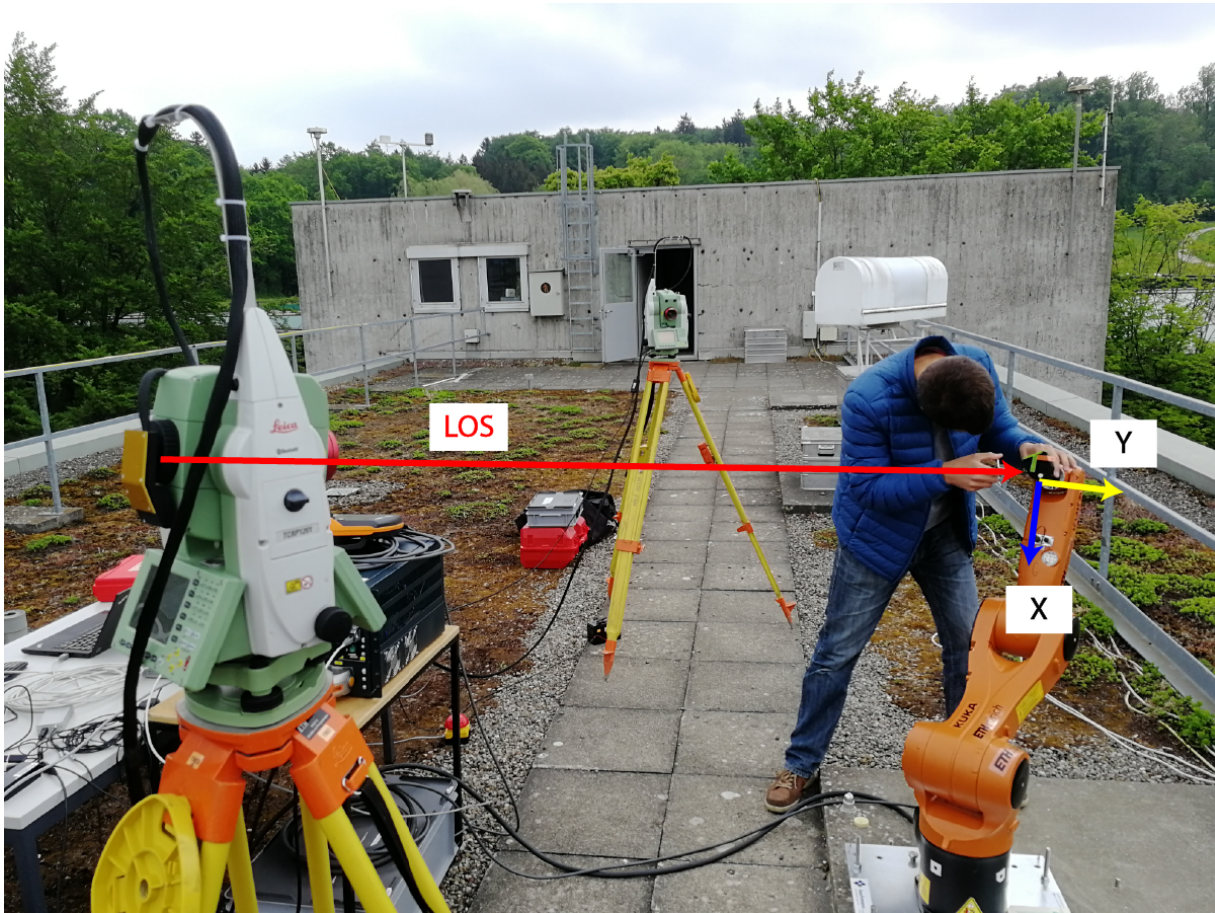


Fig. 8. Tool offset measurement: the QDaedalus station and the robot tool are aligned with respect to each other along the line of sight (LOS) in order to calibrate the tool offsets in X and Y. With help of the theodolite, a very precise alignment can be achieved. The vertical and horizontal angles are measured with QDaedalus. The operator is dismounting the tool in order to rotate it by 180 deg before the horizontal and vertical angles are measured again. The distance is measured with a yardstick.

MEASUREMENT CAMPAIGNS

A total of four datasets were acquired in three campaigns. Table 6 summarizes these campaigns. In the first campaign, two datasets A and B are acquired. The first goal is to verify that a set of DH calibration parameters estimated out of the data A can be applied to reduce the standard deviation of the positions calculated from dataset B. A second dataset was acquired seven days later. In between, the robot was disconnected from power supply, dismantled from the roof and transported to an office located nearby (20 m walking distance, the robot is manually lifted and transported by 3 people). The goal of this robot calibration campaign 2 is to verify that the obtained DH calibration parameters can be applied even after the robot was dismantled. This is very important, as it corresponds to the current robot operation mode for GNSS antenna calibrations with the robot.

In the first three campaigns 1A, 1B and 2, no corrections are applied to the motion of the robot (corresponding to an uncalibrated robot). The corrections are applied in post-processing and the

Table 6. Information on the three campaigns conducted. The times are given in Central European Summer Time (UTC+2), which is the local time. The temperatures were observed at a nearby meteo-station (150 m away) during the time of the measurements.

Campaign	Date	Day	Number of points	Start time (local time)	End time (local time)	Temperature (deg Celsius)
Calibration 1A	11.4.2018	0	1114	14:16	15:12	17
Calibration 1B	11.4.2018	0	1129	15:32	16:21	18
Calibration 2	18.4.2018	7	1101	15:40	16:35	23
Validation V	4.5.2018	23	199	14:07	14:15	17

residuals are analyzed. Our hypothesis is that a set of DH parameters can not only be used to correct positions in post-processing but also in real-time and that the standard deviation will be reduced in the same manner as if applied in post-processing. This means that the estimated DH calibration parameters are used by the custom software steering the robotic arm. In order to verify this last hypothesis, a validation dataset V was acquired in the last campaign, using the calibrated robot. This last step is very important as well, as for GNSS antenna calibration, always the calibrated robot will be used and no further corrections will be applied in the GNSS antenna calibration procedure. If the robot is used with the DH calibration parameters, always the most recent set of DH parameters is used. The validation dataset V is shorter than the 3 other datasets, but the conclusions will not be affected as the order of the rotations in the sequence is randomized.

RESULTS

The results from the offset calibration, which is performed prior to the measurements according to the method presented above, are shown in Table 7. Between campaign 1 and 2, the target was removed from its mount and put back. This explains the changes in offset. The offsets in campaign 2 and V are expected to be identical, as the tool was not modified. The small difference is in good agreement with the measurement accuracy of one and three hundredths of millimeters.

Figure 9 shows the histogram of the residuals before and after the estimation of DH parameters. The pre-fit residuals were obtained by subtracting the computed from the observed positions. The observed positions are provided by QDaedalus measurement, while the computed values are the positions obtained from forward kinematics using the nominal DH parameters of Table 1. The distribution is unsymmetrical and shows a standard deviation of roughly half a millimeter. The lower part of the diagram shows the post-fit residuals. The standard deviation dropped significantly to below 0.1 mm. The standard deviation of every component can be found in Table 8.

In the estimation process, the tool offsets were constrained to the precisely measured values presented in the previous section. The DH parameters that resulted from this calibration (campaign 1A) are displayed in Table 9 and their formal errors in Table 10. The improvement on

Table 7. Results of the offset estimation. The standard deviations are the empirical standard deviations. The offset in Z was measured with a slide gauge. The standard deviation of the slide gauge measurement was empirically estimated to 0.07 mm.

	X [mm]	Y [mm]	Z [mm]	Std. dev. X [mm]	Std. dev. Y [mm]
1	0.549	-0.099	82.615	0.007	0.002
2	0.445	-0.047	82.550	0.034	0.011
V	0.424	-0.037	82.550	0.007	0.005

the angular parameter is up to one hundredth of a rad ($\delta\Theta_4$) and half a millimeter for the length parameters (d_6). The formal errors reveal that 7 parameters out of the 24 are significant to 1σ or more.

As correlation is present in the parameters (see the correlation matrix in Figure 10), the interpretation of this significance based solely on the variance of a parameter has to be interpreted conservatively. Regarding the strong correlations nearly reaching 1 or -1, the reader has to keep in mind that a decorrelation of the parameters is not targeted, but only the reduction of the variance of the positioning with the robot.

More interestingly, DH parameters determined once are able to reduce the variance of the robot positions during later campaigns. The DH parameter estimated from dataset 1A were applied to the data from campaign 1B and 2. With uniquely determined parameters, the standard deviation of the robot positions can be reduced to below a tenth of a millimeter, as shown in Table 11.

Finally, a validation was conducted. The DH parameters estimated with the dataset 2 were introduced into the robot controller and the positions of the robot were measured. Theoretically, a reduction of the standard deviation to similar levels as before (below 0.1 mm) is expected. This goal was achieved, as Table 12 confirms. The standard deviation of the robot positions is nine, eight and six hundredths of a millimeter in X, Y and Z respectively. The correction of the position by the robot is successful; the newly estimated DH parameters can be applied in the robot controller to pilot the robotic arm in an open loop manner with a precision of several hundredths of millimeters. The precision is only marginally improved by fitting the model through the validation data, as can be seen from the second line in Table 12. Note that the very small value of 0.04 mm for the post-fit standard deviation is probably due to two effects: i) the precision of the micro-triangulation system is increased with smaller movements of the target and ii) the sequence consists of only 200 points. Although the sequence is randomized, the shorter sequence could have a small impact. In order to assess this effect, subsets of datasets 1A, 1B and 2 were analyzed. The full sets were found to have an 18% larger standard deviation in average. The last line in Table 12 was scaled accordingly. The robot positions measured with QDaedalus did not show this behavior in the other datasets, therefore, no scaling needs to be applied.

Table 8. Pre- and post-fit standard deviation for the robot positions measured in campaign 1. The standard deviation is computed empirically from the coordinate series and is a measure of the position scatter.

	Std. dev. X [mm]	Std. dev. Y [mm]	Std. dev. Z [mm]
Pre-fit	0.53	0.58	0.71
Post-fit	0.08	0.07	0.06

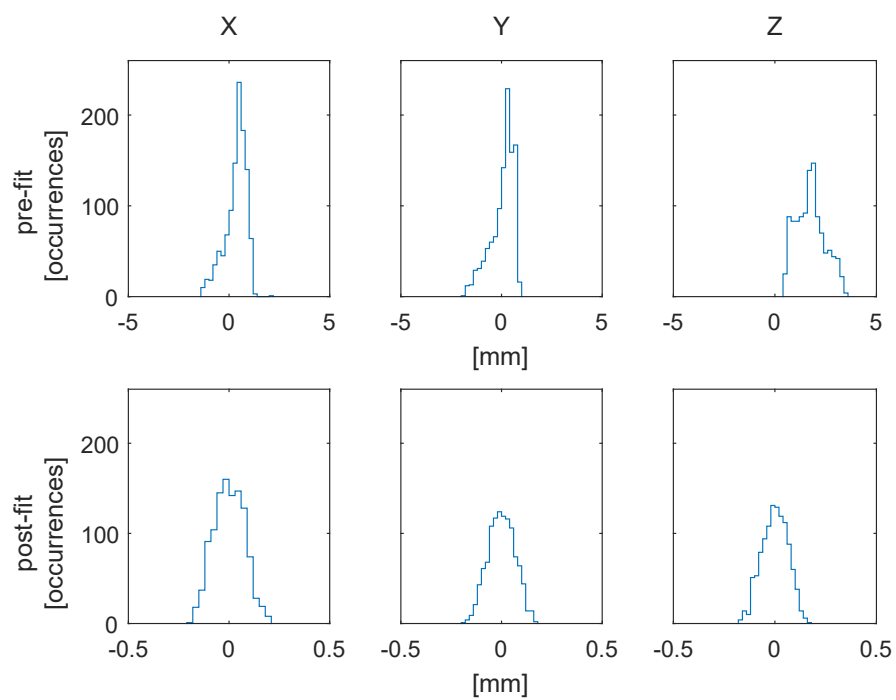


Fig. 9. Histogram of the residuals of the X, Y and Z coordinates, before and after fit of the DH parameter model for the dataset 1A.

Table 9. DH parameters estimated from campaign 1A. * means the parameter change with respect to the nominal geometry is significant to 1σ , ** to 2σ and *** to 3σ .

	$\delta\Theta$ [rad]	α [rad]	a [mm]	d [mm]
1	0.0000	1.5709	24.8968	400.0069
2	**0.0005	*0.0003	***455.4262	-0.0166
3	1.5674	-1.5706	34.8471	-0.0166
4	***0.0097	1.5708	-0.0942	** -419.7903
5	-0.0005	-1.5718	0.0057	0.0503
6	3.1414	3.1413	***0.0575	***-79.4468

Table 10. Formal errors (1 sigma) of the DH parameters estimated from campaign 1A. The standard deviation of constrained parameters is left blank.

	$\delta\Theta$ [rad]	α [rad]	a [mm]	d [mm]
1		0.0002	0.1154	0.1191
2	0.0002	0.0002	0.0893	0.0963
3	0.0001	0.0003	0.0464	0.0963
4	0.0003	0.0003	0.0245	0.0858
5	0.0007	0.0007	0.1190	0.1028
6	0.0119	0.0001	0.0038	0.0336

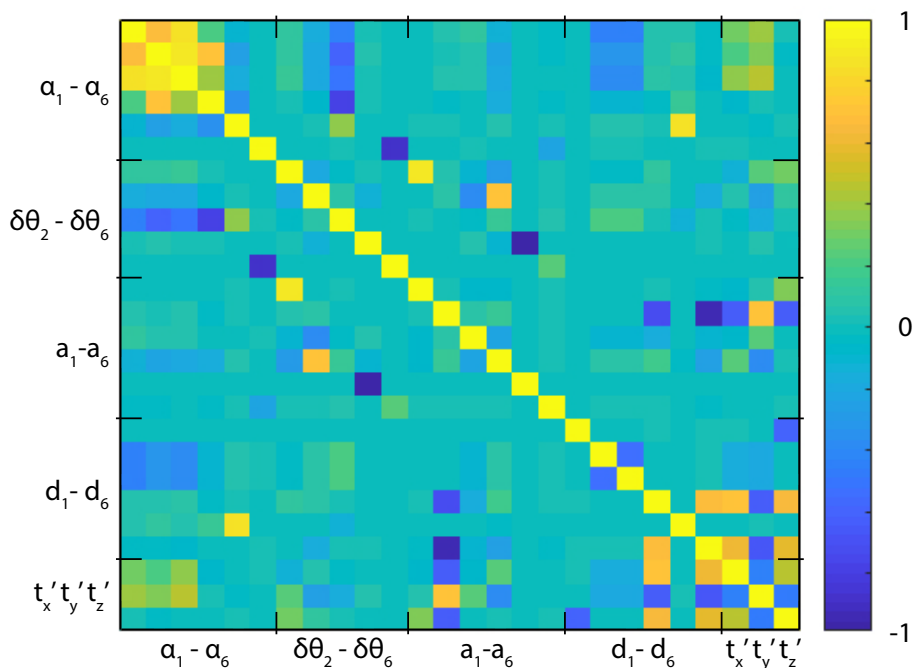


Table 11. Standard deviation of datasets 1B and 2 before any correction and after applying the DH parameters estimated with dataset 1A. The standard deviation is computed empirically from the coordinate series and is a measure of the position scatter.

	Std. dev. X [mm]	Std. dev. Y [mm]	Std. dev. Z [mm]
1B pre-fit	0.51	0.58	0.70
1B corrected	0.11	0.08	0.05
2 pre-fit	0.56	0.57	0.73
2 corrected	0.12	0.12	0.08

Table 12. Standard deviation of the robot positions acquired during the validation. The positions were executed by the robot using DH parameters estimated with dataset 2. The first line shows the standard deviation of the unprocessed positions. The second line shows the standard deviation after fit of the DH parameters were estimated. In the datasets with more than 1000 points, the whole series (with all points) had, in average, a 18% higher standard deviation than the first 200 points. To account for this effect, the line with an asterisk was scaled accordingly. No such effect could be observed in the robot positions measured with QDaedalus. Here, the subset of the first 200 points systematically had a slightly lower standard deviation (up to 10%).

	Std. dev. X [mm]	Std. dev. Y [mm]	Std. dev. Z [mm]
Direct robot positions	0.09	0.08	0.06
Post-fit residuals	0.04	0.04	0.04
Corrected Post-fit residuals*	0.05	0.05	0.05

SUMMARY

We were able to show that the precision of the uncalibrated KUKA Agilus KR 6 R900 sixx lies around 0.5 to 0.7 mm and is therefore not sufficient for GNSS antenna calibration, which requires a precision of 0.1 mm. A robot calibration model and a robot calibration procedure were developed for the specific task of positioning scatter reduction for GNSS antenna calibration. This task was accomplished successfully, as the standard deviations of the positions are reduced to below 0.1 mm. This means that the scatter of the coordinates is smaller than 0.1 mm in terms of standard deviation. The model developed uses a Denavit-Hartenberg parametrization to model the geometry of the robot. This precision was achieved without a model of the robot joint elasticity. The calibration procedure is highly efficient, as the measurements can be automatically achieved in less than one hour. We showed that the estimated DH calibration parameters remain useful and efficient to reduce the scatter of the positions of the robot, even after the robot was disconnected from its power supply, moved to its storage location and moved back to the Institute's roof. A validation showed that the parameters can as well be used to pilot the robot, reaching similar precision as if the model

parameters were estimated in post-processing.

The final result is a calibrated robot, which is now ready to be deployed for GNSS antenna calibration. As by-product, a method for the precise estimation of X and Y offsets of the robot tool was developed. The method shows repeatabilities of about a hundredth of a millimeter.

The results obtained could be further consolidated with additional studies: the behavior of the robot under different loads (payload masses) should be further examined. A model of the robot joint elasticity might enhance the precision with different payloads. Large temperature changes within a calibration sequence should be studied as well. Finally, recalibrations in regular intervals will reveal the long-term behavior of the robot and its calibration.

ACKNOWLEDGEMENTS

We would like to thank Robert Presl and Alexander Wolf for the manufacturing of the illuminated sphere target, Jules Fenner for the help with the robot set-up, Michael Lyrenmann for the helpful advice regarding the operation of the robot and Valérie Hellmüller and Patrik Eugster for carrying out most of the measurements.

REFERENCES

- Allman, M., Novotny, D., and Gordon, J. (2018). “Calibration of a 6-axis serial robotic arm mounted to a moveable base at the national institute of standards and technology.” *Proceedings of the Coordinate Metrology Systems Conference (CMSC) 2018, Orlando, FL, USA*.
- Bilich, A., Erickson, B., and Geoghegan, C. (2018). “6-axis robot for absolute antenna calibration at the US national geodetic survey.” *IGS Workshop 2018, Wuhan, Hubei, China*.
- Bilich, A. and Mader, G. L. (2010). “GNSS absolute antenna calibration at the national geodetic survey.” *Proceedings of the 23rd International Technical Meeting of The Satellite Division of the Institute of Navigation (ION GNSS 2010), Portland, OR, USA*, 1369–1377.
- Brandstötter, M., Angerer, A., and Hofbauer, M. (2014). “An analytical solution of the inverse kinematics problem of industrial serial manipulators with an ortho-parallel basis and a spherical wrist (revised version).” *Proceedings of the Austrian Robotics Workshop 2014, Linz, Austria*, 7–11.
- Bürki, B., Guillaume, S., Sorber, P., and Oesch, H.-P. (2010). “DAEDALUS: A versatile usable digital clip-on measuring system for Total Stations.” *International Conference on Indoor Positioning and Indoor Navigation (IPIN) 2010, IEEE*, 1–10.
- Corke, P. I. (2017). *Robotics, vision and control: fundamental algorithms in MATLAB*. Springer International Publishing, Berlin, Germany, ISBN 978-3-319-54413-7.
- Guillaume, S., Bürki, B., Griffet, S., and Mainaud-Durand, H. (2012). “QDaedalus: augmentation of total stations by CCD sensor for automated contactless high-precision metrology.” *FIG Working Week*, 1–15.
- Hu, Z., Zhao, Q., Chen, G., Wang, G., Dai, Z., and Li, T. (2015). “First results of field absolute calibration of the GPS receiver antenna at wuhan university.” *Sensors*, 15(11), 28717–28731.

- Kersten, T. (2014). *Bestimmung von Codephasen-Variationen bei GNSS-Empfangsantennen und deren Einfluss auf Positionierung, Navigation und Zeitübertragung*. Dissertation. Leibniz University Hanover, Germany.
- Kuka (2018). “Kr agilus sixx specification.” *KUKA Deutschland GmbH, Germany*.
- Menge, F. (2003). *Zur Kalibrierung der Phasenzentrumsvariationen von GPS Antennen für die hochpräzise Positionsbestimmung*. Dissertation. Leibniz University Hanover, Germany.
- Motta, J. M. S., de Carvalho, G. C., and McMaster, R. S. (2001). “Robot calibration using a 3d vision-based measurement system with a single camera.” *Robotics and Computer-Integrated Manufacturing*, 17(6), 487–497.
- Nubiola, A. and Bonev, I. A. (2013). “Absolute calibration of an ABB IRB 1600 robot using a laser tracker.” *Robotics and Computer-Integrated Manufacturing*, 29(1), 236–245.
- Riddell, A., Moore, M., and Hu, G. (2015). “Geoscience Australia’s GNSS antenna calibration facility: Initial results.” *Proceedings of IGNSS Symposium 2015 (IGNSS2015)*, Surfers Paradise, QLD, Australia.
- Rothacher, M. and Schmid, R. (2010). “Antex: The antenna exchange format version 1.4.” *Format specification, IGS Central Bureau, Pasadena, CA, USA*.
- Schmitz, M., Wübbena, G., and Boettcher, G. (2002). “Tests of phase center variations of various GPS antennas, and some results.” *GPS Solutions*, 6(1), 18–27.
- Schröer, K. (1999). “Precision and Calibration.” *Handbook of Industrial Robotics*, S. Y. Nof, ed., John Wiley & Sons, Inc., Hoboken, NJ, USA, 795–810.
- Schröer, K., Albright, S. L., and Grethlein, M. (1997). “Complete, minimal and model-continuous kinematic models for robot calibration.” *Robotics and Computer-Integrated Manufacturing*, 13(1), 73–85.
- Siciliano, B. and Khatib, O. (2008). *Springer handbook of robotics*. Springer International Publishing, Berlin, ISBN 978-3-540-30301-5.
- Teunissen, P. J. and Montenbruck, O. (2017). *Springer Handbook of Global Navigation Satellite Systems*. Springer International Publishing, Berlin, ISBN 978-3-319-42926-7 978-3-319-42928-1.
- Willi, D., Koch, D., Meindl, M., and Rothacher, M. (2018). “Absolute GNSS antenna phase center calibration with a robot.” *Proceedings of the 31st International Technical Meeting of The Satellite Division of the Institute of Navigation (ION GNSS+ 2018)*, Miami, FL, USA, 3909 – 3926.
- Wübbena, G., Schmitz, M., Menge, F., Böder, V., and Seeber, G. (2000). “Automated absolute field calibration of GPS antennas in real-time.” *Proceedings of the 13th International Technical Meeting of the Satellite Division of The Institute of Navigation (ION GPS 2000)*, Salt Lake City, UT, USA, 2512 – 2522.

Appendix D

Paper IV

Title	Absolute GNSS Antenna Phase Center Calibration with a Robot
Authors	Daniel WILLI, Donovan KOCH, Michael MEINDL, Markus ROTHACHER
Proceedings	Proceedings of the 31st International Technical Meeting of The Satellite Division of the Institute of Navigation (ION GNSS+ 2018), September 24 - 28, 2018, Hyatt Regency Miami, Miami, Florida
Pages	3909 – 3926
Link	www.ion.org/publications/abstract.cfm?articleID=16040
Peer review	Yes

A reprint within the own PhD is allowed according to an e-mail confirmation from 13 November 2018 by Miriam Lewis from ION.

Absolute GNSS Antenna Phase Center Calibration with a Robot

Daniel Willi, Donovan Koch, Michael Meindl, Markus Rothacher, *Institute of Geodesy and Photogrammetry, ETH Zürich*

BIOGRAPHIES

Daniel Willi is Ph.D. student at the Institute of Geodesy and Photogrammetry, ETH Zurich. He holds a Master degree in Geomatics Engineering from ETH Zurich. His research interest is GNSS in general and GNSS antenna calibrations in particular.

Donovan Koch is a scientific assistant at the Institute of Geodesy and Photogrammetry, ETH Zurich. He holds a Master Degree in Applied Physics from the Ecole Polytechnique Fédérale de Lausanne. His recent research focusses on kinematic estimation of GNSS satellite orbit using satellite clock modelling. Donovan Koch currently works as an airline pilot.

Michael Meindl works as a senior scientist at the Institute of Geodesy and Photogrammetry at ETH Zurich. He was heavily involved in the development of the scientific Bernese GNSS Software becoming an expert on GNSS modelling and algorithms. His research interests cover modelling the atmosphere, ambiguity resolution, orbit determination, reference frames, and the consistent combination of different satellite systems. In his current position he is responsible for the scientific payload of the small satellite mission CubETH.

Markus Rothacher is Professor of Mathematical and Physical Geodesy at ETH Zurich. His research interests comprise high-precision GNSS applications, space geodesy, satellite missions, orbit determination, and earth rotation. For many years he was Chair of the Global Geodetic Observing System (GGOS) and Analysis Coordinator of the IERS. He presently serves on the Galileo Science Advisory Committee (GSAC) of ESA.

ABSTRACT

GNSS antennas suffer from errors, dependent on the direction of the incoming GNSS signal. These errors can be calibrated. We present an absolute field calibration method based on a 6-axis industrial robot. The antenna to be calibrated is set-up on the robot at one end of a short baseline. The robot brings the antenna into 1440 different orientations without changing its coordinates, every orientation lasting for 1 second. The data is analyzed in a triple-difference approach. The estimated GPS L1 phase center corrections show a repeatability better than a millimeter (0.6 mm RMS). We believe that this new method is of interest to the scientific community, as only a few independent field calibration systems exist.

INTRODUCTION

GNSS antennas commonly used in geodesy as well as in navigation suffer from direction dependent errors. In the case of carrier phase observations, these errors typically lie in the range of a few to several millimeters in high-quality antennas (Rothacher 2001), but can reach centimeter level in low-cost antennas (Willi et al. 2017). As the accuracy of carrier phase measurements reach millimeter level, these direction dependent errors are significant. Since the very beginning of GPS, the calibration of so-called Phase Center Corrections (PCC) has been attempted, for instance by Sims (1985), but the topic is still being investigated nowadays (Kallio et al. 2018). Although from a physical point of view, no such thing as a phase center exists, this terminology is widely used within the antenna calibration community. The methods for PCC calibration can be divided into three groups (Rothacher 2001):

- Relative field calibrations
- Anechoic chamber measurements
- Absolute field calibrations

The three methods are summarized in Table 1. In relative field calibrations, baseline measurements between a reference antenna and the antenna to be calibrated are carried out (Rothacher et al. 1995). The data is analyzed and the result is a calibration relative to the reference antenna. The reference antenna can either be chosen by convention or an absolutely calibrated antenna can be used as reference. Field methods are easy to carry out but typically suffer from multipath. Relative field calibrations require at least 24h of data.

In anechoic chamber measurements, an artificial signal is generated and sent to the antenna (Sims 1985, Tranquilla and Colpitts 1989, Schupler et al. 1994). The interference of the received with the original signal allows to measure the phase delay. Then, either the emitter is moved or the antenna is rotated, in order to cover the whole antenna hemisphere. Anechoic chamber measurements provide absolute PCC. The experiment is demanding in infrastructure and difficult to carry out, as the synchronization of all signals has to be very accurate. In order to combine the advantages of the two previous methods, namely obtaining absolute calibrations with reduced multipath, absolute field calibrations using robots were developed (Wübbena et al. 1997). Nowadays, this kind of calibration is performed routinely, e.g., by Geo++, the University of Hannover and the US National Geodetic Survey (Bilich et al. 2012, Görres et al. 2006). Geo++ and the University of Hannover use the same software, based on processing of zero-differences (Wübbena et al. 1997), and a 6-axis robot, the National Geodetic Survey uses a 2-axis robots and has plans to upgrade to a 6-axis robot (Bilich 2017). A 6-axis robot has the advantage of keeping the coordinates of the antenna reference point fixed during rotation. Beside these two groups, Geoscience Australia is using a robot from Geo++ and, in parallel, develops its own system (Riddell et al. 2015).

The group for Mathematical and Physical Geodesy at ETH Zurich recently acquired a 6-axis robot (see Figure 1). In previous studies (Willi et al. 2017), antenna calibrations with the relative field method showed promising results. However, due to the limitations inherent to the relative field calibration method, no conclusion about the impact of multipath on the results is possible. For that reason, an absolute robot calibration was set up. Compared to others, we use a triple-difference approach. Theoretically, and particularly in combination with high rate GNSS receivers and a fast robot, this method is very efficient. The next section holds details on the processing strategy followed by the latest results.

Table 1 Summary of the three classes of methods for GNSS antenna calibration.

	Relative field calibration	Anechoic chamber measurements	Absolute field calibrations
Real GNSS signal	Yes	No, artificial signal	Yes
Fast movement of the antenna	No, manual rotation every 24h	Yes, rotation by a robot or displacement of the signal source	Yes, rotation by a robot
Multipath	Present in the result	Eliminated through design (chamber)	Eliminated through data analysis
Antenna coverage	Limited by the horizon	Unlimited	Unlimited
Infrastructure	Virtually none	Very demanding	Demanding

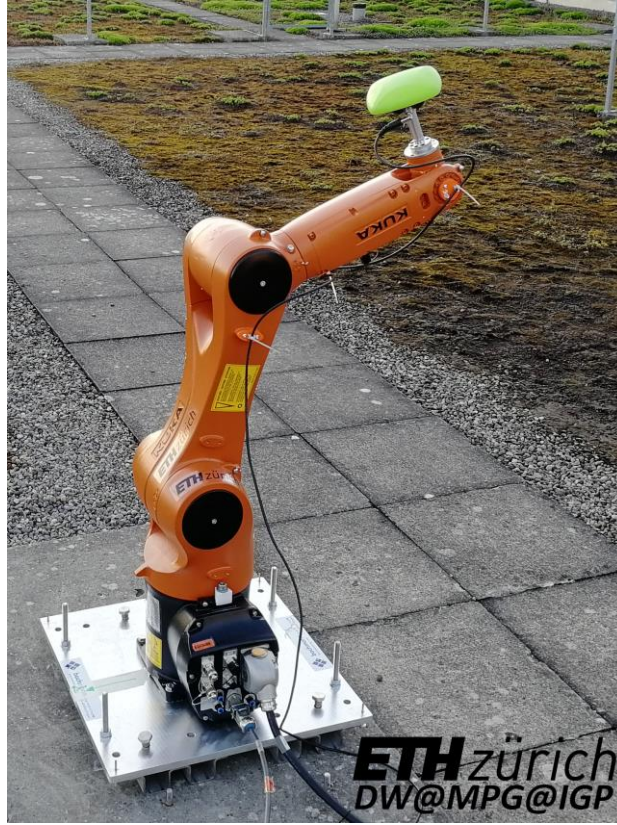


Fig. 1 KUKA Agilus KR 6 R900 sixx industrial robot for absolute antenna calibrations.

GOVERNING EQUATIONS

The Antenna Reference Point (ARP) is the mechanical reference mark of an antenna. The Mean Phase Center (MPC) is an arbitrary point, which usually represents a best-fit phase center. The Phase Center Offset (PCO) links the coordinates of the ARP \mathbf{X}_{ARP} and the MPC \mathbf{X}_{MPC} :

$$\mathbf{X}_{MPC} = \mathbf{X}_{ARP} + \mathbf{PCO} \quad (1)$$

The PCO is meant to reduce the size of the direction-dependent corrections Φ_A :

$$\Phi_A^i = \Phi_A(\alpha^i, z^i) \quad (2)$$

where Φ_A^i is the Phase Center Variation (PCV) correction function for the range measurement between satellite i and antenna A , α^i is the azimuth of the received signal and z^i its zenith angle, both with respect to an antenna reference frame. The observation equation for a phase measurement subsequently reads:

$$\begin{aligned} P_A^i &= \mathbf{e}_A^{i\top} \left(\mathbf{X}^i - (\mathbf{X}_{ARP} + \mathbf{PCO}) \right) + c \delta t_A - c \delta t^i + \lambda N_A^i + \Phi_A^i + T_A^i - I_A^i + W_A^i + v_A^i \\ &= \rho_A^i + c \delta t_A - c \delta t^i + \lambda N_A^i + \Phi_A^i + T_A^i - I_A^i + W_A^i + v_A^i \end{aligned} \quad (3)$$

P_A^i is a phase measurement from GNSS satellite i to antenna A and ρ_A^i is the corresponding geometrical distance. \mathbf{e}_A^i is the line-of-sight unit vector. \mathbf{X}^i is the position, at signal emission time, of the emitting GNSS satellite antenna. c is the speed of light, δt_A is the receiver clock error, δt^i is the GNSS satellite clock error, λ is the carrier phase wavelength, N_A^i is the integer phase ambiguity, Φ_A^i is the PCV, T_A^i is the tropospheric signal delay, I_A^i is the ionospheric signal delay, W_A^i is the phase wind-up, and v_A^i is the observation noise. This equation is in agreement

with the ANTEX sign convention (Rothacher and Schmid, 2006). From Eqs. 1 to 3 it is clear that the choice of the MPC is purely arbitrary, if a consistent PCV is applied. One could chose the MPC to coincide with the ARP, leading to a PCO of zero. In this case, the whole correction would be contained in Φ_A^i . Historically, this is not the case as often PCO were applied but Φ_A^i was not. Therefore, it made sense to have a PCO which approximates the MPC as good as possible. The combination of PCO and PCV is called PCC. A PCV and PCO pair can be transformed to another PCO with using following relationship:

$$\Phi'(\alpha, z) = \Phi(\alpha, z) + \mathbf{e}^T(\mathbf{PCO}' - \mathbf{PCO}) \quad (4)$$

where Φ' is the PCV that belongs to \mathbf{PCO}' and Φ is the PCV that belongs to \mathbf{PCO} . If used consistently, as in Eq. 3, both pairs lead to the same total correction; they are the same PCC.

The PCV correction function can be modelled either as a grid or as a spherical harmonics expansion. In the case of a grid, the correction value for each range is obtained after two linear interpolations, one in azimuth and one in elevation, between the four closest cell corners. Figure 2 illustrates this process. In the estimation process, the huge number of parameters in his parametrization can be problematic. A typical resolution of 5 degrees results in 1296 parameters. Moreover, the observations are inhomogeneously distributed among the grid cells. The cells close to zenith cover a much smaller solid angle than the grid cells close to the horizon. Therefore, very often, the spherical harmonics approach is preferred:

$$\Phi_A(\alpha^i, z^i) = \sum_{m=0}^{m_{\max}} \sum_{n=0}^m \tilde{P}_{mn}(\cos z^i) (a_{mn} \cos n\alpha^i + b_{mn} \sin n\alpha^i) \quad (5)$$

\tilde{P}_{mn} is the normalized associated Legendre polynomial of degree m and order n , a_{mn} and b_{mn} are the coefficients to be estimated. Typically, patterns are estimated with spherical harmonics up to degree and order 12.

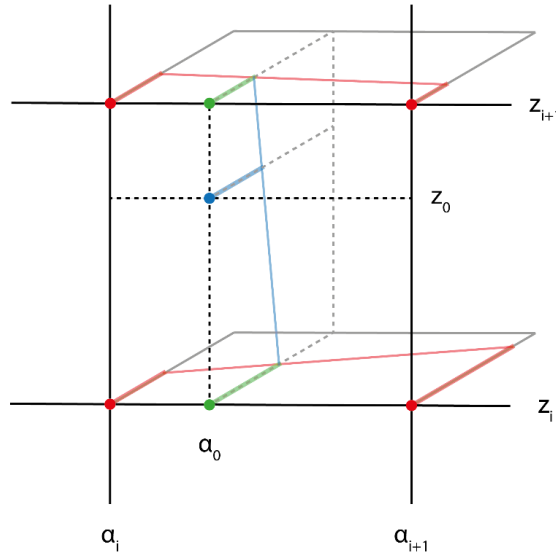


Fig. 2 Illustration of the grid interpolation process. The four red dots are the values at the grid cell corners. These values are the parameters of the estimation process. The interpolated value at α_0 and z_0 are obtained after linear interpolation in azimuth (leading to the green dots) and a linear interpolation along the zenith angle. The out-of-plane axis holds the values of $\Phi(\alpha, z)$ at each of the dots.

Degree of freedom

Both parametrizations, the grid and the spherical harmonics, are fundamentally different and differ in their respective degree of freedom. For a gridded PCV, the number of parameters equals:

$$k_{grid} = \left(\frac{90}{res_{zen}} + 1 \right) \frac{360}{res_{az}} \quad (6)$$

Where k_{grid} is the number of parameters, res_{zen} is the resolution in zenith (in degrees) and res_{az} is the resolution in azimuth (in degrees). This result is obtained assuming that the values for $az = 360$ deg equal the grid values for $az = 0$ deg (explaining the absence of a +1 on the right hand side of Eq. 6). The absolute term of the pattern correlates with the receiver clock error, as can be seen from Eq. 3: any constant value added on Φ_A^i would be fully absorbed by $c \delta t_A$. In order to avoid any singularity, the zenith values of the pattern are therefore constrained to zero. This reduces the number of parameters, leading to:

$$k_{grid} = \frac{90}{res_{zen}} \cdot \frac{360}{res_{az}} \quad (7)$$

In summary, a 10×10 deg² resolution grid has 324 parameters, a 5×5 deg² grid 1296. A resolution below 10 degrees is not suitable for PCV whereas a resolution higher than 5 degrees seems not practical because of the high number of parameters. It is not necessary to set up the PCO as explicit parameters, as the grid can absorb any offset (see Eq. 4). The whole PCC will then be contained in the PCV.

In the most frequent case that the degree and order is equal ($m = n$), the number of parameters of a spherical harmonics expansion is:

$$k_{SH} = (m + 1)(n + 1) \quad (8)$$

With m being the degree and n the order of the spherical harmonics expansion (see also Eq. 3). This count does not include the terms b_{mn} , $n = 0$, since $\sin n\alpha^i = 0$, if $n = 0$. The term a_{00} is the absolute term and correlates with the clock; it has to be constrained to zero (see Figure 3). The spherical harmonics are designed to represent a scalar field on a sphere and not only its upper hemisphere. As no observations are present in the lower hemisphere of the antenna, the odd terms of the spherical harmonics expansion must be constrained to zero. The odd terms are depicted in green in Figure 3. We end up with following number of parameters:

$$k_{SH} = \frac{(m+2)(n+1)}{2} \quad (9)$$

Typical resolutions for spherical harmonics developments of PCV are degree and order 8 or degree and order 12, resulting in 45 respectively 91 parameters. Table 2 summarizes the two parametrizations, grid and spherical harmonics.

					a_{00}						
			b_{11}		a_{10}	a_{11}					
		b_{22}	b_{21}		a_{20}	a_{21}	a_{22}				
		b_{33}	b_{32}	b_{31}	a_{30}	a_{31}	a_{32}	a_{33}			
	b_{44}	b_{43}	b_{42}	b_{41}	a_{40}	a_{41}	a_{42}	a_{43}	a_{44}		
	b_{55}	b_{54}	b_{53}	b_{52}	b_{51}	a_{50}	a_{51}	a_{52}	a_{53}	a_{54}	a_{55}

Fig. 3 Spherical harmonics coefficient up to degree and order 5. The red term is the absolute term that correlates with the receiver clock error. The blue terms represent the PCO and the green terms represent anti-symmetry. The terms b_{m0} are not shown in this figure.

Table 2 Summary of the two parametrizations for PCV.

	Grid	Spherical harmonics
Number of parameters	$\frac{90}{res_{zen}} \cdot \frac{360}{res_{az}}$	$\frac{(m+2)(m+1)}{2}$
Typical resolution 1	$10 \times 10 \text{ deg}^2$	Degree and order 8
Number of parameters	324	45
Typical resolution 2	$5 \times 5 \text{ deg}^2$	Degree and order 12
Number of parameters	1296	91

Triple-difference approach

The antenna to be calibrated is mounted on the robot nearby to a reference station. Eight measurements from two antennas to two satellites at two different epochs are differenced against each other, leading to the triple-difference formulation (see also Figure 4):

$$P_{AB,t_1t_2}^{ij} = (P_B^j - P_A^j - P_B^i + P_A^i)_{t_2} - (P_B^j - P_A^j - P_B^i + P_A^i)_{t_1} \quad (10)$$

Where $P_{AB,t_1t_2}^{ij}$ is a carrier phase triple-difference observation, P_A^i is a zero-difference phase observation (see Eq. 3), t_1 and t_2 are the two measurement epochs, i and j stand for the two GNSS satellites, A stands for the antenna to be calibrated and B for the reference antenna. Under the assumption that the baseline is short and that therefore the ionosphere and the troposphere effects are eliminated, substitution of Eq. 3 into Eq. 10 leads to the following expression:

$$\begin{aligned} P_{AB,t_1t_2}^{ij} = & (\rho_{B,t_2}^j - \rho_{A,t_2}^j - \rho_{B,t_2}^i + \rho_{A,t_2}^i) - (\rho_{B,t_1}^j - \rho_{A,t_1}^j - \rho_{B,t_1}^i + \rho_{A,t_1}^i) \\ & + (\Phi_B(\alpha_{B,t_2}^j, z_{B,t_2}^j) - \Phi_A(\alpha_{A,t_2}^j, z_{A,t_2}^j) - \Phi_B(\alpha_{B,t_2}^i, z_{B,t_2}^i) + \Phi_A(\alpha_{A,t_2}^i, z_{A,t_2}^i)) \\ & - (\Phi_B(\alpha_{B,t_1}^j, z_{B,t_1}^j) - \Phi_A(\alpha_{A,t_1}^j, z_{A,t_1}^j) - \Phi_B(\alpha_{B,t_1}^i, z_{B,t_1}^i) + \Phi_A(\alpha_{A,t_1}^i, z_{A,t_1}^i)) \\ & + (W_{B,t_2}^j - W_{A,t_2}^j - W_{B,t_2}^i + W_{A,t_2}^i) - (W_{B,t_1}^j - W_{A,t_1}^j - W_{B,t_1}^i + W_{A,t_1}^i) + v_{AB,t_1t_2}^{ij} \end{aligned} \quad (11)$$

where $v_{AB,t_1t_2}^{ij}$ is the triple-difference noise which is $2\sqrt{2}$ times higher than the zero-difference observation noise. The phase ambiguities, provided no cycle slips occurred between the two epochs, have vanished. Cycle slips will appear as outliers in the triple-difference residuals. As the reference antenna B is not rotated and because the time between t_1 and t_2 is only a few seconds, $\alpha_{B,t_1} \approx \alpha_{B,t_2}$, $z_{B,t_1} \approx z_{B,t_2}$ and $W_{B,t_1} \approx W_{B,t_2}$. Introducing these simplifications into Eq. 11 and merging the geometric terms into a single expression leads to:

$$\begin{aligned} P_{AB,t_1t_2}^{ij} = & \rho_{AB,t_1t_2}^{ij} - \Phi_A(\alpha_{A,t_2}^j, z_{A,t_2}^j) + \Phi_A(\alpha_{A,t_2}^i, z_{A,t_2}^i) + \Phi_A(\alpha_{A,t_1}^j, z_{A,t_1}^j) - \Phi_A(\alpha_{A,t_1}^i, z_{A,t_1}^i) - W_{A,t_2}^j + W_{A,t_2}^i \\ & + W_{A,t_1}^j - W_{A,t_1}^i + v_{AB,t_1t_2}^{ij} \end{aligned} \quad (12)$$

At this stage, it is obvious that the triple-differences mainly reflect the difference in pattern of the antenna to be calibrated. As the phase wind-up terms do not vanish for the antenna to be calibrated, they are modelled. Further information on phase wind-up can be found in Wu et al. (1993). Eq. 12 supposes that the whole PCC is contained in the PCV. Otherwise, the PCO would explicitly appear in this equation (in $\rho_{AB,t_1t_2}^{ij}$).

Another way of thinking about triple-differences is in term of rates. Triple-differences are time-differences of double-differences. As nearly all effects vanish in double-differences taken over very short baselines (for example the troposphere and the ionosphere), these effects do not show up in triple-differences. Only the PCV rate of the antenna to be calibrated (i), the change in geometry (ii) and the phase wind-up (iii) are present in the triple-differences. The PCV rate (i) is artificially increased by rotating the antenna A between the two epochs t_1 and t_2 , leading to $\alpha_{A,t_1} \neq \alpha_{A,t_2}$ and $z_{A,t_1} \neq z_{A,t_2}$. The change in geometry (ii) is due solely to the motion of the GNSS satellites in the time interval between t_1 and t_2 . The coordinates of the nominal MPC of the antenna to be calibrated is kept fixed in space during the calibration. In consequence, the relative position between the reference antenna and the antenna to be calibrated remains unchanged during the whole calibration and the relative coordinates between the two antennas vanish to the first order. The red line in Figure 4 illustrates this constant baseline.

The PCV of the reference antenna vanishes to first order as well: Φ_B is absent from Eq. 12. This proves that the triple-difference approach leads to an absolute calibration. This is in opposition to calibrations obtained with a

double-difference approach: the PCV of the reference antenna does not vanish and therefore, the calibrations are not absolute but relative to the reference antenna. Note that Eq. 12 is very well suited to get an intuitive understanding of the estimation procedure. In practice, however, Eq. 11 is used to compute the observation equation, in order to include the mentioned second order effects.

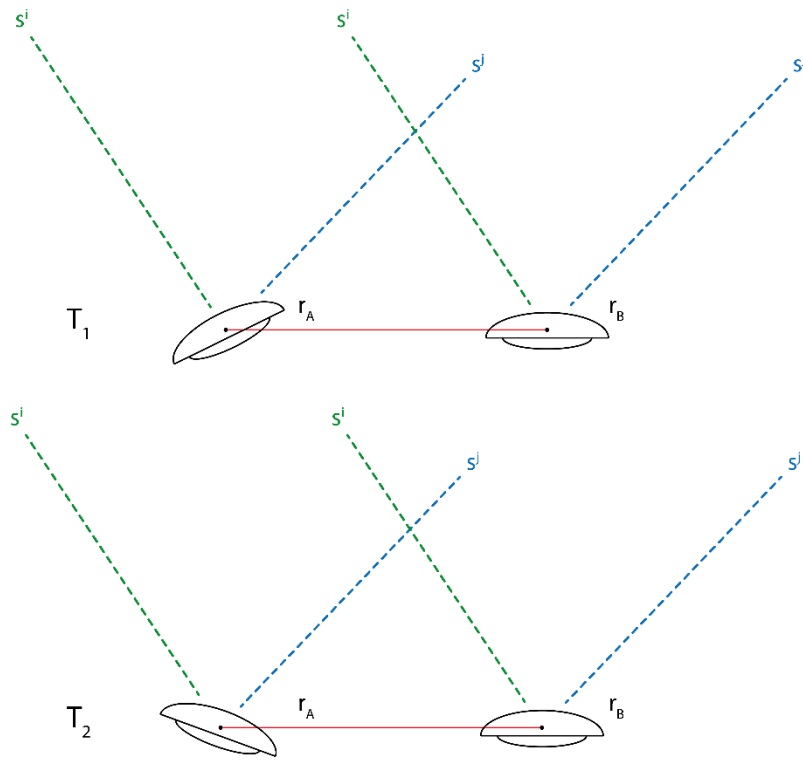


Fig. 4 Schematic representation of triple-differences used for GNSS antenna calibration. The upper part shows the antenna to be calibrated (*A*) and the reference antenna (*B*) during epoch T_1 . The lower part shows the second epoch. The orientation of antenna *A* changes between the epochs, its coordinates however remain unchanged. Therefore, the baseline shown in red is unchanged as well.

EXPERIMENTAL SET-UP

The KUKA Agilus KR 6 R900 sixx robot holding the antenna to be calibrated is set up at one end of a 5 m baseline, the reference antenna on the other end (see Figure 5). The reference antenna is a reference station grade Septentrio PolaNt Choke Ring B3/E6 antenna with dome, mounted on a geodetic pillar. Each of the antennas is connected to a Septentrio PolaRx5 geodetic multi-GNSS receiver.

Calibration sequence

The software QKuka, developed at the Chair of Mathematical and Physical Geodesy at ETH Zurich, controls the motion of the KUKA robot. The robot itself was calibrated before the measurements by means of an optical micro-triangulation system. This ensures that the coordinates of the nominal MPC are kept fixed in space with an accuracy of 0.1 mm (Willi and Guillaume, 2018). The robot calibration parameters obtained from the micro-triangulation, including the orientation and the position of the robot in the WGS84 frame, are used by the QKuka software and applied during the GNSS antenna calibration sequence. The GNSS antenna calibration sequence consists of 1440 different orientations. The base position of the antenna is horizontal and north pointing. Firstly, rotations around the antenna vertical axis are applied in 7.5 degrees steps (leading to 48 different orientations). Secondly, the antenna is tilted in 5 degrees steps up to 70 degrees of tilt (leading to 15 different orientations). The robot tilts the antenna around the y-axis, in order to make the north marker point towards the ground. The resulting 720 orientations are put in a randomized order. Finally, two random rotations between 0 and 360 degree around the antenna vertical axis are applied, leading to the final 1440 orientations. The randomization ensures a good distribution of the satellites over the antenna hemisphere. Furthermore, the randomization ensures that time correlated effects do not have a systematic effect on the final estimation of the PCV. Examples for such effects are residual errors in the robot motion, multipath that is not eliminated by triple-differencing or second order errors due to errors in the PCV of the reference antenna.



Fig. 5 GNSS antenna calibration set-up. The KUKA robot with a JAVAD GrAnt-G3T antenna (to calibrate) is visible in the foreground on the left. On the right, on the white pillar, the reference antenna of type Septentrio PolaNt Choke Ring B3/E6. The length of the baseline is approximately 5 m.

Processing

The robot stays stationary for one second at every of the 1440 orientations, while the average time needed to drive from one orientation to the next is approximately one second as well. The QKuka software logs the start and the end of the robot motion. QKuka is synchronized by a NTP time server, guaranteeing an accuracy better than one millisecond. This information is used to align the 20 Hz GNSS measurements with the robot orientations. One second per orientation and 20 Hz measurements is a good tradeoff between the number of measurements and the total duration of the calibration sequence. On the one hand, the calibration sequence lasts less than one hour. On the other hand, approximately 20 measurements per satellite are available for every orientation, allowing for reasonable outlier detection and rejection and a meaningful statistical analysis. The triple-differences are formed sequentially in time, as displayed in Figure 6. Every observation is used only once. Because every observation is used only once, the triple-differences for orientation k and $k + 1$ are independent from the triple-differences for orientation $k + 1$ and $k + 2$ and the adjustment can be processed sequentially. Unity weighing is applied to the zero-difference observations and the variance-covariance of the triple-differences is obtained after error propagation. The traditional way of weighting observations is a decreased weight with decreasing satellite elevation. This is a consequence of the combination of (i) the longer travel path of signals through the atmosphere and (ii) a smaller GNSS antenna gain for low elevation. The longer travel distance through the atmosphere (i) leads to higher variance of the observations. Furthermore, the signal received at low elevations experience less signal gain because of the gain pattern of the GNSS antenna (ii), which decreases their signal to noise ratio and increases the measurement noise. Decreasing weight with decreasing satellite elevation is meaningful for static antennas because these two effects combine. This is not the case for a rotating antenna, which is potentially tilted in every direction; a low elevation satellite might be received with the maximal antenna gain since the signal enters the antenna at its top. Rather than applying a weighting scale without theoretical evidence, we decided to apply unit weighting.

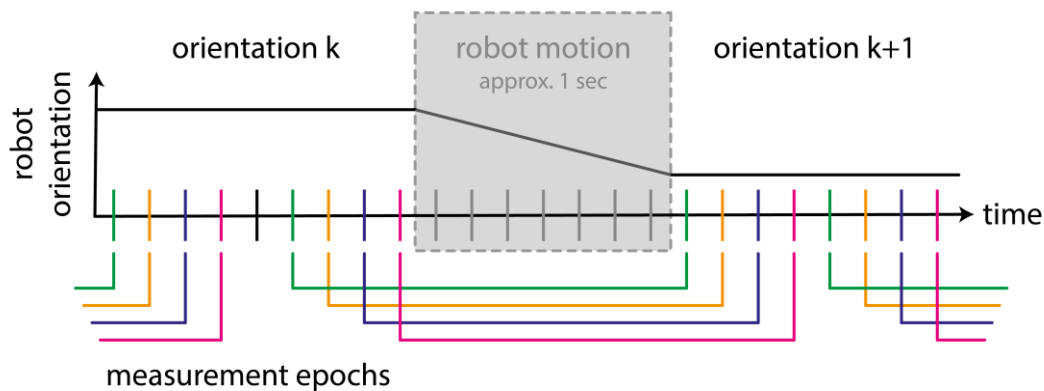


Fig. 6 Illustration of the sequential differencing process. Every stripe is a GNSS measurement epoch. The last n epochs of orientation k are subtracted from the n first epochs of orientation $k + 1$. Every observation is used only once. Supernumerary observations are discarded (for example the 5th observation, shown in black). In case of 20 Hz measurements and 1 second lasting orientations, $n \approx 10$.

CALIBRATION CAMPAIGN RESULTS

A JAVAD GrAnt-G3T geodetic grade GNSS antenna underwent a measurement campaign on 31.1.2018. Three independent calibrations were performed. Table 3 shows the start and the end time of the three calibration sessions. The same calibration sequence was used for the three session. The first 25 minutes of calibration 1 could not be processed, because the measurements are of too poor quality: a very high number of outliers is present in this section of the data. The reason is unknown and the problem could not be reproduced. Possible hypothesis are connection problems between the antenna and the receiver or interferences (unintentional jamming). The data was processed according to the theory and the methodology presented in the previous sections. GPS L1 PCV based on four different parametrizations were generated. Table 4 summarizes the four chosen parametrizations.

Repeatability

Figure 7 illustrates three PCV maps based on a SH12 parametrization. The three PCV were estimated with three different datasets (campaign 1, campaign 2 and campaign 3), using a 20 degree elevation cut-off. At first sight, the pattern look very similar. The main structures are present in all three patterns, namely a plateau at small zenith angles, a hole around azimuth 100 degrees and 60 degrees zenith angle and four main peaks at 90 degrees zenith angle. Calibration 1 differs more, which is due to the fewer data, as mentioned above.

In order to compare two PCV maps, four transformation parameters between the two PCV maps are estimated in a least-squares adjustment and the residuals are analyzed. The spherical harmonics PCC were evaluated at the grid points of a 5×5 deg² grid beforehand. The four parameters are the PCO components δX , δY and δZ (see Eq. 4) and a constant term. Because spherical harmonics are periodic signals, comparisons have to be interpreted with care; a phase shift between the two PCV maps for example would lead to significant differences. The PCO components δX , δY and δZ must be interpreted conservatively as well, as equally weighted grid points are used to estimate the four parameters. Keeping these aspects in mind, the split into PCO difference and PCV difference serves the ease of interpretation.

Another way of comparing PCC would be to analyze coordinate differences between two sets of PCC, as done by Kallio et al. (2018) in a real data experiment. This approach however raises other questions, as the dependency of coordinate repeatability to the satellite geometry or sensitivity to the elevations cut-off angle.

Figure 8 displays the difference between the PCV from campaign 2 and the PCV from campaign 3. The graphical difference shows a better agreement for elevations mid-range than for very high zenith angles. The numerical comparison in Table 5 confirms the very good agreement between the PCV patterns from the three campaigns. Keeping in mind that campaign 1 is weaker, the differences between campaign 2 and campaign 3 are more representative: the difference in horizontal offset is in the range of 0.2 to 0.3 mm, in vertical offset in the range of half a millimeter. The root mean square differences (RMS) is of about 0.6 mm, which indicates a very good agreement between the three maps. The maximum and minimum errors are between approximately -3 mm to 3 mm. They occur close to 90 degrees zenith angle, where the magnitude range of the PCV maps is approximately -3 mm to 6 mm. Overall, these numbers indicate a sub-millimeter repeatability of the PCV estimation.

The difference in vertical offset of 0.59 mm however is higher than expected. Visual inspection of the PCV values for small zenith angles in Figure 7 reveals the origin of these differences. The slope of this very first part of the three patterns is different. However, the questionable part of the pattern covers only a tiny part of the antenna if projected onto a hemisphere and the differences in vertical offsets are clearly overestimated. This is well illustrated by the increase of RMS of only 0.02 mm from 0.62 mm to 0.64 mm when dZ is constrained to zero (see second line of Table 5).

Table 3 Start and end time of the three calibrations performed on 31.1.2018 with the JAVAD GrAnt-G3T geodetic grade antenna and the PRN numbers of the visible GPS satellite. *The first 25 minutes in calibration 1 were discarded because of poor quality. The reason therefor is unknown.

	Start time (GPS time)	End time (GPS time)	GPS PRN #'s
Calibration 1	10 h 26 min 53 sec*	11 h 6 min 27 sec	2, 12, 14, 24, 25, 29, 31, 32
Calibration 2	12 h 21 min 32 sec	13 h 0 min 44 sec	21, 25, 26, 29, 31
Calibration 3	14 h 27 min 31 sec	15 h 6 min 43 sec	16, 20, 21, 26, 27, 29, 31

Table 4 The four chosen parametrizations.

SH8	Spherical harmonics	Order and degree 8
SH12	Spherical harmonics	Order and degree 12
Grid10	Grid	10 x 10 deg ²
Grid5	Grid	5 x 5 deg ²

Table 5 Quantitative comparison between the PCV of campaign 1, 2 and 3 (SH12 parametrization). δX , δY and δZ are the difference in offset (see Eq. 4), RMS is the root mean square of the residuals and Min and Max are the minimum and maximum residuals. * indicates that δZ was constrained to zero.

campaigns	δX [mm]	δY [mm]	δZ [mm]	RMS [mm]	Min [mm]	Max [mm]
31 – 32	-0.03	0.31	1.25	0.64	-2.93	3.45
31 – 33	0.16	0.35	1.84	0.60	-2.49	2.24
32 – 33	0.19	0.04	0.59	0.62	-1.95	2.57
*32 – 33	0.18	0.04	*0	0.64	-1.77	2.90

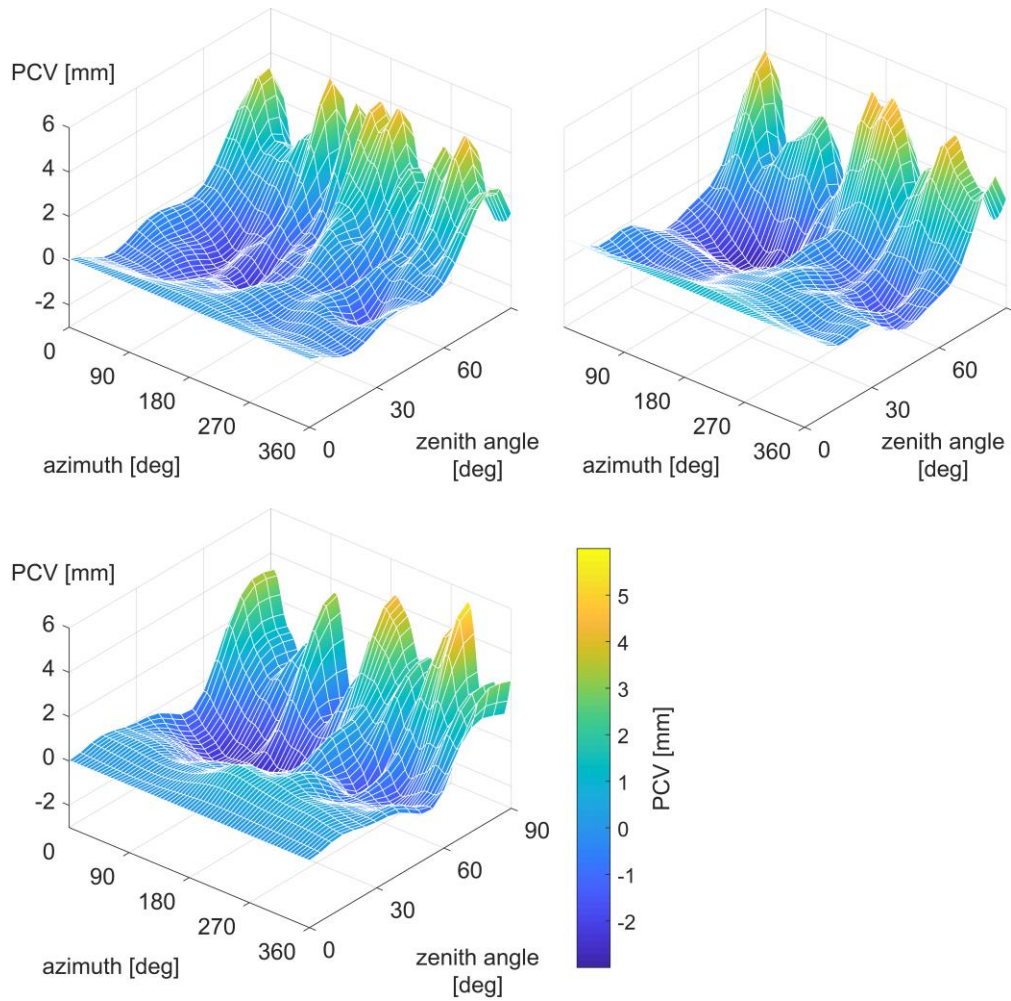


Fig. 7 PCV of campaign 1 (top left), campaign 2 (top right) and campaign 3 (bottom). The parametrization is SH12. The three patterns show the same major structures. Differences arise for low elevations.

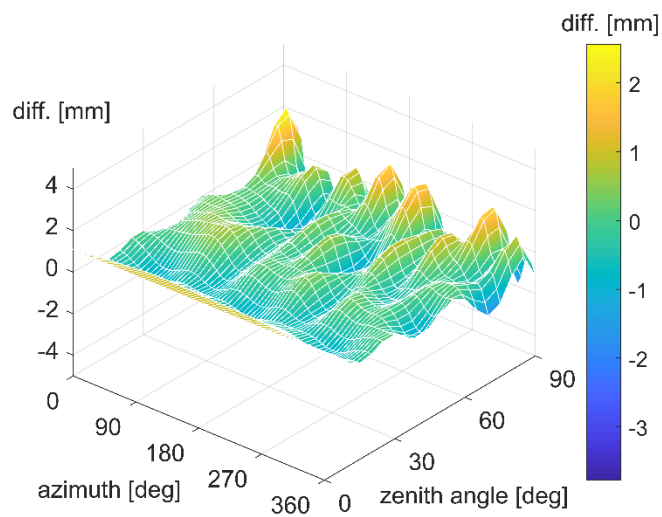


Fig. 8 Residuals between the PCV of campaign 2 and campaign 3 (SH12 parametrization).

Formal errors

Error propagation leads to formal errors between 0.8 mm and 0.9 mm for the PCV map (not shown). These values are in good agreement with the empirical repeatability. Figure 9 shows the ratio between the absolute value of a parameter and its standard deviation: 77 out of the 91 unconstrained parameters are significant to 1σ or more. This indicated that the estimated pattern is significantly present in the data. The standard deviation of an observation a posteriori is 1.55 mm, 1.19 mm and 1.70 mm for campaign 1, 2 and 3 respectively.

Sensitivity to elevation cut-off

The sensitivity of the results to a change in elevation cut-off angle is an indicator for the impact of multipath. The repeatability over different sessions, as presented in the previous section, provides an indication about multipath as well, as multipath is time varying. However, the repeatability is potentially also affected by changes in the satellite constellation geometry. Table 6 holds the results: campaign 2 was processed with an elevation angle of 20 degrees, 25 degrees and 30 degrees. The RMS of the differences does not exceed 0.2 mm. The maximal errors are below 1.5 mm. This indicates that the PCV maps are well decorrelated from multipath, as satellites in low elevations are typically more likely subject to multipath, as low elevation signals have more opportunities to interact with reflectors on ground (Braasch 2017).

Parametrization

Figure 10 presents the two grids, Grid10 and Grid5, estimated with the data from campaign 2. Due to the high number of parameters, the estimations are extremely noisy. The main features visible within the spherical harmonics expansions (see Figure 7) are visible as well (for instance the hole at 100 degrees azimuth and 60 degrees zenith angle). The four peaks at low elevations are present as well, at least in the Grid10 variant. Note that a 10 degree elevation cut-off angle was used to estimate the grids. A cut-off angle of more than 20 degree led to singularities, because not all parameters are observed anymore.

Figure 11 presents the SH8 and the SH12 parametrizations, applied on the same dataset (campaign 2). Expectedly, the resolution increases with a higher degree and order of the spherical harmonics expansion. The main features, however, are preserved even if the resolution is decreased to order and degree 8. In general, both patterns look very similar. Table 7 holds a quantitative comparison. The RMS of the difference is below 0.3 mm and the maximal and minimal errors do not exceed 1.5 mm. As both parametrization, SH8 and SH12, converge to a similar result, we are confident that a SH12 parametrization is a reasonable choice: A further increase in degree and order would reveal more details, but not fundamentally change the PCV map.

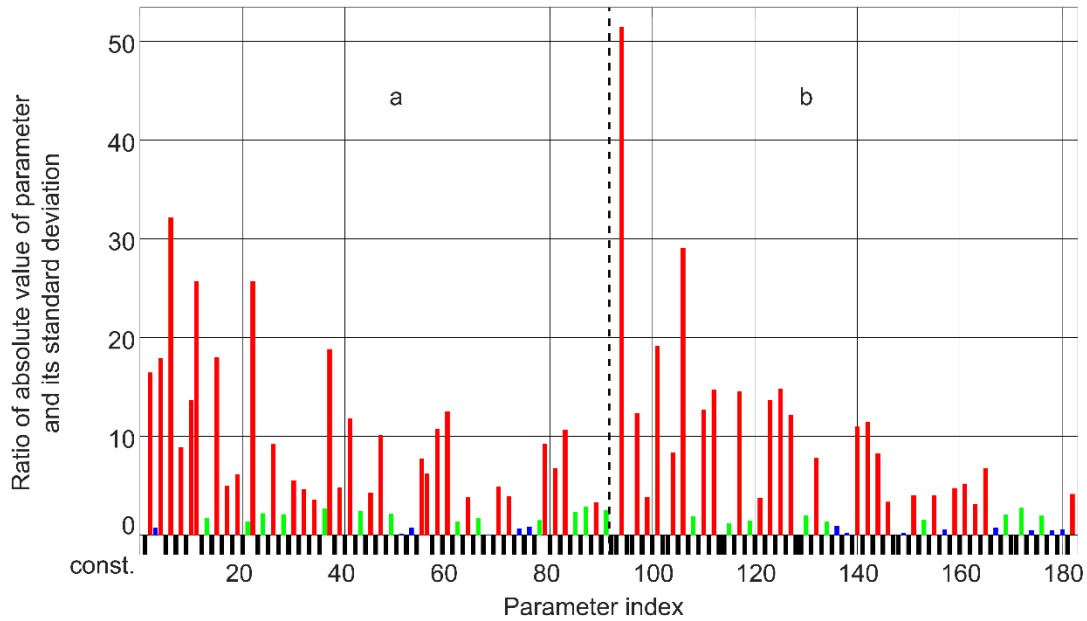


Fig. 9 Ratio between the magnitude of a parameter and its standard deviation for campaign 2 and the SH12 parametrization. Parameters significant to 3σ are shown in red (55 parameters), to σ in green (22 parameters) and not significant parameters (14 parameters) are shown in blue. The parameters shown in black (91 parameters) were constraint to zero during the adjustment (see previous section). The parameters appear in following order: $a_{00}, a_{10}, a_{11}, a_{20}, \dots, a_{87}, a_{88}$, dashed line, $b_{00}, b_{10}, b_{11}, b_{20}, \dots, b_{87}, b_{88}$. Please observe that the coefficients b_{n0} are present in this plot, which is not the case in Figure 3.

Table 6 Quantitative comparison between the PCV of campaign 2 (SH12 parametrization) with 20 degrees, 25 degrees and 30 degrees elevation cut-off. δX , δY and δZ are the difference in offset (see Eq. 4), RMS is the root mean square of the residuals and Min and Max are the minimum and maximum residuals.

	δX	δY	δZ	RMS	Min	Max
elevation masks	[mm]	[mm]	[mm]	[mm]	[mm]	[mm]
20 deg – 25 deg	-0.02	0.00	0.04	0.06	-0.26	0.26
20 deg – 30 deg	0.00	-0.02	-0.16	0.18	-1.43	0.78
25 deg – 30 deg	0.01	-0.02	-0.20	0.16	-1.26	0.61

Table 7 Quantitative comparison between the SH8 and the SH12 PCV (campaign 2).

	δX	δY	δZ	RMS	Min	Max
elevation masks	[mm]	[mm]	[mm]	[mm]	[mm]	[mm]
SH12 - SH8	-0.03	-0.01	0.04	0.28	-1.36	1.42

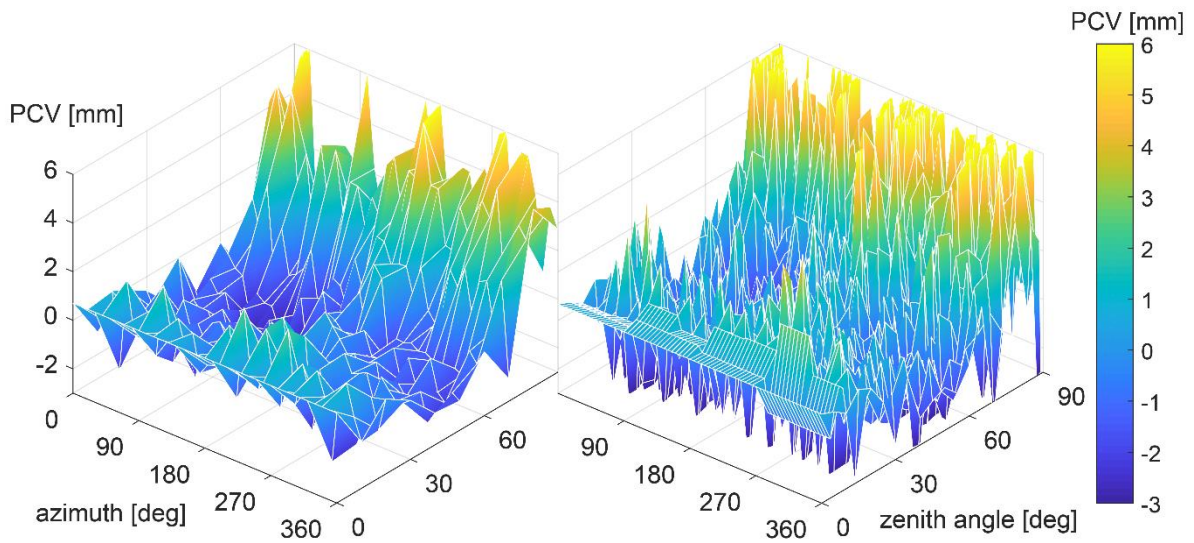


Fig. 10 Grid10 (left) and Grid5 (right) parametrizations (estimated with data from campaign 2). The 5 degrees zenith angle cells were combined to only 4 values, the 10 degree zenith angle cells were combined to only 8 values in order to avoid singularity. For that reason, the right images looks "pixelated" for the values with low zenith angles. Both grids were estimated using a 10 degrees elevation cut-off angle.

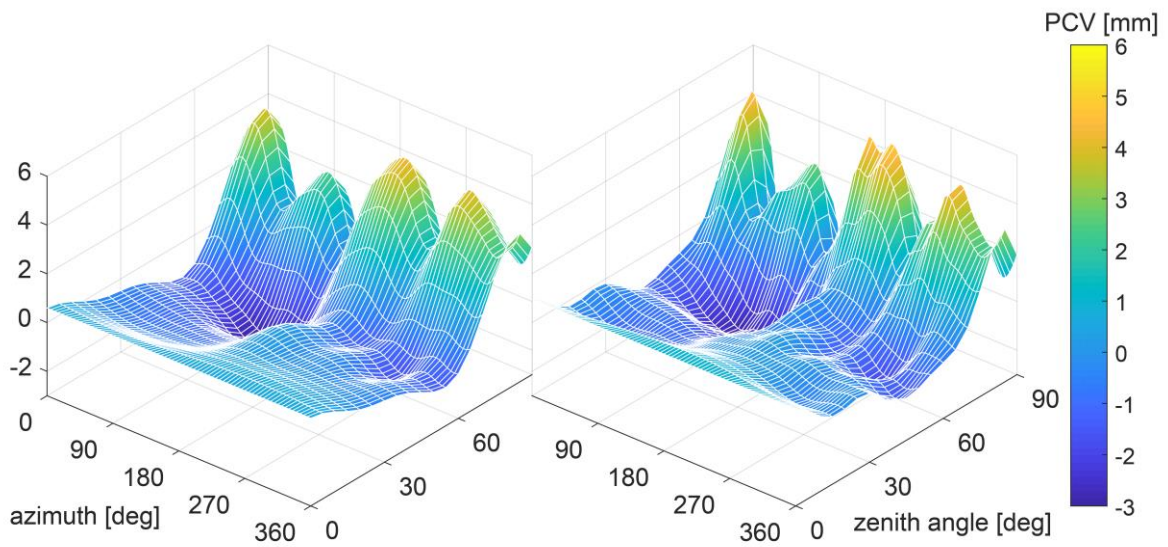


Fig. 11 SH8 (left) and SH12 (right) parametrizations (estimated with data from campaign 2).

CONCLUSIONS

We successfully set up a calibration procedure for GNSS antennas using a KUKA industrial robot. The estimated patterns are plausible. A close look at the formal errors revealed that the PCC are significant. In the case of spherical harmonics, 77 out of the 91 parameters were significant to 1σ or more. We investigated the repeatability of the pattern over three sessions distributed among a quarter of a day. The repeatability is better than a millimeter (RMS of about 0.6 mm), indicating a very good consistency. Another test showed that the PCC are mostly insensitive to a change in the elevation cut-off angle, giving evidence for a good decorrelation from multipath. The RMS difference was always smaller than 0.2 mm. All results were generated with a calibration of only about 40 minutes length. We believe that our calibration system is of interest to the scientific community, as it is already able to provide a fully independent PCV estimation for GPS L1 using real signal.

Outlook

At the time of writing, two Trimble Zephyr antennas, previously individually calibrated by Geo++, are being calibrated with the new system. The goal is a comparison of the Geo++ PCC with our fully independent PCC. If the comparison is successful, PCC for other GNSS and other signals will be estimated. The employed GNSS receivers as well as the processing software is ready for all new signals, including Galileo E5. Additional investigations will contribute to bring the system to more maturity. We see two main fields of improvements: The length of the calibration sequence (i) has to be optimized. The current calibration sequence is rather short. We expect that longer calibration sequences further increase the results. The weighting of the observations (ii) is currently unitary. A signal to noise ratio dependent weighting could enhance the results. A zero-baseline test will show whether such a weighting scheme suits the observations or not.

ACKNOWLEDGMENTS

We would like to thank Robert Presl for the great hardware support, which was essential for the realization of the present study. This work was supported by ETH Research Grant ETH-43 14-2.

REFERENCES

- Bilich A (2017) A new 6-axis robot for absolute antenna calibration at the US National Geodetic Survey. In IGS Workshop 2017, 2017.
- Bilich A, Schmitz M, Görres B, Zeimet P, Mader G, Wübbena G (2012) Three-method absolute antenna calibration comparison. In IGS Workshop 2012, 2012, vol. 23, pp. 631–653.
- Braasch M (2017) Multipath. In Teunissen P and Montenbruck O (Eds) Springer handbook of global navigation satellite systems, 2017. Heidelberg, Germany, pp. 443–468.
- Görres B, Campbell J, Becker M, Siemes M (2006) Absolute calibration of GPS antennas: laboratory results and comparison with field and robot techniques. *GPS Solutions* 10(2):136–145.
- Kallio U, Koivula H, Lahtinen S, Nikkonen V, Poutanen M (2018) Validating and comparing GNSS antenna calibrations. *Journal of Geodesy*, DOI: <https://doi.org/10.1007/s00190-018-1134-2>.
- Riddell A, Moore M, Hu G (2015) Geoscience Australia's GNSS antenna calibration facility: Initial results. In Proceedings of IGNS Symposium 2015 (IGNSS2015), 2015.
- Rothacher M (2001) Comparison of absolute and relative antenna phase center variations. *GPS Sol*, 4(4):55-60.

Rothacher M, Schaer S, Mervart L, Beutler G (1995) Determination of antenna phase center variations using GPS data. In Gendt G, Dick G (Eds) Special Topics and New Directions, 1995 IGS Workshop. Potsdam, Germany, pp. 205–220.

Rothacher M, Schmid R (2006) ANTEX: The antenna exchange format version 1.3, Format specification, IGS Central Bureau, Pasadena.

Schupler BR, Allshouse RL, Clark TA (1994) Signal characteristics of GPS user antennas. *Navigation*, 41(3):276–296.

Sims ML (1985) Phase center variation in the geodetic TI4100 GPS receiver system's conical spiral antenna. In Proceedings of the first International Symposium on Precise Positioning with the Global Positioning System, Rockville, Maryland, USA, pp. 227–244.

Tranquilla JM, Colpitts BG (1989) GPS antenna design characteristics for high-precision applications. *Journal of Surveying Engineering*, 115(1):2–14.

Willi D, Guillaume S (2018) Calibration of a Six Axis Robot for GNSS Antenna Phase Center Estimation. *Journal of Surveying Engineering*, submitted.

Willi D, Meindl M, Hui X, Rothacher M (2017) GNSS Antenna Phase Center Variation Calibration for Attitude Determination on Short Baselines. In Proceedings of ION GNSS+, Portland, Oregon, USA.

Wu JT, Wu SC, Hajj GA, Bertiger WI, Lichten SM (1993) Effects of antenna orientation on GPS carrier phase. *Manuscripta geodaetica*, 18:91–98, 1993.

Wübbena G, Schmitz M, Menge F, Seeber G, Völksen C (1997) A New Approach for Field Calibration of Absolute GPS Antenna Phase Center Variations. *Navigation*, 44(2):247–255.

Appendix E

Curriculum vitae

General data

Name	Daniel Henry WILLI
Date of birth	27.08.1990
Nationality	Swiss
Place of origin	Domat/Ems GR
Postal address	Chemin des Pavés 30, 2000 Neuchâtel
E-Mail	daniel.willi@gmail.com
Languages	Bilingual French (mothertongue) and German
LinkedIn	https://www.linkedin.com/in/daniel-willi-5587a8a1

Education

2012 – 2014	Master in Geomatics and Planing, ETH Zürich. Major in Engineering Geodesy and Satellite Geodesy, and in Geoinformation Sciences and Cartography.
2009 – 2012	Bachelor in Environmental Engineering, EPFL.
2006 – 2009	Federal general qualification for university entrance ('maturité fédérale') with distinction ('mention très bien'), Lycée Denis-de-Rougemont in Neuchâtel.
Before	Primary and secondary school in Täsch, Brig and Neuchâtel.

Professional experience

Since March 2015	Doctoral student at the Institute of Geodesy and Photogrammetry at ETH Zurich.
Since December 2014	Scientific assistant at the Institute of Geodesy and Photogrammetry at ETH Zurich.
January to November 2014	Civil service at the Federal Office for the Environment, Ittigen.
June and July 2012	Internship as surveying engineer at Geoconseil SA, Colombier.

Other activities

- Since 2014 Secretary of the management board of the marching band Neuchâtel.
2010 – 2012 Student member of the EPFL ethics commission.

Awards

- September 2017 Best presentation award in Session F4 at the ION GNSS+ conference 2017, Portland, USA.
October 2016 Best presentation award of the session at the ‘Meet & Share Your Research Day’ of the department D-BAUG, ETH Zurich.
November 2014 Geosuisse-Award for the best master thesis in Geomatics, ETH Zurich.
2009 Physics-Award for the best grade in physics, Lycée Denis-de-Rougemont in Neuchâtel.